Synthesis and oxidation kinetics of Cr_2AlC, V_2AlC & Ti_3AlC_2 MAX phases

A

Thesis

Submitted for partial fulfillment of the requirements for the award of

Doctor of Philosophy

THAPAR INSTITUTE
OF ENGINEERING & TECHNOLOGY
(Deemed to be University)

By

Piyush Sharma

(Registration No. 901412018)

Under the supervision of

Dr. O. P. Pandey
Senior Professor and Head
School of Physics & Materials Science
Thapar Institute of Engineering & Technology, Patiala
Punjab-147004

February, 2021

Dedicated to my grandparents

Late Smt. Usha Rani

&

Sh. Baldev Raj Sharma

Declaration

This is to certify that the thesis entitled **"Synthesis and oxidation kinetics of Cr_2AlC, V_2AlC & Ti_3AlC_2 MAX phases"** being submitted by me **(Piyush Sharma)** in the partial fulfilment of the requirement for the award of the degree of DOCTOR OF PHILOSOPHY in the School of Physics and Materials Science (SPMS), Thapar Institute of Engineering and Technology (TIET), Patiala, Punjab is an authentic record of my own work carried out under the supervision and guidance of **Dr. O. P. Pandey**. The matter presented in the thesis has not been in part or full to any other University or Institute for the award of any other degree.

Piyush

Piyush Sharma

This is to certify that the above statement made by the candidate is true to the best of my knowledge.

8/2/2021

Dr. O. P. Pandey

Senior Professor and Head

School of Physics and materials Science

Thapar Institute of Engineering and Technology

Table of contents

Acknowledgement

It is my pleasure to convey thanks and gratitude to every individual who aided me during my course since I begin the thesis work and ultimately came to the destination.

First and foremost, I would like to express sincere thanks to my supervisor **Dr. O. P. Pandey**, Senior Professor and Head, School of Physics and Materials Science (SPMS), Thapar Institute of Engineering and Technology (TIET), Patiala (India) for giving me the opportunity to work on such a fascinating topic with all necessary supports and continuous guidance throughout my study. His insightful feedback pushed me to sharpen my thinking and brought my work to a higher level. I am deeply grateful to him for providing invaluable, creative and scholarly guidance throughout the course. Honestly, without him the work would not have been crowned with success. His teaching style and enthusiasm for the topic made a strong impression on me and I have always carried positive memories of our discussion sessions. I believe myself lucky to work with such a dynamic, inspiring and courageous personality. There were several moments where he helped me unconditionally and enlighten me with the right passage. Words cannot express how grateful I am for his kindness and generosity.

I would like to thank to **Doctoral Committee** members **Dr. Puneet Sharma**, **Dr. B.N Chudasama** and **Dr. Amjad Ali**, Head School of Chemistry and Bio-Chemistry (SCBC), TIET Patiala for the encouragement, suggestions and fruitful discussions.

I want to express my appreciation to **Dr. Kulvir Singh** for the kindness shown me during difficult times. He extended a helping hand to me when I needed it most. I am eternally grateful to him for believing in me and providing his laboratory access.

I extend my gratitude to all faculty members of the SPMS who supported and encouraged me especially **Dr. B. C. Mohanty**, **Dr. Soumendu Jana** and **Dr. Chandini Khurana**.

I'm deeply indebted to **Dr. P. K. Diwan** Assistant Professor, Department of Applied Physics, U.I.E.T., Kurukshetra University, Kurukshetra (India) for encouraging and supporting during this journey. I really admire one of the precious moments during M.Tech., when he shakes hand to me and said "you are top of the class". He always helped me whenever I approached him.

I truly express my gratitude to one of most wonderful senior **Dr. Gurbinder Kaur** for the valuable suggestions, invaluable contribution, moral support, and guidance to enhance the working skills. She consistently pushed the envelope and churning out new ideas to work competently. She has such a strong positive aura that encouraged each and every person in her surroundings.

I am also grateful to **Dr. Gourav Singla** for familiarizing me with transition metal carbides and autoclave synthesis. His suggestions and help during work inspired me a lot. I am thankful to my seniors **Dr. Suresh Kumar**, **Dr. Paramjot Jha**, **Dr. Gaurav Sharma**, **Dr. Mani Mahajan**, **Dr. Manish Mittal, Dr Suninderjeet and Dr. Mintu Tyagi** for the suggestions and valuable help. I am grateful to **Dr. Akshay Kumar**, Assistant Professor, SGGSWU for valuable help. I am thankful to my colleagues and my lab mates **Dr. Rameez Ahmad Mir, Ruby Priya, Dr. Shivani Singla, Sanjay Upadhay, Raveena, Punit Sharma,** and **Sandeep Kaur** for their company during my research work. My special thanks to **Dr. Rameez Ahmad Mir** for his kind support during the entire journey.

I would also like to thank **Purshottam Singh**, **Mr. Jant Singh**, **Mr. Lal Ji**, **Mr. S. P. Verma**, **Mr. Indermani Mishra**, **Mrs. Neelam Sadana**, **Mrs. Amandeep Kaur** and **Mr. Pardeep Singla** for their help at various stages.

A happy cheerful and joyful environment created by my friends **Dr. Rameez Ahmad Mir**, **Dr. Chhavi Pahwa** and **Dr. Ishita Sharma** is always memorable. I am especially thankful to **Dr. Shagun Kainth** for the moral support. She always supported and encouraged me during all the bad moments. I express my thanks to **Davinder Maan**, **Dr. Aadil Bathla**, **Devender Sillu**, **Dr. Vagish Dwibedi**, **Santosh Kumar Rath, Dr. Nandan Sarkar**, **Arun Rana**, **Santhosh Kumar**, **Kaushlendra Pandey** and **Savidh Khan** for their help whenever required. **Davinder Maan** always encouraged and supported me to finish the work in the best possible way. A special thanks to **Rohit Kumar** (Research Scholar) IITR, Roorkee for the fruitful discussions and suggestions. I am highly thankful to **Dr. Rameez Ahmad Mir**, **Ruby Priya** and **Santhosh Kumar** for helping me to learn Rietveld refinements.

I would like to extend my thanks to **Mr. Ghanshyam Morya**, **Mr. Pradeep** and **Mr. Mukesh Aggarwal** at SAI labs, TIET for their continues support for material characterizations. I am thankful to AIRF JNU and IISER Mohali for TEM/HRTEM and Raman spectroscopy, SAIF PU for FESEM, IIC IITR for TGA/DTA and **D. D. Pal**, IIT Kanpur for XPS.

I owe a debt of heartfelt gratitude to my Mother, **Smt. Uma Sharma** and Father, **Sh. Vipin Sharma**, who always stood my myside and supported unconditionally in every way to achieve what I am today. They made many countless sacrifices and efforts for me to achieve heights. It is worthwhile to acknowledge extraordinary contribution of my grandmother **Late Smt. Usha Rani** and my grandfather **Sh. Baldev Raj Sharma**. They showered their blessing and inspire me for the higher education. I will always remain in debt to them for giving me strength to reach for the stars and chase my dreams. Sometimes we need someone to simply be there. Not to fix our trouble but just to feel that how much we are precious.

I am indebted to my lovable little sister **Mrs. Swatti Sharma**. She supported me relentlessly and made my journey joyful, happier and cheerful. She gave me the strength to live my life to fullest even through difficult times. It is hard to use words to convey my genuine appreciation for the kind of support of **CPT Kapil Sharma** and my beloved nephew **Reyan Sharma**. You are indeed good friends for life. Thanks to never-ending support from all my family members, who provided me encouragements, prayers, and supreme affection.

Above all, I surrender before **Almighty God** to reveal my deepest sense of gratitude to **Bless** me with this beautiful life endeavors. Thanks to God for everything in my life. The good and the bad. Some were blessings and some were lessons. I feel fortunate to have an opportunity of exploring the graces of the nature.

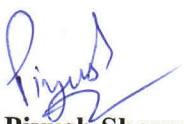

Piyush Sharma

List of Publications

From Ph.D. work

1. **Piyush Sharma**, Kulvir Singh and O.P. Pandey, *Investigation on oxidation stability of V_2AlC MAX phase,* Thermochimica Acta (2021).
2. **Piyush Sharma** and O.P. Pandey, *Thermal kinetics involved during the solid-state synthesis of Cr_2AlC MAX phase,* Journal of Thermal Analysis and Calorimetry 143 (2021) 3997-4008.
3. **Piyush Sharma** and O.P. Pandey, *Non-isothermal oxidation kinetics of nano-laminated Cr_2AlC MAX phase,* Journal of Alloys and Compounds 773 (2019) 872-882.
4. **Piyush Sharma** and O.P. Pandey, *State-of-the-art for the ternary nanolaminated MAX phases: A review* (Comunicated).
5. **Piyush Sharma**, Kulvir Singh and O.P. Pandey, *Synthesis and oxidation kinetics of Ti_3AlC_2 MAX phase under non-isothermal conditions* (Under review).

Other than Ph.D. work

1. Sonia Rani, Sunil Kumar, **Piyush Sharma**, Urmila Berar, S.A. Khan and P.K. Diwan, Energy loss straggling of energetic ions in varying thicknesses of Titanium foils, Vacuum 188 (2021) 110170.
2. Sonia Rani, Sunil Kumar, **Piyush Sharma**, S.A. Khan and P.K. Diwan, Energy loss straggling and subsequent higher order parameters in silver metallic foils, Nuclear Instruments and Methods in Physics Research B 494–495 (2021) 68–73
3. Gurwinder Kaur, **Piyush Sharma**, Ruby Priya and O.P. Pandey, *Thermal dehydration kinetics involved during the conversion of gadolinium hydroxide to gadolinium oxide,* Journal of Alloys and Compounds 822 (2020) 153450.
4. Sunil Kumar, Sonia Rani, **Piyush Sharma**, S.A. Khan and P.K. Diwan, *Energy loss and associated parameters in energy spectra of Li, C and O ions in Nickel foils*, Vacuum 181 (2020) 109606.
5. Aneesh Nair, **Piyush Sharma**, Vishal Sharma and P.K. Diwan, *Effect of UV-irradiation on the optical properties of transparent PET polymeric foils*, Materials Today: Proceedings 21 (2020) 2105-2111.
6. **Piyush Sharma**, P.K. Diwan and O.P. Pandey, *Impact of environment on the kinetics involved in the solid-state synthesis of bismuth ferrite*, Materials Chemistry and Physics 233 (2019) 171-179.

7. **Piyush Sharma**, O.P. Pandey and P.K. Diwan, *Non-isothermal kinetics of pseudo-components of waste biomass*, Fuel 253 (2019) 1149-1161.
8. Rupinderjeet Bains, **Piyush Sharma**, Rameez Ahmad Mir, Suninder Jeet, Gurbinder Kaur, Om Prakash Pandey "*Influence of CuO/MgO ratio on the gene expression, cytocompatibilty, and antibacterial/anticancerous/analgesic drug loading kinetics for (15-x) CuO-xMgO-10P2O5-60SiO2-10CaO-5ZnO (2.5≤ x≤ 12.5) mesoporous bioactive glasses*", Journal of Bio Medical Research A 106 (2018) 2116-2130.
9. **Piyush Sharma**, Taranpreet Kaur, O.P. Pandey, *In-situ single-step reduction and silicidation of MoO_3 to form $MoSi_2$*, Journal of the American Ceramic Society (2018).
10. **Piyush Sharma**, Paramjyot Kumar Jha, P.K. Diwan, O.P. Pandey, *Impact of CuS on the crystallization kinetics of Na_2S-P_2S_5 glasses*, Journal of Non-Crystalline Solids 477 (2017) 31-41.
11. **Piyush Sharma**, P.K. Diwan, *Study of thermal decomposition process and kinetic mechanism of eucalyptus wood*, Wood Science and Technology 51 (2017) 1081-1094.
12. Ramiz Mir Ahmed, **Piyush Sharma,** O.P. Pandey, *Thermal and structural studies of carbon coated Mo_2C synthesized via in-situ single step reduction-carburization*, Scientific Reports 7 (2017) 3518.
13. **Piyush Sharma**, Poonam Uniyal, *Investigating thermal and kinetic parameters of formation of lithium titanate by solid state method*, Journal of Thermal Analysis and Calorimetry 128 (2017) 875-882.
14. **Piyush Sharma**, P.K. Diwan, *Investigation of thermal decomposition parameters of flame retardant impregnated eucalyptus wood*, International Wood Products Journal 7 (2016) 144-148.
15. Gurwinder Kaur, **Piyush Sharma**, Rohit Kumar and O.P. Pandey, *Reaction kinetics during non-isothermal solid-state synthesis of boron trioxide via boric acid dehydration* (Comunicated).

List of Conferences, Seminars, Schools and Workshops (National/International)

1. ICRTRESD 2018 2nd International Conference, January 30-31, BIT Raipur, Chhattisgarh, India.
2. ECERS 2018 Summer School "Process and Properties of Electroceramics for Energy Applications" July 6-7, University of Hasselt, Hasselt, Belgium.
3. Materials Science and Technology (MS&T 2017) October 8–12, David L. Lawrence Convention Center Pittsburgh, PA, USA.
4. ECERS 2017 Summer School "Innovative technologies in the field of ceramic manufacturing" July 7-8, Hotel Novotel Danube, Budapest, Hungary.
5. International Conference on role of microscopy and allied techniques in the development of multifunctional nanomaterials (ICMAMN 2016) November 25-27, Fakir Mohan University, Balasore. Orissa.
6. Summer School of Magnetism (SSM-2016) July 11-15, Thapar University, Patiala. Punjab.
7. 2nd Conference on Microscopy in Materials Science (AMST-2016) February 25-27, Thapar University, Patiala. Punjab.
8. National Workshop on Advanced Techniques for Surface Characterization (2015) October 28-30, Thapar University, Patiala. Punjab.

List of Tables

List of Figures

Chapter 5

Synthesis & Oxidation Kinetics of Ti_3AlC_2 MAX Phase

Chapter 6

Synthesis & Oxidation Kinetics of V_2AlC MAX Phase

PREFACE

MAX phases are the promising class of materials owing to their superior combination of both metal and ceramic properties. This includes high thermal and electrical conductivity, good machinability, great damage tolerability, and outstanding thermal shock resistance. MAX phases are also highly resistant to fatigue, creep, and oxidation. The reports on MAX phases increased exponentially after the discovery of their derivative, i.e., MXenes. Attempts are being made to develop novel MAX phases and their derivatives. This work sheds light on the fundamental aspects, including structure and defects together with the synthesis protocols and oxidation resistance of the MAX phases. The prime objective is to attain a stronger understanding of the synthesis protocol and oxidation performance of the MAX phases. The efforts have been carried out to bring insight knowledge related to mechanisms associated during non-isothermal oxidation in the MAX phases. The oxidation kinetic analysis is performed to gain further knowledge related to oxidation in the MAX phases. The complete work conducted in the present thesis is systematically presented in the seven chapters.

Chapter 1: In this chapter, the current state of the MAX phases (M is an early transition metals, A is a group 13 – 16 elements, X is either C or N) has been addressed. The objective is to introduce basic fundamental aspects related to the MAX phases. A comprehensive discussion referred to the crystal structure of the MAX phases is presented. The theoretical understanding associated to electronic structure and atomic bonding in MAX phases is elaborated. The classification of the MAX phases on the basis of chemical versatility is reviewed. Efforts are also made to bring insight knowledge related to superior properties of the MAX phases. Moreover, the emergent need and significance of Cr_2AlC, Ti_3AlC_2 and V_2AlC MAX phases has been discussed.

Chapter 2: Presents the literature survey on the work done for MAX phases. The progress in the synthesis and characterization of MAX phases has contributed to a stronger understanding of the properties. This chapter focuses to address recent growth in the MAX phase. A better understanding related to the vital role of processing routes to obtain highly pure MAX phases is addressed. Novel synthesis approaches to prepare bulk as well as thin films are highlighted. In addition, some of the MAX phases have shown good resistant to oxidation. The isothermal and non-isothermal oxidation behavior of the MAX phases is elaborated. New strategies developed to design MAX phases with better oxidation resistance and use these phases in nuclear power plants and aerospace industries are discussed. According to literature survey, drawbacks associated to obtain Cr_2AlC, Ti_3AlC_2 and V_2AlC MAX phases and lack of

non-isothermal oxidation studies are discussed. Finally, the objectives of the current thesis are framed on the basis of lacuna observed in the literature.

Chapter 3: In this chapter, the materials and methods employed for the synthesis of Cr_2AlC, Ti_3AlC_2 and V_2AlC MAX phases are presented in details. The synthesis parameters such as temperature, composition and holding time are optimized. The synthesized MAX phases are characterized through numerous techniques such as X-ray diffraction (XRD), Field emission scanning electron microscopy (FESEM), Transmission electron microscopy (TEM), High resolution (HRTEM), Selected area energy diffraction (SAED), X-ray photoelectron spectroscopy (XPS), Thermogravimetry analysis (TGA) and Differential thermal analysis (DTA). A concise summary of all the characterization techniques is presented in this chapter. The procedure adopted to examine the non-isothermal synthesis and oxidation kinetics of Cr_2AlC, Ti_3AlC_2 and V_2AlC is elaborated. The theoretical background associated with the thermal kinetics analysis is presented.

Chapter 4: The formation of nanolaminated Cr_2AlC MAX phase by using solid state synthesis route has been investigated. The mixture of chromium (Cr), aluminum (Al) and graphite (C) in different compositions are sintered at various temperatures (800 – 1300 ℃). The intermediate phases formed during synthesis of Cr_2AlC phase are determined and reaction pathway is established. The synthesis kinetics involved during formation of Cr_2AlC phase is also determined. The prepared Cr_2AlC phase is characterized through XRD, FESEM, HRTEM and SAED techniques. The non-isothermal oxidation kinetics of the Cr_2AlC phase is examined through a TGA/DTA technique, at variable heating rates. The TGA/DTA results show that the oxidation of the Cr_2AlC phase occurred in two stages. The multi-stage kinetic analysis is performed to establish the nature of the oxidation process. The kinetic triplets (activation energy, pre-exponential factor and reaction mechanism) are estimated for the oxidation process in the Cr_2AlC MAX phase.

Chapter 5: The synthesis of Ti_3AlC_2 MAX phase is presented in the chapter. The role of experimental conditions to obtain highly pure Ti_3AlC_2 phase is investigated. The mixture of titanium (Ti), titanium carbide (TiC) and aluminum in different molar ratios are pelletized and heat treated in an argon atmosphere. The pathway responsible for the formation of Ti_3AlC_2 is identified. The synthesis kinetic parameters are also evaluated during formation of Ti_3AlC_2 MAX phase. The micrographs of fractured Ti_3AlC_2 demonstrated a layered structure corresponding to the MAX phases. HR-TEM, SAED and XPS analysis also confirmed the formation of Ti_3AlC_2 MAX phase. The oxidation stability of Ti_3AlC_2 is testified under non-isothermal condition through a DTA technique. The oxidation kinetics responsible for the

oxidation of Ti_3AlC_2 MAX phases is evaluated. The kinetic triplets involved during oxidation process are determined. The oxidation reaction pathway is proposed and the oxidation reaction mechanism is evaluated.

Chapter 6: The impact of synthesis parameters during the formation of V_2AlC MAX phase is studied. The formation pathway of V_2AlC is proposed with the help of XRD analysis. A highly pure V_2AlC phase is observed when the vanadium, aluminum and carbon are mixed in 2:1.3:1 and sintered at 1500 ℃ in an argon atmosphere. The synthesized sample is characterized through XRD, FESEM, HRTEM, SAED, XPS and DTA techniques. The stability of V_2AlC phase is examined in air atmosphere and oxidation kinetic analysis is performed. The reactions involved during oxidation of V_2AlC phase are determined through thermodynamic calculations and XRD results. The DTA analysis demonstrated two exothermic peaks during oxidation of V_2AlC MAX phase. The kinetic parameters are evaluated for both oxidation stages. Finally, the reaction mechanism responsible for the oxidation in V_2AlC is proposed.

Chapter 7: The outcome of the present thesis is concluded in this chapter. The results demonstrated that the synthesis parameters play vital role during synthesis of the MAX phases. The oxidation of the MAX phases under non-isothermal conditions is outlined. The reaction pathways responsible for the synthesis and oxidation of the MAX phases is compiled. The oxidation kinetic analysis of Cr_2AlC, Ti_3AlC_2 and V_2AlC MAX phases is summarized. The future prospective of the prepared MAX phases are suggested in the chapter.

CHAPTER 1
INTRODUCTION

Overview

MAX phases are the class of layered nanolaminated materials that possess the combination of astonishing properties of metals and ceramics. These include high thermal and electrical conductivity, excellent machinability, good damage tolerability and superb thermal shock resistance when compared with binary carbides and nitrides. In addition, some of the MAX phases are good resistant to fatigue, creep, and oxidation. The reports on MAX phases increased exponentially after the discovery of their derivative, i.e., MXenes. In this chapter, the fundamental aspects, classification, properties and applications of MAX phases have been discussed.

1.1. Introduction

Over the years, the refractory binary transition metal carbides and nitrides have emerged as a crucial industrial materials [1]. These binary compounds are commonly named as MX phases, in which M refers to transition metals and X refers to C or N. The MX phases possess high elastic moduli, good mechanical properties, high oxidation, and corrosion resistance, etc. These phases have shown great potential in variety of industrial applications such as cutting and grinding tools, bearings, textile-machinery components, semiconductors and oxidation-resistant gas burners etc. [2–5]. However, beside of their wide range of applications, MX phases are poor in thermal and electrical conductivity, hard to machine, low damage tolerability and highly brittle. A possible way to overcome these drawbacks is to introduce metallic properties in the MX phases. This results into the discovery of the nano-laminated carbides and nitrides known as MAX phases, here A represents metals.

The history of the MAX phases began with the report of Nowotny and co-workers [6] in 1960s. They were the first to discover large number of layered carbides and nitrides and labelled them as H-phases, where H denotes hexagonal close-packed structure. These phases possess general formula M_2AX and termed as 211 phases. Later in 1967, two new 312 phases (Ti_3SiC_2 and Ti_3GeC_2) with chemistry M_3AX_2 were added by the Nowotny's group [7,8]. Furthermore, the Russians in mid 70s also published series of reports on the MAX phases [9–11]. Despite of this great success, these phases remained unexplored until 1990s. The interest in the MAX phases was revived after approximately 30 years with the revolutionary contribution of Barsoum and El-Raghy [12]. They synthesized pure phase Ti_3SiC_2 and investigated mechanical, electrical, and thermal properties. This research group recognized MAX phase as thermodynamically stable class of layered nanolaminated compounds. Afterwards, MAX phases significantly attracted the scientific community due to its remarkable blend of both metal and ceramic properties [13]. These phases are light in weight, offers good stiffness, easily machinable, high thermal shock and oxidation resistant. Through these reports, it was confirmed that these phases have a basic structure and exhibit similar properties. The unique combination of properties emphasizes the potential of MAX phases for plethora of applications such as in high temperature structural applications, protective coatings, sensors, low friction surfaces, electrical contacts and many more [14].

Recently, the discovery of quaternary MAX phases took the curtain back for many more possible MAX phases. The chemical diversity is the potential pathway to hunt new MAX phases with desired properties [15]. In addition, MAX phases are precursors to their two-dimensional (2D) derivatives, i.e., MXenes [16]. The MXenes are proven to be large host for

various technological applications. These advancements have boost attention of scientific community in MAX phases. Several articles have been published to address various synthesis procedure, chemical diversity, and properties of bulk as well as thin film MAX phases. Such growth in research interest is advantageous for the development of novel MAX phases with superior properties.

1.2. Fundamental of the MAX phases

The $M_{n+1}AX_n$ phases are nanolaminated hexagonal compounds with space group $P6_3/mmc$. This general term ($M_{n+1}AX_n$) was latter abbreviated as MAX phase, where *M* is an early transition metals, *A* is a group 13 – 16 elements, *X* is either C or N and *n* being integer (*n* = 1 to 3) [13]. Till date, the elements considered to prepare MAX phases are presented in Fig. 1.1. The fundamentals of MAX phases comprise of structure, and atomic bonding.

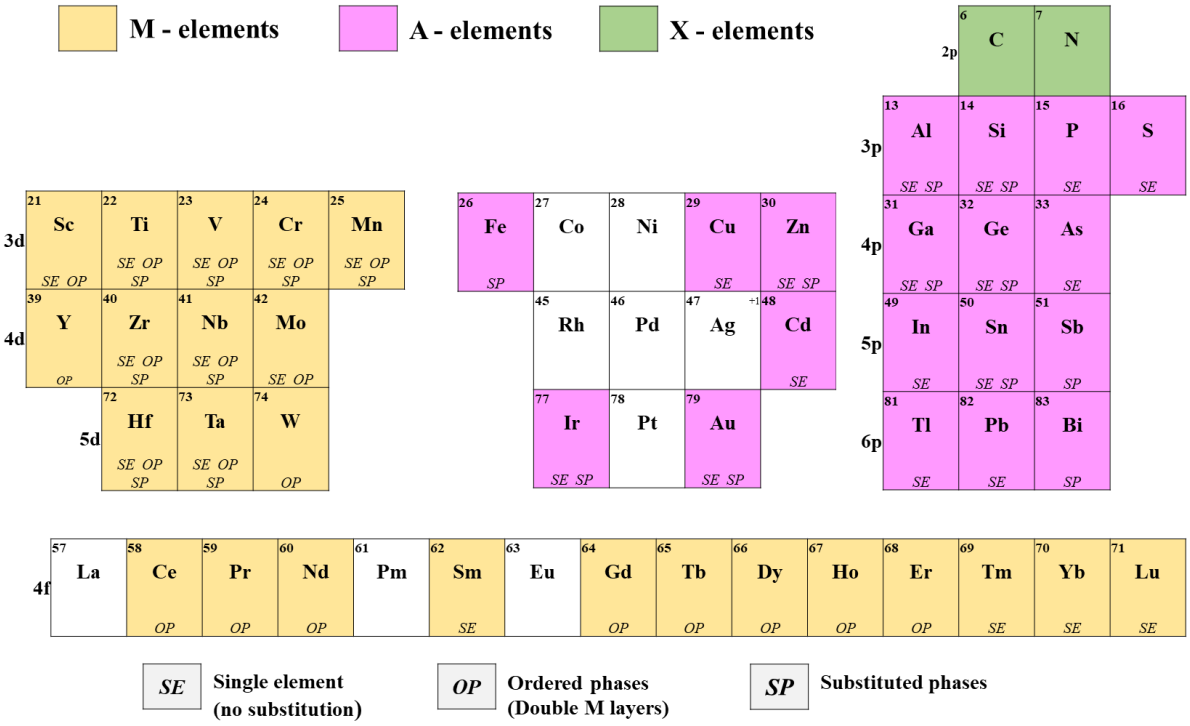

Fig. 1.1 Elements in periodic table that reacts to form MAX phases.

1.2.1. Structure of the MAX Phases

The $M_{n+1}AX_n$ phases possess two formula units per unit cell. The *M* layers are intercalated with a single *A* layer, having *X* in the octahedral sites between *M* layers [17]. The atoms of the *A* layers are accommodated in the core of the larger right angled trigonal prism. The major difference in the structure with different *n* values is the number of *M* layers splitting *A* layers (Fig. 1.2) e.g. in the M_2AX (211) phase, there are two, in M_3AX_2 (312) phase, it is

three and four in the M_4AX_3 (413) phase. The edge-sharing MX_6 octahedra are one of the fundamental building blocks of MAX phases.

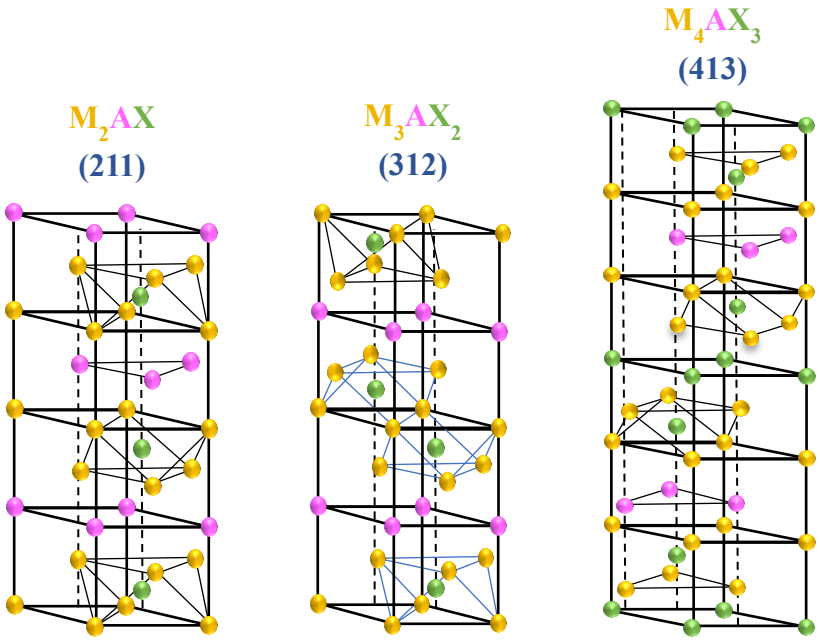

Fig. 1.2 The crystal structure of 211, 312 and 413 MAX phases.

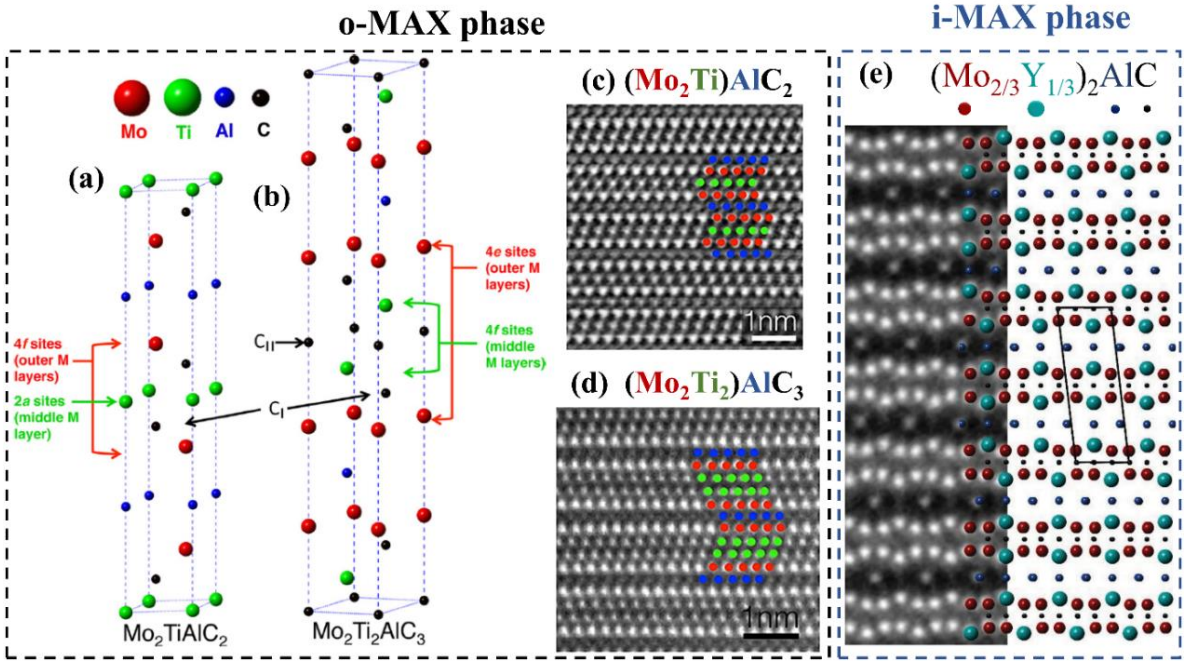

Fig. 1.3 The chemical order in (a-d) $(M^I, M^{II})_3AX_2$, $(M^I, M^{II})_4AX_3$ o-MAX phases[18,19] and (e) i-MAX phases [20]. (Taken with permission)

These octahedra have NaCl-type structure like that of the binary carbides and nitrides. Moreover, there are two M sites in M_3AX_2 (312) and M_4AX_3 (413) phases [21]. One of the M site (M_I) is next to A and another one (M_{II}) is close to X. In addition to two M sites, the M_4AX_3 (413) MAX phases also possess two non-equivalent X sites (X_I, X_{II}). In 413 phases, M_I site is

attached to X_I and M_{II} with X_{II}. This results into the appearance of the MX layers twinning with A layer as a mirror plane. Fig. 1.3 a-e demonstrates the twinning of the MX layers and the typical 'zig-zag' stacking in the MAX phases.

In the MAX phases, there is a correlation between the lattice parameter and the distance between M-M layers in the corresponding binary carbides and nitrides (d_{M-M}). The M-M layer distance in the MAX phases is almost similar with the MX phases. In the view point of the MX phases, the MAX phases are considered as the interstitial compounds where *A* and *X* atoms are located at the interstitial sites [22]. This results into increase in the *c* parameter. Therefore, the *c* parameter in 211, 312 and 413 MAX phases is composed of 4, 6 and 8 *M* layers per unit cell, respectively. Further, the relationship between the *c* parameter and diameter (d_A) of A element is complex. When d_A < 2.5 Å, the *c* parameter is small and increases slightly with increase in d_A. This is due to the small size of A atoms that allow to form strong d-d bonds between the M-M layers. At around 2.5 Å, the dependency of *c* parameter is strong. In the case of d_A > 2.6 Å, the value of *c* parameter is more or less independent of d_A. It implies that the d-d bonds between A atoms and M-M layers are not formed or quite weak and hence, *c*-axis increases. The MAX phases own anisotropic structure and possess typical values of the lattice parameters. The value of *a* lattice parameter is ~ 3 Å for the 211, 312, and 413 MAX phases. However, the value of *c* parameters varies with the stoichiometry of the MAX phases i.e. ~ 13 Å for 211, ~ 18 Å for 312, and ~ 23 – 24 Å for 413 phases [21]. In the MAX phases, c/a ratio rely in between 4 – 8. It is worthwhile to point out that the integer *n* value in $M_{n+1}AX_n$ phases may be greater than three. The literature evidenced the existence of Ta_6AlC_5 [23], Ti_7SnC_6 [24] and $(Ti_{0.5},Nb_{0.5})_5AlC_4$ [25] MAX phases. However, the synthesis of these phases is complex and to date, no MAX phase with n > 3 has been synthesized in the pure form. The increase in the value of *n* also brings more similarities in the properties of the MAX phases and their corresponding MX phases.

1.2.2. Electronic structure and atomic bonding

The MAX phases hold blend of metallic, covalent, and ionic bonding. Several research groups are actively working to understand the electronic structure and bonding in MAX phases through theoretical modelling [26,27]. The first theoretical study was conducted by Ivanovsky and co-workers [28] on the electronic structure of Ti_3SiC_2 MAX phase. In the early days, the total density of states (DOS) and computed data was compared with the XPS experimental results. Afterwards, the discovery of new MAX phases draws attention of many theoretical scientist to explore their electronic structures. This led to the implementation of novel computational methods to understand the electronic structure of the MAX phases [29]. Hence,

literature evidenced various theoretical studies on the electronic structure and bonding in the MAX phase. The theoretical work suggested that the electronic structure of MAX phases exhibits strong covalent d orbitals of the M and 2p orbitals X atoms. These strong interactions are observed in between -2 to -5 eV below the E_F. While pd_σ bonds form in between the M and A atoms. The overlapping between the d electrons of M and p electrons of A are weaker as compared to M-X bonding, in the energy range -1 to 0 eV from E_F. The theoretical studies also revealed that mostly d-d M orbitals are present at the Fermi level. Furthermore, the Raman vibrations for the MAX phases were decoded and found to be comparable with the experimental results [30]. In MAX phases, the low-energy shear mode and high-energy vibrations are observed along *a* and *c* direction, respectively. The shear mode occurred due to M and A atoms, while high energy vibrations are associated with the involvement of X atoms. The low energy vibration clearly indicated the weak bonds between M and A atoms as compared to the M-X. Since, a large number new MAX phases have been discovered, so, more theoretical studies are required to understand and confirm the above conclusion related to the electronic structure of MAX phases.

1.3. Classification of MAX phases

MAX phases comprise of M (transition metals), A (metals) and X (carbon or nitrogen) elements. In the periodic table, there are 24 M elements, 19 A elements, and 2 X elements (Fig. 1.1). The chemical versatility of MAX phases possesses several permutations and combinations [31]. On the behalf of chemical versatility, the MAX phases can be classified in four types such as MAX phases without substitution or doping, solid solutions of MAX phases, ordered MAX phases and intergrown MAX phases.

1.3.1. MAX phases without substitution or doping

In these MAX phases, there are only three elements corresponding to transition metals (M), metals (A) and carbon or nitrogen (X). For example, Cr_2AlC, V_2AlC, Mo_2GaC, Ti_2AlC, Ti_3AlC_2 and many more.

1.3.2. Solid solution of MAX phases

In MAX phases, there are multiple sites for substitution or doping. Therefore, solid solutions can be formed either at M, A, X, or a combination. This brings new opportunities to design and fabricate MAX phases for a specific application. Schuster and co-workers [32,33] were first to attempt the synthesis of MAX phases solid solutions. After the renewed interest in MAX phases, the previously prepared solid solutions were further optimized. The properties of the MAX phases changes with the substitution such as addition of Mn and Fe at M site and brought magnetic properties in different MAX phases such as $(Cr,Mn)_2AlC$ [34], $(Cr,Fe)_2AlC$

[34], and $(V,Mn)_3GaC_2$ [35]. Magnetic MAX phases are also reported with substitution of Fe, Co, Ni, Mn at A site [36]. The substitution of Cu at A site results in the change of MAX phases symmetry to the monoclinic C2/c space group [37]. At X site, C is substituted with N for example $Ti_3Al(C_{0.5}N_{0.5})_2$ and $Ti_2Al(C_xN_{(1-x)})$ [38]. It is observed that these X site substituted carbonitrides have 20 % vacancies on X site. A broadening of XRD peaks is observed in carbonitrides. This strong broadening is associated with the content of C and N in the MAX phases.

1.3.3. Ordered MAX phases

Ordered MAX phases have been discovered with M site substitution. The ordered MAX phases can be classified into two types, i.e., out-of-plane (o-MAX) and in-plane (i-MAX) ordered MAX phases. Lui and co-workers [39] were the first to discover $(M^I, M^{II})_3AC_2$ (312) o-MAX phase by substituting Ti with Cr in Cr_2TiAlC_2. The crystal structure, symmetry, and stacking of the Cr_2TiAlC_2 quaternary phase were the same as that of M_3AX_2 (312) phases. The general formula that describes o-MAX is $(M^I, M^{II})_{n+1}AC_n$. In the o-MAX phases, one M^I layer is sandwiched in between two M^{II} layers in all M-X blocks. Fig. 1.3 demonstrates the chemical order in $(M^I, M^{II})_3AX_2$ and $(M^I, M^{II})_4AX_3$ o-MAX phases. In $(M^I, M^{II})_3AX_2$ o-MAX phase, M^I element is present at 4f Wyckoff site and M^{II} element (substituent) resides at 2a Wyckoff site. However, M^I and M^{II} elements in $(M^I, M^{II})_4AX_3$ o-MAX phases are positioned at two 4e and two 4f Wyckoff sites, respectively. The origin of the o-MAX phases is associated with the interference of the M^{II} element that disturbs the stacking of the M^I element. The substituent (M^{II}) breaks the stacking of M^I elements, where the rock salt structure is missing and restrict center layer occupation. Meshkian and co-workers [40] used rare earth (RE) elements as a substitute in MAX phases. They synthesized Mo_2ScAlC_2 o-MAX phase through pressureless sintering at 1700 °C. However, very few MAX phases with substituted RE elements have been synthesized. The i-MAX phases (In-plane ordered) possess general formula $(M^I_{2/3}, M^{II}_{1/3})AC_3$ and the ratio of $M^I: M^{II} = 2:1$. In these phases, the M^{II} atoms are encapsulated in the hexagonal sequence of M^I atoms (Fig. 1.3). Tao and co-workers [41] were the first to report $(Mo_{2/3}Sc_{1/3})AlC_2$ in-plane MAX phase in 2017. In i-MAX phases, A site atoms possess Kagome lattice-like arrangement. These phases can crystalize in the Cmcm orthorhombic or C2/c monoclinic structures. The M^I and M^{II} atoms reside in the 8f Wycoff site as i-MAX phases crystallize in the C2/c space group. However, A-site atoms acquire partial 4e and 8f Wyckoff sites and X-site atoms partially acquire 4d and 8f. When the i-MAX phase crystallizes in the Cmcm space group, the M^I and M^{II} atoms occupy 16h and 8f sites, respectively. While A-site atoms acquire 8g and 4c and X-site atoms acquire 4b and 8e Wycoff sites.

1.3.4. Intergrown MAX phases

Intergrown MAX phases are the combination of two lower integer *n* value MAX phases. For example, 523 MAX phases comprised of 211 and 312 MAX phases. Palmquist and co-workers [42] were the first to recognize intergrown phases. In intergrown MAX phase, the stacking repeats thrice in the unit cells and the value of c-axis is nearly three times higher than two lower integer *n* value MAX phases. This also results in failure of P63/mmc space group symmetry. In 2011, Scabarozi et al. [43] prepare $Ti_7Si_2C_5$ thin film, where combination of 312 and 413 was observed.

1.4. Properties of MAX phases

The main motivation behind the emergent MAX phases is because of their exceptional properties. In this section, the electrical, magnetic, tribological, and corrosion properties of these nano-laminated compounds are discussed.

1.4.1. Electrical properties

MAX phases are metal-like electrical conductors with very less resistivity at room temperature. Even Ti_3SiC_2 and Ti_3AlC_2 are superior conductors in comparison with Ti metal. The electrical properties of the MAX phases are abstemiously anisotropic because of the difference in the conductivity along the c-axis and a-axis [44]. Some MAX phases (Cr_2AlC and V_2AlC) exhibited higher anisotropy in electrical properties [45]. The resistivity significantly varies with the choice of M element in comparison with A and X elements [46]. A linear increment in the resistivity of MAX phases is observed with a temperature rise. The resistivity also significantly depends on the purity, substitution, synthesis procedure, and crystallinity [47]. The presence of lattice defects and impurities at room temperature results in residual resistivity, which is temperature independent. Higher the ratio of residual resistivity (RRR) signifies that defects or impurities are very few in a crystalline material [48].

Typically, the electrical charge transfer capability of a material is characterized by the Hall Effect, the Seebeck Effect, and magnetoresistance (MR) measurements. MAX phases possess a small value of Hall constant (R_H), which is less susceptible to the temperature. The lowest positive value of R_H was observed with Ti_4AlN_3 where hole carriers were mainly responsible for electrical conductivity [49]. The Hall constant (R_H) value of the Ti_3SiC_2 MAX phase strongly depends on temperature below 100K [50]. As the temperature is raised, the dependency of R_H on temperature decreased for the Ti_3SiC_2 MAX phase. At higher temperatures, the mobility of free electrons is restricted owing to the mobilization of metal ions. The Seebeck coefficient (S) or thermoelectric power values were low in the MAX phases [47]. These studies concluded that the density of electrons and holes remains identical in most

of the MAX phases. Furthermore, the mobility of the charge carriers in the MAX phases was determined by measuring the magnetoresistance (MR). Scabarozi and co-workers [51] found that the magnetoresistance coefficient (α) for different phases of Ti_2GeC is positive. The thin films of Ti_2GeC have a higher magnetoresistance coefficient (α) compared to the bulk. Apart from the above electrical properties, MAX phases also showed superconductivity. Mo_2GaC was the first to be recognized as a superconductor and showed a superconductivity transition at 4.1 K [52]. The reason behind superconductivity in MAX phases might be associated with the populated A layers [53]. It is expected that the T_c could be further improved with doping or substitution in the MAX phases.

1.4.2. Magnetic properties

Several magnetic MAX phases have been theoretically predicted, but surprisingly few were synthesized [54]. Most of the magnetic MAX phases were synthesized in the form of thin films [55]. The bulk synthesis of magnetic MAX phases is challenging job and requires new synthesis strategies. To date, comprehensive knowledge related to the magnetic behavior of MAX phases is rare in literature. The unique mechanical properties of MAX phases open new gateways to support or enhance their magnetic properties. The first theoretical magnetic MAX phase (Cr_2AlC) was thought to exhibit a metastable ferromagnetic configuration [56]. The reason behind ferromagnetic ordering is associated with non-trivial blunders in the calculations. Later, the theoretical model was revised and the antiferromagnetic (AFM) ordering was found to be effective [57]. Unfortunately, both the predictions were not appropriate for the experimental studies. Jaouen and coworkers [58] were the first to evaluate magnetic properties of the Cr_2AlC MAX phase. The average magnetic moment (0.002 μ_B per Cr atom) experimentally observed in Cr_2AlC MAX phase was way less than the prediction (0.9 μ_B per Cr atom).

1.4.3. Tribological properties

MAX phases possess superior mechanical properties that include excellent damage tolerability, ease to machine, and offers high resistance towards thermal shocks. The Vickers hardness of MAX phases lies in between 2-8 GPa. Some MAX phases exhibit a ductile to brittle transition at a temperature above 1000 °C [59]. The nanolaminated structure of MAX phases makes them a suitable candidate as lubricants. These extraordinary properties have shown the application of the MAX phases in the field of tribology. El-Raghy and co-workers [60] studied the tribological behavior of the Ti_3SiC_2 MAX phase. They used the pin-on-disc method to measure the coefficient of friction (μ) and wear rate (WR). It was found that the friction coefficient values linearly increased from 0.15 – 0.4 and then stabilized to 0.8 for fine and

coarse Ti_3SiC_2. Whereas a high average sliding wear rate was observed for fine (1.34×10^{-3} mm^3/Nm) and course (4.25×10^{-3} mm^3/Nm) Ti_3SiC_2. Afterward, various test methods such as oscillating pin-on-disc, ball-on-disc, tab-on-disk, and block-on-disk were used to investigate the tribological properties of the Ti_3SiC_2 MAX phase [61].

1.4.4. Corrosion resistance

The corrosion resistance of many MAX phases has been investigated in acidic as well as basic mediums. Barsoum and his colleagues [62–66] studied the corrosion resistance of Ti_2AlC, $(Ti,Nb)_2AlC$, V_2AlC, V_2GeC, Cr_2AlC, Ti_2AlN, Ti_4AlN_3, Ti_3SiC_2 and Ti_3GeC_2 MAX phases. These studies indicated that Ti-based MAX phases were more susceptible to passivation. A decent corrosion resistance observed in MAX phases is related to the distance between A-layer and M-X layers. Among these MAX phases, Ti_3SiC_2 demonstrated superior corrosion resistance even better than pure Ti. The formation of a SiO_2-based layer was the major reason behind corrosion-resistant of Ti_3SiC_2. Zhu and co-workers [67] compared the electrochemical corrosion behavior of Ti_3SiC_2 with commercially pure Ti. During the anodic oxidation of Ti_3SiC_2 surfaces, the corrosion behavior of Ti_3SiC_2 MAX phase was found to be superior as compared to Ti [64]. The higher corrosion resistance of Ti_3SiC_2 is due to the formation of a thin layer of SiO_2 that passivate the surface from further corrosion. However, under the conditions of the industrial electrolysis of HCl the passivation ability of Ti is found to be higher than Ti_3SiC_2. The higher passivation ability results in better corrosion resistance. The reason behind weaker passivation ability is associated with the layered structure of Ti_3SiC_2 MAX phase and distance between chemical bonds of Ti–C and Ti–Si. The weakly bonded Si and Ti-C layer promoted outward diffusion of Si and resulted in further decomposition of the Ti_3SiC_2 MAX phase. Consequently, a massive amount of Si and Ti was dissolved in the solution with increasing polarization potential. The efficacy of the passivating layer was reduced due to the inhomogeneous diffusion of Si and Ti. However, Ti atoms diffuse homogenously, as a result, passivating ability is enhanced. Recently, the corrosion behavior of Al/Ti_3SiC_2 composite coating on carbon steel was also studied [68,69]. Increasing the content of Ti_3SiC_2 in Al coating increased the corrosion resistance. A substantial increase of 34% in corrosion resistance was observed when 15 % of Ti_3SiC_2 was added to the Al matrix. Therefore, the addition of Ti_3SiC_2 enhanced the durability of the Al coatings on the carbon steels. This coating is highly promising to use carbon steels in the Marine industries.

1.5. Applications of MAX phases

The MAX phases are promising materials for several applications. The potential application of MAX phases in different fields are discussed in detail:

1.5.1. Higher temperature applications

MAX phases possess excellent wear and oxidation resistance even at elevated temperature. The heating element made of MAX phase possesses stable resistance, versatile and applicable for higher temperatures upto 1400 ºC in both inert (argon, nitrogen) and non-inert (air, oxygen) atmospheres [70]. MAX phases are also used to develop foil bearing that can be operatable upto 550 ºC. The superior higher temperature properties of MAX phases also make it suitable to replace metallic alloy-based nozzles in gas burner.

1.5.2. Electrical contacts

MAX phases have shown good electrical conductivity alongwith excellent tribological properties and reasonable mechanical properties. This blend of properties is appropriate for a conductive material used in spark plugs and other parts of an engine [70]. At present, MAX phases are also used to develop pantographs for high-speed electric train in China. In addition, Ti_3SiC_2 MAX phase is also found suitable for electric contacts with SiC based electronic devices.

1.5.3. Nuclear industry

There are few titanium-based MAX phases that offers good damage resistance against radiation. These MAX phases are applicable to enhance the tolerance of Zircaloy tubes to hold the fuel [71]. In this case, MAX phases are sprayed over the Zircaloy tube. This makes Zircaloy tubes more resistant to Pb (lead) or Pb-based alloys.

1.5.4. Aerospace

The coatings of MAX phases can be used to protect the surfaces of the engine components used in the aircrafts [71].

1.5.5. Biomedical

Many researchers have reported biomedical application of Ti_3SiC_2 MAX phase [72]. They found Ti_3SiC_2-hydroxyapatite composite suitable to repair or replace bones. Gao and co-workers [73] suggested Ti_3SiC_2 as a biocompatible material.

1.5.6. MAX phases for Catalysis

MAX phases have also shown potential for catalytic applications. Kumar and co-workers [74] investigated the electrocatalytic activity of various MAX phases including Ti_2AlC, Ta_2AlC, Ti_2SnC, Ti_3SiC_2, V_2AlC, Mo_2TiAlC_2, and Cr_2AlC. The study suggested that Mo_2TiAlC_2 MAX phase demonstrated better catalytic activity for hydrogen evolution reaction in comparison to other un-doped MAX phases.

1.6. Cr_2AlC, V_2AlC and Ti_3AlC_2 MAX phases

Cr_2AlC, V_2AlC and Ti_3AlC_2 MAX phases are extensively studied due to their unusual electrical, magnetic and elastic properties. Among these phases, Cr_2AlC possess better oxidation and corrosion resistance. Sun and co-workers [75] conducted theoretical studies on the elastic properties of the five M_2AlC phases (M: V, Cr, Ta, Ti, Nb). They suggested that the Cr_2AlC phase exhibits the highest Bulk Modulus, the Shear Modulus and the Young's Modulus among the V_2AlC, Ta_2AlC, Ti_2AlC and Nb_2AlC phases [75]. Recently, Pei and co-workers [76] testified that the Cr_2AlC possesses a self-crack healing property at elevated temperatures. In addition, Cr_2AlC MAX phase emerges as a potential candidate for concentrated solar power (CSP) applications. Sarwar et al. [77] studied the thermal performance, flux transmission performance and optical properties of Cr_2AlC and Ti_2AlC MAX phases. They suggested that Cr_2AlC is a better solar receiver as compared to Ti_2AlC. In addition, Cr_2AlC and V_2AlC phases have shown significant potential for magnetic applications in comparison to other MAX phases [78]. The magnetic properties of these phases can be further improved with the substitution or doping. The isothermal oxidation kinetics of Cr_2AlC, V_2AlC and Ti_3AlC_2 MAX phases have been investigated because of the ease of the theoretical interpretation of the data [79–81]. All these unique properties of the Cr_2AlC, V_2AlC and Ti_3AlC_2 depends on the phase purity. These phases have been synthesized in bulk as well as thin films by adopting different synthesis protocols. The advancement in the synthesis protocols and oxidation resistance of these MAX phases are discussed in the next chapter.

References

[1] H. Kindlund, D.G. Sangiovanni, I. Petrov, J.E. Greene, L. Hultman, A review of the intrinsic ductility and toughness of hard transition-metal nitride alloy thin films, Thin Solid Films. 688 (2019) 137479. https://doi.org/10.1016/j.tsf.2019.137479.

[2] L. Toth, Transition Metal Carbides and Nitrides, 1971.

[3] E.R. Hamo, P. Tereshchuk, M. Zysler, D. Zitoun, A. Natan, B.A. Rosen, Corrosion Resistance and Acidic ORR Activity of Pt-based Catalysts Supported on Nanocrystalline Alloys of Molybdenum and Tantalum Carbide, J. Electrochem. Soc. 166 (2019) F1292–F1300. https://doi.org/10.1149/2.0251916jes.

[4] A. Upadhyaya, D. Sarathy, G. Wagner, Advances in alloy design aspects of cemented carbides, Mater. Des. 22 (2001) 511–517. https://doi.org/10.1016/S0261-3069(01)00003-6.

[5] N. Senthilnathan, A. Raja Annamalai, G. Venkatachalam, Sintering of Tungsten and Tungsten Heavy Alloys of W–Ni–Fe and W–Ni–Cu: A Review, Trans. Indian Inst. Met. 70 (2017) 1161–1176. https://doi.org/10.1007/s12666-016-0936-2.

[6] J.C. Schuster, H. Nowotny, C. Vaccaro, The ternary systems: Cr–Al–C, V–Al–C, and Ti–Al–C and the behavior of H-phases (M_2AlC), J. Solid State Chem. 32 (1980) 213–219. https://doi.org/10.1016/0022-4596(80)90569-1.

[7] W. Jeitschko, H. Nowotny, Die Kristallstruktur von Ti3SiC2-ein neuer Komplexcarbid-Typ, Monatshefte Für Chemie. 98 (1967) 329–337. https://doi.org/10.1007/BF00899949.

[8] H. Wolfsgruber, H. Nowotny, F. Benesovsky, Die Kristallstruktur von Ti_3GeC_2 - Kurze Mitteilung, Monatshefte Für Chemie. 98 (1967) 2403–2405. https://doi.org/10.1007/BF00902438.

[9] V.I. Ivchenko, T.Y. Kosolapova, Conditions of preparation of ternary Ti-Al-C alloy powders, Sov. Powder Metall. Met. Ceram. 14 (1975) 431–433. https://doi.org/10.1007/BF00823497.

[10] V.I. Ivchenko, M.I. Lesnaya, V.F. Nemchenko, T.Y. Kosolapova, Some physical properties of ternary compounds in the system Ti-Al-C, Sov. Powder Metall. Met. Ceram. 15 (1976) 367–369. https://doi.org/10.1007/BF00806472.

[11] V.I. Ivchenko, T.Y. Kosolapova, Abrasive properties of the ternary compounds in the systems Ti-Al-C and Ti-Al-N, Sov. Powder Metall. Met. Ceram. 15 (1976) 626–628. https://doi.org/10.1007/BF01159451.

[12] M.W. Barsoum, T. El-Raghy, Synthesis and characterization of a remarkable ceramic: Ti_3SiC_2, J. Am. Ceram. Soc. 79 (1996) 1953–1956. https://doi.org/10.1111/j.1151-2916.1996.tb08018.x.

[13] M.W. Barsoum, MAX phases: properties of machinable carbides and nitrides, 2013th ed., Wiley-VCH, Singapore, n.d.

[14] P. Eklund, J. Rosen, P.O.Å. Persson, Layered ternary Mn+1AXnphases and their 2D derivative MXene: An overview from a thin-film perspective, J. Phys. D. Appl. Phys. 50 (2017). https://doi.org/10.1088/1361-6463/aa57bc.

[15] M. Sokol, V. Natu, S. Kota, M.W. Barsoum, On the Chemical Diversity of the MAX Phases, Trends Chem. 1 (2019) 210–223. https://doi.org/10.1016/j.trechm.2019.02.016.

[16] Y. Zhong, X.H. Xia, F. Shi, J.Y. Zhan, J.P. Tu, H.J. Fan, Transition metal carbides and nitrides in energy storage and conversion, Adv. Sci. 3 (2015) 1–28. https://doi.org/10.1002/advs.201500286.

[17] B.M. Radovic, M.W. Barsoum, MAX phases : Bridging, Am. Ceram. Soc. Bull. 92 (n.d.) 20–27.

[18] B. Anasori, M. Dahlqvist, J. Halim, E.J. Moon, J. Lu, B.C. Hosler, E.N. Caspi, S.J. May, L. Hultman, P. Eklund, J. Rosén, M.W. Barsoum, Experimental and theoretical

characterization of ordered MAX phases Mo_2TiAlC_2 and $Mo_2Ti_2AlC_3$, J. Appl. Phys. 118 (2015) 094304. https://doi.org/10.1063/1.4929640.

[19] B. Anasori, Y. Xie, M. Beidaghi, J. Lu, B.C. Hosler, L. Hultman, P.R.C. Kent, Y. Gogotsi, M.W. Barsoum, Two-Dimensional, Ordered, Double Transition Metals Carbides (MXenes), ACS Nano. 9 (2015) 9507–9516. https://doi.org/10.1021/acsnano.5b03591.

[20] I. Persson, A. el Ghazaly, Q. Tao, J. Halim, S. Kota, V. Darakchieva, J. Palisaitis, M.W. Barsoum, J. Rosen, P.O.Å. Persson, Tailoring Structure, Composition, and Energy Storage Properties of MXenes from Selective Etching of In-Plane, Chemically Ordered MAX Phases, Small. 14 (2018) 1703676. https://doi.org/10.1002/smll.201703676.

[21] M. Magnuson, M. Mattesini, Chemical bonding and electronic-structure in MAX phases as viewed by X-ray spectroscopy and density functional theory, Thin Solid Films. 621 (2017) 108–130. https://doi.org/10.1016/j.tsf.2016.11.005.

[22] M.W. Barsoum, M. Radovic, Mechanical Properties of the MAX Phases, in: Encycl. Mater. Sci. Technol., 2004: pp. 1–16. https://doi.org/10.1016/b0-08-043152-6/01931-8.

[23] Z. Lin, M. Zhuo, Y. Zhou, M. Li, J. Wang, Microstructures and theoretical bulk modulus of layered ternary tantalum aluminum carbides, J. Am. Ceram. Soc. 89 (2006) 3765–3769. https://doi.org/10.1111/j.1551-2916.2006.01303.x.

[24] J. Zhang, B. Liu, J.Y. Wang, Y.C. Zhou, Low-temperature instability of Ti_2SnC: A combined transmission electron microscopy, differential scanning calorimetry, and x-ray diffraction investigations, J. Mater. Res. 24 (2009) 39–49. https://doi.org/10.1557/jmr.2009.0012.

[25] L. Zheng, J. Wang, X. Lu, F. Li, J. Wang, Y. Zhouw, $(Ti_{0.5}Nb_{0.5})_5AlC_4$: A new-layered compound belonging toMAX phases, J. Am. Ceram. Soc. 93 (2010) 3068–3071. https://doi.org/10.1111/j.1551-2916.2010.04056.x.

[26] Y.L. Du, Z.M. Sun, H. Hashimoto, W.B. Tian, First-principles study of polymorphism in Ta_4AlC_3, Solid State Commun. 145 (2008) 461–464. https://doi.org/10.1016/j.ssc.2007.12.018.

[27] P. Rana, R.P. Chauhan, Size and irradiation effects on the structural and electrical properties of copper nanowires, Phys. B Condens. Matter. 451 (2014) 26–33. https://doi.org/10.1016/j.physb.2014.06.015.

[28] A.L. Ivanovsky, D.L. Novikov, G.P. Shveikin, Electronic Structure of Ti_3SiC_2, Mendeleev Commun. 5 (1995) 90–91. https://doi.org/10.1070/MC1995v005n03ABEH000469.

[29] M.T. Nasir, A.K.M.A. Islam, MAX phases Nb_2AC (A = S, Sn): An ab initio study, Comput. Mater. Sci. (2012). https://doi.org/10.1016/j.commatsci.2012.08.003.

[30] O.D. Leaffer, S. Gupta, M.W. Barsoum, J.E. Spanier, On Raman scattering from selected M2AC compounds, J. Mater. Res. 22 (2007) 2651–2654. https://doi.org/10.1557/jmr.2007.0376.

[31] Y. Gogotsi, B. Anasori, The Rise of MXenes, ACS Nano. 13 (2019) 8491–8494. https://doi.org/10.1021/acsnano.9b06394.

[32] J.C. Schuster, H. Nowotny, Investigations of the ternary systems (zr, hf, nb, ta)-al-c and studies on complex carbides., Zeitschrift Fuer Met. Res. Adv. Tech. 71 (1980) 341–346.

[33] S. Sridharan, H. Nowotny, Studies in the ternary system Ti-Ta-Al and in the quaternary system Ti-Ta-Al-C, Zeitschrift Fuer Met. 74 (1983) 468–472.

[34] C.M. Hamm, J.D. Bocarsly, G. Seward, U.I. Kramm, C.S. Birkel, Non-conventional synthesis and magnetic properties of MAX phases $(Cr/Mn)_2AlC$ and $(Cr/Fe)_2AlC$, J. Mater. Chem. C. 5 (2017) 5700–5708. https://doi.org/10.1039/c7tc00112f.

[35] Q. Tao, R. Salikhov, A. Mockute, J. Lu, M. Farle, U. Wiedwald, J. Rosen, Thin film synthesis and characterization of a chemically ordered magnetic nanolaminate

$(V,Mn)_3GaC_2$, APL Mater. 4 (2016). https://doi.org/10.1063/1.4961502.

[36] Y. Li, J. Lu, M. Li, K. Chang, X. Zha, Y. Zhang, K. Chen, P.O.Å. Persson, L. Hultman, P. Eklund, S. Du, J.S. Francisco, Z. Chai, Z. Huang, Q. Huang, Multielemental single–atom-thick A layers in nanolaminated $V_2(Sn, A)C$ (A = Fe, Co, Ni, Mn) for tailoring magnetic properties, Proc. Natl. Acad. Sci. U. S. A. 117 (2020) 820–825. https://doi.org/10.1073/pnas.1916256117.

[37] M. Nechiche, T. Cabioc'H, E.N. Caspi, O. Rivin, A. Hoser, V. Gauthier-Brunet, P. Chartier, S. Dubois, Evidence for Symmetry Reduction in $Ti_3(Al_{1-\delta}Cu_\delta)C_2$ MAX Phase Solid Solutions, Inorg. Chem. 56 (2017) 14388–14395. https://doi.org/10.1021/acs.inorgchem.7b01003.

[38] T. Cabioc'h, P. Eklund, V. Mauchamp, M. Jaouen, Structural investigation of substoichiometry and solid solution effects in $Ti_2Al(C_x,N_{1-x})_y$ compounds, J. Eur. Ceram. Soc. 32 (2012) 1803–11. https://doi.org/10.1016/j.jeurceramsoc.2011.12.011.

[39] Z. Liu, E. Wu, J. Wang, Y. Qian, H. Xiang, X. Li, Q. Jin, G. Sun, X. Chen, J. Wang, M. Li, Crystal structure and formation mechanism of $(Cr_{2/3}Ti_{1/3})_3AlC_2$ MAX phase, Acta Mater. 73 (2014) 186–193. https://doi.org/10.1016/j.actamat.2014.04.006.

[40] R. Meshkian, Q. Tao, M. Dahlqvist, J. Lu, L. Hultman, J. Rosen, Theoretical stability and materials synthesis of a chemically ordered MAX phase, Mo_2ScAlC_2, and its two-dimensional derivate Mo_2ScC_2 MXene, Acta Mater. 125 (2017) 476–480. https://doi.org/10.1016/j.actamat.2016.12.008.

[41] Q. Tao, M. Dahlqvist, J. Lu, S. Kota, R. Meshkian, J. Halim, J. Palisaitis, L. Hultman, M.W. Barsoum, P.O.Å. Persson, J. Rosen, Two-dimensional $Mo_{1.33}C$ MXene with divacancy ordering prepared from parent 3D laminate with in-plane chemical ordering, Nat. Commun. 8 (2017). https://doi.org/10.1038/ncomms14949.

[42] J.P. Palmquist, S. Li, P.O.. Persson, J. Emmerlich, O. Wilhelmsson, H. Högberg, M.I. Katsnelson, B. Johansson, R. Ahuja, O. Eriksson, L. Hultman, U. Jansson, $M_{n+1}AX_n$ phases in the Ti-Si-C system studied by thin-film synthesis and ab initio calculations, Phys. Rev. B - Condens. Matter Mater. Phys. 70 (2004) 1–13. https://doi.org/10.1103/PhysRevB.70.165401.

[43] T.H. Scabarozi, J.D. Hettinger, S.E. Lofland, J. Lu, L. Hultman, J. Jensen, P. Eklund, Epitaxial growth and electrical-transport properties of $Ti_7Si_2C_5$ thin films synthesized by reactive sputter-deposition, Scr. Mater. 65 (2011) 811–814. https://doi.org/10.1016/j.scriptamat.2011.07.038.

[44] A. Nassour, V. Mauchamp, W. Yu, T. Cabioch, L. Piraux, V. Gauthier-Brunet, S. Dubois, Key role of electron-phonon interactions in the electronic conductivity of Ti_3SiC_2: Experiment and ab initio calculations, Phys. Rev. B. 93 (2016). https://doi.org/10.1103/PhysRevB.93.085119.

[45] T. Ouisse, L. Shi, B.A. Piot, B. Hackens, V. Mauchamp, D. Chaussende, Magnetotransport properties of nearly-free electrons in two-dimensional hexagonal metals and application to the $M_{n+1}AX_n$ phases, Phys. Rev. B - Condens. Matter Mater. Phys. 92 (2015). https://doi.org/10.1103/PhysRevB.92.045133.

[46] M.W. Barsoum, I. Salama, T. El-Raghy, J. Golczewski, W.D. Porter, H. Wang, H.J. Seifert, F. Aldinger, Thermal and electrical properties of Nb_2AlC, $(Ti,Nb)_2AlC$ and Ti_2AlC, Metall. Mater. Trans. A Phys. Metall. Mater. Sci. 33 (2002) 2775–2779. https://doi.org/10.1007/s11661-002-0262-7.

[47] T. Scabarozi, A. Ganguly, J.D. Hettinger, S.E. Lofland, S. Amini, P. Finkel, T. El-Raghy, M.W. Barsoum, Electronic and thermal properties of $Ti_3Al(C_{0.5},N_{0.5})_2$, $Ti_2Al(C_{0.5}, N_{0.5})$ and Ti_2AlN, J. Appl. Phys. 104 (2008). https://doi.org/10.1063/1.2979326.

[48] D. Gehlawat, R.P. Chauhan, Study of electronic transport in gamma ray exposed

nanowires, Mater. Res. Bull. 49 (2014) 454–461. https://doi.org/10.1016/j.materresbull.2013.09.032.

[49] P. Finkel, M.W. Barsoum, J.D. Hettinger, S.E. Lofland, H.I. Yoo, Low-temperature transport properties of nanolaminates Ti_3AlC_2 and Ti_4AlN_3, Phys. Rev. B - Condens. Matter Mater. Phys. 67 (2003). https://doi.org/10.1103/PhysRevB.67.235108.

[50] L. Chaput, G. Hug, P. Pécheur, H. Scherrer, Anisotropy and thermopower in Ti_3SiC_2, Phys. Rev. B - Condens. Matter Mater. Phys. 71 (2005). https://doi.org/10.1103/PhysRevB.71.121104.

[51] T.H. Scabarozi, P. Eklund, J. Emmerlich, H. Högberg, T. Meehan, P. Finkel, M.W. Barsoum, J.D. Hettinger, L. Hultman, S.E. Lofland, Weak electronic anisotropy in the layered nanolaminate Ti_2GeC, Solid State Commun. 146 (2008) 498–501. https://doi.org/10.1016/j.ssc.2008.03.026.

[52] L.E. Toth, High superconducting transition temperatures in the molybdenum carbide family of compounds, J. Less-Common Met. 13 (1967) 129–131. https://doi.org/10.1016/0022-5088(67)90055-0.

[53] A.D. Bortolozo, O.H. Sant'Anna, M.S. da Luz, C.A.M. dos Santos, A.S. Pereira, K.S. Trentin, A.J.S. Machado, Superconductivity in the Nb_2SnC compound, Solid State Commun. 139 (2006) 57–59. https://doi.org/10.1016/j.ssc.2006.05.006.

[54] A.S. Ingason, A. Petruhins, M. Dahlqvist, F. Magnus, A. Mockute, B. Alling, L. Hultman, I.A. Abrikosov, P.O.Å. Persson, J. Rosen, A nanolaminated magnetic phase: Mn_2GaC, Mater. Res. Lett. 2 (2017) 89–93. https://doi.org/10.1080/21663831.2013.865105.

[55] A.S. Ingason, A. Mockute, M. Dahlqvist, F. Magnus, S. Olafsson, U.B. Arnalds, B. Alling, I.A. Abrikosov, B. Hjörvarsson, P.O.. Persson, J. Rosen, Magnetic self-organized atomic laminate from first principles and thin film synthesis, Phys. Rev. Lett. 110 (2013). https://doi.org/10.1103/PhysRevLett.110.195502.

[56] M. Dahlqvist, B. Alling, I.A. Abrikosov, J. Rosen, Magnetic nanoscale laminates with tunable exchange coupling from first principles, Phys. Rev. B - Condens. Matter Mater. Phys. 84 (2011). https://doi.org/10.1103/PhysRevB.84.220403.

[57] M. Dahlqvist, B. Alling, J. Rosen, A critical evaluation of GGA+U modeling for atomic, electronic and magnetic structure of Cr_2AlC, Cr_2GaC and Cr_2GeC, J. Phys. Condens. Matter. 27 (2015). https://doi.org/10.1088/0953-8984/27/9/095601.

[58] M. Jaouen, P. Chartier, T. Cabioc'h, V. Mauchamp, G. André, M. Viret, Invar like behavior of the Cr_2AlC MAX phase at low temperature, J. Am. Ceram. Soc. 96 (2013) 3872–3876. https://doi.org/10.1111/jace.12635.

[59] P. Eklund, M. Beckers, U. Jansson, H. Högberg, L. Hultman, The $M_{n+1}AX_n$ phases: Materials science and thin-film processing, Thin Solid Films. 518 (2010) 1851–1878. https://doi.org/10.1016/j.tsf.2009.07.184.

[60] T. El-Raghy, P. Blau, M.W. Barsoum, Effect of grain size on friction and wear behavior of Ti_3SiC_2, Wear. 238 (2000) 125–130. https://doi.org/10.1016/S0043-1648(99)00348-8.

[61] F. AlAnazi, S. Ghosh, R. Dunnigan, S. Gupta, Synthesis and tribological behavior of novel Ag- and Bi-based composites reinforced with Ti_3SiC_2, Wear. 376–377 (2017) 1074–1083. https://doi.org/10.1016/j.wear.2017.01.107.

[62] V.D. Jovic, B.M. Jovic, S. Gupta, T. El-Raghy, M.W. Barsoum, Corrosion behavior of select MAX phases in NaOH, HCl and H_2SO_4, Corros. Sci. 48 (2006) 4274–4282. https://doi.org/10.1016/j.corsci.2006.04.005.

[63] V.D. Jovic, M.W. Barsoum, B.M. Jovic, A. Ganguly, T. El-Raghy, Corrosion Behavior of Ti_3GeC_2 and Ti_2AlN in 1 M NaOH, J. Electrochem. Soc. 153 (2006) B238. https://doi.org/10.1149/1.2199247.

[64] V.D. Jovic, M.W. Barsoum, Corrosion Behavior and Passive Film Characteristics Formed on Ti, Ti_3SiC_2, and Ti_4AlN_3 in H_2SO_4 and HCl, J. Electrochem. Soc. 151 (2004) B71. https://doi.org/10.1149/1.1637897.

[65] J. Travaglini, M.W. Barsoum, V. Jovic, T. El-Raghy, The corrosion behaviour of Ti_3SiC_2 in common acids and dilute NaOH, Corros. Sci. 45 (2003) 1313–1327. https://doi.org/10.1016/S0010-938X(02)00227-5.

[66] C. Padmavathi, A. Upadhyaya, D. Agrawal, Corrosion behavior of microwave-sintered austenitic stainless steel composites, Scr. Mater. 57 (2007) 651–654. https://doi.org/10.1016/j.scriptamat.2007.06.007.

[67] M. Zhu, R. Wang, C. Chen, H. Zhang, G. Zhang, Electrochemical study on the corrosion behavior of Ti_3SiC_2 in 3.5% NaCl solution, RSC Adv. 7 (2017) 12534–12540. https://doi.org/10.1039/c6ra26239b.

[68] R. Jamshidi, O. Bayat, A. Heidarpour, Effect of Ti_3SiC_2 content on the corrosion behavior of Al/Ti_3SiC_2 composite coatings, Mater. Corros. (2020) 1–12. https://doi.org/10.1002/maco.202011635.

[69] R. Jamshidi, O. Bayat, A. Heidarpour, Tribological and corrosion behavior of flame sprayed Al–10 wt% Ti_3SiC_2 composite coating on carbon steel, Surf. Coatings Technol. 358 (2019) 1–10. https://doi.org/10.1016/j.surfcoat.2018.10.087.

[70] M. Atikur Rahman, Study on Structural, Electronic, Optical and Mechanical Properties of MAX Phase Compounds and Applications Review Article, Am. J. Mod. Phys. 4 (2015) 75. https://doi.org/10.11648/j.ajmp.20150402.15.

[71] O. Berger, The correlation between structure, multifunctional properties and application of PVD MAX phase coatings. Part III. Multifunctional applications, Surf. Eng. 36 (2020) 303–325. https://doi.org/10.1080/02670844.2019.1656861.

[72] S.L. Shi, W. Pan, M.H. Fang, Z.Y. Fang, Reinforcement of hydroxyapatite bioceramic by addition of Ti_3SiC_2, J. Am. Ceram. Soc. 89 (2006) 743–745. https://doi.org/10.1111/j.1551-2916.2005.00764.x.

[73] N.F. Gao, Y. Miyamoto, H. Oonishi, D. Zhang, Investigation on the application of Ti_3SiC_2 ceramics for biomaterials, J. Mater. Sci. Lett. 21 (2002) 783–785. https://doi.org/10.1023/A:1015753826417.

[74] K.P. Akshay Kumar, O. Alduhaish, M. Pumera, Electrocatalytic activity of layered MAX phases for the hydrogen evolution reaction, Electrochem. Commun. 125 (2021). https://doi.org/10.1016/j.elecom.2021.106977.

[75] Z. Sun, S. Li, R. Ahuja, J.M. Schneider, Calculated elastic properties of M_2AlC (M = Ti, V, Cr, Nb and Ta), Solid State Commun. 129 (2004) 589–592. https://doi.org/10.1016/j.ssc.2003.12.008.

[76] R. Pei, S.A. McDonald, L. Shen, S. van der Zwaag, W.G. Sloof, P.J. Withers, P.M. Mummery, Crack healing behaviour of Cr_2AlC MAX phase studied by X-ray tomography, J. Eur. Ceram. Soc. 37 (2017) 441–450. https://doi.org/10.1016/j.jeurceramsoc.2016.07.018.

[77] J. Sarwar, T. Shrouf, A. Srinivasa, H. Gao, M. Radovic, K. Kakosimos, characterization of thermal performance, flux transmission performance and optical properties of MAX phase materials under concentrated solar irradiation, Sol. Energy Mater. Sol. Cells. 182 (2018) 76–91. https://doi.org/10.1016/j.solmat.2018.03.018.

[78] A.S. Ingason, M. Dahlqvist, J. Rosen, Magnetic MAX phases from theory and experiments; A review, J. Phys. Condens. Matter. 28 (2016) 433003. https://doi.org/10.1088/0953-8984/28/43/433003.

[79] J. Gonzalez-Julian, S. Onrubia, M. Bram, C. Broeckmann, R. Vassen, O. Guillon, High-temperature oxidation and compressive strength of Cr_2AlC MAX phase foams with controlled porosity, J. Am. Ceram. Soc. 101 (2018) 542–552.

https://doi.org/10.1111/jace.15224.

[80] B. Wang, A. Zhou, Q. Hu, L. Wang, Synthesis and oxidation resistance of V_2AlC powders by molten salt method, Int. J. Appl. Ceram. Technol. 14 (2017) 873–879. https://doi.org/10.1111/ijac.12723.

[81] X.H. Wang, Y.C. Zhou, Microstructure and properties of Ti_3AlC_2 prepared by the solid-liquid reaction synthesis and simultaneous in-situ hot pressing process, Acta Mater. 50 (2002) 3143–3151. https://doi.org/10.1016/s1359-6454(02)00117-9.

CHAPTER 2
LITERATURE REVIEW

Overview

The exceptional properties of the MAX phases have drawn significant attention by the scientific society. Many efforts are carried out to expand the MAX phase family for which synthesis protocols are crucial. The appropriate selection of synthesis protocol also holds the key to hunt many theoretically predicted MAX phases. Several synthesis protocols have been followed to prepare MAX phases. Moreover, MAX phases are eminently applicable for higher temperature applications owing to its superior oxidation resistance. In this chapter, an overview is provided to widen the access of synthesis protocols to produce high-purity MAX phases in bulk, thick and thin films with desired property. The focus is also given to address the oxidation resistance of various MAX phases.

In the previous chapter, details about the MAX phases, their classification, properties and applications have been reviewed and presented systematically. It is realized that the synthesis and thermal stability of the MAX phases are crucial parameters. Considering these aspects, the details of the synthesis protocols and thermal properties of different MAX phases are reviewed with aim to search the existing literature gap and also plan to the research work to be carried for the award of the Ph.D. degree.

2.1. Synthesis Protocols of the MAX phases

Numerous efforts have been made to develop suitable synthesis route to obtain single phase of MAX phases. There are several review articles (Table 2.1) published to address various synthesis protocols, chemical diversity, and properties of bulk as well as thin-film MAX phases. Such expansion in research activity is helpful for the development of novel MAX phases with superior properties. Different procedures have been adopted to get high purity MAX phases. The basic aim of employing different procedures is to improve the purity of the MAX phases. These include pressure-less sintering (PS), reactive hot pressing (HP), hot isostatic pressing (HIP), pulse discharge sintering (PDS), spark plasma sintering (SPS), molten salt method and arc melting. Moreover, thin and thick films of MAX phases are also prepared by chemical vapor deposition (CVD) and physical vapor deposition (PVD) techniques. In this section, synthesis of bulk and films of the MAX phases are reviewed.

2.1.1. Bulk synthesis of MAX phases

In general, synthesis of bulk MAX phase comprises of two processing steps, viz., shaping and sintering. For it the starting materials are milled and converted into desired shapes through various shaping processes (uniaxial pressing, cold isostatic pressing, extrusion etc.). After this, the shaped samples are sintered to obtain dense and strong component. There are some methods that combine these two steps into one step such as HP, HIP and SPS. The early synthesis of MAX phases began in 1960s, when Nowotny and coworkers [1–4] synthesized 30 Hagg phases and some relevant compounds like Ti_3SiC_2 and Ti_3GeC_2 along with impurity phases. Ti_3SiC_2 compound was synthesized through heat treatment of sealed precursors in a graphite capsule at 2000 °C. A series of work on the synthesis of Ti_3SiC_2 was reported by Lis and co-workers [5–7]. They employed combustion synthesis method and thereafter combined combustion method with HIP to obtain dense Ti_3SiC_2. The combustion synthesis method is rapid but results into formation of impure phases. Consequently, the early attempts failed to obtain pure Ti_3SiC_2 MAX phases and unwanted phases were observed in all the cases. Later, Barsoum and El-Raghy [8] synthesized bulk Ti_3SiC_2 by employing HP route at 1600 °C for 4 h with applied load of 40 MPa. They investigated mechanical, electrical and thermal properties

of the prepared Ti_3SiC_2 MAX phase. The results revealed that the compressive strength of the material was 600 MPa, at room temperature. The prepared Ti_3SiC_2 sample showed plastic deformation at higher temperature.

Table 2.1 List of recent review articles published in last five years.

S.No.	Focus/ Outlook	Year	Reference
1.	→ The review compared spark plasma sintering (SPS) with other synthesis methods of MAX-phases. → The impact of different sintering techniques on the mechanical behavior of the MAX phases is addressed.	2020	[9]
2.	→ The review covered all synthesis protocol employed for the synthesis of MAX phases. → An overview is provided to widen the access of synthesis routes to produce high-purity MAX phases with desired property.	2020	[10]
3.	→ The review is focused on the variety of structural defects with different dimension in MAX phases. → The relationship between defects and properties of the MAX phases have been discussed.	2020	[11]
4.	→ The prime objective of the review is to present the chemical diversity of the MAX phases. → The conclusions are drawn related to the possibilities of hunting novel MAX phases.	2019	[12]
5.	→ The review discussed variety of parameters that plays crucial role during thermal decomposition kinetics of Ti-based MAX phases.	2019	[13]
6.	→ The review highlighted the chemical bonding and electronic structure in MAX phases through X-ray spectroscopy and DFT (density functional theory). → A comparison is provided on the trend and relationship between the properties of the MAX phases to the parent binary MX phases.	2017	[14]
7.	→ The review discussed the synthesis and properties of MAX phases and their derivatives from a thin film perspective.	2017	[15]
8.	→ The review summarized the toughening mechanisms in MAX phases and their composites. → Various ways to improve the toughening of MAX phases have been discussed.	2017	[16]
9.	→ The review is focused on the DFT studies conducted on MAX phases, including crystal structure, electronic structure, point defects, lattice dynamics, and related properties, phase stability, compressibility, and elastic properties.	2017	[17]
10.	→ The review presented the experimental and theoretical work on the magnetic MAX phases. → It also summaries the magnetic properties of MAX phases that can be tuned with substitution or doping.	2016	[18]

Afterwards, many MAX phases (Ti_4AlN_3, Ti_3GeC_2, Ti_2AlC, Ti_2AlN, Ti_2GeC, V_2AlC, Ta_2AlC and Nb_2AlC) were reported by Barsoum and co-workers by following reactive hot pressing (HP) and hot isostatic pressing (HIP) synthesis routes [19,20]. In addition, reactive hot isostatic pressing (HIP) technique was employed to prepare Ti_3AlC_2 MAX phase [21]. The results showed 4 vol% secondary phases (mostly Al_2O_3) at a pressure of 70MPa and a temperature of 1400 °C for 16 h. They observed that this compound is isostructural as compared to Ti_3SiC_2. The obtained Ti_3AlC_2 MAX phase was relatively soft, elastically stiff and easily machinable. The failure due to compression of Ti_3AlC_2 was somehow plastic. This revealed that MAX phase compounds are promising nominee for structural applications at both room and elevated temperatures. In order to hunt more suitable routes, many research groups tried and compared different synthesis method to obtain pure and highly dense MAX phases. Wang and Zhou [22] compared two synthesis routes i.e. solid-liquid reaction and HP to fabricate a dense polycrystalline Ti_3AlC_2 MAX phase. In this work, the MAX phase synthesized from simultaneous in-situ hot pressing process resulted into dense Ti_3AlC_2 MAX phase. While in solid-liquid reaction, the milled starting materials were placed in Differential Thermal Analyser (DTA) and the reaction path was investigated. They proposed the reaction path for the formation of Ti_3AlC_2 from Ti, Al and graphite as follows: Firstly, Al powders were melted at around 660 °C; then, Ti–Al intermetallics were formed. Simultaneously, the Ti particles got embedded inside the molten aluminum at 740 °C. After that, the carbon diffusion in the Ti–Al intermetallics at higher temperature led to the formation of carbides Ti_2AlC, Ti_3AlC_2 and TiC. Finally, at 1420 °C Ti_3AlC_2 MAX phase was obtained from the reactions between carbides and unreacted carbon. Furthermore, mechanically activated self-propagating high temperature synthesis (MASHS) route was also tested to obtain Ti_2AlC and Ti_3AlC_2 [23]. The synthesis method combines short time milling process with a self-sustaining combustion (SHS). The presence of TiC was found as impurity, even after taking exact stoichiometry of starting compounds. The results revealed that the SHS method is suitable for MAX phase synthesis because of short processing time that prevented TiC_x saturation with C and Al. At elevated temperatures, the SHS method was not found advantageous for the MAX phase synthesis. The reactivity increased by milling process due to which the formation of MAX phase delayed. The researchers also tested to get novel $M_{n+1}AX_n$ phases with higher *n* value by heat treating prepared 211 phases or the lower *n* value phases. Nb_4AlC_3 MAX phase was firstly synthesized by Hu et al. [24] through annealing of bulk Nb_2AlC at 1700 °C. It was found that the crystal structure of Nb_4AlC_3 was similar as that of Ti_4AlN_3. They also reported that the

Nb_4AlC_3 ceramic has superior anisotropic mechanical properties and exhibit quasi-plasticity [25].

The major issue that arises in the synthesis of bulk MAX phases is the densification. To overcome the issue, pulse discharge sintering (PDS) or spark plasma sintering (SPS) was introduced. Through SPS method, highly dense and rapid sintering of ceramics can be achieved. In this method, rapid sintering of the samples is carried out in a graphite die. The heating is performed by applying direct current (DC) with electrodes connected at the top and bottom of the graphite die. Zhang et al. [26] synthesized of bulk Ti_3SiC_2 MAX phase at 1200°–1400 °C through SPS method. The Ti_3SiC_2 was obtained with < 5 wt% TiC, which was due to the pure starting materials of Ti and Si. The sintering influenced the synthesis of the MAX phase and high purity (> 97 wt%) Ti_2SiC was successfully obtained even at lower temperatures as compared to HIP. They also compared the synthesis of bulk Ti_3SiC_2 by varying starting mixture such as Ti/Si/C, Ti/SiC/C and Ti/Si/TiC. The comparison revealed that the pure Ti_3SiC_2 was fabricated with Ti/Si/TiC mixture at relatively lower temperature with the help of SPS, as compared to other mixtures. Among all these efforts, mainly single phase and dense Ti_3SiC_2 MAX phase was obtained. Afterwards, SPS method was also used to synthesis other MAX phases [27–31]. Besides of all these advantages, HP, HIP and SPS methods cannot be practically used for the large-scale production of MAX phases. In this context, pressureless sintering (PS) method is economical and offers ease of fabrication. The downside of this method is associated with the presence of high content unwanted phases. To overcome these flaws, PS method is combined with HP, HIP and SPS to enhance the densification of MAX phases.

2.1.2. Thin and thick films of MAX phases

In the early days, Ti_3SiC_2 thin films were prepared through chemical vapor deposition (CVD) synthesis method. In the first report, thin film of Ti_3SiC_2 was deposited with a help of gas mixture $TiCl_4$, $SiCl_4$, CCl_4 and H_2 [32]. Afterwards, efforts have been made to establish an optimum condition to obtain pure film of MAX phase. Basically, to synthesize MAX phase thin film through CVD technique required higher temperatures 1000 to 1300 °C. The resulting thin films were impure may be due to the higher decomposition temperature and the presence of unwanted phases on the surfaces. Interestingly, CVD technique shows that thin films of MAX phases can be obtained through simultaneous deposition of all elements as well as a reaction between solid and gas phases. This reaction termed as reactive CVD, which was used to produce MAX phase films [33–35]. To prepare Ti_3SiC_2 thin films through reactive CVD, a thin film of SiC is firstly deposited followed by deposition of $TiCl_4/H_2$ pulse. The formation of

Ti_3SiC_2 occurred due the reaction of the gas with SiC. Besides all these efforts, thin film obtained through CVD contains unwanted phases. Consequently, the CVD method was not considered as an appropriate method for the development of MAX phases thin films. Predominantly single-phase thin film of MAX phase can be prepared through the physical vapor deposition (PVD) technique. Most of the thin films of the MAX phases are synthesized by sputtering techniques. The first thin film of MAX phases was demonstrated by Seppänen et al. [36] and Palmquist et al. [37] through magnetron sputtering technique. They successfully prepared thin film of Ti_3SiC_2 MAX phase. An epitaxial c-axis oriented thin films of Nb_2AlC (211) MAX phase was synthesized by Scabarozi et al. [66] via magneto sputtering. The results showed the growth of a secondary phase $Nb_5Al_3C_x$ with a- and c-axis lattice constants of 7.746 Å and 5.246 Å, respectively. However, $Nb_5Al_3C_x$ compound was not observed in bulk synthesis of Nb_2AlC. A single crystal thin films of Ge-based MAX phases (Ti_2GeC, Ti_3GeC_2 and Ti_4GeC_3) was also synthesized by employing the same technique [44]. New phases $Ti_5Ge_2C_3$ and $Ti_7Ge_2C_5$ were obtained when Ti-Ge-C system was deposited on (0001) Al_2O_3 at 1000 ^{0}C. Later, thin films of other MAX phases were prepared by adopting similar method. However, most of MAX phases thin films were processed at substrate temperatures in the range 800–1000 °C. This restricts the use of substrates that are sensitive to higher temperatures. Furthermore, few MAX phases thin films (Cr_2AlC [67] and V_2GeC [68]) has been synthesized at lower temperature at 450 °C with magneto-sputtering technique. The prime challenge is to reduce the deposition temperature in PVD technique for the synthesis of thin films. In this context, recent approaches such as cathodic arc deposition and pulsed laser deposition (PLD) emerged as promising route for the synthesis of thin films at lower temperatures. Mockut and co-workers [69] synthesized $(Cr_{1-x}\ Mn_x)_2AlC$ through cathodic arc deposition at 600 °C. The Epitaxial (000*n*)-oriented $(Cr_{1-x}\ Mn_x)_2AlC$ showed a magnetic response for highest incorporation Mn (10 at%) above room temperature. Consequently, they verified theoretical prediction of an antiferromagnetic or ferromagnetic ground state for Cr_2AlC upon alloying with Mn. Recently, thin film of Ti_4AlN_3 has been synthesized at lower temperature ~ 450 °C by using the same technique [70]. However, use of the cathodic arc deposition technique to synthesis MAX phase thin film is scarce in literature.

Furthermore, PLD techniques offers capability to handle complex stoichiometries in comparison with other PVD techniques. In other words, exact stoichiometric transfer can be achieved with a single target and highly dense film is obtained. PLD technique require more energy in comparison with other PVD techniques. As a result, processing temperature might reduce during deposition. Many researchers failed to prepare thin film of pure MAX phase via

PLD method [71–75]. Lange et al. [76] attempted to synthesize Cr_2AlC MAX phase by using a pre-synthesized Cr_2AlC target. However, variation in the composition was observed in the prepared films. The thin film of Ti_2AlC was synthesized on the single substrate made of Ti-6Al-4V alloy by using Nd:YAG laser [77]. Recently, Biswas and co-workers [78] successfully developed Ti_3AlC_2 film through PVD technique. They observed that the film was highly oriented along axis (103). Thin film of Ti_3AlC_2 with 2 nm thickness possesses high conductivity and optical transparency. These films demonstrated TENG-based biomechanical touch sense ability. According to the literature survey, the synthesis of the pure MAX phase is challenging, and many compounds of the family require processing breakthroughs.

2.2. Chemical versatility of MAX phases

MAX phases comprise M (transition metals), A (metals) and X (carbon or nitrogen) elements. In the periodic table, there are 24 M elements, 19 A elements, and 2 X elements. The chemical versatility of MAX phases possesses several permutations and combinations [79]. The substitution or doping further extends the possibilities of newer MAX phases. Table 2.2 list all the MAX phases prepared to date without substitution or doping. Moreover, there are three sites in MAX phases for substitution or doping. Therefore, solid solutions can be formed either at M, A, X, or a combination. This brings new opportunities to design and fabricate MAX phases for a specific application. Schuster and co-workers [65,80] were first to attempt the synthesis of MAX phases solid solutions. After the renewed interest in MAX phases, the previously prepared solid solutions were further optimized. Table 2.3 – 2.5 list all the MAX phases with substitution at a single site or multiple sites. The properties of the MAX phases changes with the substitution such as addition of Mn and Fe at M site brought magnetic properties in $(Cr,Mn)_2AlC$ [81], $(Cr,Mn)_2GeC$ [82], $(Cr,Mn)_2GaC$ [83], $(Cr,Fe)_2AlC$ [81], $(Mo,Mn)_2GaC$ [84], $(V,Mn)_2AlC$ [85], and $(V,Mn)_3GaC_2$ [86]. Magnetic MAX phases are also reported with substitution of Fe, Co, Ni, Mn at A site [87]. The substitution of Cu at A site results in the change of MAX phases symmetry to the monoclinic C2/c space group [88]. Horlaits and co-worker [89] prepared Bi-containing $Zr_2(Al_{1-x}Bi_x)C$ ($0 \geq x \leq 1$) MAX phases. They successfully synthesized $Zr_2(Al_{1-0.42}Bi_{0.58})C$ at 1350°C with pressure-less sintering, as it was the only stable composition in the Zr-Al-Bi-C system. Interestingly, the substitution of Bi, Cu, and Au at the A site results in the development of novel MAX phases.

Additionally, ordered MAX phases have been discovered with M site substitution. The ordered MAX phases can be classified into two types, i.e., out-of-plane (o-MAX) and in-plane (i-MAX) ordered MAX phases. Table 2.6 presents ordered MAX phases synthesized to date. Lui and co-workers [90] were the first to discover $(M^I, M^{II})_3AC_2$ (312) o-MAX phase by

substituting Ti with Cr in Cr_2TiAlC_2. Initially, they synthesized the Cr_2AlC MAX phase by using the hot pressing (HP) technique. Thereafter, Cr_2AlC was mixed with TiC in 1:1 and pressureless sintering (PS) was performed at 1500 °C in an argon atmosphere. The crystal structure, symmetry, and stacking of the Cr_2TiAlC_2 quaternary phase were the same as that of M_3AX_2 phases. The general formula that describes o-MAX is $(M^I, M^{II})_{n+1}AC_n$.

Table 2.2 List of MAX phases prepared till date without substitution or doping.

TMs	Without substitution or doping						
	211		312		413		Higher order
Ti	Ti_2AlC[a]	Ti_2GaC[a]	Ti_3AlC_2[38]	Ti_3SiC_2[a]	Ti_4SiC_3[39]	Ti_4AlN_3[40]	Ti_7SnC_6[41]
	Ti_2ZnC[42]	Ti_2SnC[a]	Ti_3GaC_2[a]	Ti_3GeC_2[a]	Ti_4GaC_3[43]	Ti_4GeC_3[44]	
	Ti_2GeC[a]	Ti_2TlC[a]	Ti_3ZnC_2[42]	Ti_3InC_2[45]			
	Ti_2InC[a]	Ti_2PbC[a]	Ti_3SnC_2[46]	Ti_3AuC_2[47]			
	Ti_2CdC[a]	Ti_2SC[a]	Ti_3IrC_2[47]				
	Ti_2AlN[a]	Ti_2GaN[48]					
	Ti_2ZnN[42]	Ti_2InN[a]					
	Ti_2AuN[49]						
Cr	Cr_2AlC[a]	Cr_2GeC[a]					
	Cr_2GaC[a]	Cr_2GaN[48]					
V	V_2AlC[a]	V_2PC[a]			V_4AlC_3[50]		
	V_2GeC[a]	V_2AsC[a]					
	V_2GaC[a]	V_2GaN[48]					
	V_2SnC[51]	V_2ZnC[42]					
Mn	Mn_2GaC[52]						
Zr	Zr_2AlC[53]	Zr_2SC[a]	Zr_3AlC_2[54]	Zr_3SnC_2[28]			
	Zr_2InC[a]	Zr_2InN[a]					
	Zr_2SnC[a]	Zr_2PbC[a]					
	Zr_2TlC[a]	Zr_2TlN[a]					
Nb	Nb_2AlC[a]	Nb_2GeC[55]			Nb_4AlC_3[24]		
	Nb_2AsC[a]	Nb_2InC[a]					
	Nb_2SnC[a]	Nb_2CuC					
	Nb_2GaC[a]	Nb_2SC[a]					
	Nb_2PC[a]	Nb_2CuC[56]					
Mo	Mo_2GaC[a]	Mo_2AuC[57]					
Hf	Hf_2SC[a]	Hf_2InC[58]	Hf_3SnC_2[28]	Hf_3AlC_2[59]			
	Hf_2SnC[a]	Hf_2SnN[60]					
	Hf_2PbC[a]	Hf_2AlC[a]					
Ta	Ta_2AlC[a]	Ta_2GaC[a]	Ta_3AlC_2[61]		Ta_4AlC_3[62]	Ta_4GaC_3[43]	Ta_6AlC_5[61]
Lu	Lu_2SnC[63]						

TMs = Transition Metals. [a]Early MAX phases discovered by Nowotny and co-workers [64,65].

Table 2.3 List of MAX phases prepared till date with M-site substitution or doping.

TMs	M-site substitution			
	211	**312**	**413**	**Higher Order**
Ti	$(Ti_{1-x}Nb_x)_2AlC$[91] $(Ti_{1-x}Ta_x)_2AlC$[80] $(Ti_{1-x}V_x)_2AlC$[64] $(Ti,Zr)_2InC$[92] $(Ti,Hf)_2InC$[93] $(Ti_{1-x}Mo_x)AlC$[94]	$(Ti_{0.5}V_{0.5})_3AlC_2$[95]		$(Ti_{0.5}Nb_{0.5})_5AlC_4$[96]
V	$(V_{0.96}Mn_{0.04})_2AlC$[85]	$(V_{1-x}Cr_x)_3AlC_2$[97]	$(V_{0.5}Cr_{0.5})_4AlC_3$[97]	$(V_{0.5}Cr_{0.5})_4Al_2C_4$[97]
Cr	$(Cr_{1-x}Mn_x)_2GeC$[98] $(Cr_{1-x}V_x)_2GeC$[99] $(Cr_{1-x}Fe_x)_2GeC$[100] $(Cr_{1-x}Ti_x)_2GeC$[100] $(Cr_{0.5}Mn_{0.5})_2AuC$[101] $(Cr_{0.5}Mn_{0.5})_2GaC$[101] $(Cr_{1-x}Fe_x)_2AlC$[81] $(Cr_{1-x}Mn_x)_2AlC$[81] $(Cr_{1-x}V_x)_2AlC$[102] $(Cr_{1-x}Ti_x)_2AlC$[103]	$(Cr_{1-x}Ti_x)_3AlC_2$[104]	$(Cr_{5/8}Ti_{3/8})_4AlC_3$[104]	
Zr	$(Zr_{1-x}Nb_x)_2AlC$[105]	$(Zr_{1-x}Ti_x)_3AlC_2$[106]	$(Zr_{1-x}Nb_x)_4AlC_3$[107]	
Nb	$(Nb_{1-x}Zr_x)_2AlC$[95] $(Nb_{1-x}V_x)_2AlC$[95] $(Nb_{2/3}Sc_{1/3})_2AlC$[108]		$(Nb_{0.5}V_{0.5})_4AlC_3$[95] $(Nb_{0.8}Ti_{0.2})_4AlC_3$[109] $(Nb_{0.8}Zr_{0.2})_4AlC_3$[110] $(Nb_{0.9}Ti_{0.1})_4AlC_3$[111] $(Nb_{0.9}Zr_{0.1})_4AlC_3$[111] $(Nb_{0.9}Hf_{0.1})_4AlC_3$[111] $(Nb_{0.9}V_{0.1})_4AlC_3$[111] $(Nb_{0.9}Ta_{0.1})_4AlC_3$[111]	
Mo				Mo_4VAlC_4[112]
Ta			$(Ta_{1-x}Hf_x)_4AlC_3$[113] $(Ta_{1-x}Nb_x)_4AlC_3$[113]	

TMs = Transition Metals.

In the o-MAX phases, one M^I layer is sandwiched in between two M^{II} layers in all M-X blocks. Vanadium (V) was also used as a substituent to prepare Cr_2VAlC_2 (312) and $Cr_2V_2AlC_2$ (413) o-MAX phases through a single step pressureless sintering route [102]. In Cr_2VAlC_2, the layers of V are fully ordered and 25% V atoms were found in the center of Cr

layers. However, 30 % and 75 % V atoms were confined in the inner of Cr and V layers in $Cr_2V_2AlC_2$, respectively. Moreover, C vacancies were substantial in Cr_2VAlC_2 and $Cr_2V_2AlC_2$ o-MAX phases. These vacancies were considered aiding in upholding the structure of the MAX phase. In 2015, Ti act as a substituent in Mo_2TiAlC_2 and $Mo_2Ti_2AlC_2$ o-MAX phases by a pressureless sintering route at 1600 °C [114]. In the Mo_2TiAlC_2 phase, 25 % of Ti atoms were present in the center of Mo layers, while 100 % of Ti atoms were present in Ti layers. While in $Mo_2Ti_2AlC_2$, 23% and 14% Ti atoms were occupied by the inner of Mo and Si layers, respectively. The ratio of M^{II} atoms occupied outside the M^{I} layer was increased from 2 to 3 with an increase in integer value (*n*). In other words, the total number of M_{II} layers were higher in 312 in comparison with 413. In $(M^{I}, M^{II})_3AX_2$ o-MAX phase, M^{I} element is present at 4f Wyckoff site and M^{II} element (substituent) resides at 2a Wyckoff site. However, M^{I} and M^{II} elements in $(M^{I}, M^{II})_4AX_3$ o-MAX phases are positioned at two 4e and two 4f Wyckoff sites, respectively. The origin of the o-MAX phases is associated with the interference of the M^{II} element that disturbs the stacking of the M^{I} element. The substituent (M^{II}) breaks the stacking of M^{I} elements, where the rock salt structure is missing and restrict center layer occupation. Meshkian and co-workers [115] used rare earth (RE) elements as a substitute in MAX phases. They synthesized Mo_2ScAlC_2 o-MAX phase through pressureless sintering at 1700 °C. However, very few MAX phases substituted with RE elements have been synthesized. Furthermore, o-MAX phases gained more attention not entirely due to their unique structure but also in bringing alternative opportunities for the synthesis of MXenes. For example, the synthesis of Cr-based MXenes from Cr_3AlC_2 is not feasible but with the substitution of Ti, Cr_2TiAlC_2 o-MAX phase has been synthesized [116]. The etching of $(Cr_{2/3}Ti_{1/3})_3AlC_2$ o-MAX phase results in the formation of 2D MXenes flake.

The i-MAX phases (In-plane ordered) possess general formula $(M^{I}_{2/3}, M^{II}_{1/3})AC_3$ and the ratio of $M^{I}: M^{II} = 2:1$. In these phases, the M^{II} atoms are encapsulated in the hexagonal sequence of M^{I} atoms. Tao and co-workers [117] were the first to report $(Mo_{2/3}Sc_{1/3})AlC_2$ in-plane MAX phase in 2017. They calcined the elemental mixture of Mo, Sc, Al, and C at 1500°C for 20 hr in an argon atmosphere. In i-MAX phases, A site atoms possess Kagome lattice-like arrangement. These phases can crystalize in the Cmcm orthorhombic or C2/c monoclinic structures. The M^{I} and M^{II} atoms reside in the 8f Wycoff site as i-MAX phases crystallize in the C2/c space group. However, A-site atoms acquire partial 4e and 8f Wyckoff sites and X-site atoms partially acquire 4d and 8f. When the i-MAX phase crystallizes in the Cmcm space group, the M^{I} and M^{II} atoms occupy 16h and 8f sites, respectively. While A-site atoms acquire 8g and 4c and X-site atoms acquire 4b and 8e Wycoff sites. Afterward, the Dahlqvist group

[118] discovered four new i-MAX phases i.e., $(V_{2/3}Zr_{1/3})_2AlC$, $(Mo_{2/3}Y_{1/3})_2AlC$, $(Mo_{2/3}Y_{1/3})_2GaC$, and $(Mo_{2/3}Sc_{1/3})_2GaC$. The Ga-based i-MAX phases were synthesized by mixing elemental powders of Mo, Sc, or Y and C with shots of Ga in a molar ratio of 4:2:3:3 [119]. The mixture was heat-treated in the presence of an argon atmosphere. Later, Sc and Y rare earth (RE) elements were also used to synthesize W-based i-MAX phases, i.e., $(W_{2/3}Sc_{1/3})_2AlC$ and $(W_{2/3}Y_{1/3})_2AlC$ [120]. The swift expansion in the chemical diversity with the discovery of i-MAX phases attracted the scientific community, and many new i-MAX phases have been developed. Lu and colleagues [121] also used RE elements and synthesized Cr-based MAX phases. They observed that $(Cr_{2/3}Sc_{1/3})_2AlC$ and $(Cr_{2/3}Y_{1/3})_2AlC$ i-MAX phases crystalize in the C2/c monoclinic structure and Cmcm orthorhombic structure, respectively. It was interesting to note that $(Cr_{2/3}Sc_{1/3})_2AlC$ phases possess C2/c symmetry in majority and Cmcm in minority. However, the reverse was observed in $(Cr_{2/3}Y_{1/3})_2AlC$ i-MAX phase. The DFT studies also suggested both the symmetry have similar energy and Sc elements form in-plane ordered MAX phases. However, the discovery of $(Nb_{2/3}Sc_{1/3})_2AlC$ MAX phase was disordered [122]. Consequently, it is not always required that the substitution of Sc and Y elements results in the formation of i-MAX phases. Recently, two new phases have been included to the list of i-MAX phases such as $(V_{2/3}Zr_{1/3})_2AlC$ and $(Cr_{2/3}Zr_{1/3})_2AlC$ [123].

Table 2.4 List of MAX phases prepared till date with A-site and X-site substitution or doping.

TMs	A-site substitution		X-site substitution	
	211	312	211	312
Ti	$Ti_2(Al_{0.1}Cu_{0.9})C$[56]	$Ti_3(Ge_{1-x}Si_x)C_2$[124] $Ti_3(Si_{1-x}Pd_x)C_2$[125] $Ti_3(Al_{1-x}Sn_x)C_2$[126] $Ti_3(Al_{1-x}Cu_x)C_2$[127] $Ti_3(Al_{1-x}Si_x)C_2$[128]	$Ti_2Al(C_xN_{(1-x)})$[129]	$Ti_3Al(C_{0.5}N_{0.5})_2$[129]
V	$V_2(Al_xGa_{1-x})C$[43]			
Cr	$Cr_2(Al_{0.97}Si_{0.03})C$[130] $Cr_2(Al_xGe_{1-x})C$[131]			
Zr	$Zr_2(Al_{1-x}Sn_x)C$[132] $Zr_2(Al_{1-x}Bi_x)C$[89] $Zr_2(Al_{0.3}Sb_{0.7})C$[132] $Zr_2(Al_{0.35}Pb_{0.65})C$[132]	$Zr_3(Al_{1-x}Si_x)C_2$[133]		
Mo	$Mo_2(Ga_{0.33}Fe_{0.5}Au_{0.16})C$[134] $Mo_2(Au_{1-x}Ga_x)_2C$[57]			

2.3. Oxidation resistance of the MAX phases

For high temperature applications, thermal stability of MAX phases is important. MAX phases demonstrated superior oxidation resistance even at elevated temperatures as compared

to their binary compounds. The oxidation properties of the MAX phases can be investigated through isothermal and non-isothermal experiments.

Table 2.5 List of MAX phases prepared till date with double-site substitution or doping.

TMs	o-MAX phases		i-MAX phases
	312	413	211
V			$(V_{2/3}Zr_{1/3})_2AlC$[118] $(V_{2/3}Sc_{1/3})_2AlC$[138]
Cr	$(Cr_{2/3}Ti_{1/3})_3AlC_2$[139] $(Cr_{2/3}V_{1/3})_3AlC_2$[102]	$(Cr_2V_2)AlC_3$[102]	$(Cr_{2/3}Sc_{1/3})_2AlC$[121] $(Cr_{2/3}Y_{1/3})_2AlC$[121] $(Cr_{2/3}Zr_{1/3})_2AlC$[123] $(Cr_{2/3}Sc_{1/3})_2GaC$[140]
Mn			$(Mn_{2/3}Sc_{1/3})_2GaC$[140]
Mo	$(Mo_2Sc)AlC_2$[115] $(Mo_2Ti)AlC_2$[141]	$(Mo_2Ti_2)AlC_3$[141]	$(Mo_{2/3}M1_{1/3})_2AlC$[142] $(Mo_{2/3}M2_{1/3})_2GaC$[143]
W			$(W_{2/3}Sc_{1/3})_2AlC$[120] $(W_{2/3}Y_{1/3})_2AlC$[120]

TMs = Transition Metals, *M1*: Ce, Pr, Nd, Sm, Gd, Tb, Dy, Ho, Er, Tm, and Lu

M2: Gd, Tb, Dy, Ho, Er, Tm, Yb, and Lu

Table 2.6 List of out-of-plane (o-MAX) and in-plane (i-MAX) ordered MAX phases prepared till date.

TMs	Double-site substitution		
	211	312	413
Ti		$(Ti, Cu)_3(Al,Cu)C_2$[135]	
Zr	$(Zr, Nb)_2(Al, Sn)C$[136] $(Zr, Ti)_2(Al, Sn)C$[137]		
Ta	$(Ta, Nb)_2(Al, Sn)C$[113]		$(Ta, Hf)_4(Al, Sn)C_3$[113] $(Ta, Nb)_4(Al, Sn)C_3$[113]

2.3.1. Isothermal oxidation

It was observed that oxidation kinetics of Ti_3SiC_2 MAX phase was parabolic, when isothermal heating was performed in the temperature range 900 – 1400 °C for 12 h [144]. The rate of oxidation reduced with the formation of oxides (SiO_2 and TiO_2). Initially, amorphous SiO_2 formed at lower temperature and with increase in temperature (1240 °C) crystalline SiO_2 appeared. In this case, oxygen tends to diffuse inside the MAX phase, while Ti and C diffuse outwards. This results into the formation of SiO_2 layer over the surface of the MAX phase at 1000 °C. When isothermal heat treatment was given for 1500h in the temperature range 875 – 1200 °C, then the oxidation kinetics became linear [145]. The reason behind the transformation might be associated with the presence of microcracks at the surface. However, literature evidenced no clear explanation related to the transition of parabolic to linear with increase in

time. Similar, results were obtained when Ti_3AlC_2 phases were heat treated in the presence of air [146]. The study revealed that there was formation of oxide layer (TiO_2 and Al_2O_3) over the surface of MAX phases. The oxide layer enhances the oxidation resistance of the MAX phases. Ti_3AlC_2 demonstrated better oxidation resistance in comparison to Ti_3SiC_2. Basically, Al_2O_3 protective layer formed underneath TiO_2 layer and both layers act as a protective shield for the MAX phase. Hence, oxidation resistance improved significantly. It was found that parabolic oxidation kinetics dominates in Ti_3AlC_2 MAX phase. However, a careful analysis revealed that the oxidation kinetic was cubic rather than parabolic. In general, the oxidation kinetics is crucial to be known before designing a material for a particular application. A material with cubic oxidation kinetics is more durable and offers better oxidation resistance.

Furthermore, Ti_2AlC also exhibit good oxidation resistant. Sundberg and co-workers [147] found 15 μm thin layer of dense alumina over the surface of Ti_2AlC after 8000 cyclic heating up to 1350 °C. It was identified in the earlier studies that the oxidation of T_2AlC was parabolic. However, recent studies confirmed that the oxidation kinetic is cubic in Ti_2AlC [148]. In this case, isothermal heating of the Ti_2AlC for 25 h was done at 1400 °C. A protective layer of Al_2O_3 with thickness ~ 15 μm was observed over the surface of Ti_2AlC. The oxidation kinetics was found to be cubic in nature. Afterwards, the performance of Ti_2AlC was testified for 120 h at 1000 – 1300 °C in air and water vapours [149]. The oxidation kinetics was found to be cubic and activation energy was 270 kJ/mol. The formation of Al_2O_3 layer with TiO_2 was observed in both cases. However, TiO_2 layer got volatized to form $TiO(OH)_2$ at temperature above 1200 °C in water vapours. Fig. 2.1 compares the parabolic vs. linear vs. cubic oxidation kinetics. To further confirm the oxidation behaviour of Ti_2AlC, long term isothermal oxidation was studied [150]. The oxidation was performed at 1200 °C for different dwell durations (25, 100, 500, 1000, 2000 and 2873 h). It led to formation of 21 μm thickness Al_2O_3 layer after 2873 h. The most probable reason behind outstanding oxidation behaviour relied with the close match of thermal expansion of Ti_2AlC and protective layer (Al_2O_3). Interestingly, the formation of Al_2TiO_5 was observed after heating Ti_2AlC above 1400 °C. The crack formation during cooling was found to be a dominant reason behind Al_2TiO_5 formation. Hence, it is crucial to avoid formation of Al_2TiO_5 to obtain better oxidation properties. The oxidation behavior of Ti_3AlC_2 and Ti_2AlC was found to be similar. There was formation of alumina layer of 14.1 μm, 15.9 μm, 19.1 μm and 24.7 μm thickness after 20 h isothermal oxidation of Ti_3AlC_2 at 1000, 1100, 1200 and 1300°C, respectively [146].

In addition, these phases demonstrated a self-crack healing property. This phenomenon occurred due to the oxidation reactions that results into the formation of oxides that fill the

crack faces. These oxides constitute Al_2O_3 and some TiO_2. The filling of cracks mainly occurred during high temperature oxidation reactions. The weakly bonded Al element oxidized to form α-Al_2O_3 and fills the cracks with decent bonding. The reason behind good adhesion is related to the close value of thermal expansion coefficient of α-Al_2O_3 ($7.5 – 9.6 \times 10^{-6}\ K^{-1}$) and Ti_2AlC ($8.2 \times 10^{-6}\ K^{-1}$) MAX phase. Another reason is associated with the stiffness of the crack filler with the parent material that refurnish the tensile strength of the filled crack. Interestingly, a drop in the value of fracture toughness from ≈ 6.5 MPa/m^2, to about 3 MPa/m^2 was observed when the crack got extended to 7 times in Ti_2AlC MAX phase [152]. The extension of crack was performed in a way that healing of crack occurred in between every extension. It was noticed that after 7th crack extension the crack was healed about 1 mm. In addition, Ti_2AlC has shown potential for multiple crack healing. The healing of crack was observed due to the formation of oxide layers. However, the initiation of crack healing occurred at higher temperatures, i.e., ~ 900 °C. Consequently, the reduction in crack healing temperature may further enhance the oxidation resistance of Ti_2AlC MAX phase.

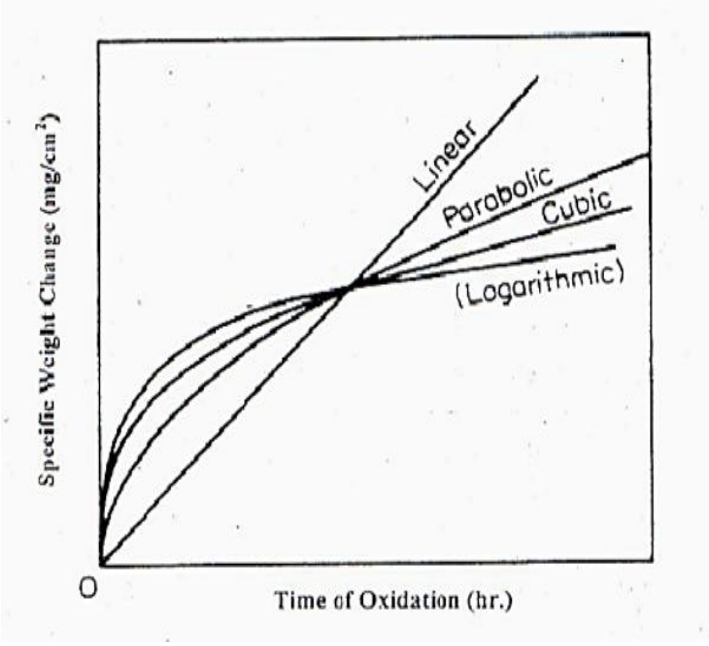

Fig. 2.1 Comparison of parabolic vs. linear vs. cubic vs. logarithmic oxidation kinetics [151].

Sloof and co-workers [153] have shown repeated crack healing potential of Ti_2AlC MAX phase by employing 4D in situ synchrotron X-ray tomographic microscopy. The study suggested that the crack formation might follow the previous pathway in the process of mechanical re-loading. In other words, cracking would initiate from earlier filled cracks during re-loading process. A zig-zag growth of crack occurred along the basal planes of randomly oriented grains of Ti_2AlC. This also results in the flat appearance of the fracture surfaces. Ti_2AlC MAX phase possesses typical feature of grain pull-out, crack branching and bridging.

Recently, substitution of Sn was done at A-site to reduce the crack healing temperature to 700 °C [154]. The layer of SnO_2 and TiO_2 act as crack filler in Ti_2AlC.

Moreover, the oxidation properties of Cr_2AlC MAX phases are still unclear. Most of researchers have shown that oxidation of Cr_2AlC dominated by parabolic oxidation kinetic [155–159]. After a careful investigation, it was found that the oxidation kinetics was neither parabolic nor cubic. The oxidation of Cr_2AlC at 700 °C, 1000 °C, and 1300 °C was slower than cubic and exponent was below 1/3. At 1200 °C, the oxidation kinetic was more likely to be cubic [150]. The oxidation occurred in two steps: first steps involved the formation of Al_2O_3 layer, while in the second step densification of Al_2O_3 layer occurred. There was a formation of thick Cr_7C_3 layer underneath Al_2O_3 layer. The reason behind formation of Cr_7C_3 was due to the Al consumption in top layer to form Al_2O_3. Among all the MAX phases, Cr_2AlC is the only phase that demonstrated the formation of carbide layer. The oxidation resistant improved with the strong bonding between Cr-C and Cr-Cr in Cr_7C_3 layers. It was found that after 30 days of isothermal oxidation of Cr_2AlC at 1000 °C the thickness of Al_2O_3 (3.5 μm) tends to remain constant. An increment of only ~ 2 μm was seen when isothermal heating was extended to 330 days. Beside superior oxidation properties, the oxidation resistance reduced in Cr_2AlC during cyclic oxidation due to formation of the voids. Interestingly, Cr_2AlC has proven to the best strength recovery after healing the cracks in comparison to other MAX phases [160]. The recovery strength of Cr_2AlC significantly depends on the healing time. The cracks in Cr_2AlC were filled with oxides and strong bonding was observed on the crack faces. The composition of crack filler changes by varying the healing time. When the healing time was 4 h, then cracks filler composition was Al-containing Cr_2O_3. Whereas, only α-Al_2O_3 was found as crack filler if the healing time was 100 h. The consumption of Cr_2AlC and evaporation of Cr_2O_3 increased with healing time. It was suggested that the cracks filled with α-Al_2O_3 possess more strength recovery. The cubic oxidation kinetic was found to be dominant during oxidation of Cr_2AlC.

Recently, Wang and colleagues [161] reported that the parabolic oxidation kinetics is responsible in Cr_2AlC coatings. They studied 40 h isothermal oxidation at 900, 1000 and 1100 °C. At 900 °C, a protective layer of Al_2O_3 appeared and results into reduction of Al in Cr_2AlC. As the content of Al reduced, formation of Cr_7C_3 and Cr_3C_2 phases were observed underneath Al_2O_3 layer. When the temperature was further increased, mixed layer constituting Cr_2O_3 and Al_2O_3 was observed. At higher temperature, formation of α-Al_2O_3 significantly improved the oxidation resistance of Cr_2AlC. A self-crack healing phenomenon was also observed in the case of Cr_2AlC MAX phase. Pie and co-workers [162] revealed that the crack filler constitute Cr_7C_3 phase beneath Al_2O_3, when the crack width exceeds 2 μm. About 12 μm crack width was

completely healed during oxidation at 1200 °C within 12 h. It was observed that the formation of crack in Cr_2AlC also followed the basal plane and as a result zig-zag growth of the crack occurs. This zig-zag shape of crack also brought difficulties in transferring oxygen from the crack surface to root. Consequently, the rate of crack healing with oxides might vary depending upon the partial pressures of oxygen at a particular crack location. There was presence of two sublayer consisting of dense (1.5 μm) and porous (1 μm) Al_2O_3 on the surface of 4h isothermally oxidized Cr_2AlC at 1200 °C. The crack tip has the dense Al_2O_3 layer. These studies indicated that the strength recovery in Cr_2AlC MAX phase significantly depends on the structure and region of the crack.

2.3.2. Non-isothermal oxidation

The non-isothermal oxidation studies provide significant understanding related to the feasibility of a material to be used for practical applications. These experiments also offer advantages over isothermal experiments such as no leakage of gas and very less or no rapid change in temperature, time, and gas flow rate [163]. However, non-isothermal studies on MAX phases are very few in the literature. Several researchers investigated oxidation of variety of materials though non-isothermal studies [164–170]. They used thermal analysis techniques (Thermogravimetry analysis (TGA), Differential scanning calorimetry (DSC), and Differential thermal analysis (DTA)) to explore the oxidation behaviour under non-isothermal conditions. In non-isothermal conditions, the experiments must be performed at variety of heating rates. The oxidation kinetics involved during non-isothermal heating is crucial to forecast material's oxidation properties at higher temperatures. The kinetic triplets (activation energy, pre-exponential factor, and reaction mechanism) that governs the non-isothermal oxidation are determined. The activation energy is the minimum energy required for a reaction to initiate. Whereas pre-exponential factor is related to the vibrations in a particular reaction. Later, reaction mechanism provides information about the mechanism followed by a reaction.

There are several reaction mechanisms that have been proposed. These include random nucleation, nucleation and growth, diffusion and phase boundary-controlled mechanisms. Furthermore, these kinetic triplets are determined by following the model fitting and model free kinetic methods. The detailed theoretical description related to non-isothermal kinetics is discussed in the next section. Recently, Mane and co-workers [171] investigated the non-isothermal oxidation kinetics of Ti_3GeC_2 MAX phase by using thermogravimetry analysis (TGA) and differential scanning calorimetry (DSC) techniques. They performed thermal analysis at 5, 10, 12.5, and 15 °C/min from room temperature to 1200 °C. The results indicated that the oxidation of Ti_3GeC_2 occurred in three temperature zones. The value of activation

energy and pre-exponential factor were determined by using the Kissinger's model for each temperature zone. The study indicated that the formation of TiO_2 occurred first and then CO and GeO_2 formed.

2.4. Gaps in study

According to the literature survey, the unique properties of the MAX phases significantly depend on the phase purity. Still the synthesis of pure MAX phase is challenging job, and many compounds of the family require processing breakthrough. The pressureless sintering method turned out to be suitable method to obtain pure bulk MAX phases. However, no pure Cr_2AlC, V_2AlC and Ti_3AlC_2 MAX phases have been reported to date. There is always a formation of unwanted carbide phases along with MAX phases as is evident from the X-ray diffraction patterns in the published literature [11,12]. Hence, there is a need to investigate the optimum synthesis condition for the formation of a highly pure Cr_2AlC, V_2AlC and Ti_3AlC_2 MAX phase. In this context, it is crucial to study the thermal kinetic parameters involved during non-isothermal synthesis of Cr_2AlC, V_2AlC and Ti_3AlC_2 MAX phases. The reports on the synthesis kinetics of Cr_2AlC, V_2AlC and Ti_3AlC_2 are scarce in the literature.

Furthermore, these MAX phases have shown oxidation resistance. There are several reports conducted on the isothermal oxidation of Cr_2AlC, V_2AlC and Ti_3AlC_2 MAX phases because of the ease of the theoretical interpretation of the data. However, non-isothermal oxidation studies on these phases are rarely available in the literature. In fact, a non-isothermal heating process is practically involved during oxidation of a particular compound [17]. The non-isothermal oxidation study will provide guidelines for the practical application of the MAX phases. Also, the isothermal oxidation experiments suffer from certain limitations such as leakage of gas and sudden variation in temperature, time, and gas flow rate [17]. These parameters significantly affect the accuracy of the isothermal oxidation process. So, it is crucial to investigate non-isothermal oxidation kinetics of Cr_2AlC, V_2AlC and Ti_3AlC_2 MAX phases.

The aim of the present study is to synthesis pure Cr_2AlC, V_2AlC and Ti_3AlC_2 MAX phases via pressureless sintering route. The role of composition in the synthesis of the MAX phases will be explored. In order to obtain pure MAX phases, the impact of temperature and dwell time is examined. The thermal kinetics parameters such as activation energy, pre-exponential factor and reaction mechanism involved during oxidation of these MAX phases will be investigated. On the basis of gaps in study, following objectives have been framed in the present study:

1. To synthesize MAX phase compounds with Cr, V, Ti as M-elements Al as A-element and C as X-element.

2. To study the oxidation kinetics of the as-prepared MAX phases.
3. To investigate structural and thermal properties of the as-prepared MAX phases.

The procedure adopted for the above objectives have been discussed in the next chapter.

References

[1] V.H. Nowotny, Strukturchemie einiger Verbindungen der Übergangsmetalle mit den elementen C, Si, Ge, Sn, Prog. Solid State Chem. 5 (1971) 27–70. https://doi.org/10.1016/0079-6786(71)90016-1.

[2] H. Nowotny, S. Windisch, High Temperature Compounds, Annu. Rev. Mater. Sci. 3 (1973) 171–194. https://doi.org/10.1146/annurev.ms.03.080173.001131.

[3] W. Jeitschko, H. Nowotny, Die Kristallstruktur von Ti_3SiC_2-ein neuer Komplexcarbid-Typ, Monatshefte Für Chemie. 98 (1967) 329–337. https://doi.org/10.1007/BF00899949.

[4] H. Wolfsgruber, H. Nowotny, F. Benesovsky, Die Kristallstruktur von Ti_3GeC_2 - Kurze Mitteilung, Monatshefte Für Chemie. 98 (1967) 2403–2405. https://doi.org/10.1007/BF00902438.

[5] R. Pampuch, J. Lis, L. Stobierski, M. Tymkiewicz, Solid combustion synthesis of Ti_3SiC_2, J. Eur. Ceram. Soc. 5 (1989) 283–287. https://doi.org/10.1016/0955-2219(89)90022-8.

[6] J. Lis, R. Pampuch, J. Piekarczyk, L. Stobierski, New ceramics based on Ti_3SiC_2, Ceram. Int. (1993). https://doi.org/10.1016/0272-8842(93)90052-S.

[7] J. Lis, Y. Miyamoto, R. Pampuch, K. Tanihata, Ti3SiC-based materials prepared by HIP-SHS techniques, Mater. Lett. 22 (1995) 163–168. https://doi.org/10.1016/0167-577X(94)00246-0.

[8] M.W. Barsoum, T. El-Raghy, Synthesis and characterization of a remarkable ceramic: Ti_3SiC_2, J. Am. Ceram. Soc. 79 (1996) 1953–1956. https://doi.org/10.1111/j.1151-2916.1996.tb08018.x.

[9] J. Lyu, E.B. Kashkarov, N. Travitzky, M.S. Syrtanov, A.M. Lider, Sintering of MAX-phase materials by spark plasma and other methods, J. Mater. Sci. 56 (2021) 1980–2015. https://doi.org/10.1007/s10853-020-05359-y.

[10] J. Haemers, R. Gusmão, Z. Sofer, Synthesis Protocols of the Most Common Layered Carbide and Nitride MAX Phases, Small Methods. 4 (2020) 1900780. https://doi.org/10.1002/smtd.201900780.

[11] H. Zhang, T. Hu, X. Wang, Y. Zhou, Structural defects in MAX phases and their derivative MXenes: A look forward, J. Mater. Sci. Technol. 38 (2020) 205–220. https://doi.org/10.1016/j.jmst.2019.03.049.

[12] M. Sokol, V. Natu, S. Kota, M.W. Barsoum, On the Chemical Diversity of the MAX Phases, Trends Chem. 1 (2019) 210–223. https://doi.org/10.1016/j.trechm.2019.02.016.

[13] I.M. Low, An overview of parameters controlling the decomposition and degradation of Ti-based $M_{n+1}AX_n$ phases, Materials (Basel). 12 (2019) 473. https://doi.org/10.3390/ma12030473.

[14] M. Magnuson, M. Mattesini, Chemical bonding and electronic-structure in MAX phases as viewed by X-ray spectroscopy and density functional theory, Thin Solid Films. 621 (2017) 108–130. https://doi.org/10.1016/j.tsf.2016.11.005.

[15] P. Eklund, J. Rosen, P.O.Å. Persson, Layered ternary $M_{n+1}AX_n$ phases and their 2D derivative MXene: An overview from a thin-film perspective, J. Phys. D. Appl. Phys. 50 (2017) 113001. https://doi.org/10.1088/1361-6463/aa57bc.

[16] X. Chen, G. Bei, Toughening mechanisms in nanolayered MAX phase ceramics-a review, Materials (Basel). 10 (2017) 366. https://doi.org/10.3390/ma10040366.

[17] Y. Bai, N. Srikanth, C.K. Chua, K. Zhou, Density Functional Theory Study of $M_{n+1}AX_n$ Phases: A Review, Crit. Rev. Solid State Mater. Sci. 44 (2019) 56–107. https://doi.org/10.1080/10408436.2017.1370577.

[18] A.S. Ingason, M. Dahlqvist, J. Rosen, Magnetic MAX phases from theory and experiments; A review, J. Phys. Condens. Matter. 28 (2016) 433003.

https://doi.org/10.1088/0953-8984/28/43/433003.

[19] M.W. Barsoum, D. Brodkin, T. El-Raghy, Layered machinable ceramics for high temperature applications, Scr. Mater. 36 (1997) 535–541. https://doi.org/10.1016/S1359-6462(96)00418-6.

[20] M.W. Barsoum, G. Yaroschuk, S. Tyagi, Fabrication and characterization of M_2SnC (M = Ti, Zr, Hf and Nb), Scr. Mater. 37 (1997) 1583–1591. https://doi.org/10.1016/S1359-6462(97)00288-1.

[21] N. V. Tzenov, M.W. Barsoum, Synthesis and characterization of Ti_3AlC_2, J. Am. Ceram. Soc. 83 (2000) 825–832. https://doi.org/10.1111/j.1151-2916.2000.tb01281.x.

[22] X. Wang, Y. Zhou, Solid–liquid reaction synthesis of layered machinable Ti_3AlC_2 ceramic, J. Mater. Chem. 12 (2002) 455–460. https://doi.org/10.1039/b108685e.

[23] A. Hendaoui, D. Vrel, A. Amara, P. Langlois, M. Andasmas, M. Guerioune, Synthesis of high-purity polycrystalline MAX phases in Ti-Al-C system through Mechanically Activated Self-propagating High-temperature Synthesis, J. Eur. Ceram. Soc. 30 (2010) 1049–1057. https://doi.org/10.1016/j.jeurceramsoc.2009.10.001.

[24] C. Hu, F. Li, J. Zhang, J. Wang, J. Wang, Y. Zhou, Nb_4AlC_3: A new compound belonging to the MAX phases, Scr. Mater. 57 (2007) 893–896. https://doi.org/10.1016/j.scriptamat.2007.07.038.

[25] C. Hu, Y. Sakka, S. Grasso, T. Nishimura, S. Guo, H. Tanaka, Shell-like nanolayered Nb_4AlC_3 ceramic with high strength and toughness, Scr. Mater. 64 (2011) 765–768. https://doi.org/10.1016/j.scriptamat.2010.12.045.

[26] Z.F. Zhang, Z.M. Sun, H. Hashimoto, T. Abe, Fabrication and microstructure characterization of Ti_3SiC_2 synthesized from Ti/Si/2TiC powders using the pulse discharge sintering (PDS) technique, J. Am. Ceram. Soc. 86 (2003) 431–436. https://doi.org/10.1111/j.1151-2916.2003.tb03317.x.

[27] M. Hossein-Zadeh, O. Mirzaee, H. Mohammadian-Semnani, An investigation into the microstructure and mechanical properties of V_4AlC_3 MAX phase prepared by spark plasma sintering, Ceram. Int. 45 (2019) 7446–7457. https://doi.org/10.1016/j.ceramint.2019.01.036.

[28] T. Lapauw, B. Tunca, T. Cabioc'h, J. Vleugels, K. Lambrinou, Reactive spark plasma sintering of Ti_3SnC_2, Zr_3SnC_2 and Hf_3SnC_2 using Fe, Co or Ni additives, J. Eur. Ceram. Soc. 37 (2017) 4539–4545. https://doi.org/10.1016/j.jeurceramsoc.2017.06.041.

[29] V.G. Gilev, M.N. Kachenyuk, Phase Formation in the Synthesis of Ti_2AlN by Spark Plasma Sintering in the Ti/AlN System, Refract. Ind. Ceram. 59 (2019) 658–662. https://doi.org/10.1007/s11148-019-00291-4.

[30] W. Zhou, L. Liu, J. Zhu, S. Tian, Facile synthesis of high-purity Ti_2SC powders by spark plasma sintering technique, Ceram. Int. 43 (2017) 9363–9368. https://doi.org/10.1016/j.ceramint.2017.04.104.

[31] W. Zhou, K. Li, J. Zhu, S. Tian, Rapid synthesis of highly pure Nb_2AlC using the spark plasma sintering technique, J. Phys. Chem. Solids. 120 (2018) 218–222. https://doi.org/10.1016/j.jpcs.2018.04.029.

[32] J.J. Nickl, K.K. Schweitzer, P. Luxenberg, Gasphasenabscheidung im system TiSiC, J. Less-Common Met. 26 (1972) 335–353. https://doi.org/10.1016/0022-5088(72)90083-5.

[33] S. Jacques, H. Di-Murro, M.P. Berthet, H. Vincent, Pulsed reactive chemical vapor deposition in the C-Ti-Si system from $H_2/TiCl_4/SiCl_4$, Thin Solid Films. 478 (2005) 13–20. https://doi.org/10.1016/j.tsf.2004.09.043.

[34] H. Fakih, S. Jacques, M.P. Berthet, F. Bosselet, O. Dezellus, J.C. Viala, The growth of Ti_3SiC_2 coatings onto SiC by reactive chemical vapor deposition using H_2 and $TiCl_4$, Surf. Coatings Technol. 201 (2006) 3748–3755.

https://doi.org/10.1016/j.surfcoat.2006.09.040.

[35] H. Fakih, S. Jacques, O. Dezellus, M.P. Berthet, F. Bosselet, M. Sacerdote-Peronnet, J.C. Viala, Phase equilibria and reactive chemical vapor deposition (RCVD) of Ti_3SiC_2, J. Phase Equilibria Diffus. 29 (2008) 239–246. https://doi.org/10.1007/s11669-008-9284-1.

[36] T. Seppänen, J. Palmquist, P. Persson, J. Emmerlich, J. Molina, J. Birch, U. Jansson, P. Isberg, L. Hultman, J. Keränen, K. Sillanpää, Structural Characterization of Epitaxial Ti_3SiC_2 Films, in: 53rd Annu. Meet. Scand. Soc. Electron Microsc., 2002: p. 142.

[37] J.P. Palmquist, U. Jansson, T. Seppänen, P.O.A. Persson, J. Birch, L. Hultman, P. Isberg, Magnetron sputtered epitaxial single-phase Ti_3SiC_2 thin films, Appl. Phys. Lett. 81 (2002) 835–837. https://doi.org/10.1063/1.1494865.

[38] M.A. Pietzka, J.C. Schuster, Summary of constitutional data on the Aluminum-Carbon-Titanium system, J. Phase Equilibria. 15 (1994) 392–400. https://doi.org/10.1007/BF02647559.

[39] J.P. Palmquist, S. Li, P.O.. Persson, J. Emmerlich, O. Wilhelmsson, H. Högberg, M.I. Katsnelson, B. Johansson, R. Ahuja, O. Eriksson, L. Hultman, U. Jansson, $M_{n+1}AX_n$ phases in the Ti-Si-C system studied by thin-film synthesis and ab initio calculations, Phys. Rev. B - Condens. Matter Mater. Phys. 70 (2004) 1–13. https://doi.org/10.1103/PhysRevB.70.165401.

[40] M.W. Barsoum, L. Farber, I. Levin, A. Procopio, T. El-Raghy, A. Berner, High-resolution transmission electron microscopy of Ti4AlN3, or $Ti_3Al_2N_2$ revisited, J. Am. Ceram. Soc. 82 (1999) 2545–2547. https://doi.org/10.1111/j.1151-2916.1999.tb02117.x.

[41] J. Zhang, B. Liu, J.Y. Wang, Y.C. Zhou, Low-temperature instability of Ti_2SnC: A combined transmission electron microscopy, differential scanning calorimetry, and x-ray diffraction investigations, J. Mater. Res. 24 (2009) 39–49. https://doi.org/10.1557/jmr.2009.0012.

[42] M. Li, J. Lu, K. Luo, Y. Li, K. Chang, K. Chen, J. Zhou, J. Rosen, L. Hultman, P. Eklund, P.O.Å. Persson, S. Du, Z. Chai, Z. Huang, Q. Huang, Element Replacement Approach by Reaction with Lewis Acidic Molten Salts to Synthesize Nanolaminated MAX Phases and MXenes, J. Am. Chem. Soc. 141 (2019) 4730–4737. https://doi.org/10.1021/jacs.9b00574.

[43] J. Etzkorn, M. Ade, D. Kotzott, M. Kleczek, H. Hillebrecht, Ti_2GaC, Ti_4GaC_3 and Cr_2GaC-Synthesis, crystal growth and structure analysis of Ga-containing MAX-phases $M_{n+1}GaC_n$ with M=Ti, Cr and n=1, 3, J. Solid State Chem. 182 (2009) 995–1002. https://doi.org/10.1016/j.jssc.2009.01.003.

[44] H. Högberg, P. Eklund, J. Emmerlich, J. Birch, L. Hultman, Epitaxial Ti_2GeC, Ti_3GeC_2, and Ti_4GeC_3 MAX-phase thin films grown by magnetron sputtering, J. Mater. Res. 20 (2005) 779–782. https://doi.org/10.1557/JMR.2005.0105.

[45] D.T. Cuskelly, E.R. Richards, E.H. Kisi, V.J. Keast, Ti_3GaC_2 and Ti_3InC_2: First bulk synthesis, DFT stability calculations and structural systematics, J. Solid State Chem. 230 (2015) 418–425. https://doi.org/10.1016/j.jssc.2015.07.028.

[46] S. Dubois, T. Cabioc'H, P. Chartier, V. Gauthier, M. Jaouen, A new ternary nanolaminate carbide: Ti_3SnC_2, J. Am. Ceram. Soc. 90 (2007) 2642–2644. https://doi.org/10.1111/j.1551-2916.2007.01766.x.

[47] H. Fashandi, M. Dahlqvist, J. Lu, J. Palisaitis, S.I. Simak, I.A. Abrikosov, J. Rosen, L. Hultman, M. Andersson, A. Lloyd Spetz, P. Eklund, Synthesis of Ti_3AuC_2, $Ti_3Au_2C_2$ and Ti_3IrC_2 by noble metal substitution reaction in Ti_3SiC_2 for high-temperature-stable Ohmic contacts to SiC, Nat. Mater. 16 (2017) 814–818. https://doi.org/10.1038/nmat4896.

[48] A. Bouhemadou, Structural, electronic and elastic properties of MAX phases M_2GaN (M = Ti, V and Cr), Solid State Sci. 11 (2009) 1875–1881. https://doi.org/10.1016/j.solidstatesciences.2009.08.002.

[49] S. Kashiwaya, C.C. Lai, J. Lu, A. Petruhins, J. Rosen, L. Hultman, Formation of Ti_2AuN from Au-Covered Ti_2AlN Thin Films: A General Strategy to Thermally Induce Intercalation of Noble Metals into MAX Phases, Cryst. Growth Des. 20 (2020) 4077–4081. https://doi.org/10.1021/acs.cgd.0c00355.

[50] C. Hu, J. Zhang, J. Wang, F. Li, J. Wang, Y. Zhou, Crystal structure of V_4AlC_3: A new layered ternary carbide, J. Am. Ceram. Soc. 91 (2008) 636–639. https://doi.org/10.1111/j.1551-2916.2007.02136.x.

[51] Q. Xu, Y. Zhou, H. Zhang, A. Jiang, Q. Tao, J. Lu, J. Rosén, Y. Niu, S. Grasso, C. Hu, Theoretical prediction, synthesis, and crystal structure determination of new MAX phase compound V_2SnC, J. Adv. Ceram. 9 (2020) 481–492. https://doi.org/10.1007/s40145-020-0391-8.

[52] A.S. Ingason, A. Petruhins, M. Dahlqvist, F. Magnus, A. Mockute, B. Alling, L. Hultman, I.A. Abrikosov, P.O.Å. Persson, J. Rosen, A nanolaminated magnetic phase: Mn_2GaC, Mater. Res. Lett. 2 (2017) 89–93. https://doi.org/10.1080/21663831.2013.865105.

[53] T. Lapauw, K. Lambrinou, T. Cabioc'h, J. Halim, J. Lu, A. Pesach, O. Rivin, O. Ozeri, E.N. Caspi, L. Hultman, P. Eklund, J. Rosén, M.W. Barsoum, J. Vleugels, Synthesis of the new MAX phase Zr_2AlC, J. Eur. Ceram. Soc. 36 (2016) 1847–1853. https://doi.org/10.1016/j.jeurceramsoc.2016.02.044.

[54] T. Lapauw, J. Halim, J. Lu, T. Cabioc'h, L. Hultman, M.W. Barsoum, K. Lambrinou, J. Vleugels, Synthesis of the novel Zr_3AlC_2 MAX phase, J. Eur. Ceram. Soc. 36 (2016) 943–947. https://doi.org/10.1016/j.jeurceramsoc.2015.10.011.

[55] P. Eklund, M. Dahlqvist, O. Tengstrand, L. Hultman, J. Lu, N. Nedfors, U. Jansson, J. Rosén, Discovery of the ternary nanolaminated compound Nb_2GeC by a systematic theoretical-experimental approach, Phys. Rev. Lett. 109 (2012). https://doi.org/10.1103/PhysRevLett.109.035502.

[56] H. Ding, Y. Li, J. Lu, K. Luo, K. Chen, M. Li, P.O.Å. Persson, L. Hultman, P. Eklund, S. Du, Z. Huang, Z. Chai, H. Wang, P. Huang, Q. Huang, Synthesis of MAX phases Nb_2CuC and $Ti_2(Al_{0.1}Cu_{0.9})N$ by A-site replacement reaction in molten salts, Mater. Res. Lett. 7 (2019) 510–516. https://doi.org/10.1080/21663831.2019.1672822.

[57] C.C. Lai, H. Fashandi, J. Lu, J. Palisaitis, P.O.Å. Persson, L. Hultman, P. Eklund, J. Rosen, Phase formation of nanolaminated Mo_2AuC and $Mo_2(Au_{1-x}Ga_x)_2C$ by a substitutional reaction within Au-capped Mo_2GaC and Mo_2Ga_2C thin films, Nanoscale. 9 (2017) 17681–17687. https://doi.org/10.1039/c7nr03663a.

[58] L.E. Toth, W. Jeitschko, C.M. Yen, The superconducting behavior of several complex carbides and nitrides, J. Less-Common Met. 10 (1966) 29–32. https://doi.org/10.1016/0022-5088(66)90041-5.

[59] T. Lapauw, B. Tunca, T. Cabioc'H, J. Lu, P.O.Å. Persson, K. Lambrinou, J. Vleugels, Synthesis of MAX Phases in the Hf-Al-C System, Inorg. Chem. 55 (2016) 10922–10927. https://doi.org/10.1021/acs.inorgchem.6b01398.

[60] T. El-Raghy, S. Chakraborty, M.W. Barsoum, Synthesis and characterization of Hf_2PbC, Zr_2PbC and M_2SnC (M = Ti, Hf, Nb or Zr), J. Eur. Ceram. Soc. 20 (2000) 2619–2625. https://doi.org/10.1016/S0955-2219(00)00127-8.

[61] Z. Lin, M. Zhuo, Y. Zhou, M. Li, J. Wang, Microstructures and theoretical bulk modulus of layered ternary tantalum aluminum carbides, J. Am. Ceram. Soc. 89 (2006) 3765–3769. https://doi.org/10.1111/j.1551-2916.2006.01303.x.

[62] B. Manoun, S.K. Saxena, T. El-Raghy, M.W. Barsoum, High-pressure x-ray diffraction

study of Ta_4AlC_3, Appl. Phys. Lett. 88 (2006). https://doi.org/10.1063/1.2202387.

[63] S. Kuchida, T. Muranaka, K. Kawashima, K. Inoue, M. Yoshikawa, J. Akimitsu, Superconductivity in Lu_2SnC, Phys. C Supercond. Its Appl. 494 (2013) 77–79. https://doi.org/10.1016/j.physc.2013.04.050.

[64] J.C. Schuster, H. Nowotny, C. Vaccaro, The ternary systems: Cr–Al–C, V–Al–C, and Ti–Al–C and the behavior of H-phases (M_2AlC), J. Solid State Chem. 32 (1980) 213–219. https://doi.org/10.1016/0022-4596(80)90569-1.

[65] J.C. Schuster, H. Nowotny, Investigations of the ternary systems (Zr, Hf, Nb, Ta)-Al-C and studies on complex carbides., Zeitschrift Fuer Met. Res. Adv. Tech. 71 (1980) 341–346.

[66] T.H. Scabarozi, J. Roche, A. Rosenfeld, S.H. Lim, L. Salamanca-Riba, G. Yong, I. Takeuchi, M.W. Barsoum, J.D. Hettinger, S.E. Lofland, Synthesis and characterization of Nb_2AlC thin films, Thin Solid Films. 517 (2009) 2920–2923. https://doi.org/10.1016/j.tsf.2008.12.047.

[67] C. Walter, D.P. Sigumonrong, T. El-Raghy, J.M. Schneider, Towards large area deposition of Cr_2AlC on steel, Thin Solid Films. 515 (2006) 389–393. https://doi.org/10.1016/j.tsf.2005.12.219.

[68] O. Wilhelmsson, P. Eklund, H. Högberg, L. Hultman, U. Jansson, Structural, electrical and mechanical characterization of magnetron-sputtered V-Ge-C thin films, Acta Mater. 56 (2008) 2563–2569. https://doi.org/10.1016/j.actamat.2008.01.036.

[69] A. Mockute, P.O.. Persson, F. Magnus, A.S. Ingason, S. Olafsson, L. Hultman, J. Rosen, Synthesis and characterization of arc deposited magnetic $(Cr,Mn)_2AlC$ MAX phase films, Phys. Status Solidi - Rapid Res. Lett. 8 (2014) 420–423. https://doi.org/10.1002/pssr.201409087.

[70] I.C. Schramm, C. Pauly, M.P. Johansson Jõesaar, P. Eklund, J. Schmauch, F. Mücklich, M. Odén, Solid state formation of Ti_4AlN_3 in cathodic arc deposited (Ti1−xAlx)Ny alloys, Acta Mater. 129 (2017) 268–277. https://doi.org/10.1016/j.actamat.2017.03.001.

[71] T. Zehnder, J. Matthey, P. Schwaller, A. Klein, P.A. Steinmann, J. Patscheider, Wear protective coatings consisting of TiC-SiC-a-C: H deposited by magnetron sputtering, Surf. Coatings Technol. 163–164 (2003) 238–244. https://doi.org/10.1016/S0257-8972(02)00477-2.

[72] W. Gulbiński, A. Gilewicz, T. Suszko, B. Warcholiński, Z. Kukliński, Ti-Si-C sputter deposited thin film coatings, Surf. Coatings Technol. 180–181 (2004) 341–346. https://doi.org/10.1016/j.surfcoat.2003.10.084.

[73] W. Gulbiński, T. Suszko, A. Gilewicz, B. Warcholiński, Z. Kukliński, Structure and high-temperature tribological behavior of Ti-Si-C nanocomposite thin films, Surf. Coatings Technol. 200 (2006) 4179–4184. https://doi.org/10.1016/j.surfcoat.2004.12.011.

[74] M. Rester, J. Neidhardt, P. Eklund, J. Emmerlich, H. Ljungcrantz, L. Hultman, C. Mitterer, Annealing studies of nanocomposite Ti-Si-C thin films with respect to phase stability and tribological performance, Mater. Sci. Eng. A. 429 (2006) 90–95. https://doi.org/10.1016/j.msea.2006.05.053.

[75] J.J. Hu, J.E. Bultman, S. Patton, J.S. Zabinski, T. Ti, Pulsed Laser Deposition and Properties of $M_{n+1}AX_n$ Phase Formulated Ti_3SiC_2 Thin Films, Tribol. Lett. 16 (2004) 113–122.

[76] C. Lange, M. Hopfeld, M. Wilke, J. Schawohl, T. Kups, M.W. Barsoum, P. Schaaf, Pulsed laser deposition from a pre-synthesized Cr_2AlC MAX phase target with and without ion-beam assistance, Phys. Status Solidi Appl. Mater. Sci. 209 (2012) 545–552. https://doi.org/10.1002/pssa.201127537.

[77] M. Bahiraei, Y. Mazaheri, M. Sheikhi, A. Heidarpour, A new approach to synthesis

Ti_2AlC MAX phase using PVD coating and post-laser treatment, Surf. Coatings Technol. 385 (2020) 125314. https://doi.org/10.1016/j.surfcoat.2019.125314.

[78] A. Biswas, A. Sengupta, U. Rajput, S.K. Singh, V. Antad, S.M. Hossain, S. Parmar, D. Rout, A. Deshpande, S. Nair, S. Ogale, Growth, Properties, and Applications of Pulsed Laser Deposited Nanolaminate Ti_3AlC_2 Thin Films, Phys. Rev. Appl. 13 (2020) 1. https://doi.org/10.1103/PhysRevApplied.13.044075.

[79] Y. Gogotsi, B. Anasori, The Rise of MXenes, ACS Nano. 13 (2019) 8491–8494. https://doi.org/10.1021/acsnano.9b06394.

[80] S. Sridharan, H. Nowotny, Studies in the ternary system Ti-Ta-Al and in the quaternary system Ti-Ta-Al-C, Zeitschrift Fuer Met. 74 (1983) 468–472.

[81] C.M. Hamm, J.D. Bocarsly, G. Seward, U.I. Kramm, C.S. Birkel, Non-conventional synthesis and magnetic properties of MAX phases $(Cr/Mn)_2AlC$ and $(Cr/Fe)_2AlC$, J. Mater. Chem. C. 5 (2017) 5700–5708. https://doi.org/10.1039/c7tc00112f.

[82] O. Rivin, E.N. Caspi, A. Pesach, H. Shaked, A. Hoser, R. Georgii, Q. Tao, J. Rosen, M.W. Barsoum, Evidence for ferromagnetic ordering in the MAX phase $(Cr_{0.96}Mn_{0.04})_2GeC$, Mater. Res. Lett. 5 (2017) 465–471. https://doi.org/10.1080/21663831.2017.1317295.

[83] A. Mockute, J. Lu, E.J. Moon, M. Yan, B. Anasori, S.J. May, M.W. Barsoum, J. Rosen, Solid solubility and magnetism upon Mn incorporation in the bulk ternary carbides Cr_2AlC and Cr_2GaC, Mater. Res. Lett. 3 (2014) 16–22. https://doi.org/10.1080/21663831.2014.944676.

[84] R. Meshkian, A.S. Ingason, U.B. Arnalds, F. Magnus, J. Lu, J. Rosen, A magnetic atomic laminate from thin film synthesis: $(Mo_{0.5}Mn_{0.5})_2GaC$, APL Mater. 3 (2015). https://doi.org/10.1063/1.4926611.

[85] C.M. Hamm, M. Dürrschnabel, L. Molina-Luna, R. Salikhov, D. Spoddig, M. Farle, U. Wiedwald, C.S. Birkel, Structural, magnetic and electrical transport properties of non-conventionally prepared MAX phases V_2AlC and $(V/Mn)_2AlC$, Mater. Chem. Front. 2 (2018) 483–490. https://doi.org/10.1039/c7qm00488e.

[86] Q. Tao, R. Salikhov, A. Mockute, J. Lu, M. Farle, U. Wiedwald, J. Rosen, Thin film synthesis and characterization of a chemically ordered magnetic nanolaminate $(V,Mn)_3GaC_2$, APL Mater. 4 (2016). https://doi.org/10.1063/1.4961502.

[87] Y. Li, J. Lu, M. Li, K. Chang, X. Zha, Y. Zhang, K. Chen, P.O.Å. Persson, L. Hultman, P. Eklund, S. Du, J.S. Francisco, Z. Chai, Z. Huang, Q. Huang, Multielemental single–atom-thick A layers in nanolaminated $V_2(Sn, A)C$ (A = Fe, Co, Ni, Mn) for tailoring magnetic properties, Proc. Natl. Acad. Sci. U. S. A. 117 (2020) 820–825. https://doi.org/10.1073/pnas.1916256117.

[88] M. Nechiche, T. Cabioc'H, E.N. Caspi, O. Rivin, A. Hoser, V. Gauthier-Brunet, P. Chartier, S. Dubois, Evidence for Symmetry Reduction in $Ti_3(Al_{1-\delta}Cu_\delta)C_2$ MAX Phase Solid Solutions, Inorg. Chem. 56 (2017) 14388–14395. https://doi.org/10.1021/acs.inorgchem.7b01003.

[89] D. Horlait, S.C. Middleburgh, A. Chroneos, W.E. Lee, Synthesis and DFT investigation of new bismuth-containing MAX phases, Sci. Rep. 6 (2016) 18829. https://doi.org/10.1038/srep18829.

[90] Z. Liu, E. Wu, J. Wang, Y. Qian, H. Xiang, X. Li, Q. Jin, G. Sun, X. Chen, J. Wang, M. Li, Crystal structure and formation mechanism of $(Cr_{2/3}Ti_{1/3})_3AlC_2$ MAX phase, Acta Mater. 73 (2014) 186–193. https://doi.org/10.1016/j.actamat.2014.04.006.

[91] I. Salama, T. El-Raghy, M.W. Barsoum, Synthesis and mechanical properties of Nb_2AlC and $(Ti,Nb)_2AlC$, J. Alloys Compd. 347 (2002) 271–278. https://doi.org/10.1016/S0925-8388(02)00756-9.

[92] B. Manoun, O.D. Leaffer, S. Gupta, E.N. Hoffman, S.K. Saxena, J.E. Spanier, M.W.

Barsoum, On the compression behavior of Ti_2InC, $(Ti_{0.5}, Zr_{0.5})_2InC$, and M_2SnC (M = Ti, Nb, Hf) to quasi-hydrostatic pressures up to 50 GPa, Solid State Commun. 149 (2009) 1978–1983. https://doi.org/10.1016/j.ssc.2009.05.043.

[93] M.W. Barsoum, J. Golczewski, H.J. Seifert, F. Aldinger, Fabrication and electrical and thermal properties of Ti_2InC, Hf_2InC and $(Ti,Hf)_2InC$, J. Alloys Compd. 340 (2002) 173–179. https://doi.org/10.1016/S0925-8388(02)00107-X.

[94] R. Pan, J. Zhu, Y. Liu, Synthesis, microstructure and properties of $(Ti_{1-x}, Mo_x)_2AlC$ phases, Mater. Sci. Technol. (United Kingdom). 34 (2018) 1064–1069. https://doi.org/10.1080/02670836.2017.1419614.

[95] M. Naguib, G.W. Bentzel, J. Shah, J. Halim, E.N. Caspi, J. Lu, L. Hultman, M.W. Barsoum, New solid solution MAX phases: $(Ti_{0.5}, V_{0.5})_3AlC_2$, $(Nb_{0.5}, V_{0.5})_2AlC$, $(Nb_{0.5},V_{0.5})_4AlC_3$ and $(Nb_{0.8},Zr_{0.2})_2AlC$, Mater. Res. Lett. 2 (2014) 233–240. https://doi.org/10.1080/21663831.2014.932858.

[96] L. Zheng, J. Wang, X. Lu, F. Li, J. Wang, Y. Zhouw, $(Ti_{0.5}Nb_{0.5})_5AlC_4$: A new-layered compound belonging to MAX phases, J. Am. Ceram. Soc. 93 (2010) 3068–3071. https://doi.org/10.1111/j.1551-2916.2010.04056.x.

[97] Y. Zhou, F. Meng, J. Zhang, New MAX-phase compounds in the V-Cr-Al-C system, J. Am. Ceram. Soc. 91 (2008) 1357–1360. https://doi.org/10.1111/j.1551-2916.2008.02279.x.

[98] Z. Liu, T. Waki, Y. Tabata, H. Nakamura, Mn-doping-induced itinerant-electron ferromagnetism in Cr_2GeC, Phys. Rev. B - Condens. Matter Mater. Phys. 89 (2014). https://doi.org/10.1103/PhysRevB.89.054435.

[99] N.A. Phatak, S.K. Saxena, Y. Fei, J. Hu, Synthesis of a new MAX compound $(Cr_{0.5}V_{0.5})_2GeC$ and its compressive behavior up to 49 GPa, J. Alloys Compd. 475 (2009) 629–634. https://doi.org/10.1016/j.jallcom.2008.07.102.

[100] S. Lin, Y. Huang, L. Zu, X. Kan, J. Lin, W. Song, P. Tong, X. Zhu, Y. Sun, Alloying effects on structural, magnetic, and electrical/thermal transport properties in MAX-phase $Cr_{2-x}M_xGeC$ (M = Ti, V, Mn, Fe, and Mo), J. Alloys Compd. 680 (2016) 452–461. https://doi.org/10.1016/j.jallcom.2016.04.197.

[101] C.C. Lai, Q. Tao, H. Fashandi, U. Wiedwald, R. Salikhov, M. Farle, A. Petruhins, J. Lu, L. Hultman, P. Eklund, J. Rosen, Magnetic properties and structural characterization of layered $(Cr_{0.5}Mn_{0.5})_2AuC$ synthesized by thermally induced substitutional reaction in $(Cr_{0.5}Mn_{0.5})_2GaC$, APL Mater. 6 (2018). https://doi.org/10.1063/1.5006304.

[102] E.N. Caspi, P. Chartier, F. Porcher, F. Damay, T. Cabioc'h, Ordering of (Cr,V) layers in nanolamellar $(Cr_{0.5}V_{0.5})_{n+1}AlC_n$ compounds, Mater. Res. Lett. 3 (2015) 100–106. https://doi.org/10.1080/21663831.2014.975294.

[103] D. Horlait, S. Grasso, N. Al Nasiri, P.A. Burr, W.E. Lee, Synthesis and Oxidation Testing of MAX Phase Composites in the Cr-Ti-Al-C Quaternary System, J. Am. Ceram. Soc. 99 (2016) 682–690. https://doi.org/10.1111/jace.13962.

[104] Z. Liu, L. Zheng, L. Sun, Y. Qian, J. Wang, M. Li, $(Cr_{2/3}Ti_{1/3})_3AlC_2$ and $(Cr_{5/8}Ti_{3/8})_4AlC_3$: New MAX-phase compounds in Ti-Cr-Al-C system, J. Am. Ceram. Soc. 97 (2014) 67–69. https://doi.org/10.1111/jace.12731.

[105] M.A. Hadi, U. Monira, A. Chroneos, S.H. Naqib, A.K.M.A. Islam, N. Kelaidis, R. V. Vovk, Phase stability and physical properties of $(Zr_{1-x}Nb_x)_2$ AlC MAX phases, J. Phys. Chem. Solids. 132 (2019) 38–47. https://doi.org/10.1016/j.jpcs.2019.04.010.

[106] E. Zapata-Solvas, M.A. Hadi, D. Horlait, D.C. Parfitt, A. Thibaud, A. Chroneos, W.E. Lee, Synthesis and physical properties of $(Zr_{1-x},Ti_x)_3AlC_2$ MAX phases, J. Am. Ceram. Soc. 100 (2017) 3393–3401. https://doi.org/10.1111/jace.14870.

[107] T. Lapauw, D. Tytko, K. Vanmeensel, S. Huang, P.P. Choi, D. Raabe, E.N. Caspi, O. Ozeri, M. To Baben, J.M. Schneider, K. Lambrinou, J. Vleugels, $(Nb_x,Zr_{1-x})_4AlC_3$ MAX

Phase Solid Solutions: Processing, Mechanical Properties, and Density Functional Theory Calculations, Inorg. Chem. 55 (2016) 5445–5452. https://doi.org/10.1021/acs.inorgchem.6b00484.

[108] J. Halim, J. Palisaitis, J. Lu, J. Thörnberg, E.J. Moon, M. Precner, P. Eklund, P.O.A. Persson, M.W. Barsoum, J. Rosen, Synthesis of two-dimensional $Nb_{1.33}C$ (mxene) with randomly distributed vacancies by etching of the quaternary solid solution $(Nb_{2/3}Sc_{1/3})_2AlC$ max phase, ACS Appl. Nano Mater. (2018). https://doi.org/10.1021/acsanm.8b00332.

[109] J. Gu, L. Pan, J. Yang, L. Yu, H. Zhang, W. Zou, C. Xu, C. Hu, T. Qiu, Mechanical properties and oxidation behavior of Ti-doped Nb_4AlC_3, J. Eur. Ceram. Soc. 36 (2016) 1001–1008. https://doi.org/10.1016/j.jeurceramsoc.2015.10.023.

[110] J. Yang, M. Naguib, M. Ghidiu, L.M. Pan, J. Gu, J. Nanda, J. Halim, Y. Gogotsi, M.W. Barsoum, Two-Dimensional Nb-Based M_4C_3 Solid Solutions (MXenes), J. Am. Ceram. Soc. 99 (2016) 660–666. https://doi.org/10.1111/jace.13922.

[111] T. Lapauw, A.K. Swarnakar, B. Tunca, K. Lambrinou, J. Vleugels, Nanolaminated ternary carbide (MAX phase) materials for high temperature applications, Int. J. Refract. Met. Hard Mater. 72 (2018) 51–55. https://doi.org/10.1016/j.ijrmhm.2017.11.038.

[112] G. Deysher, C.E. Shuck, K. Hantanasirisakul, N.C. Frey, A.C. Foucher, K. Maleski, A. Sarycheva, V.B. Shenoy, E.A. Stach, B. Anasori, Y. Gogotsi, Synthesis of Mo4VAlC4 MAX Phase and Two-Dimensional Mo_4VC_4 MXene with Five Atomic Layers of Transition Metals, ACS Nano. 14 (2020) 204–217. https://doi.org/10.1021/acsnano.9b07708.

[113] M. Griseri, B. Tunca, S. Huang, M. Dahlqvist, J. Rosén, J. Lu, P.O.Å. Persson, L. Popescu, J. Vleugels, K. Lambrinou, Ta-based 413 and 211 MAX phase solid solutions with Hf and Nb, J. Eur. Ceram. Soc. 40 (2020) 1829–1838. https://doi.org/10.1016/j.jeurceramsoc.2019.12.052.

[114] B. Anasori, M. Dahlqvist, J. Halim, E.J. Moon, J. Lu, B.C. Hosler, E.N. Caspi, S.J. May, L. Hultman, P. Eklund, J. Rosén, M.W. Barsoum, Experimental and theoretical characterization of ordered MAX phases Mo_2TiAlC_2 and $Mo_2Ti_2AlC_3$, J. Appl. Phys. 118 (2015) 094304. https://doi.org/10.1063/1.4929640.

[115] R. Meshkian, Q. Tao, M. Dahlqvist, J. Lu, L. Hultman, J. Rosen, Theoretical stability and materials synthesis of a chemically ordered MAX phase, Mo_2ScAlC_2, and its two-dimensional derivate Mo_2ScC_2 MXene, Acta Mater. 125 (2017) 476–480. https://doi.org/10.1016/j.actamat.2016.12.008.

[116] B. Anasori, Y. Xie, M. Beidaghi, J. Lu, B.C. Hosler, L. Hultman, P.R.C. Kent, Y. Gogotsi, M.W. Barsoum, Two-Dimensional, Ordered, Double Transition Metals Carbides (MXenes), ACS Nano. 9 (2015) 9507–9516. https://doi.org/10.1021/acsnano.5b03591.

[117] Q. Tao, M. Dahlqvist, J. Lu, S. Kota, R. Meshkian, J. Halim, J. Palisaitis, L. Hultman, M.W. Barsoum, P.O.Å. Persson, J. Rosen, Two-dimensional $Mo_{1.33}C$ MXene with divacancy ordering prepared from parent 3D laminate with in-plane chemical ordering, Nat. Commun. 8 (2017). https://doi.org/10.1038/ncomms14949.

[118] M. Dahlqvist, J. Lu, R. Meshkian, Q. Tao, L. Hultman, J. Rosen, Prediction and synthesis of a family of atomic laminate phases with Kagomé-like and in-plane chemical ordering, Sci. Adv. 3 (2017). https://doi.org/10.1126/sciadv.1700642.

[119] M. Dahlqvist, A. Petruhins, J. Lu, L. Hultman, J. Rosen, Origin of chemically ordered atomic laminates (i-MAX): Expanding the elemental space by a theoretical/experimental approach, ACS Nano. 12 (2018) 7761–7770. https://doi.org/10.1021/acsnano.8b01774.

[120] R. Meshkian, M. Dahlqvist, J. Lu, B. Wickman, J. Halim, J. Thörnberg, Q. Tao, S. Li,

S. Intikhab, J. Snyder, M.W. Barsoum, M. Yildizhan, J. Palisaitis, L. Hultman, P.O.Å. Persson, J. Rosen, W-Based Atomic Laminates and Their 2D Derivative $W_{1.33}C$ MXene with Vacancy Ordering, Adv. Mater. 30 (2018). https://doi.org/10.1002/adma.201706409.

[121] J. Lu, A. Thore, R. Meshkian, Q. Tao, L. Hultman, J. Rosen, Theoretical and Experimental Exploration of a Novel In-Plane Chemically Ordered $(Cr_{2/3}M_{1/3})_2AlC$ i-MAX Phase with M = Sc and Y, Cryst. Growth Des. 17 (2017) 5704–5711. https://doi.org/10.1021/acs.cgd.7b00642.

[122] J. Halim, J. Palisaitis, J. Lu, J. Thörnberg, E.J. Moon, M. Precner, P. Eklund, P.O.A. Persson, M.W. Barsoum, J. Rosen, Synthesis of two-dimensional $Nb_{1.33}C$ (mxene) with randomly distributed vacancies by etching of the quaternary solid solution $(Nb_{2/3}Sc_{1/3})_2AlC$ max phase, ACS Appl. Nano Mater. 1 (2018) 2455–2460. https://doi.org/10.1021/acsanm.8b00332.

[123] L. Chen, M. Dahlqvist, T. Lapauw, B. Tunca, F. Wang, J. Lu, R. Meshkian, K. Lambrinou, B. Blanpain, J. Vleugels, J. Rosen, Theoretical Prediction and Synthesis of $(Cr_{2/3}Zr_{1/3})_2AlC$ i-MAX Phase, Inorg. Chem. 57 (2018) 6237–6244. https://doi.org/10.1021/acs.inorgchem.8b00021.

[124] A. Ganguly, T. Zhen, M.W. Barsoum, Synthesis and mechanical properties of Ti_3GeC_2 and $Ti_3(Si_xGe_{1-x})C_2$ (x = 0.5, 0.75) solid solutions, J. Alloys Compd. 376 (2004) 287–295. https://doi.org/10.1016/j.jallcom.2004.01.011.

[125] G.W. Bentzel, M. Sokol, J. Griggs, A.C. Lang, M.W. Barsoum, On the interactions of Ti_2AlC, Ti_3AlC_2, Ti_3SiC_2 and Cr_2AlC with palladium at 900 °C, J. Alloys Compd. 771 (2019) 1103–1110. https://doi.org/10.1016/j.jallcom.2018.08.127.

[126] Z. Huang, H. Xu, H. Zhai, Y. Wang, Y. Zhou, Strengthening and tribological surface self-adaptability of Ti_3AlC_2 by incorporation of Sn to form $Ti_3Al(Sn)C_2$ solid solutions, Ceram. Int. 41 (2015) 3701–3709. https://doi.org/10.1016/j.ceramint.2014.11.042.

[127] Y. Li, M. Li, J. Lu, B. Ma, Z. Wang, L.Z. Cheong, K. Luo, X. Zha, K. Chen, P.O.Å. Persson, L. Hultman, P. Eklund, C. Shen, Q. Wang, J. Xue, S. Du, Z. Huang, Z. Chai, Q. Huang, Single-Atom-Thick Active Layers Realized in Nanolaminated $Ti_3(Al_xCu_{1-x})C_2$ and Its Artificial Enzyme Behavior, ACS Nano. 13 (2019) 9198–9205. https://doi.org/10.1021/acsnano.9b03530.

[128] Y.C. Zhou, J.X. Chen, J.Y. Wang, Strengthening of Ti3AlC2 by incorporation of Si to form $Ti_3Al_{1-x}Si_xC_2$ solid solutions, Acta Mater. 54 (2006) 1317–1322. https://doi.org/10.1016/j.actamat.2005.10.057.

[129] T. Cabioc'h, P. Eklund, V. Mauchamp, M. Jaouen, Structural investigation of substoichiometry and solid solution effects in $Ti_2Al(C_x,N_{1-x})_y$ compounds, J. Eur. Ceram. Soc. 32 (2012) 1803–1811. https://doi.org/10.1016/j.jeurceramsoc.2011.12.011.

[130] W. Yu, S. Li, W.G. Sloof, Microstructure and mechanical properties of a $Cr_2Al(Si)C$ solid solution, Mater. Sci. Eng. A. 527 (2010) 5997–6001. https://doi.org/10.1016/j.msea.2010.05.093.

[131] T. Cabioch, P. Eklund, V. Mauchamp, M. Jaouen, M.W. Barsoum, Tailoring of the thermal expansion of $Cr_2(Al_x,Ge_{1-x})C$ phases, J. Eur. Ceram. Soc. 33 (2013) 897–904. https://doi.org/10.1016/j.jeurceramsoc.2012.10.008.

[132] D. Horlait, S. Grasso, A. Chroneos, W.E. Lee, Attempts to synthesise quaternary MAX phases $(Zr,M)_2AlC$ and $Zr_2(Al,A)C$ as a way to approach Zr_2AlC, Mater. Res. Lett. 4 (2016) 137–144. https://doi.org/10.1080/21663831.2016.1143053.

[133] E. Zapata-Solvas, S.R.G. Christopoulos, N. Ni, D.C. Parfitt, D. Horlait, M.E. Fitzpatrick, A. Chroneos, W.E. Lee, Experimental synthesis and density functional theory investigation of radiation tolerance of $Zr_3(Al_{1-x}Si_x)C_2$ MAX phases, J. Am. Ceram. Soc. 100 (2017) 1377–1387. https://doi.org/10.1111/jace.14742.

[134] C.C. Lai, A. Petruhins, J. Lu, M. Farle, L. Hultman, P. Eklund, J. Rosen, Thermally induced substitutional reaction of Fe into Mo_2GaC thin films, Mater. Res. Lett. 5 (2017) 533–539. https://doi.org/10.1080/21663831.2017.1343207.

[135] M. Nechiche, V. Gauthier-Brunet, V. Mauchamp, A. Joulain, T. Cabioc'h, X. Milhet, P. Chartier, S. Dubois, Synthesis and characterization of a new $(Ti_{1-\varepsilon},Cu_{\varepsilon})_3(Al,Cu)C_2$ MAX phase solid solution, J. Eur. Ceram. Soc. 37 (2017) 459–466. https://doi.org/10.1016/j.jeurceramsoc.2016.09.028.

[136] T. Lapauw, B. Tunca, D. Potashnikov, A. Pesach, O. Ozeri, J. Vleugels, K. Lambrinou, The double solid solution $(Zr,Nb)_2(Al,Sn)C$ MAX phase: a steric stability approach, Sci. Rep. 8 (2018). https://doi.org/10.1038/s41598-018-31271-2.

[137] B. Tunca, T. Lapauw, R. Delville, D.R. Neuville, L. Hennet, D. Thiaudière, T. Ouisse, J. Hadermann, J. Vleugels, K. Lambrinou, Synthesis and Characterization of Double Solid Solution $(Zr,Ti)_2(Al,Sn)C$ MAX Phase Ceramics, Inorg. Chem. (2019). https://doi.org/10.1021/acs.inorgchem.9b00065.

[138] J. Thörnberg, J. Halim, J. Lu, R. Meshkian, J. Palisaitis, L. Hultman, P.O.Å. Persson, J. Rosen, Synthesis of $(V_{2/3}Sc_{1/3})_2AlC$ i-MAX phase and $V_{2-x}C$ MXene scrolls, Nanoscale. 11 (2019) 14720–14726. https://doi.org/10.1039/c9nr02354b.

[139] Z. Liu, E. Wu, J. Wang, Y. Qian, H. Xiang, X. Li, Q. Jin, G. Sun, X. Chen, J. Wang, M. Li, Crystal structure and formation mechanism of $(Cr_{2/3}Ti_{1/3})_3AlC_2$ MAX phase, Acta Mater. 73 (2014) 186–193. https://doi.org/10.1016/j.actamat.2014.04.006.

[140] A. Petruhins, M. Dahlqvist, J. Lu, L. Hultman, J. Rosen, Theoretical Prediction and Experimental Verification of the Chemically Ordered Atomic-Laminate i-MAX Phases $(Cr_{2/3}Sc_{1/3})_2GaC$ and $(Mn_{2/3}Sc_{1/3})_2GaC$, Cryst. Growth Des. 20 (2020) 55–61. https://doi.org/10.1021/acs.cgd.9b00449.

[141] B. Anasori, M. Dahlqvist, J. Halim, E.J. Moon, J. Lu, B.C. Hosler, E.N. Caspi, S.J. May, L. Hultman, P. Eklund, J. Rosén, M.W. Barsoum, Experimental and theoretical characterization of ordered MAX phases Mo_2TiAlC_2 and $Mo_2Ti_2AlC_3$, J. Appl. Phys. 118 (2015) 094304. https://doi.org/10.1063/1.4929640.

[142] Q. Tao, J. Lu, M. Dahlqvist, A. Mockute, S. Calder, A. Petruhins, R. Meshkian, O. Rivin, D. Potashnikov, E.N. Caspi, H. Shaked, A. Hoser, C. Opagiste, R.M. Galera, R. Salikhov, U. Wiedwald, C. Ritter, A.R. Wildes, B. Johansson, L. Hultman, M. Farle, M.W. Barsoum, J. Rosen, Atomically Layered and Ordered Rare-Earth i-MAX Phases: A New Class of Magnetic Quaternary Compounds, Chem. Mater. 31 (2019) 2476–2485. https://doi.org/10.1021/acs.chemmater.8b05298.

[143] A. Petruhins, J. Lu, L. Hultman, J. Rosen, Synthesis of atomically layered and chemically ordered rare-earth (RE) i-MAX phases; $(Mo_{2/3}RE_{1/3})_2GaC$ with RE = Gd, Tb, Dy, Ho, Er, Tm, Yb, and Lu, Mater. Res. Lett. 7 (2019) 446–452. https://doi.org/10.1080/21663831.2019.1644684.

[144] M.W. Barsoum, T. El-Raghy, L.U.J.T. Ogbuji, Oxidation of Ti_3SiC_2 in air, J. Electrochem. Soc. 144 (1997).

[145] M.W. Barsoum, L.H. Ho-Duc, M. Radovic, T. El-Raghy, Long Time Oxidation Study of Ti_3SiC_2, Ti_3SiC_2/SiC, and Ti_3SiC_2/TiC Composites in Air, J. Electrochem. Soc. 150 (2003) B166. https://doi.org/10.1149/1.1556035.

[146] X.H. Wang, Y.C. Zhou, Oxidation behavior of Ti_3AlC_2 at 1000-1400 °C in air, Corros. Sci. 45 (2003) 891–907. https://doi.org/10.1016/S0010-938X(02)00177-4.

[147] M. Sundberg, G. Malmqvist, A. Magnusson, T. El-Raghy, Alumina forming high temperature silicides and carbides, in: Ceram. Int., 2004: pp. 1899–1904. https://doi.org/10.1016/j.ceramint.2003.12.046.

[148] J.W. Byeon, J. Liu, M. Hopkins, W. Fischer, N. Garimella, K.B. Park, M.P. Brady, M. Radovic, T. El-Raghy, Y.H. Sohn, Microstructure and residual stress of alumina scale

formed on Ti_2AlC at high temperature in air, Oxid. Met. 68 (2007) 97–111. https://doi.org/10.1007/s11085-007-9063-0.

[149] S. Basu, N. Obando, A. Gowdy, I. Karaman, M. Radovic, Long-Term Oxidation of Ti_2AlC in Air and Water Vapor at 1000–1300°C Temperature Range , J. Electrochem. Soc. 159 (2011) C90–C96. https://doi.org/10.1149/2.052202jes.

[150] D.J. Tallman, B. Anasori, M.W. Barsoum, A critical review of the oxidation of Ti_2AlC, Ti_3AlC_2 and Cr_2AlC in Air, Mater. Res. Lett. 1 (2013) 115–125. https://doi.org/10.1080/21663831.2013.806364.

[151] K.R. Trethewey, J. Chamberlain, Corrosion for Science and Engineering, Longman, 1995. https://books.google.co.in/books?id=Ir8eAQAAIAAJ.

[152] S. Li, G. Song, K. Kwakernaak, S. van der Zwaag, W.G. Sloof, Multiple crack healing of a Ti_2AlC ceramic, J. Eur. Ceram. Soc. 32 (2012) 1813–1820. https://doi.org/10.1016/j.jeurceramsoc.2012.01.017.

[153] W.G. Sloof, R. Pei, S.A. McDonald, J.L. Fife, L. Shen, L. Boatemaa, A.S. Farle, K. Yan, X. Zhang, S. Van Der Zwaag, P.D. Lee, P.J. Withers, Repeated crack healing in MAX-phase ceramics revealed by 4D in situ synchrotron X-ray tomographic microscopy, Sci. Rep. 6 (2016). https://doi.org/10.1038/srep23040.

[154] Z. Wang, J. Sun, B. Xu, Y. Liu, P. Ke, A. Wang, Reducing the self-healing temperature of Ti_2AlC MAX phase coating by substituting Al with Sn, J. Eur. Ceram. Soc. 40 (2020) 197–201. https://doi.org/10.1016/j.jeurceramsoc.2019.09.009.

[155] Z.J. Lin, M.S. Li, J.Y. Wang, Y.C. Zhou, High-temperature oxidation and hot corrosion of Cr_2AlC, Acta Mater. 55 (2007) 6182–6191. https://doi.org/10.1016/j.actamat.2007.07.024.

[156] D.B. Lee, T.D. Nguyen, J.H. Han, S.W. Park, Oxidation of Cr_2AlC at 1300 °C in air, Corros. Sci. 49 (2007) 3926–3934. https://doi.org/10.1016/j.corsci.2007.03.044.

[157] D.B. Lee, T.D. Nguyen, Cyclic oxidation of Cr_2AlC between 1000 and 1300 °C in air, J. Alloys Compd. 464 (2008) 434–439. https://doi.org/10.1016/j.jallcom.2007.10.018.

[158] D.E. Hajas, M. To Baben, B. Hallstedt, R. Iskandar, J. Mayer, J.M. Schneider, Oxidation of Cr_2AlC coatings in the temperature range of 1230 to 1410°C, Surf. Coatings Technol. 206 (2011) 591–598. https://doi.org/10.1016/j.surfcoat.2011.03.086.

[159] S. Li, X. Chen, Y. Zhou, G. Song, Influence of grain size on high temperature oxidation behavior of Cr_2AlC ceramics, Ceram. Int. 39 (2013) 2715–2721. https://doi.org/10.1016/j.ceramint.2012.09.039.

[160] S. Li, L. Xiao, G. Song, X. Wu, W.G. Sloof, S. Van Der Zwaag, Oxidation and crack healing behavior of a fine-grained Cr_2AlC ceramic, J. Am. Ceram. Soc. 96 (2013) 892–899. https://doi.org/10.1111/jace.12170.

[161] Z. Wang, G. Ma, L. Liu, L. Wang, P. Ke, Q. Xue, A. Wang, High-performance Cr_2AlC MAX phase coatings: Oxidation mechanisms in the 900–1100°C temperature range, Corros. Sci. 167 (2020). https://doi.org/10.1016/j.corsci.2020.108492.

[162] R. Pei, S.A. McDonald, L. Shen, S. van der Zwaag, W.G. Sloof, P.J. Withers, P.M. Mummery, Crack healing behaviour of Cr_2AlC MAX phase studied by X-ray tomography, J. Eur. Ceram. Soc. 37 (2017) 441–450. https://doi.org/10.1016/j.jeurceramsoc.2016.07.018.

[163] W.M. Guo, H.N. Xiao, G.J. Zhang, Kinetics and mechanisms of non-isothermal oxidation of graphite in air, Corros. Sci. 50 (2008) 2007–2011. https://doi.org/10.1016/j.corsci.2008.04.017.

[164] X. Li, X. Wang, J. Zhang, N. Hanagata, X. Wang, Q. Weng, A. Ito, Y. Bando, D. Golberg, Hollow boron nitride nanospheres as boron reservoir for prostate cancer treatment, Nat. Commun. 8 (2017) 13936. https://doi.org/10.1038/ncomms13936.

[165] Y. ting Tang, M. sheng Chu, J. Tang, L. hua Gao, Z. gen Liu, Oxidation mechanism and

non-isothermal kinetic studies on carbonate iron ore by thermogravimetric analysis, J. Iron Steel Res. Int. 25 (2018) 1223–1231. https://doi.org/10.1007/s42243-018-0065-8.

[166] K.H. Bhat, M.R. Patil, B.P. Ravi, Kinetic studies on the reoxidation of beneficiated ilmenite by non-isothermal thermogravimetric analysis, Int. J. Min. Miner. Eng. 6 (2015) 187–198. https://doi.org/10.1504/IJMME.2015.070381.

[167] G. Moser, V. Tschamber, C. Schönnenbeck, A. Brillard, J.F. Brilhac, Non-isothermal oxidation and kinetic analysis of pure magnesium powder, J. Therm. Anal. Calorim. 136 (2019) 2145–2155. https://doi.org/10.1007/s10973-018-7845-z.

[168] S. Hasani, M. Panjepour, M. Shamanian, Non-isothermal kinetic analysis of oxidation of pure aluminum powder particles, Oxid. Met. 81 (2014) 299–313. https://doi.org/10.1007/s11085-013-9413-z.

[169] P. Ouyang, G. Mi, P. Li, L. He, J. Cao, X. Huang, Non-isothermal oxidation behavior and mechanism of a high temperature near-α Titanium Alloy, Materials (Basel). 11 (2018). https://doi.org/10.3390/ma11112141.

[170] A. Rajabi, A.R. Mashreghi, S. Hasani, Non-isothermal kinetic analysis of high temperature oxidation of Ti–6Al–4V alloy, J. Alloys Compd. 815 (2020) 151948. https://doi.org/10.1016/j.jallcom.2019.151948.

[171] R.B. Mane, H. Ampolu, S. Rohila, B.B. Panigrahi, Oxidation kinetics of Ti_3GeC_2 MAX phase, Corros. Sci. 151 (2019) 81–86. https://doi.org/10.1016/j.corsci.2019.02.018.

CHAPTER 3

MATERIALS & METHODS

Overview

The experimental procedure adopted to synthesize Cr_2AlC, V_2AlC and Ti_3AlC_2 MAX phases is presented in this chapter. The formation of various phase(s) is examined by X-ray diffraction technique (XRD). The morphology and surface characteristics are studied with the help of Field emission scanning electron microscopy (FESEM), Transmission electron microscopy (TEM), High resolution (HRTEM), Selected area energy diffraction (SAED) and X-ray photoelectron spectroscopy (XPS). Further, non-isothermal oxidation kinetics is performed to testify the stability of MAX phases in air atmosphere. The details related to the theoretical background of kinetic analysis is described. A complete calculation procedure used for kinetic analysis is also presented in this chapter.

3.1. Precursors

To synthesize MAX phases with M-elements as Cr, V, Ti, A-element as Al and C as X-element various precursors are procured. The source of Cr, V, Al and C is chromium metal powder (99 %, Loba Chemie), vanadium metal powder (99.7 %, Sisco Research Laboratories), aluminum metal powder (99 %, SD fine) and graphite powder (99.99 %, Sigma Aldrich), respectively. However, two sources are used for Ti, i.e, titanium metal powders (99 %, Sigma Aldrich) and titanium carbide powder (98 %, Sigma Aldrich).

3.2. Synthesis of MAX phases

To prepare Cr_2AlC, V_2AlC and Ti_3AlC_2 MAX phases, synthesis parameters are optimized by varying the composition and temperature. The variation in aluminum content (10 – 50 mol %) from the stoichiometry ratio is done to prepare these MAX phases. Firstly, the size of chromium and vanadium metal powders is reduced to ≤ 45 μm through a PM-100 Retsch Ball Mill. In this step, the ball milling is performed at 400 rpm for 4 hours with the charge ratio 14:01. Since the size of Ti precursors is ≤ 45 μm, so, Ti precursors are not milled for size reduction. Fig. 3.1 presents the schematic diagram related to the complete synthesis protocol used in the present work. ***Many experiments with different probable combinations have been done. However, only those where tendency of formation of MAX phases are observed have been reported in the thesis.*** The stoichiometry ratio, synthesis temperature and dwell time adopted for Cr_2AlC, V_2AlC and Ti_3AlC_2 MAX phases was different and details are described below:

3.2.1. Cr_2AlC MAX phase

To synthesize Cr_2AlC MAX phase, all the starting materials, i.e., the milled chromium, aluminum, and graphite were mixed in the five different molar ratios (Cr: Al: C = 2:1.1:1, 2:1.2:1, 2:1.3:1, 2:1.4:1 and 2:1.5:1) for 30 minutes in a ball mill at 200 rpm with the charge ratio 14:1. These five powder samples were named as CAC-1, CAC-2, CAC-3, CAC-4 and CAC-5, respectively.

3.2.2. V_2AlC MAX phase

The milled vanadium metal powder was mixed with aluminum and the graphite in four different molar ratios (V: Al: C = 2:1.1:1, 2:1.2:1, 2:1.3:1, 2:1.4:1). The mixing was performed in the same way as above. The milled samples were labelled as VAC 1, VAC 2, VAC 3 and VAC 4.

3.2.3. Ti_3AlC_2 MAX phase

Ti_3AlC_2 MAX phase was synthesized by mixing the titanium metal powder, titanium carbide, aluminum and graphite in four different molar ratios (Ti: TiC: Al: C = 1: 1: 1.1: 1.9,

1: 1: 1.2: 1.9, 1: 1: 1.3: 1.9 and 1: 1: 1.4: 1.9). The mixing was performed in the same way as above. The milled samples were named as TAC 1, TAC 2, TAC 3 and TAC 4.

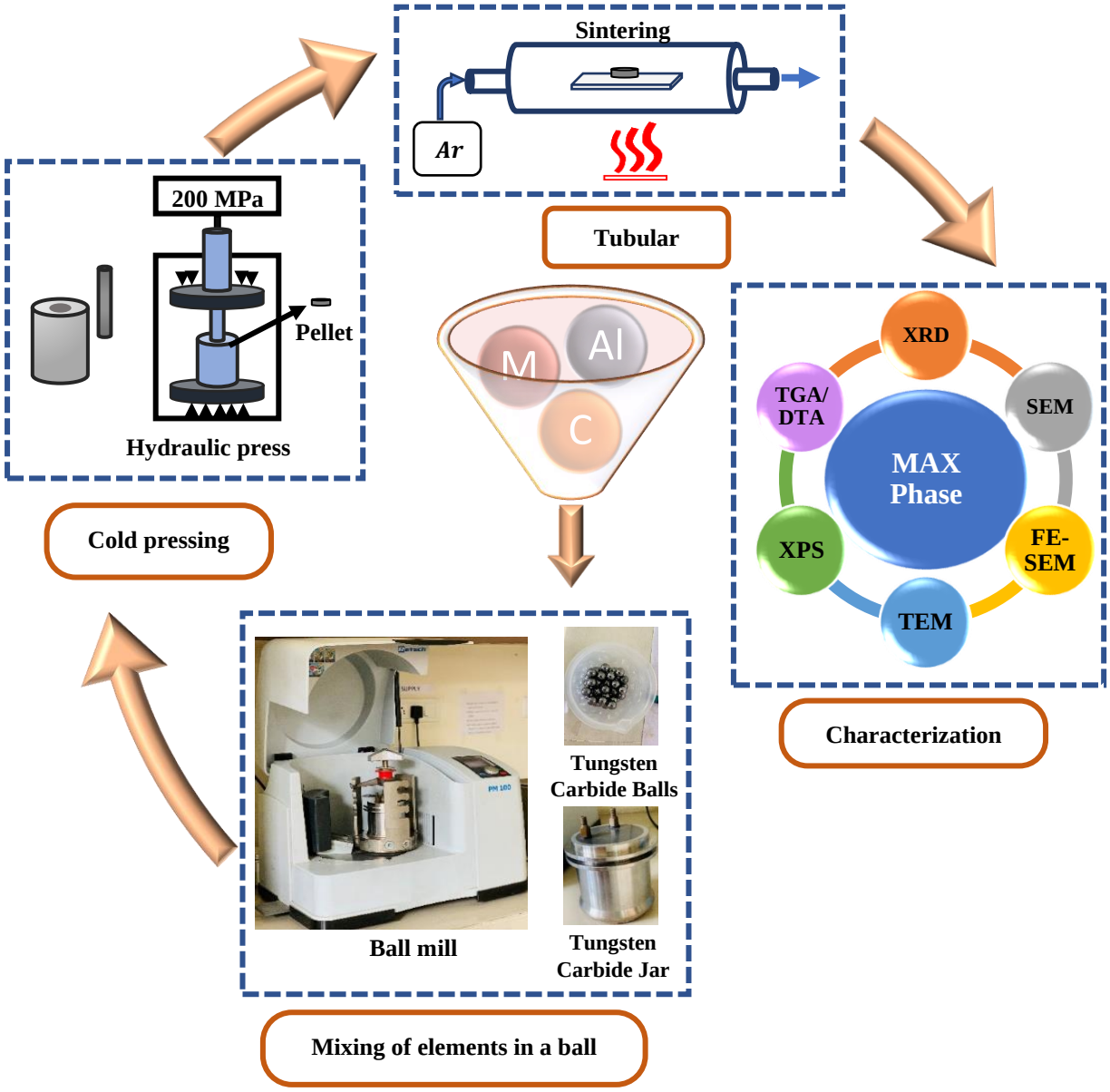

Fig. 3.1 The schematic diagram related to the complete synthesis protocol used in the present work.

3.2.4. Pressureless sintering

In order to prepare Cr_2AlC, V_2AlC and Ti_3AlC_2 MAX phases the mixed powder samples were pelletized (10 mm Dia. × 5 mm Thickness) by using a Hydraulic Press. The description related to sintering is published elsewhere [1,2]. The pressure-Less sintering of all the pellets was carried out in a Lenton Tubular Furnace (LTF 18/75/300, U.K.). The sintering of the pellets is performed by varying temperature and holding time. The tube used for sintering was made of recrystallized alumina. Before sintering, the sample was placed on an alumina

plate (120 mm Length × 60 mm Breadth × 4 mm Thickness) in the middle of tubular furnace and titanium turning were used at both ends of the tube to avoid oxidation. Further, Ar gas was flushed for 30 minutes to remove the air from the tube prior to sintering. The complete synthesis process is performed under the high purity argon atmosphere.

3.3. Characterization of MAX phases

The prepared MAX phases were characterized by various techniques as described here.

3.3.1. X-ray diffraction technique

The phase formation in the samples is examined through a PANalytical X'Pert PRO with the Ni filter. The voltage and the current of the machine are kept at 40 kV and 45 mA, respectively. All the crystalline peaks observed in the diffractograms are analyzed by the X'Pert High Score and the Origin software. The International Centre for Diffraction Data (ICDD) standard cards are used for matching the phases present in the prepared samples. The volume fraction of all the phases is calculated though XRD peak fitting by using pseudo-voigt function. Moreover, the Rietveld refinement of all the prepared samples is performed by using FullProof software. The Wycoff position for the Cr_2AlC, Ti_3AlC_2 and V_2AlC are taken from the literature [3–5]. The shape, full width at half maxima (FWHM), background, scale, overall b-factor and cell parameters are optimized step-by-step.

3.3.2. Surface morphology

The morphological and the microstructural features of the synthesized MAX phases was examined through the Field-Emission Scanning Electron Microscope (FE-SEM, Hitachi SU8010, Tokyo) and the Transmission Electron Microscope (TEM, JEOL JEM-F200, Tokyo) [6].

3.3.3. X-ray Photoelectron Spectroscopy (XPS)

The surface chemical composition and the valency states in the MAX phases was examined through the X-ray Photoelectron Spectroscopy (XPS, Physical Electronics PHI 5000 VersaProbe III, USA) with the Auger Electron Spectroscopy (AES) Module. For XPS measurements, Al-Kα radiation of 1486.7 eV was used at voltage 15 kV and current 15 mA.

3.3.4. Thermal Analysis

The oxidation kinetics of the MAX phases was analyzed through the Thermogravimetry Analysis (TGA) and the Differential Thermal Analysis (DTA) by using instruments PerkinElmer Pyris Diamond TG-DTA (USA) and SII 6300 EXSTAR (Canada). The thermal analysis was performed at multiple heating rates in the air atmosphere.

3.4. Oxidation kinetics of MAX phases

The rate of thermal oxidation reaction can be expressed as [7]:

$$\frac{d\alpha}{dt} = k(T)f(\alpha) \tag{3.1}$$

$$k(T) = Ae^{-\frac{E_a}{RT}} \tag{3.2}$$

where t is time (s), T is absolute temperature (K), $k(T)$ is the rate constant, $f(\alpha)$ is the differential form of the degree of conversion (α), R is gas constant (8.314 J/mol), A is the pre-exponential factor (min^{-1}), and E_a is the activation energy (kJ/mol). In DTA analysis, conversion value (α) is expressed [8]:

$$\alpha = \frac{A_T}{A_f} \tag{3.3}$$

where A_T is the area under a DTA peak at temperature T and A_f is final area under the curve at final temperature of a DTA peak.

The final equation for the non-isothermal oxidation process at a linear heating rate (β) can be expressed as:

$$\frac{d\alpha}{dT} = \frac{A}{\beta}e^{-E_{a/RT}}f(\alpha) \tag{3.4}$$

Heating rate (β) is defined as the change in the temperature with respect to time. In a heat treatment process, heating rate plays a crucial role and affect the formation or decomposition or phase transition in a reaction. The kinetic analysis performed at various heating rate is considered as more efficient in comparison to single heating rate [9,10]. There are several iso-conversional kinetic methods that have been developed by considering the above equation as a base. These kinetic methods adopted different temperature integral approximations for the calculation of kinetic parameters. The general equation applicable to all kinetic methods can be written as:

$$\ln\left(\frac{\beta}{T^B}\right) = constant - C\left(\frac{E_a}{RT}\right) \tag{3.5}$$

The activation energy can be calculated by plotting $\ln\left(\frac{\beta}{T^B}\right)$ vs. *1/T* and the slope of the plotted curve is equal to $C\left(\frac{E_a}{RT}\right)$.

Among these kinetic models, Kissinger–Akahira–Sunsose (KAS) [11], and Flynn-Wall-Ozawa (FWO) [12] methods are appropriate to calculate activation energy. The KAS and FWO methods are integral iso-conversional kinetic models. The former method (KAS) is based on Striank approximation [13] and can be expressed as:

$$\ln\left(\frac{\beta}{T^{1.92}}\right) = \ln\left(\frac{AR}{E_a}\right) + \ln\left(\frac{df(\alpha)}{d\alpha}\right) - 1.008\frac{E_a}{RT} \tag{3.6}$$

The FWO method is based on the Doyle approximation [14] and can be expressed as:

$$\ln(\beta) = \ln\left(\frac{AE_a}{g(\alpha)R}\right) - 5.331 - 1.052\frac{E_a}{RT} \tag{3.7}$$

The activation energy is determined through linear fitted plots obtained from KAS $\left(ln\left(\frac{\beta}{T^{1.92}}\right)\text{ vs.}\frac{1000}{T}\right)$ and FWO $\left(ln\,(\beta)\text{ vs.}\frac{1000}{T}\right)$. Moreover, the reaction mechanism involved during a non-isothermal oxidation process is identified by using the integral master plot [15] method. Through this method, the experimental and theoretical master curves are generated and compared. The integral master plot method can be expressed as:

$$g(\alpha) = \frac{AE}{\beta R}P(u) \tag{3.8}$$

where, $g(\alpha)$ is the integral function of conversion fraction α, $u = E/RT$ and $P(u)$ is the temperature integral. where, $g(\alpha)$ is the integral function of conversion fraction α, $u = E/RT$ and $P(u)$ is the temperature integral, which can be derived from relation given below:

$$P(u) \cong \frac{exp(-1.0008u - 0.312)}{u^{1.92}} \tag{3.9}$$

Table 3.1 Several reaction models responsible for thermal processes in a material.

Reaction models	**Integral form $g(\alpha)$**	**Differential form $f(\alpha)$**
Diffusion reaction models		
D_1 (1 – D diffusion)	α^2	$(1/2)\alpha$
D_2 (2 – D diffusion)	$\alpha + (1-\alpha)\,(ln(1-\alpha))$	$1/ln(1-\alpha)$
D_3 (3 – D diffusion)	$(1-(1-\alpha)^{1/3})^2$	$3(1-\alpha)^{2/3}/2(1-(1-\alpha)^{1/3})$
D_4 (Ginstling-Brounshtein)	$1 - 2\alpha/3 - (1-\alpha)^{2/3}$	$3/2\left((1-\alpha)^{-1/3} - 1\right)$
Reaction order models		
F_1 (First order)	$-ln(1-\alpha)$	$(1-\alpha)$
F_2 (Second order)	$1/(1-\alpha)$	$(1-\alpha)^2$
F_3 (Third order)	$1/2(1-\alpha)$	$(1-\alpha)^3$
Nucleation models		
A_2 (Avrami-Erofeyev)	$(-ln(1-\alpha))^{1/2}$	$2(1-\alpha)(-ln(1-\alpha))^{1/2}$
A_3 (Avrami-Erofeyev)	$(-ln(1-\alpha))^{1/3}$	$3(1-\alpha)(-ln(1-\alpha))^{2/3}$
A_4 (Avrami-Erofeyev)	$(-ln(1-\alpha))^{1/4}$	$4(1-\alpha)(-ln(1-\alpha))^{3/4}$
P2 (Power law)	$\alpha^{1/2}$	$2\alpha^{1/2}$
P3 (Power law)	$\alpha^{1/3}$	$3\alpha^{2/3}$
P4 (Power law)	$\alpha^{1/4}$	$4\alpha^{3/4}$
Geometric contraction models		
R_2 (contracting area)	$1-(1-\alpha)^{1/2}$	$2(1-\alpha)^{1/2}$
R_3 (contracting volume)	$1-(1-\alpha)^{1/3}$	$3(1-\alpha)^{2/3}$

The exact reaction mechanism can be identified by using the predetermined value of activation energy and employing $\alpha = 0.5$ as a reference, Eq. (3.8) become as:

$$g(0.5) = \frac{AE}{\beta R} P(u_{0.5}) \tag{3.10}$$

From Eq. (3.8) – (3.10), the equation for integral master-plots can be derived as:

$$\frac{g(\alpha)}{g(0.5)} = \frac{P(u)}{P(0.5)} \tag{3.11}$$

Through this method the reaction mechanism is identified through comparison of theoretical curves $g(\alpha)/g(0.5)$ (LHS of eq. 19) based on Table 3.1, while the experimental curves (RHS of eq. 11) are generated from $P(u)/P(0.5)$.

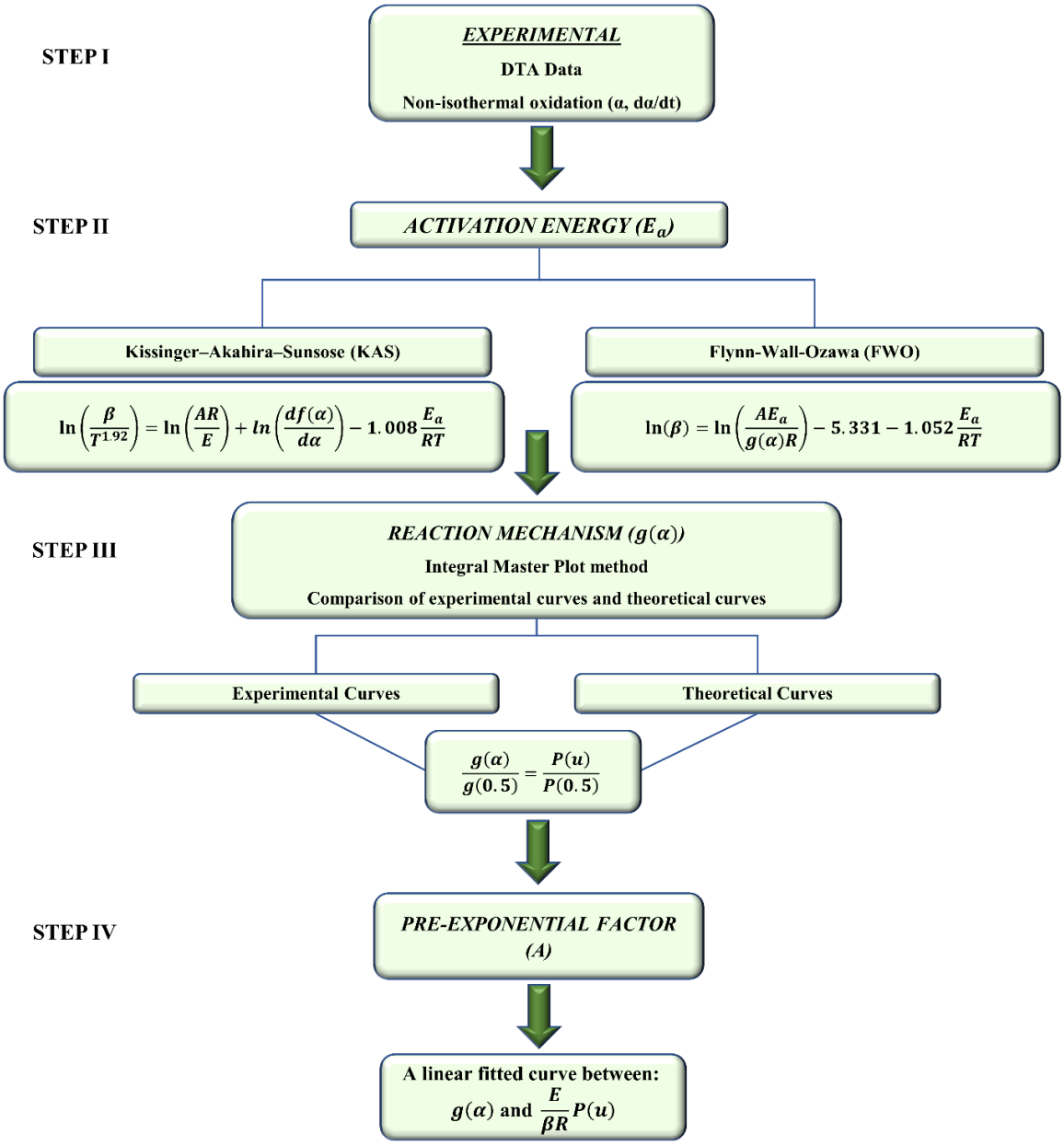

Fig. 3.2 The flow diagram of a step-wise procedure followed to perform non-isothermal kinetic analysis.

Further, to calculate pre-exponential factor eq. (3.8) is modified by substituting value of reaction mechanism ($g(\alpha)$). The pre-exponential factor is determined by using the average activation energy in Eq. 3.8. The pre-exponential factor is calculated from the slope of the linear fitted curve between $g(\alpha)$ and $\frac{E}{\beta R}P(u)$. Finally, the calculated kinetic triplets are determined for a non-isothermal oxidation process. The flow diagram (Fig. 3.2) shows the steps followed to perform non-isothermal kinetic analysis.

References

[1] K. Lu, J. Navin, M.R. Murakami, G. Pickrell, Advances in Synthesis, Processing, and Applications of Nanostructures, 2012.

[2] C.N. George, J.K. Thomas, R. Jose, H.P. Kumar, M.K. Suresh, V.R. Kumar, P.R.S. Wariar, J. Koshy, Synthesis and characterization of nanocrystalline strontium titanate through a modified combustion method and its sintering and dielectric properties, J. Alloys Compd. 486 (2009) 711–715. https://doi.org/10.1016/j.jallcom.2009.07.045.

[3] J. Liu, X. Zuo, Z. Wang, L. Wang, X. Wu, P. Ke, A. Wang, Fabrication and mechanical properties of high purity of Cr_2AlC coatings by adjustable Al contents, J. Alloys Compd. 753 (2018) 11–17. https://doi.org/10.1016/j.jallcom.2018.04.100.

[4] Y.C. Zhou, X.H. Wang, Z.M. Sun, S.Q. Chen, Electronic and structural properties of the layered ternary carbide Ti_3AlC_2, J. Mater. Chem. 11 (2001) 2336–2340. https://doi.org/10.1039/b101520f.

[5] J. Etzkorn, M. Ade, H. Hillebrecht, V_2AlC, V_4AlC_{3-x} (x approximately 0.31), and $V_{12}Al_3C_8$: synthesis, crystal growth, structure, and superstructure., Inorg. Chem. 46 (2007) 7646–53. https://doi.org/10.1021/ic700382y.

[6] N. Verma, V. Sharma, R. Kumar, R. Sharma, M.C. Joshi, G.R. Umapathy, S. Ohja, S. Chopra, On the spectroscopic examination of printed documents by using a field emission scanning electron microscope with energy-dispersive X-ray spectroscopy (FE-SEM-EDS) and chemometric methods: application in forensic science, Anal. Bioanal. Chem. 411 (2019) 3477–3495. https://doi.org/10.1007/s00216-019-01824-z.

[7] A. Khawam, D.R. Flanagan, Solid-state kinetic models: Basics and mathematical fundamentals, J. Phys. Chem. B. 110 (2006) 17315–17328. https://doi.org/10.1021/jp062746a.

[8] P. Sharma, P.K. Jha, P.K. Diwan, O.P. Pandey, Impact of CuS on the crystallization kinetics of Na_2S-P_2S_5 glasses, J. Non. Cryst. Solids. 477 (2017) 31–41. https://doi.org/10.1016/j.jnoncrysol.2017.09.046.

[9] S. Vyazovkin, K. Chrissafis, M.L. Di Lorenzo, N. Koga, M. Pijolat, B. Roduit, N. Sbirrazzuoli, J.J. Suñol, ICTAC Kinetics Committee recommendations for collecting experimental thermal analysis data for kinetic computations, Thermochim. Acta. 590 (2014) 1–23. https://doi.org/10.1016/j.tca.2014.05.036.

[10] S. Vyazovkin, A.K. Burnham, J.M. Criado, L.A. Pérez-Maqueda, C. Popescu, N. Sbirrazzuoli, ICTAC Kinetics Committee recommendations for performing kinetic computations on thermal analysis data, Thermochim. Acta. 520 (2011) 1–19. https://doi.org/10.1016/j.tca.2011.03.034.

[11] T. Akahira, T. Sunose, Method of determining activation deterioration constant of electrical insulating materials, Res. Rep. Chiba. Inst. Technol. (Sci Technol). 16 (1971) 22–31.

[12] J.H. Flynn, L.A. Wall, A quick, direct method for the determination of activation energy from thermogravimetry data, J. Polym. Sci. Part C Polym. Lett. 4 (1966) 323–328.

[13] M.J. Starink, The determination of activation energy from linear heating rate experiments: A comparison of the accuracy of isoconversion methods, Thermochim. Acta. 404 (2003) 163–176. https://doi.org/10.1016/S0040-6031(03)00144-8.

[14] T. Ozawa, A New Method of Analyzing Thermogravimetric Data, Bull. Chem. Soc. Jpn. 38 (1965) 1881–1886. https://doi.org/10.1246/bcsj.38.1881.

[15] J. Chen, Y. Wang, X. Lang, X. Ren, S. Fan, Evaluation of agricultural residues pyrolysis under non-isothermal conditions: Thermal behaviors, kinetics, and thermodynamics, Bioresour. Technol. 241 (2017) 340–348. https://doi.org/10.1016/j.biortech.2017.05.036.

CHAPTER 4

SYNTHESIS & OXIDATION KINETICS OF Cr_2AlC MAX PHASE

Overview

High purity Cr_2AlC MAX phase is prepared through the sintering method by varying the aluminum content. The formation of Cr_2AlC is confirmed through XRD, FESEM, HRTEM, SAED and XPS analysis. It is observed that the aluminum content is crucial to obtain highly pure Cr_2AlC phase. The exact sintering temperature is also identified by changing the temperature 700 – 1300 ℃. A highly pure Cr_2AlC is obtained at 1300 ℃, when Cr:Al:C = 2:1.4:1. The intermediate phases formed during synthesis of Cr_2AlC are determined and formation pathway is proposed. The kinetic triplets (activation energy, pre-exponential factor and reaction mechanism) involved during the synthesis of Cr_2AlC are estimated with the help of DTA technique. The non-isothermal oxidation kinetics of the Cr_2AlC phase is also examined through a DTA technique, at variable heating rates. The DTA results show that the oxidation of the Cr_2AlC phase occurred in two stages. The multi-stage kinetic analysis is performed to establish the nature of the oxidation process. The activation energy is calculated by following the iso-conversional kinetic methods. The reaction mechanism involved during the oxidation process is proposed through the integral master-plots method.

4.1. Introduction

In the current scenario, the MAX phases have received significant attention from the scientific point of view for their promising practical applications [1]. The reason behind the growing demand of the MAX phases is their extraordinary combination of properties which include both metals and ceramics. The properties include the high thermal and electrical conductivity, excellent machinability, good damage tolerability, high oxidation and corrosion resistance at higher temperatures, and superb thermal shock resistance [2]. These interesting properties have placed the MAX phases as a potential candidate for the higher temperature applications [3,4]. Furthermore, etching of A element in MAX phases leads to the formation of new class of materials, i.e., MXenes (two-dimensional transition metal carbides). MXenes are the potential candidate for energy conversion and storage applications [5].

In the current study, the impact of the aluminium concentration on the formation of a highly pure Cr_2AlC was conducted. The thermal stability of the Cr_2AlC MAX phase was estimated through the Thermogravimetry Analysis (TGA) and the Differential Thermal Analysis (DTA) techniques. The focus of the present work is to evaluate the optimum condition for the synthesis of Cr_2AlC phase and to study its oxidation behaviour under non-isothermal conditions. The kinetic parameters are calculated by following the Kissinger-Akahira-Sunose (KAS) and the Flynn-Wall-Ozawa iso-conversional kinetic methods. The reaction mechanism involved during the oxidation process has been proposed by using the integral master plots method.

4.2. Synthesis of Cr_2AlC MAX phase

According to the experimental details mentioned in the previous chapter, synthesis of Cr_2AlC was studied. Firstly, the synthesis temperature of Cr_2AlC MAX phase was determined. In this process, the CAC 4 sample (Cr:Al:C = 2:1.4:1) was sintered at 700, 800, 900, 1000, 1100, 1200, and 1300 °C in an argon atmosphere for 1 hour. Accordingly, the nomenclature and experimental conditions of all the prepared samples are tabulated Table 4.1.

4.2.1. XRD analysis

Fig. 4.1 shows the formation of intermediate phases at different temperatures during the synthesis of Cr_2AlC MAX phase. It was observed that the elemental weight percentage remained nearly identical. Initially, Al melts at around 665 °C (Eq. 1) and reacts with Cr (Eq. 2) to form Cr_5Al_8 intermetallic compound. The peaks associated with Cr_5Al_8 phase were more pronounced in 7CAC 4 and 8CAC 4 samples heated at 700 and 800 °C, respectively. The volume fraction of distinct intermediate phases observed in Fig. 4.1 is estimated through the

XRD data and presented in Table 4.1. Also, the presence of unreacted Cr and C was observed in 7CAC 4 and 8CAC 4 samples.

Table 4.1 Nomenclature of all the samples prepared at different experimental conditions.

Samples ID	Molar ratio			Sintering temperature (°C) for 1 hr.	Volume Fraction (%)					
	Cr	C	Al		Cr	C	Cr_5Al_8	Cr_2Al	Cr_2AlC	Cr_7C_3
7CAC 4	2	1	1.4	700	62.34	6.23	31.43	–	–	–
8CAC 4	2	1	1.4	800	43.34	5.34	51.3	–	–	–
9CAC 4	2	1	1.4	900	12.23	4.89	17.23	36.33	29.31	–
10CAC 4	2	1	1.4	1000	16.46	6.98	14.41	12.86	49.27	–
11CAC 4	2	1	1.4	1100	10.06	–	15.26	7.68	59.52	7.88
12CAC 1	2	1	1.1	1200	–	–	–	4.63	89.51	5.86
12CAC 2	2	1	1.2	1200	–	–	–	1.69	96.09	2.21
12CAC 3	2	1	1.3	1200	–	–	–	2.08	93.78	4.13
12CAC 4	2	1	1.4	1200	–	–	–	0.83	96.26	2.91
12CAC 5	2	1	1.5	1200	–	–	–	4.21	90.89	4.88
13CAC 1	2	1	1.1	1300	–	–	–	–	92.44	7.56
13CAC 2	2	1	1.2	1300	–	–	–	–	92.49	7.51
13CAC 3	2	1	1.3	1300	–	–	–	–	94.51	5.49
13CAC 4	2	1	1.4	1300	–	–	–	–	98.17	1.82
13CAC 5	2	1	1.5	1300	–	–	–	–	90.07	9.93

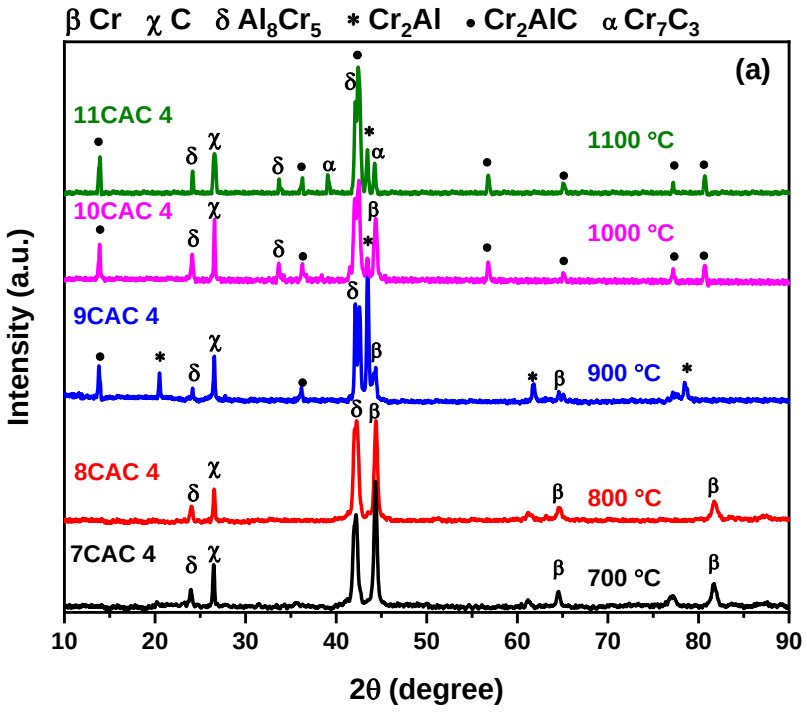

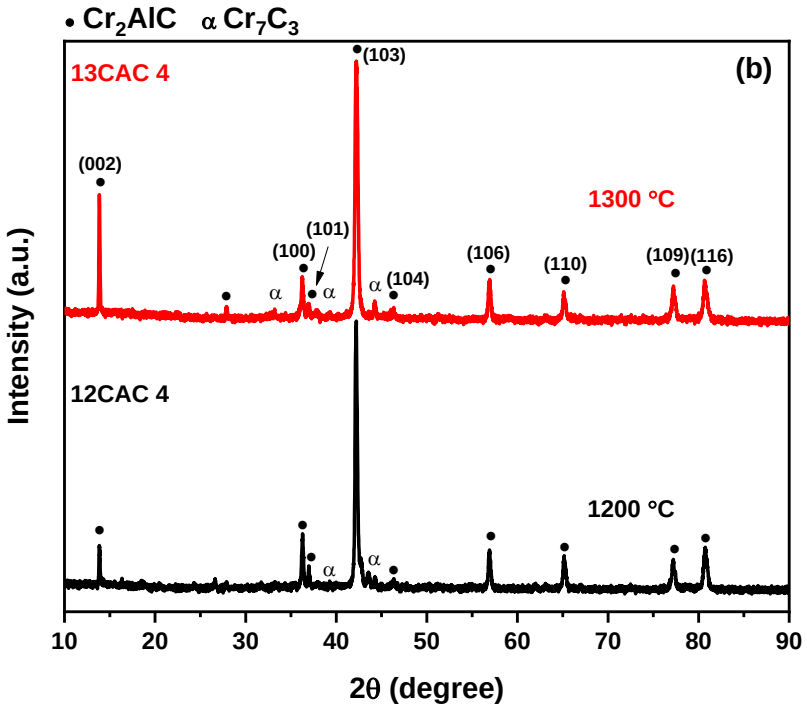

Fig. 4.1 The formation of intermediate phases at different temperatures during the synthesis of Cr_2AlC.

Further, increase in temperature up to 900 °C (9CAC 4 sample), results in the formation of Cr_2Al (Eq. 3, 4) and Cr_2AlC (Eq. 5, 6) phases along with minor phases of Cr, C and Cr_5Al_8. In this case, Cr_2Al phase was present in majority as compared to other phases (Cr_2AlC, Cr, C and Cr_5Al_8).

$$Al_{(s)} \rightarrow Al_{(l)} \quad (4.1)$$

$$5Cr + 8Al \rightarrow Cr_5Al_8 \quad (4.2)$$

$$2Cr + Al \rightarrow Cr_2Al \quad (4.3)$$

$$Cr_5Al_8 + 13Cr + Al \rightarrow 9Cr_2Al \quad (4.4)$$

$$Cr_5Al_8 + 11Cr + 8C \rightarrow 8Cr_2AlC \quad (4.5)$$

$$Cr_2Al + C \rightarrow Cr_2AlC \quad (4.6)$$

$$7Cr + 3C \rightarrow Cr_7C_3 \quad (4.7)$$

At 1000 °C, the peaks associated with Cr_2AlC becomes more pronounced along with minor phases of Cr_2Al, Cr, C and Cr_5Al_8 in 10CAC 4 samples. However, peaks associated with Cr_3C_7 are observed in 11CAC 4 sample heated at 1100 °C. The formation of Cr_3C_7 ascribed to the reaction between unreacted Cr and C (Eq. 7). It was observed that the formation of Cr_2AlC MAX phase was favorable at 1200 °C and 1300 °C. Therefore, the composition variation was done at these two temperatures. The content of aluminum was varied from 10 – 50 mol % and five samples CAC 1, CAC 2, CAC 3, CAC 4 and CAC 5 were sintered at 1200 °C and 1300 °C for an hour in argon atmosphere.

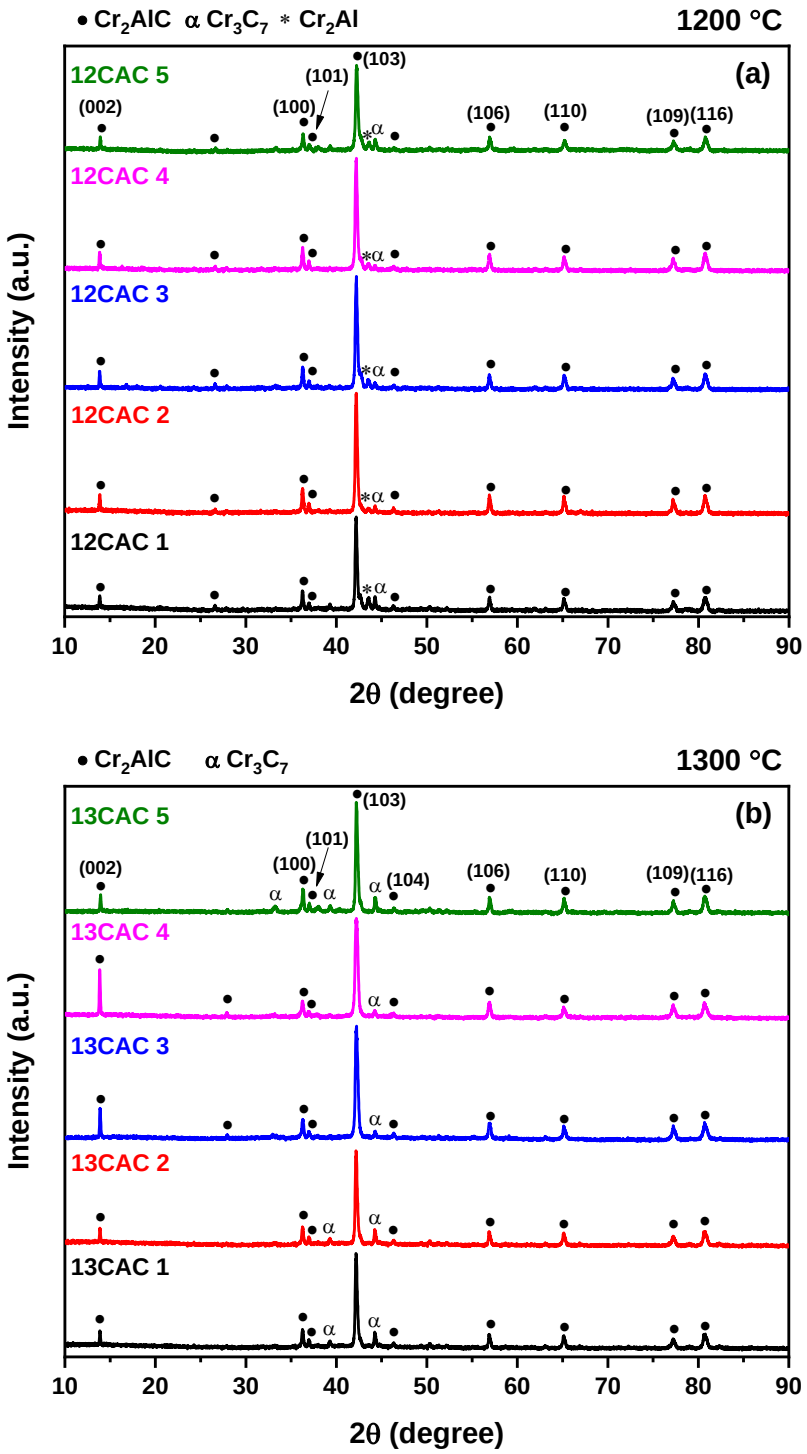

Fig. 4.2 XRD patterns of (a) 12CAC-1 – 12CAC-5 samples and (b) 13CAC-1 – 13CAC-5 samples sintered at 1200 ºC and 1300 ºC, respectively.

Fig. 4.2a shows the XRD patterns of 12CAC 1 – 12CAC 5 samples heated at 1200 ºC for an hour. The percentage composition of the distinct phases observed in these samples are estimated through the XRD data and given in Table 4.1. It is visible from Fig. 4.2 and Table 4.1 that the variation of the aluminum content influences the formation of a pure hexagonal Cr_2AlC MAX phase. The samples heated at 1200 ºC (Fig. 4.2a) reveal the formation of three

distinct Cr_2AlC, Cr_7C_3, and Cr_2Al phases. It is observed in a 12CAC 4 sample (Fig. 4.2) that the intensity of the secondary phases (Cr_7C_3 and Cr_2Al) decreased with an increase in the aluminum content up to 40 mol%. This indicates that the formation of the Cr_2AlC phase is favored with an increase in the aluminum content.

Comparable results are also reported for the synthesis of the other MAX phases by increasing the aluminum content from the stoichiometry ratio [6–8]. However, any further increment in the aluminum content in a 12CAC 5 sample leads to an increase in the peak intensity of the secondary phases (Cr_7C_3 and Cr_2Al). This could be ascribed to the excessive aluminum present in the system, which favors the formation of the Cr_2Al phase and results in more residual carbon. This residual carbon reacts with the chromium and forms a carbon-deficient chromium carbide (Cr_7C_3) phase [9]. At 1200 ºC (Fig. 4.2a), the maximum purity of the Cr_2AlC phase (96.3%) is observed in 12CAC 4 sample. The presence of the intermediate phases in all the samples sintered at 1200 ºC (Fig. 4.2a) reveals that the reaction temperature is not sufficient enough for the formation of a highly pure Cr_2AlC MAX phase. It could be possible that at the higher temperature (> 1200 ºC), where the intermediate phases (Cr_7C_3 and Cr_2Al) react with one another to form the Cr_2AlC MAX phase.

Table 4.2 The lattice parameters of Cr_2AlC phase present in prepared samples.

Temperature (ºC) for 1 hr.	Samples	Lattice Parameters of Cr_2AlC				
		a (Å)	c (Å)	χ^2	Cell Volume (Å^3)	R_{wp}
1200 ºC	12CAC-1	2.860	12.779	1.26	90.99	18.2
	12CAC-2	2.865	12.815	1.16	91.05	13.9
	12CAC-3	2.859	12.811	1.15	90.32	15.4
	12CAC-4	2.861	12.801	1.22	90.48	19.2
	12CAC-5	2.864	12.778	1.31	90.87	22.1
1300 ºC	13CAC-1	2.862	12.803	1.16	90.63	16.3
	13CAC-2	2.858	12.815	1.13	90.54	17.8
	13CAC-3	2.861	12.800	1.29	90.86	19.5
	13CAC-4	2.863	12.818	1.04	91.00	11.3
	13CAC-5	2.866	12.821	1.33	90.89	20.2

Further, 13CAC 1 – 13CAC 5 samples are sintered at higher temperature (1300 ºC). Fig. 4.2b shows the XRD patterns of all these samples. In Fig. 4.2b, there are two distinct phases, i.e., Cr_2AlC and Cr_7C_3 are present in all the samples. It is observed that an increase in the temperature favors the formation of the Cr_2AlC phase. However, no peak associated with the Cr_2Al phase is observed. An increase in the amount of the aluminum content up to 40 mol%

results in the decrease in the intensity of the secondary phase (Cr_7C_3). However, further increment in the aluminum content to 50 mol% again increases the intensity of the Cr_7C_3 phase.

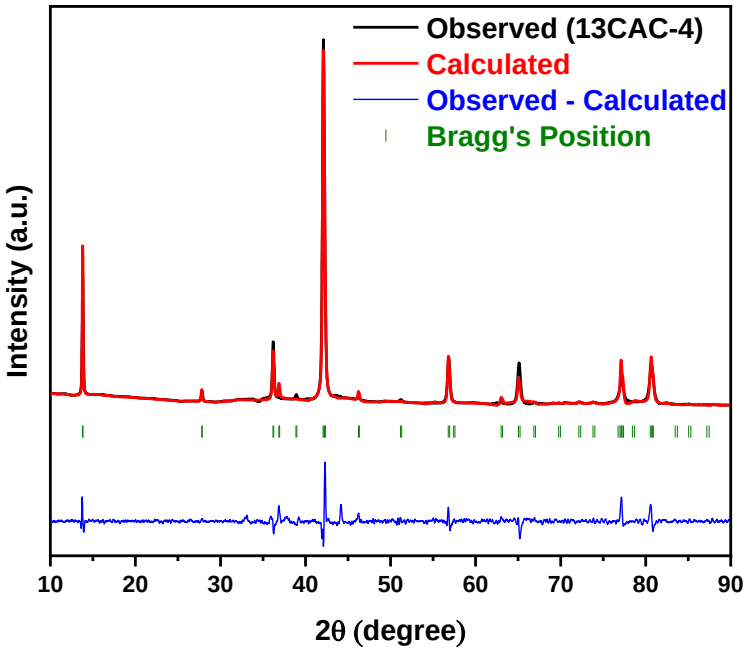

Fig. 4.3 Rietveld refinement plot of 13CAC-4 sample.

It is observed from Fig. 4.2 and Table 4.1 that the hexagonal Cr_2AlC MAX phase of purity 96.3 %, and 98.2 % is obtained in 12CAC 4 and 13CAC 4, respectively. Further, Fig. 4.3 shows Rietveld refinement plots of 13CAC 4 sample and the lattice parameters along with cell volume for all the samples is presented in Table 4.2.

4.2.2. Synthesis kinetics of Cr_2AlC MAX phase

It is observed in the previous section that the pure Cr_2AlC phase in obtained when CAC 4 sample with molar ratio Cr:Al:C = 2:1.4:1 is sintered at 1300 °C. To gain more insight related to the formation of Cr_2AlC MAX phase, synthesis kinetic analysis is performed. Many research groups conducted synthesis kinetic analysis through thermal analysis techniques [10–16]. They determined kinetic triplets (activation energy, pre-exponential factor and reaction mechanism) involved during a synthesis process by using a model based and model free kinetic methods. The model free kinetic method is most suitable to conduct kinetic analysis because this method involves no assumption of the kinetic model. In this work, kinetic analysis on the formation of Cr_2AlC MAX phase is studied at various heating rates (10, 20, 30, 40 °C/min) by using differential thermal analysis (DTA). The kinetic triplets are calculated by using the iso-conversional model free kinetic method. The value of activation energy is calculated by following most commonly used Kissinger-Akahira-Sunsose (KAS) [17,18] and Friedman (FR) [19] kinetic methods. The reaction mechanism is identified by following integral master plots method [20].

Fig. 4.4 presents DTA curves of the milled pelletized sample of chromium (Cr), aluminum (Al) and graphite (C) in ratio 2:1.4:1 at multiple heating rates (10, 20, 30, 40 °C/min) in an argon atmosphere from ambient temperature to 1250 °C. Two endothermic peaks are observed at ~ 665 °C and ~ 1053 °C in DTA curves, at 10 °C/min (Fig. 4.4a). First endothermic peak (Fig. 4.4b) is related to the melting of Al, whereas, second endothermic peak (Fig. 4.4c) corresponds to the formation of Cr_2AlC MAX phase.

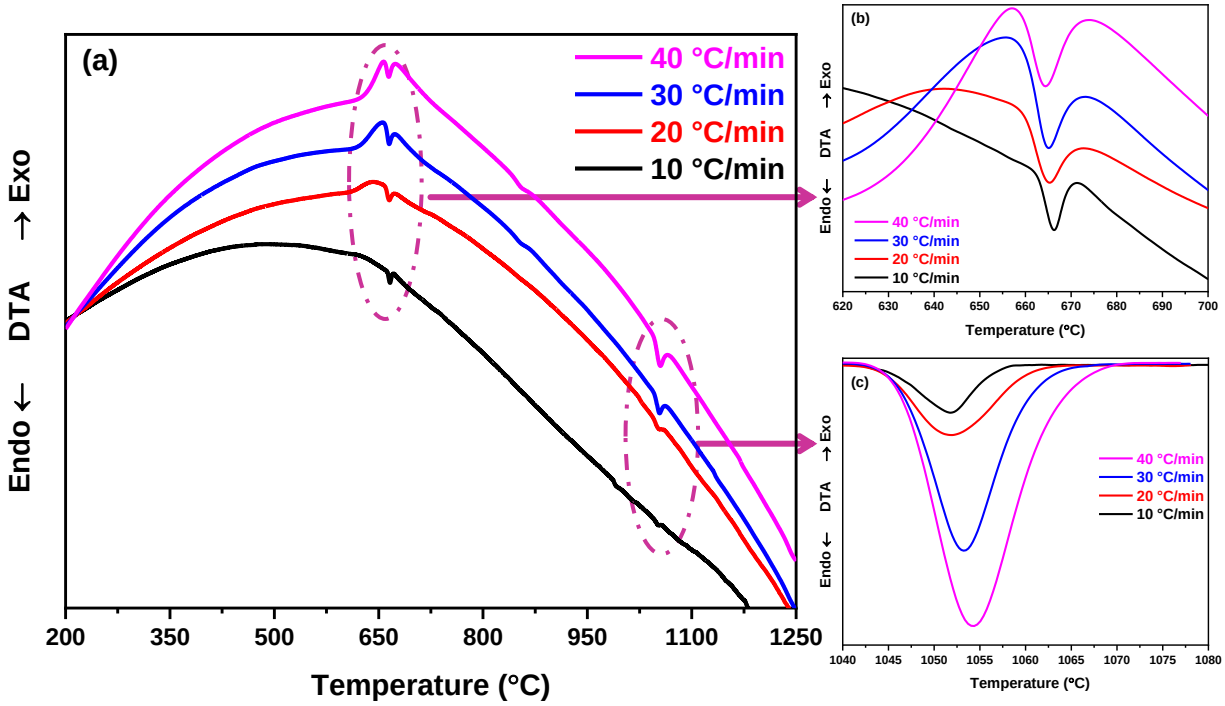

Fig. 4.4 (a) DTA curves of the milled pelletized sample of chromium, aluminum and graphite, (b) First endothermic peak, and (c) second endothermic peak at multiple heating rates (10, 20, 30, 40 °C/min) in an argon atmosphere.

Table 4.3 The initial, maximum, and final temperatures of both endothermic peaks at all heating rates.

Heating Rates	**Peak I**			**Peak II**		
(K/min)	**T_i (°C)**	**T_p (°C)**	**T_f (°C)**	**T_i (°C)**	**T_p (°C)**	**T_f (°C)**
10	657.47	666.31	671.46	1040	1051.76	1058.99
20	657.92	667.25	674.37	1040	1051.84	1063.58
30	658.12	667.37	674.65	1040	1053.22	1066.32
40	659.98	667.39	676.22	1040	1054.38	1070.49

It is observed that the endothermic peaks shifted toward higher temperatures with an increase in heating rates. This could be ascribed due to the delayed heat transfer time between the sample and the furnace. If the heating rate is slow, then the heat transfer time is more, and argon gas gets enough time to equalize the temperature of the sample and the furnace. However,

heat transfer time is less at the higher heating rate and peaks get shifted [21]. Another possible reason behind shifting is poor thermal conductivity of the reaction that resulted into thermal gradient. At slow heating rate, the value of thermal gradient is less. However, thermal gradient increased with increase in heating rate. Consequently, the reaction shifted towards higher temperature at higher heating rates. Further, the initial, maximum, and final temperatures of both endothermic peaks at all heating rates are presented in Table 4.3. The reaction involved during the formation of Cr_2AlC can be written as:

$$2Cr + Al + C \rightarrow Cr_2AlC \quad (4.8)$$

To obtain more information related to the formation of Cr_2AlC MAX phase, kinetic analysis was performed. Through kinetic analysis, kinetic triplets such as activation energy, pre-exponential factor and reaction mechanism were estimated. The procedure adopted and kinetic background is discussed in the chapter 3. The activation energy is related to the energy barrier of a reaction, while the pre-exponential factor is frequency of the vibrations occurring during a reaction. The formation of Cr_2AlC MAX phase is an endothermic process, as observed from Fig. 4.4. Fig. 4.5 shows the variation of the conversion value (α) (Fig. 4.5a) and derivative of conversion value ($d\alpha/dt$) (Fig. 4.5b) with temperature.

Fig. 4.6 shows the linear fitted curves obtained from KAS (Fig. 4.6a) and FWO (Fig. 4.6b) methods for CAC 4 sample. The calculated value of activation energy along with standard error at each conversion value, is presented in Table 4.4. Standard error associated with activation energy is calculated by following the theory of propagation of uncertainty [22]. The activation energy calculated from both methods (KAS and FWO) demonstrated $R^2 > 0.8$.

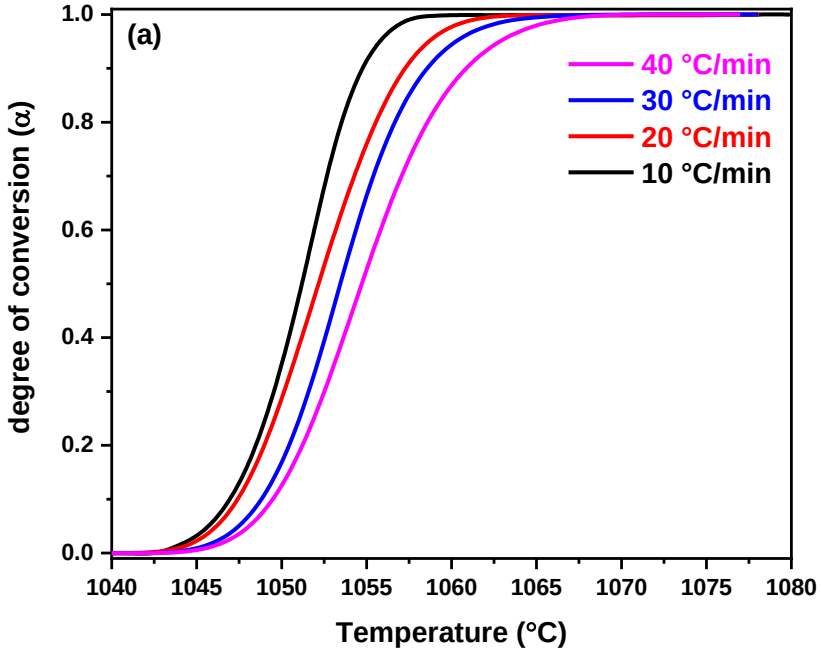

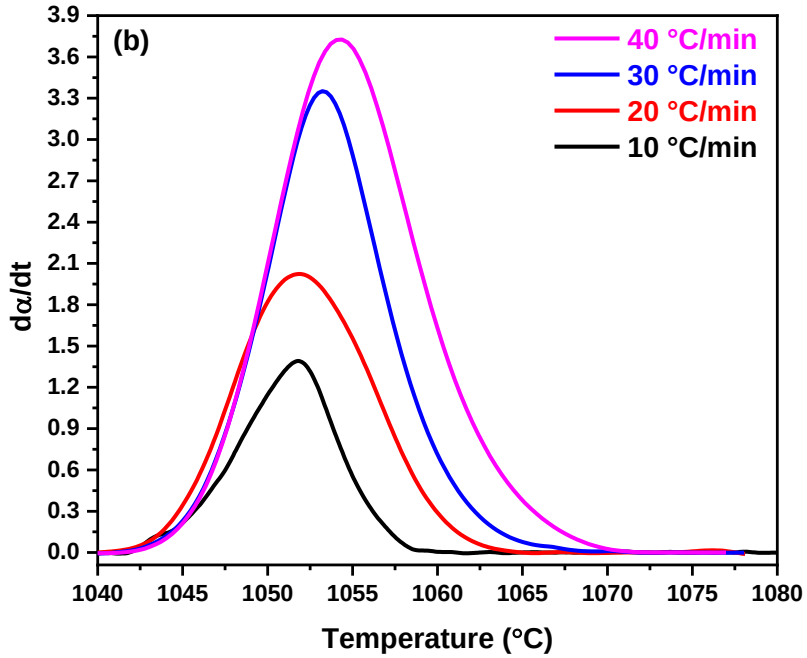

Fig. 4.5 (a) The variation of the conversion value (α) and (b) derivative of conversion value (dα/dt) with temperature.

The average activation energy value calculated from KAS (5567.17 kJ/mol) is higher than the FWO (5316.19 kJ/mol). The variation in the average activation energy value is due to different mathematical approximations used in kinetic methods (KAS and FWO). However, the trend of activation energy (Table 4.4 and Fig. 4.7) w.r.t. conversion value (α) is similar, as calculated from KAS and FWO methods.

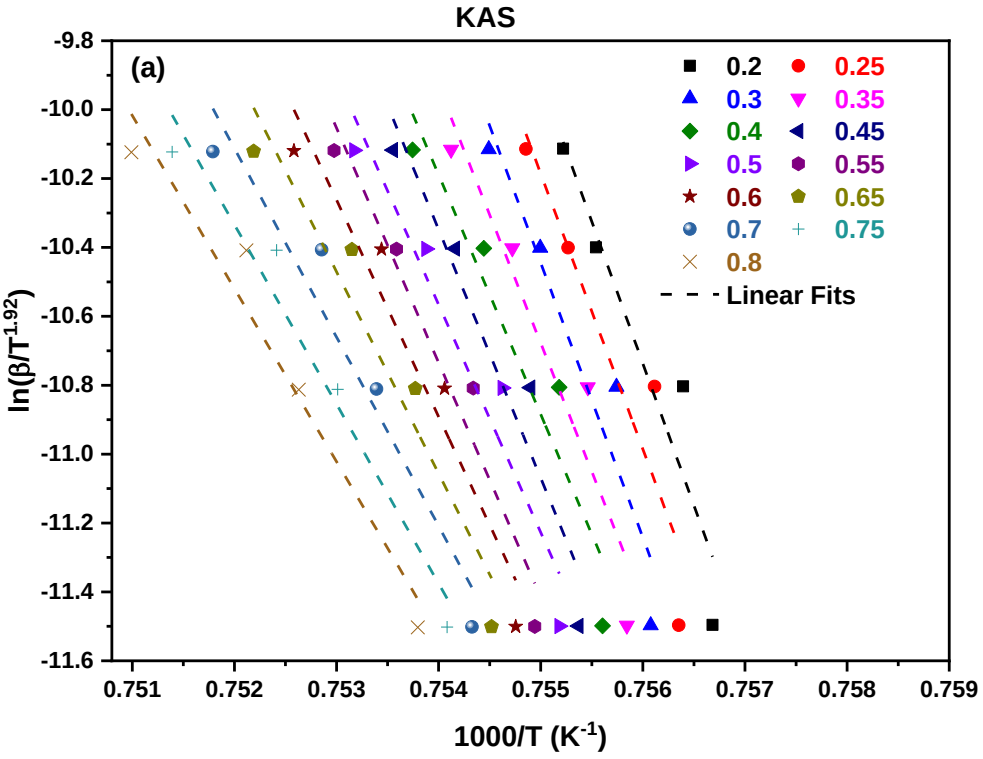

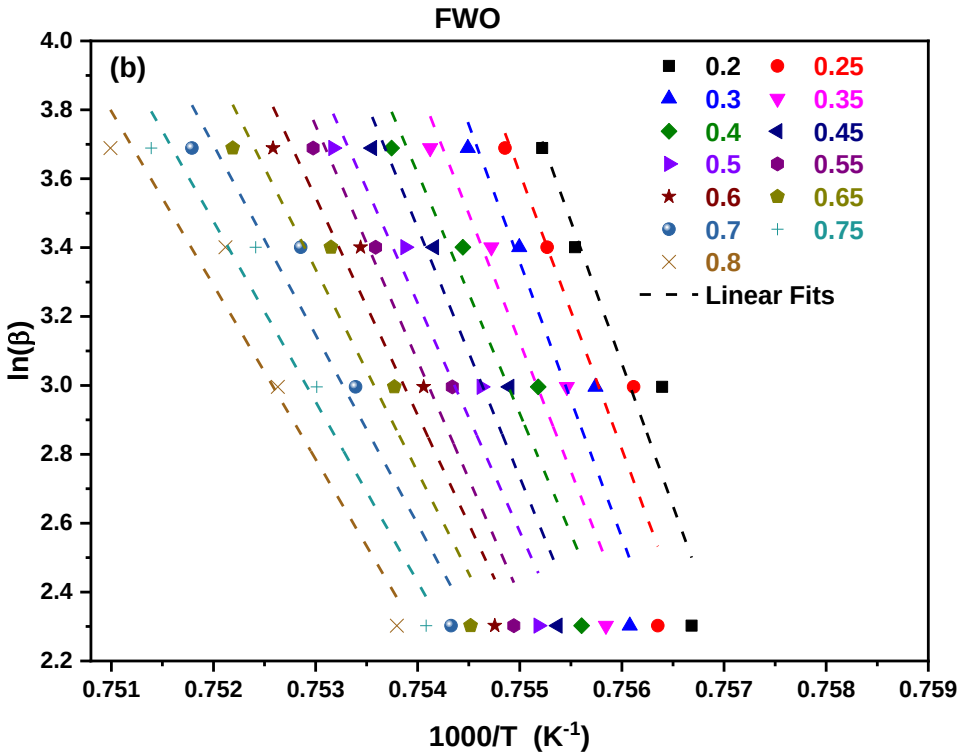

Fig. 4.6 The linear fitted curves obtained from (a) KAS and (b) FWO methods for CAC 4 sample.

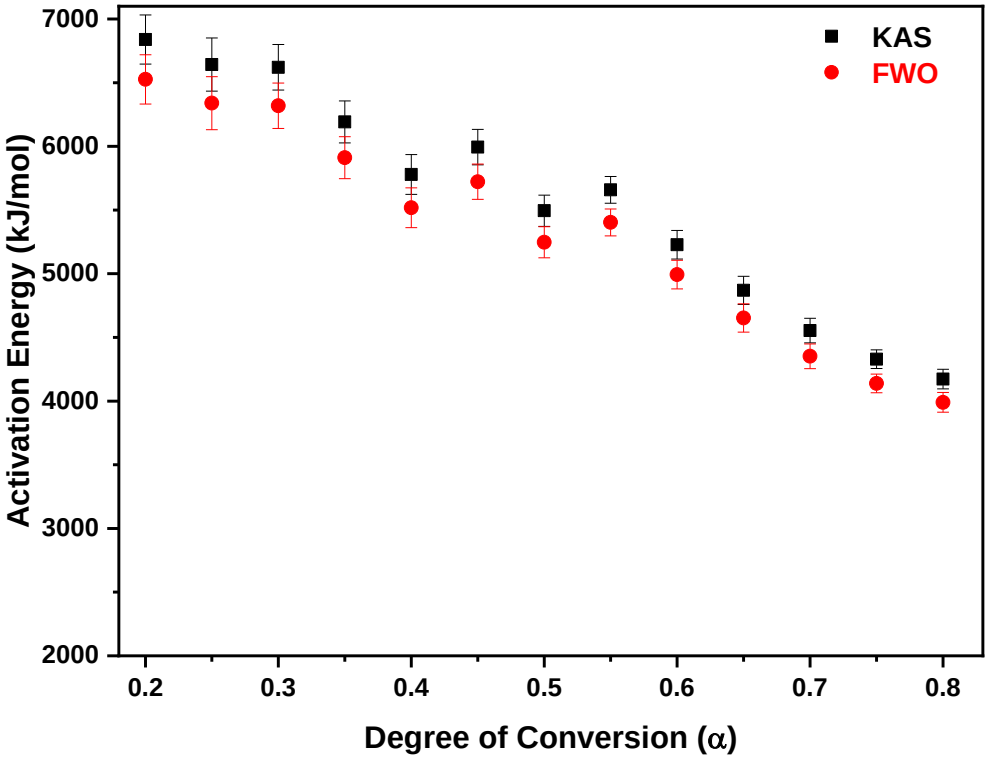

Fig. 4.7 Variation trend of activation energy calculated from KAS and FWO kinetic methods.

Table 4.4 The variation of activation energy w.r.t. conversion value (α), as calculated from KAS and FWO methods.

Conversion Value	KAS method			FWO method		
	E_a (kJ/mol)	Error	R^2	E_a (kJ/mol)	Error	R^2
0.2	6789.93	193.27	0.851	6526.01	193.27	0.852
0.25	6594.77	208.56	0.821	6339.02	208.57	0.821
0.3	6573.47	178.51	0.863	6318.63	178.51	0.864
0.35	6147.73	164.99	0.866	5910.70	164.99	0.867
0.4	5737.56	156.03	0.862	5517.70	156.04	0.864
0.45	5951.03	138.84	0.896	5722.24	138.84	0.897
0.5	5455.02	122.33	0.903	5246.99	122.34	0.905
0.55	5617.89	105.41	0.931	5403.05	105.42	0.932
0.6	5189.57	112.27	0.911	4992.65	112.27	0.911
0.65	4834.58	110.81	0.899	4652.52	110.80	0.901
0.7	4520.98	96.85	0.911	4352.04	96.85	0.913
0.75	4298.38	72.95	0.943	4138.76	72.96	0.944
0.8	4143.32	77.11	0.932	3990.20	77.10	0.933

Moreover, the reaction mechanism involved during the synthesis of Cr_2AlC MAX phase is identified by using the integral master plot [20] method. Through this method, the experimental and theoretical master curves are generated and compared.

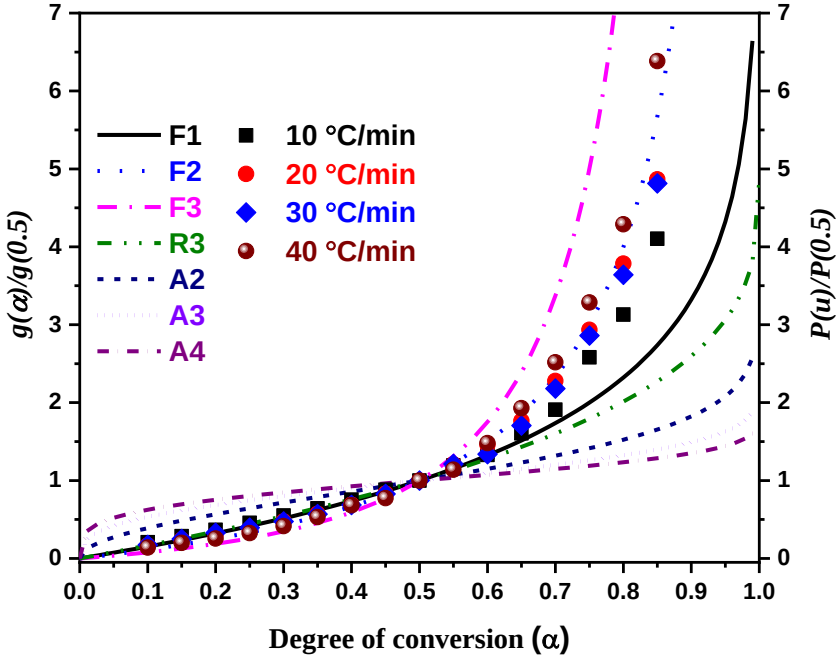

Fig. 4.8 A comparison of the experimental and theoretical master curves.

Fig. 4.8 shows a comparison of the experimental and theoretical master curves. It is observed that the F2 (second order reaction) mechanism dominated the formation of Cr_2AlC MAX phase. The F2 mechanism is the simplest based on the homogenous kinetics. The rate of reaction is directly related to the concentration, amount or fraction of remaining reactant(s) raised to a particular power (integral or fractional) which is the reaction order. In the F2 mechanism, random nucleation with two nuclei on the individual particle occurs [23,24].

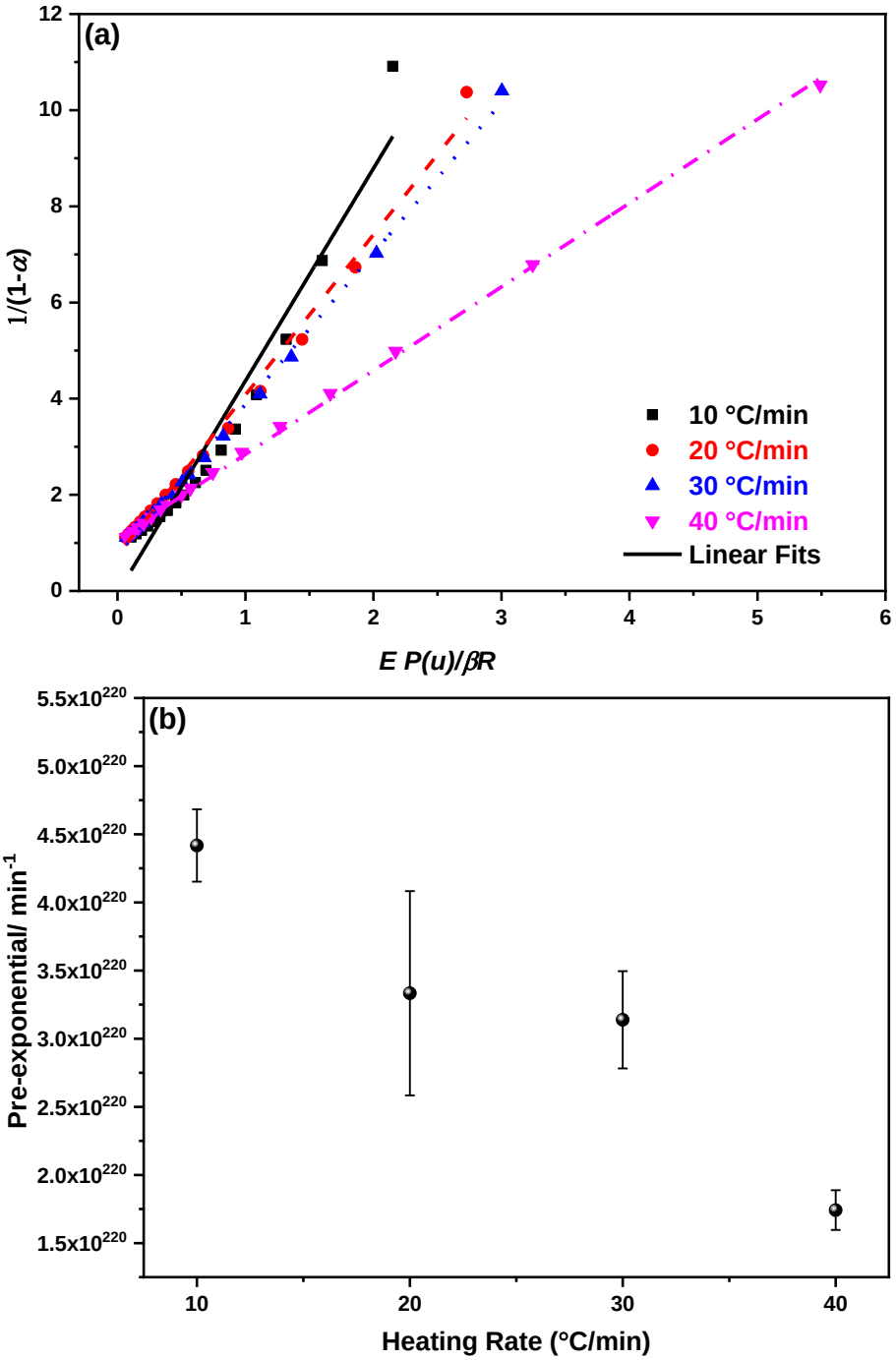

Fig. 4.9 (a) The linear fitted curve between $(1/1-\alpha)$ and $\frac{E}{\beta R}P(u)$. (b) The variation of pre-exponential w.r.t. heating rates along with the standard error.

Further, to calculate pre-exponential factor eq. (3.8) is modified by substituting value of $g(\alpha)$ corresponding to F2 mechanism i.e. $\left(g(\alpha) = \frac{1}{(1-\alpha)}\right)$. Consequently, eq. (3.8) can be written as:

$$g(\alpha) = \frac{1}{(1-\alpha)} = \frac{AE}{\beta R} P(u) \tag{4.9}$$

Further, the pre-exponential factor is determined by using the average activation energy in Eq. 4.1. The pre-exponential factor is calculated from the slope of the linear fitted curve between $(1/1-\alpha)$ and $\frac{E}{\beta R} P(u)$ (Fig. 4.9a). The variation of pre-exponential w.r.t. heating rates along with the standard error is shown in Fig. 4.9b. Finally, Table 4.5 represents the calculated kinetic triplets involved during the formation of Cr_2AlC MAX phase.

Table 4.5 Kinetic triplets involved during formation of Cr_2AlC MAX phase.

Kinetic triplets			
Average activation energy		Average pre-exponential factor	Reaction mechanism
KAS	FWO		
5527.25 ± 133.69	5316.19 ± 133.68	$3.16 \times 10^{220} \pm 0.37 \times 10^{220}$	F2

4.2.3. Microstructure Analysis

The formation of Cr_2AlC MAX phase after DTA is also confirmed through FE-SEM (Fig. 4.10) and TEM (Fig. 4.11) analysis. Fig. 4.10 shows the micrographs of the fractured CAC-4 sample after DTA analysis. A lamellar structure appears in Fig 4.10a, which corresponds to the MAX phase. A typical characteristic of the MAX phase, i.e., nano-laminated structure with the stacking of layers emerged in Fig. 4.10b. However, the complete stacking of layers is not observed due to the presence of impurities (Cr_2Al and Cr_7C_3). HR-TEM image of a CAC-4 sample after DTA is shown in Fig. 4.11a.

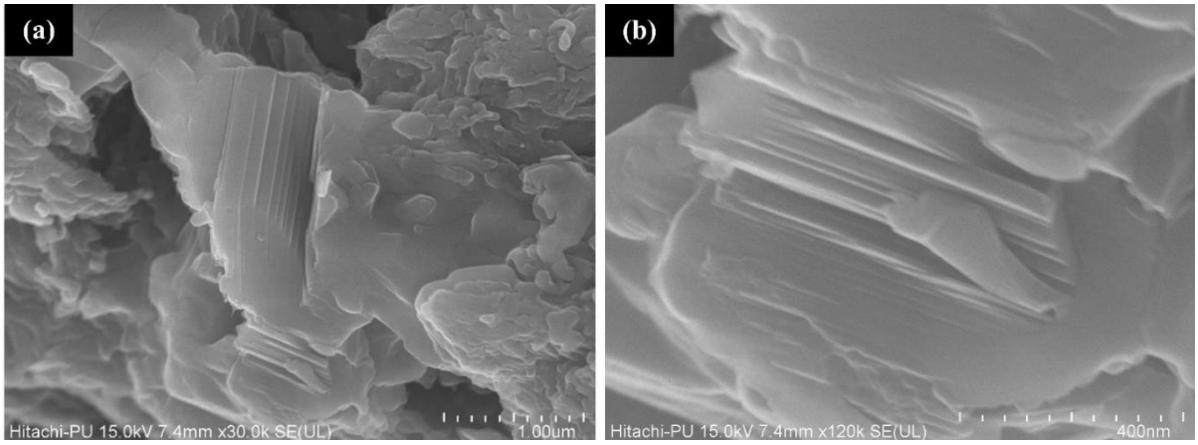

Fig. 4.10 FESEM micrographs of the fractured CAC 4 sample after DTA analysis.

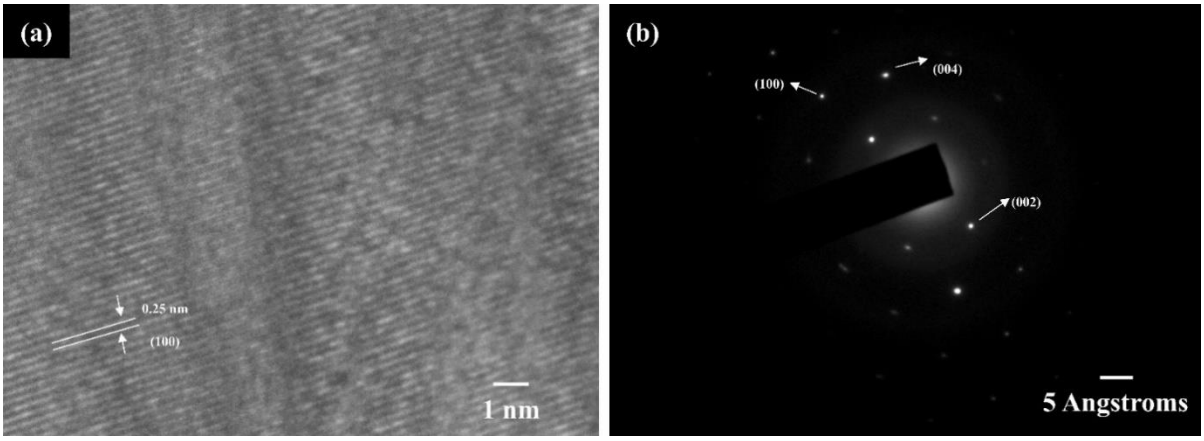

Fig. 4.11 (a) HR-TEM and (b) SAED images of a CAC 4 sample after DTA analysis.

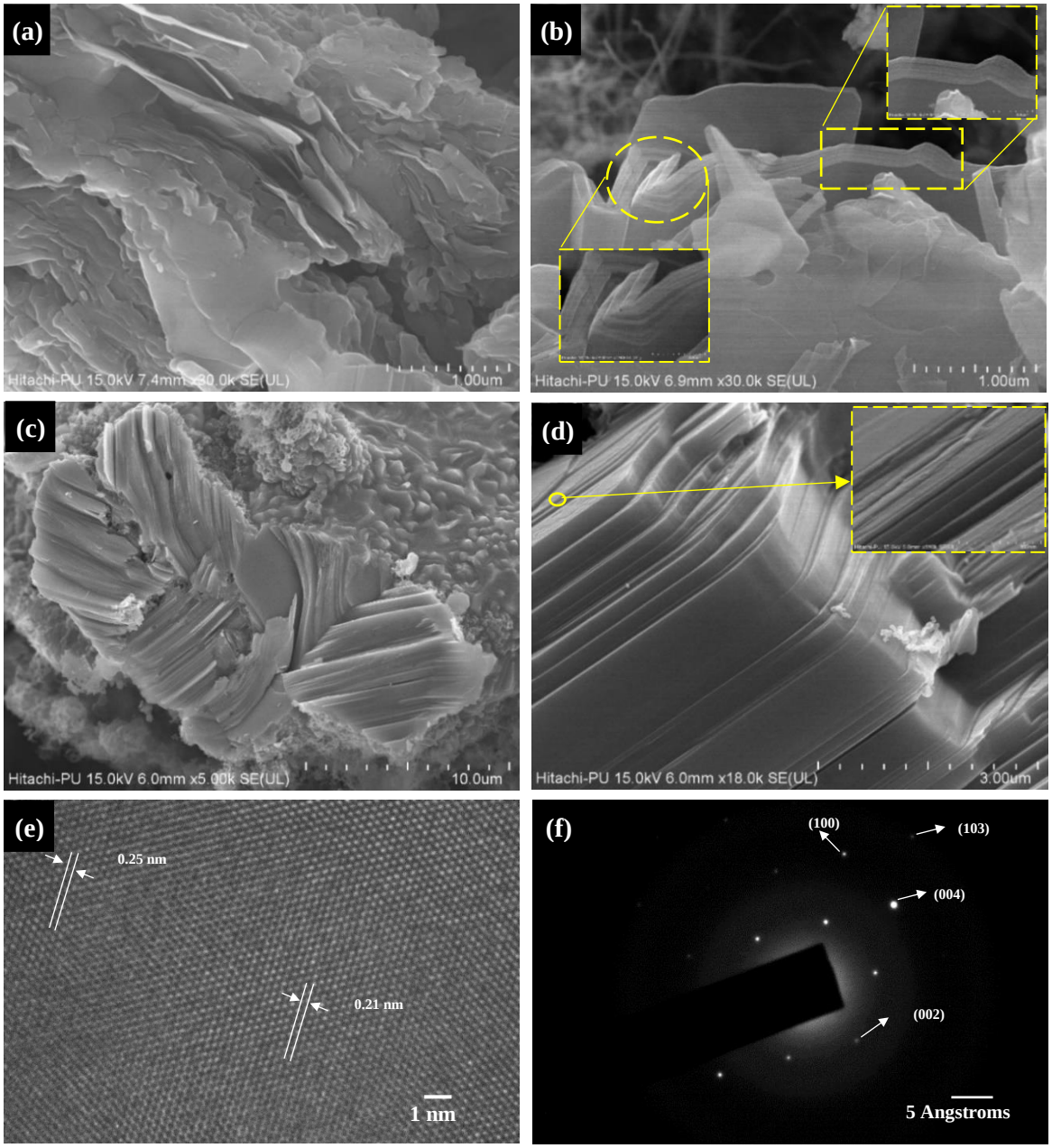

Fig. 4.12 The FE-SEM micrographs of fractured (a-b) 12CAC-4 and (c-d) 13CAC-4 samples. The HRTEM (e) and SAED (f) image of 13CAC-4 sample.

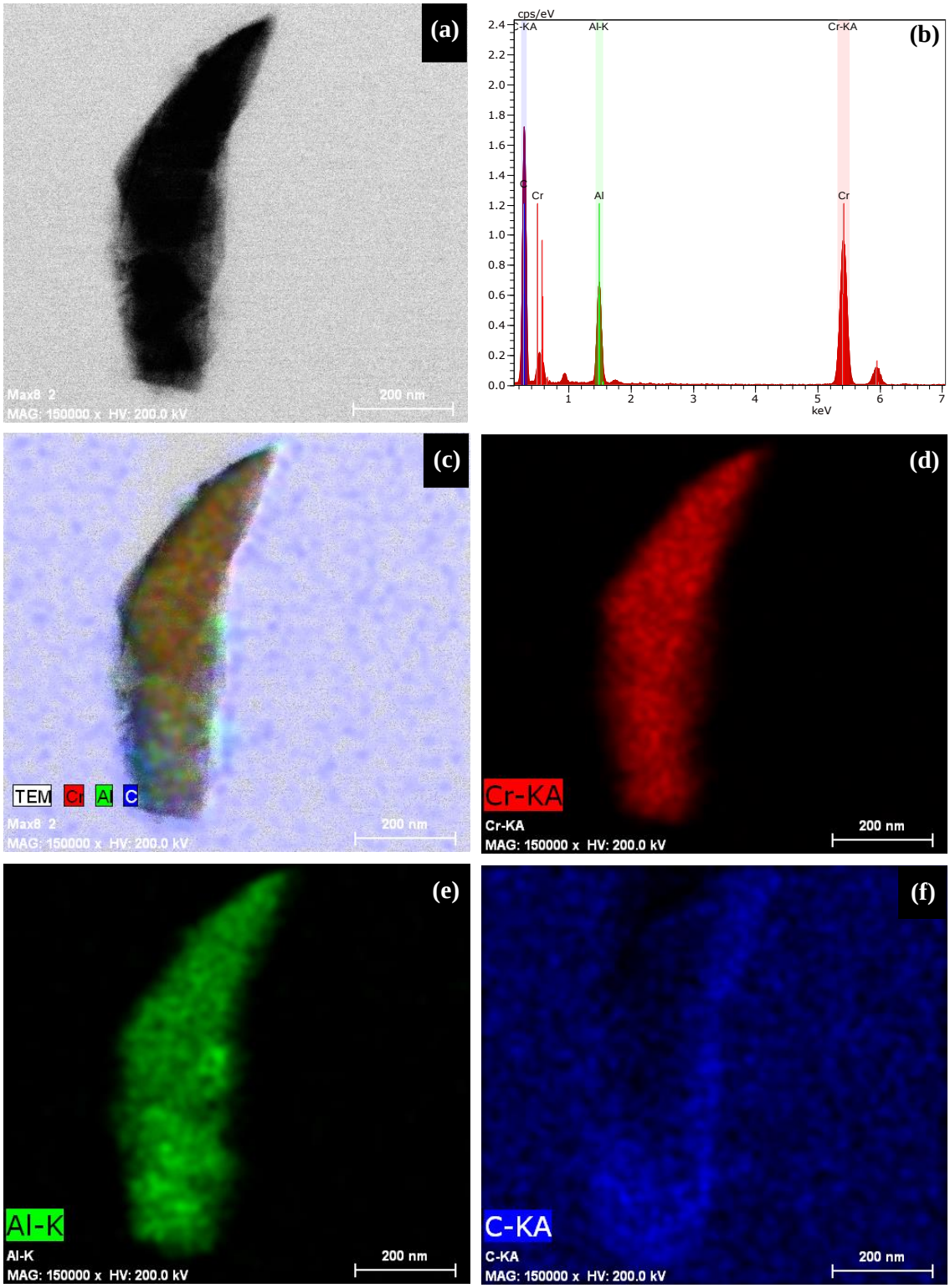

Fig. 4.13 (a) TEM image and (b) elemental composition 13CAC 4 sample. (c) The combined EDS mapping of Cr, Al and C in 13CAC 4 sample. The distribution of (d) Cr, (e) Al and (f) C in 13CAC 4 sample.

Fig. 4.11 demonstrated that the lattice fringes (0.25 nm) correspond to (100) plane of hexagonal Cr_2AlC. Furthermore, a SAED pattern (Fig. 4.11b) of CAC-4 sample after DTA analysis shows different planes. It can be seen that all the observed planes are related to the

hexagonal structure of Cr_2AlC MAX phase. Fig. 4.12 shows the FE-SEM micrographs of the fractured 12CAC 4 and 13CAC 4 samples sintered at 1200 ºC and 1300 ºC, respectively. A characteristic signature of the Cr_2AlC MAX phase formation is observed in both the samples.

It is visible in Fig. 4.12a that a lamellar sheet structure corresponding to the MAX phases is formed after sintering at 1200 ºC. However, the layers are delaminated, and the presence of the kink bands are observed in Fig. 4.12a. A belt type layered structure is also observed in a 12CAC-4 sample (Fig. 4.12b), which indicates the deformation capability of these structures. Also, the thickness of these stacked layers is non-uniform (inset of Fig. 4.12b). In a 12CAC 4 sample, the layered structure of the MAX phases is formed, but the complete stacking of layers is not achieved. This could be due to the presence of the Cr_2Al and the Cr_7C_3 phases, as observed from the XRD results. When the sintering temperature increased to 1300 ºC (13CAC 4), a highly stacked layered structure appears (Fig. 4.12c). The signatures of the kink bands, the delamination of the layers, and the particle pinning are also observed in the fractured sample. An interwoven knot of lamellar structure is also observed in 13CAC 4 sample, as is evident in Fig. 4.12c. Nano-laminated structure of the Cr_2AlC MAX phase appears in Fig. 4.12d. The inset of Fig. 4.12d also indicates that the stacked layers are non-uniform in thickness.

HR-TEM image of a 13CAC 4 sample is shown in Fig. 4.12e. This figure shows a typical signature, i.e., the nano-laminated structure of the MAX phases. The lattice fringes in the HR-TEM image corresponds to (100) and (103) planes of a hexagonal Cr_2AlC MAX phase. Also, a SAED pattern (Fig. 4.12f) shows various planes of a hexagonal Cr_2AlC MAX phase. The planes identified in a SAED pattern are analogous to the XRD results. Further, the distribution of chromium (Cr), aluminum (Al), and carbon (C) in a 13CAC 4 sample (sintered at 1300 ºC) are identified through the EDS mapping (Fig. 4.13). It is observed that all the elements are homogeneously distributed in a 13CAC 4 sample.

4.2.4. X-ray photoelectron spectroscopy (XPS) analysis

A typical Cr_{2p}, C_{1s}, Al_{2p} and O_{1s} XPS spectra of a 13CAC 4 sample is presented in Fig. 4.14. The Cr_{2p} spectra (Fig. 4.14a) shows two peaks associated with the spin orbitals of $2p_{3/2}$ and $2p_{1/2}$. The splitting of these spin orbitals depends on the oxidation states of the chromium. It is well reported that the spin-orbit splitting of 9.7 – 9.9 eV and 8.7 – 9.4 eV is ascribed to Cr^{3+} and Cr^{6+} compounds, respectively [25,26]. In a 13CAC 4 sample, the oxidation states of the chromium are Cr^{+3} and Cr^{+6}, as is evident from the difference in the binding energies (E_b). Also, the peak observed at E_b ~ 574.6 eV corresponds to Cr-C weak bond in the Cr_2AlC MAX phase [27].

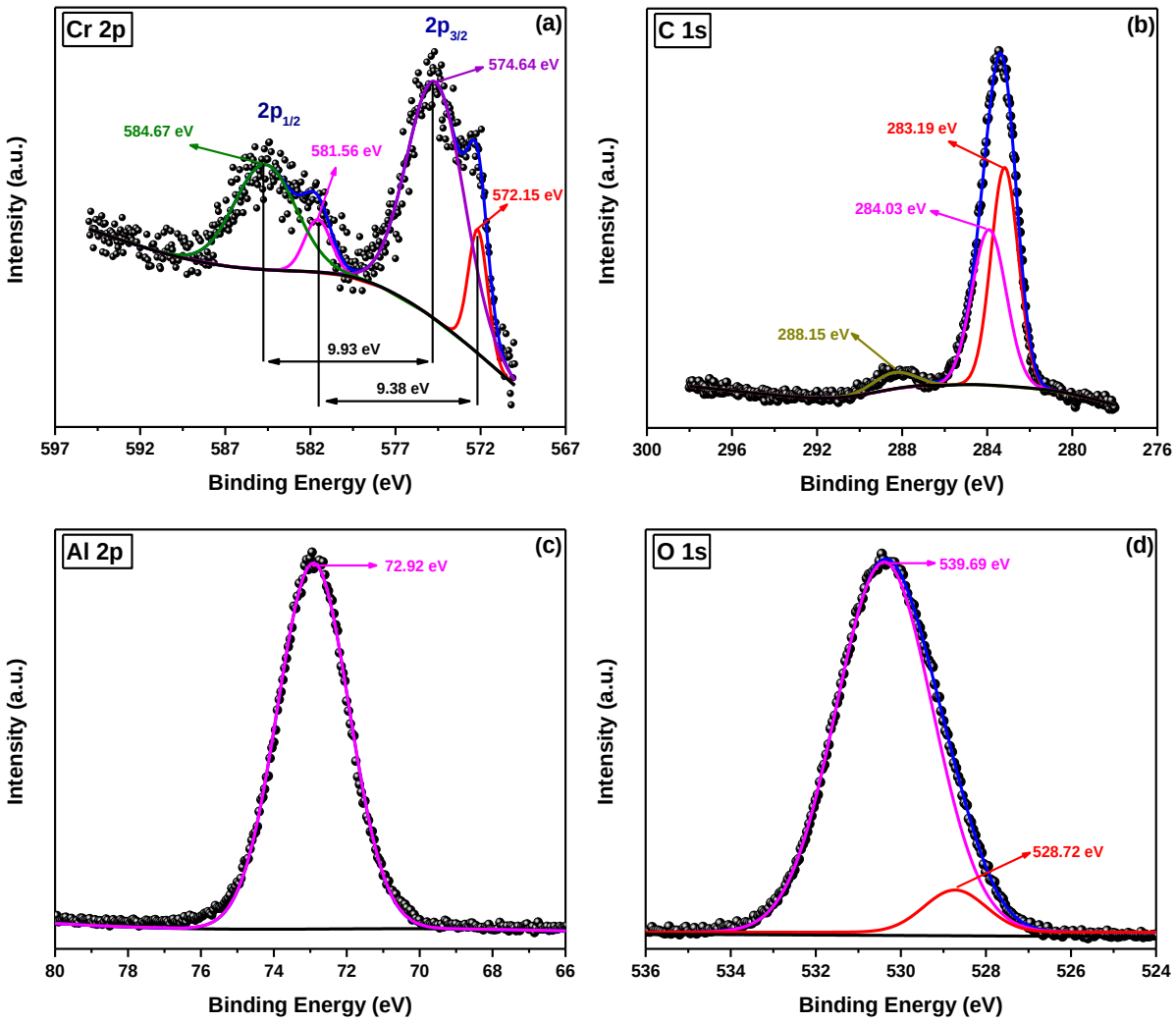

Fig. 4.14 The typical (a) Cr_{2p}, (b) C_{1s}, (c) Al_{2p} and (d) O_{1s} XPS spectra of 13CAC 4 sample.

The spectra of C_{1s} (Fig. 4.14b) shows the contribution of three different peaks at E_b ~ 283, 284, 288 eV in the sample. The former peak (~ 283 eV) is associated with the Cr-C bond, as reported for the Cr_2AlC MAX phase [27]. The second peak observed at ~ 284 eV corresponds to the residual adsorbed carbon while the third peak at ~ 288 eV ascribed to the C-O bonding [28]. In the Al_{2p} spectra, a single peak (E_b = 72.92 eV) emerges in a 13CAC 4 sample due to the Al-C bonding. Moreover, the O_{1s} spectra show two peaks at E_b ~ 530 and 528 eV. The former peak corresponds to the O-Cr_2AlC/CrC while the last peak ascribes to oxygen bonded with the various alloys (Cr_xAl_y). In the case of the Ti_2AlC MAX phase, Zhang et al. [29] also observed a similar peak at 528 eV and suggested that this peak corresponds to oxygen bonded with the alloys. The results obtained from the XPS confirmed the formation of the Cr_2AlC MAX phase.

4.2.5. Oxidation kinetics of Cr_2AlC MAX phase

Fig. 4.15a-b shows the TGA/DTA curves of a 13CAC-4 sample in the air environment at variable heating rates (10, 20, 30, 40 ºC/min). The TGA curves (Fig. 4.15a) demonstrated the higher thermal stability for a 13CAC-4 sample up to ~ 700 ºC. The mass gain ~ 17 % is observed when the sample is heated above 700 ºC. Also, the DTA curves (Fig. 4.15b) show two exothermic peaks (650, 950 ºC), which indicate that the oxidation of a 13CAC-4 sample occurred in two stages. Fig. 4.15c-d shows the variation of the conversion fraction with the temperature for both the oxidation stages of a 13CAC-4 sample. The exothermic peaks shifted towards the higher temperatures with an increase in the heating rates. The oxidation in stage I (~ 600 – 830 ºC) shows a mass gain of ~ 2 %, which may correspond to the oxidation of the surface aluminum and the impurity phase (Cr_7C_3) present in a 13CAC 4 sample.

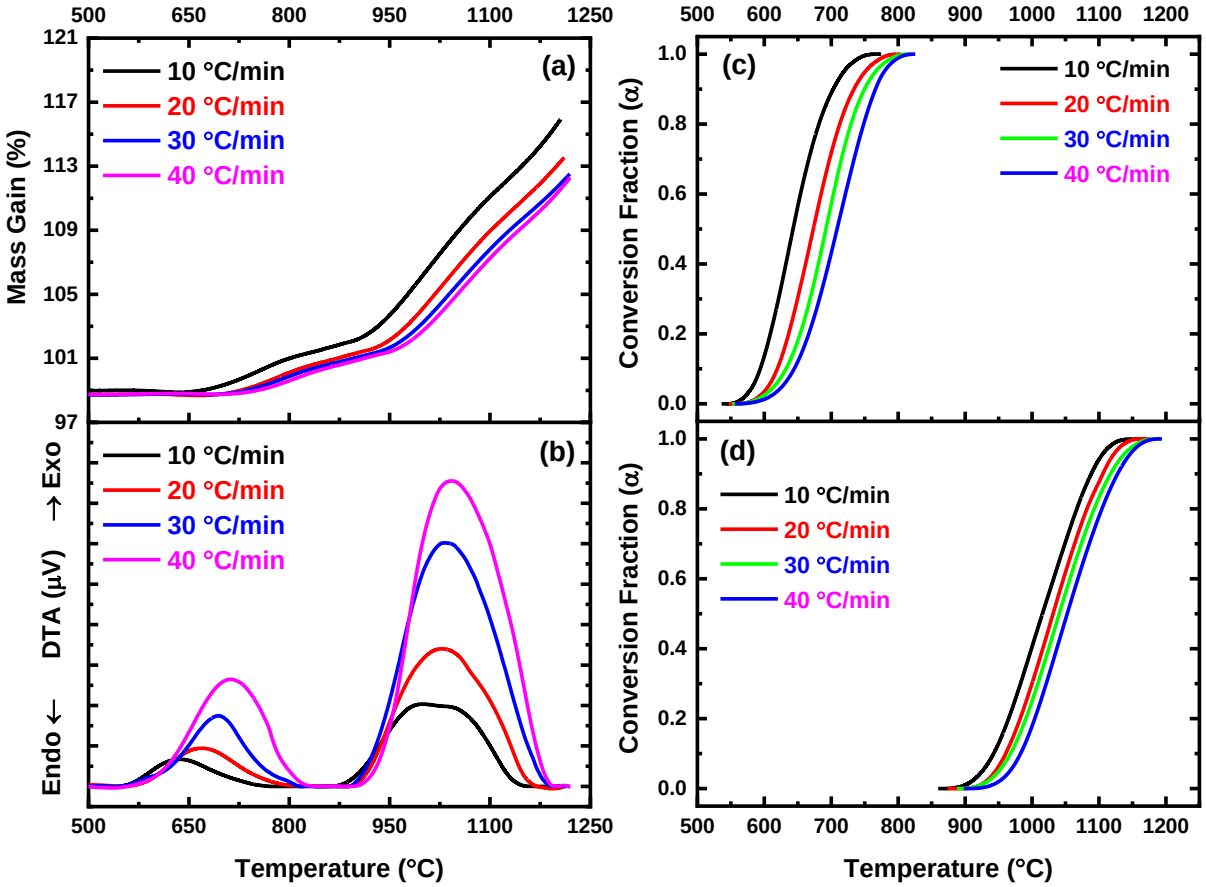

Fig. 4.15 (a) TGA and (b) DTA curves of 13CAC 4 sample in air environment at 10, 20, 30, 40 ºC/min heating rates. The variation of conversion values with temperature for (c) stage I and (d) stage II.

According to the Ellingham/Richardson diagrams, the formation of the Al_2O_3 compound (ΔG = - 921.5 kJ/mol at 650 ºC) is more favorable as compared to the Cr_2O_3 (ΔG = - 545.6 kJ/mol at 880 ºC) [30]. Li et al. [31] also proposed that the oxidation of the Cr_2AlC phase occur in two stages: an early stage relates to the formation of the Al_2O_3 compound, while

the latter stage relates to the formation of a dense alumina layer over the surface of the Cr_2AlC MAX phase. In stage II (~ 850 – 1190 ºC), the oxidation of the Cr_2AlC MAX phase occurred with a significant mass gain of ~ 15 %. The oxidation of the other MAX phases (Ti_2AlC, Ti_3AlC_2, and $Zr_3Al_3C_5$) begins at 400 ºC, while the Cr_2AlC MAX phase shows the higher oxidation resistance [32–34]. Lin et al. [3] reported that the oxidation of the Cr_2AlC MAX phase begins at ~ 800 ºC. They also proposed the possible reactions, which could occur during the oxidation of the Cr_2AlC MAX phase. The possible reactions are given below:

$$4Cr_2AlC + 13O_2 \rightarrow 4Cr_2O_3 + 2Al_2O_3 + 4CO_2 \quad (4.10)$$

$$28Cr_2AlC + 23O_2 \rightarrow 8Cr_7C_3 + 14Al_2O_3 + 4CO_2 \quad (4.11)$$

According to these reactions, the theoretical mass gain corresponding to Eq. 4.10 and Eq. 4.11 should be ~ 42 % and 16 %, respectively. The mass gain observed in stage II (~ 15%) corresponds to the theoretical mass gain of Eq. 2. However, the TGA curves (Fig. 4.15a) show no mass stability above ~ 1200 ºC. This mass instability indicates that the oxidation of a 13CAC-4 sample is incomplete. It may be possible that the oxidation of the Cr_2AlC MAX phase proceeds by following both the reactions, simultaneously. Also, there is no mass loss observed in Fig. 4.15a, which indicates that the layer of metal oxide (Al_2O_3) act as a shield for the decomposition/oxidation of the Cr_2AlC phase.

Multi-stage Kinetic Analysis is performed up to 1200 ºC, to obtain more information related to the oxidation behavior of the Cr_2AlC MAX phase. This analysis helps to derive the kinetic triplets viz. the activation energy, the pre-exponential factor, and the reaction mechanism. These kinetic parameters are essential to understand the thermal behavior of a material [35]. The value of the activation energy relates to the energy barrier and the pre-exponential factor associated with the frequency of the vibrations in the activated complex. The iso-conversional kinetic methods are extensively used to calculate the activation energy involved during thermal decomposition of a material [12,36–40]. These methods are based on the iso-conversional principle, which states that the rate of the reaction at each conversion fraction is the function of temperature. The activation energy calculated from these methods is independent of the reaction mechanism followed by the thermal decomposition process. There are several iso-conversional kinetic methods which have been reported based on different temperature integral approximations for the calculation of kinetic parameters [41–46].

According to the recommendation of the International Confederation for Thermal Analysis and Calorimetry (ICTAC) committee, the Kissinger-Akahira-Sunose (KAS) and the Flynn-Wall-Ozawa (FWO) are used for calculating kinetic parameter [41]. The linear fitted curves obtained from the KAS and FWO method for both oxidation stages of a 13CAC-4

sample are presented in Fig. 4.16 – 4.17. At each value of the conversion, the activation energy is calculated from KAS and FWO kinetic methods and given in Table 4.6 – 4.7.

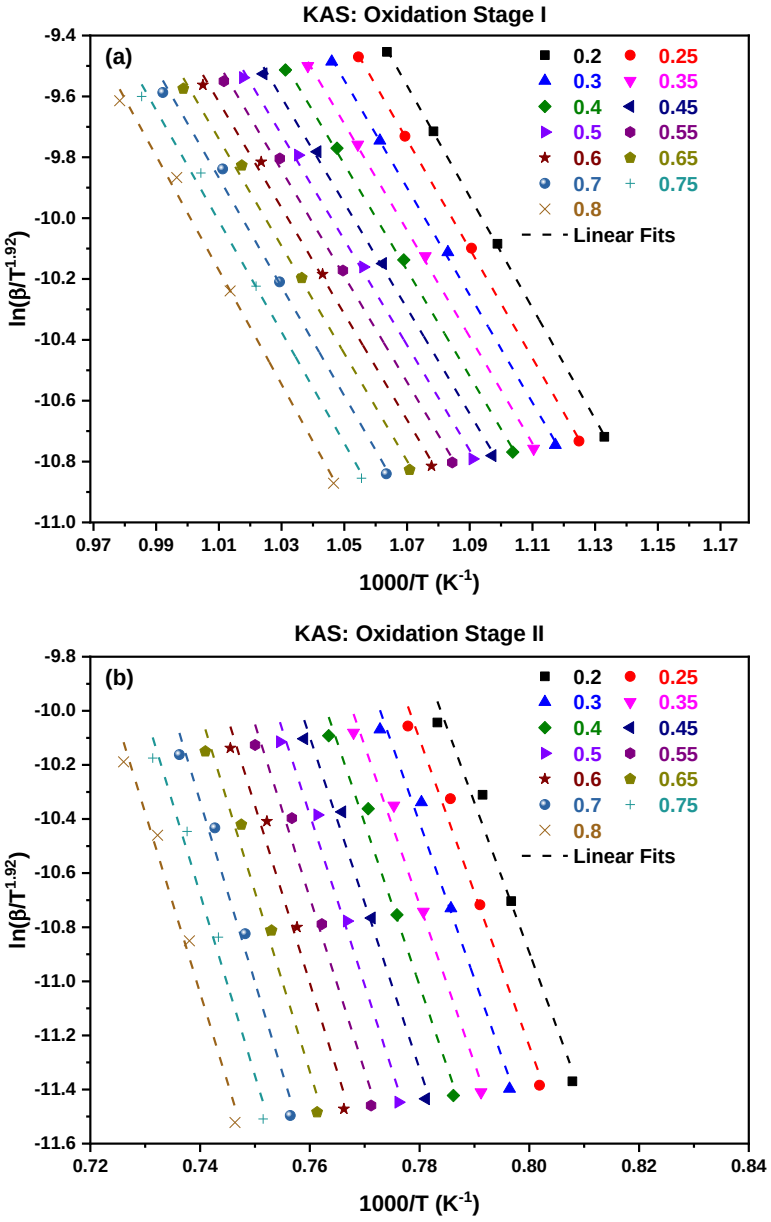

Fig 4.16 Linear fitted plots obtained from KAS iso-conversional kinetic methods for (a) oxidation stage I and (b) oxidation stage II.

The average value of the activation energy calculated from FWO method (154.62 kJ/mol) is slightly higher than the KAS method (146.38 kJ/mol) for the oxidation stage I. However, the trend of activation energy (Table 4.6 – 4.7) w.r.t. conversion fraction (α) is similar, as calculated from KAS and FWO methods. In oxidation stage II, the average value of activation energy calculated from the KAS method (513.44 kJ/mol) is also higher than that of the FWO method (511.80 kJ/mol). It is observed that the activation energy for the oxidation stage II is significantly higher than the oxidation stage I of a 13CAC-4 sample. The higher

activation energy observed in the oxidation stage II could be associated with the formation of the Al_2O_3 layer over the surface of the Cr_2AlC MAX phase. This layer also acts as an oxidation protective layer. Fig. 4.18 shows the variation in activation energy at each conversion value calculated for oxidation stage I (Fig. 4.18a) and stage II (Fig. 4.18b).

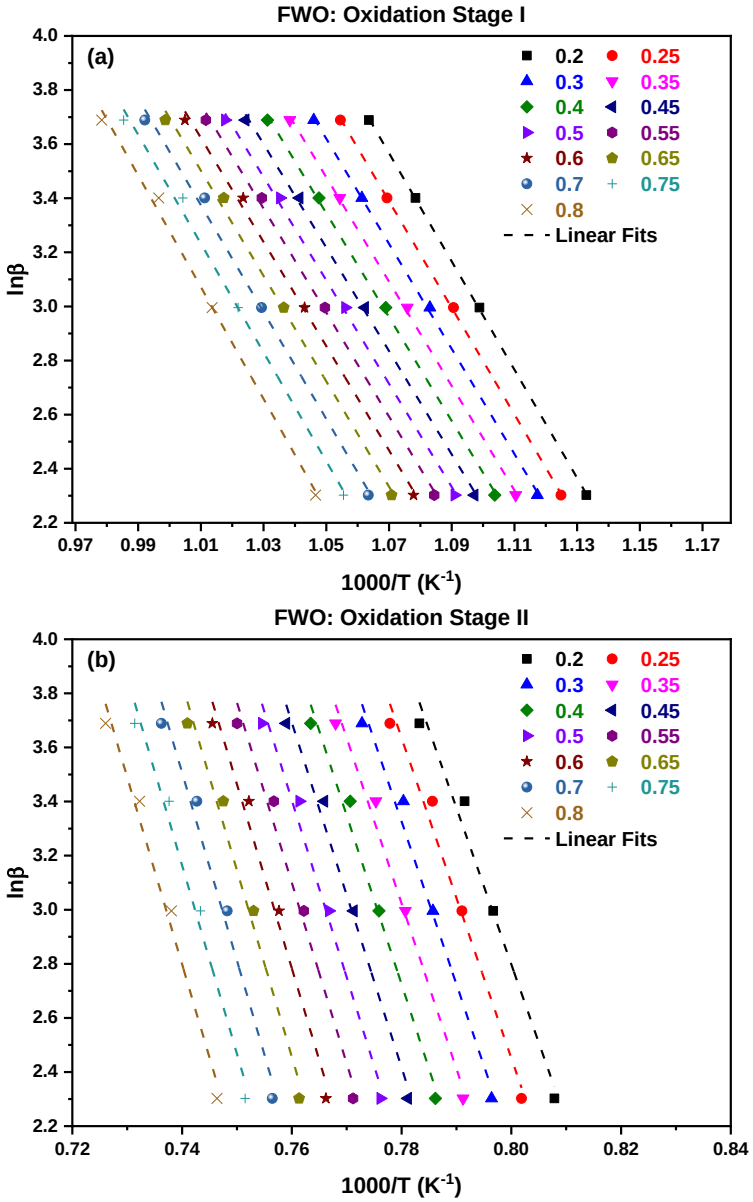

Fig 4.17 Linear fitted plots obtained from FWO iso-conversional kinetic methods for (a) oxidation stage I and (b) oxidation stage II.

The reaction mechanism involved in the oxidation of the Cr_2AlC MAX phase is identified by employing integral master plots method [20,41]. According to this method, the experimental curves at different heating rates are compared with various theoretical models. The theoretical curves are obtained from $g(\alpha)/g(0.5)$, while the experimental curves are generated from $P(u)/P(0.5)$. Fig. 4.19 shows the comparison of the theoretical master curves and the experimental curves for both the oxidation stages of the 13CAC-4 sample.

Table 4.6 The value of activation energy (E_a) evaluated for each degree of conversion through KAS and FWO methods for oxidation stage I.

Conversion Value	Oxidation Stage I					
	KAS method			FWO method		
	E_a (kJ/mol)	Error	R^2	E_a (kJ/mol)	Error	R^2
0.2	150.69	0.153	0.999	158.19	0.900	1.000
0.25	147.97	0.201	0.999	155.68	0.744	1.000
0.3	145.64	0.304	0.999	153.56	0.783	0.999
0.35	144.37	0.334	0.998	152.44	0.821	0.999
0.4	143.54	0.370	0.998	151.73	1.080	0.999
0.45	142.77	0.457	0.997	151.08	1.114	0.998
0.5	142.48	0.511	0.997	150.90	1.031	0.998
0.55	143.43	0.568	0.996	151.89	1.451	0.997
0.6	143.63	0.696	0.995	152.17	1.455	0.996
0.65	145.38	0.755	0.994	153.95	1.509	0.996
0.7	147.67	0.898	0.992	156.23	1.569	0.994
0.75	150.46	0.936	0.992	159.02	0.895	0.994
0.8	154.86	0.917	0.992	163.35	0.647	0.994

Table 4.7 The value of activation energy (E_a) evaluated for each degree of conversion through KAS and FWO methods for oxidation stage II.

Conversion Value	Oxidation Stage II					
	KAS method			FWO method		
	E_a (kJ/mol)	Error	R^2	E_a (kJ/mol)	Error	R^2
0.2	456.99	5.638	0.969	456.95	3.836	0.972
0.25	468.11	5.221	0.975	467.74	4.217	0.977
0.3	475.97	5.184	0.976	475.40	4.652	0.978
0.35	483.63	5.080	0.977	482.87	4.762	0.980
0.4	494.56	5.207	0.977	493.46	5.024	0.979
0.45	505.88	5.197	0.978	504.42	5.630	0.980
0.5	519.18	5.617	0.976	517.30	6.586	0.978
0.55	529.11	6.013	0.974	526.93	7.289	0.976
0.6	540.35	6.578	0.971	537.83	7.641	0.973
0.65	547.79	6.842	0.968	545.08	7.070	0.971
0.7	551.81	6.851	0.969	549.06	6.404	0.971
0.75	553.23	6.592	0.971	550.56	5.768	0.974
0.8	548.13	6.173	0.974	545.82	4.156	0.976

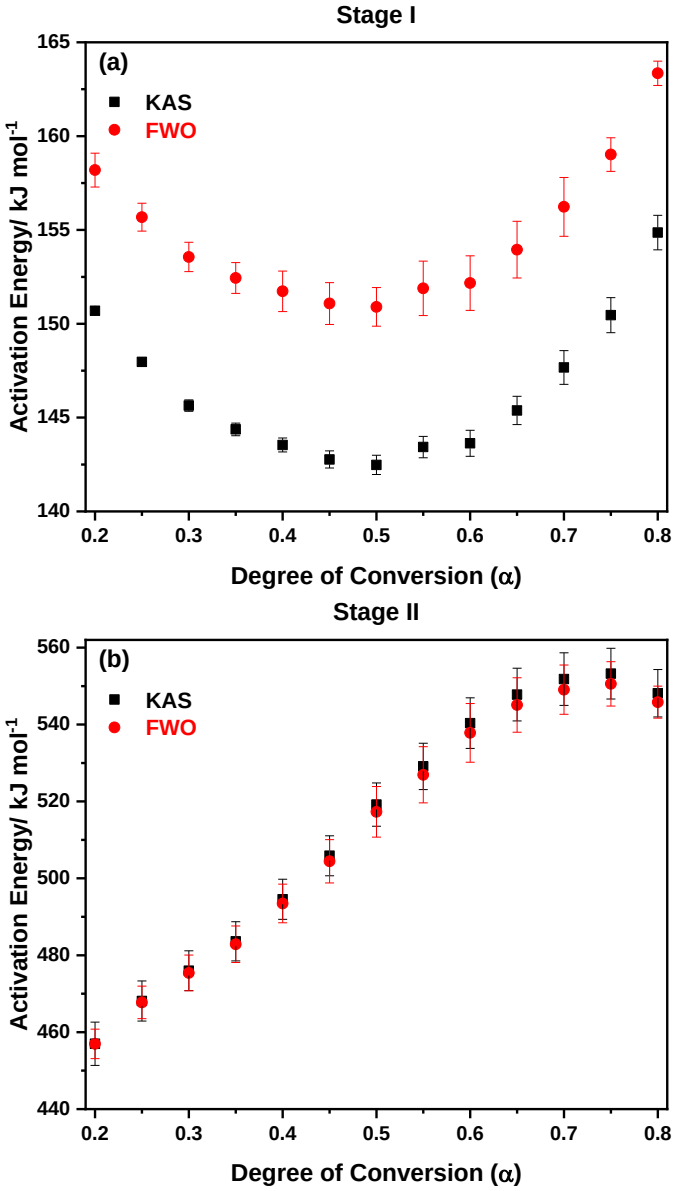

Fig. 4.18 The variation in activation energy at each conversion value calculated for oxidation (a) stage I and (b) stage II.

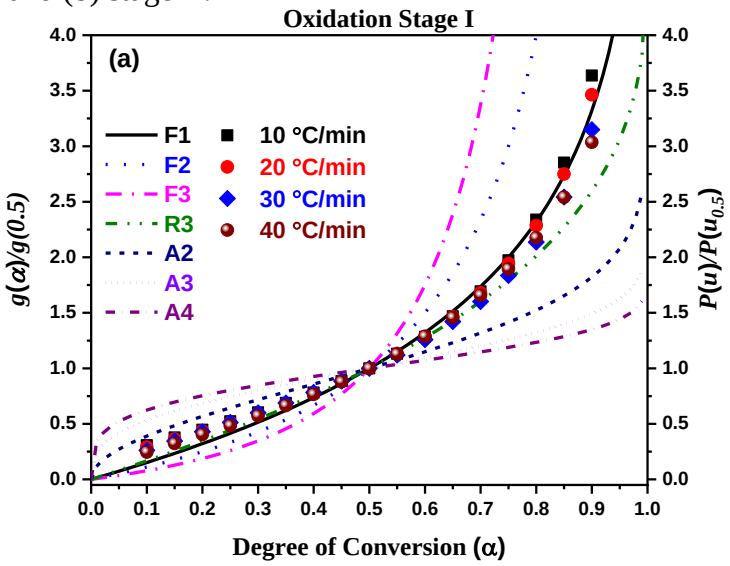

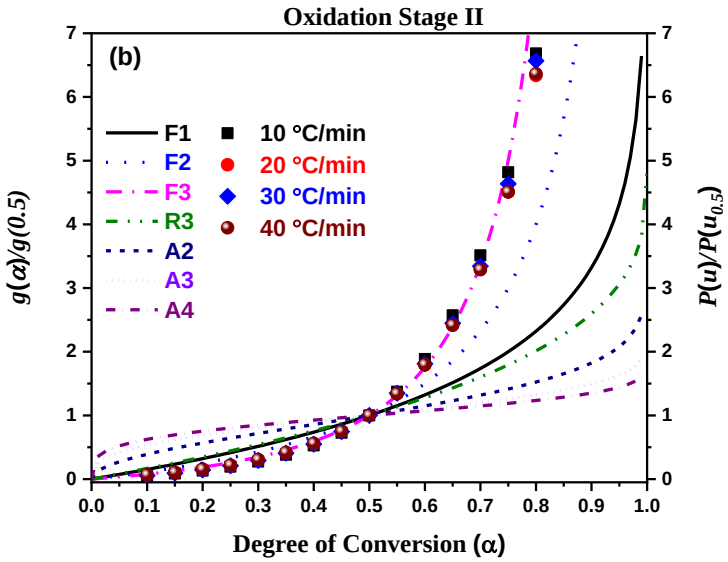

Fig. 4.19 The comparison of the theoretical master curves and the experimental curves for the (a) oxidation stage I and (b) oxidation stage II of the 13CAC-4 sample.

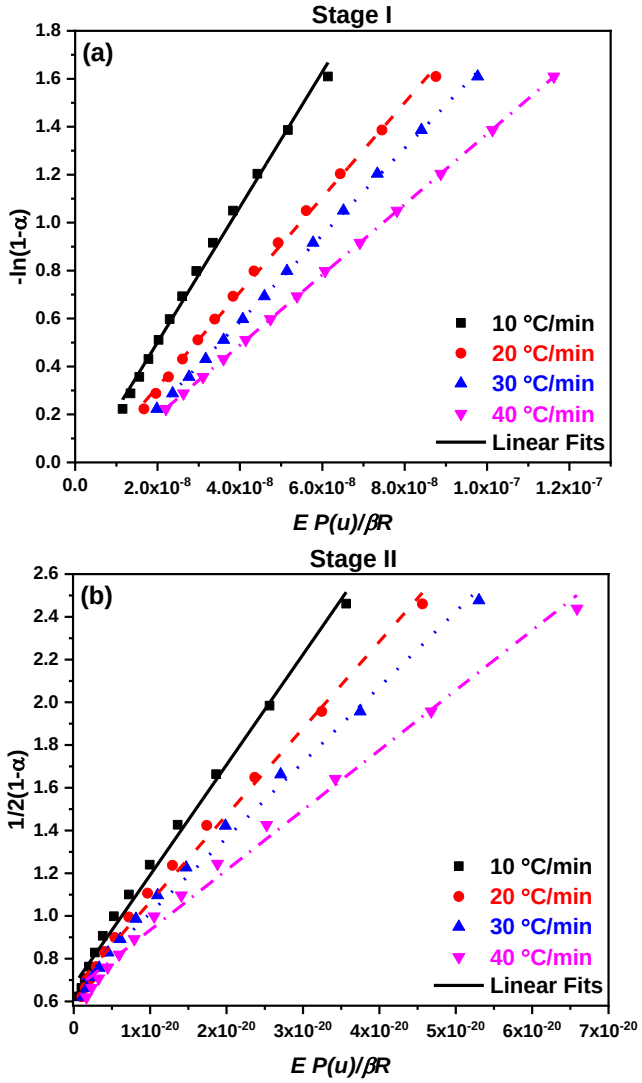

Fig. 4.20 (a) The linear fitted curve between $-\ln(1-\alpha)$ and $\frac{E}{\beta R}P(u)$. (b) The linear fitted curve between $(1/2(1-\alpha)$ and $\frac{E}{\beta R}P(u)$.

In the oxidation stage 1, the First Order Random Nucleation (F1) Mechanism dominates the oxidation of the 13CAC-4 sample. However, the Third Order Random nucleation (F3) mechanism is involved during oxidation in stage II of the 13CAC-4 sample. The change in the reaction mechanism could be ascribe to the formation of an alumina layer over the surface of the 13CAC-4 sample. Moreover, to determine the value of pre-exponential factor eq. (3.8) is modified by substituting value of $g(\alpha)$ corresponding to F1 and F3 mechanism for oxidation stage I and stage II, respectively. Consequently, eq. (3.8) can be modified for stage I (Eq. 4.12) and stage II (Eq. 4.13) as:

$$g(\alpha) = -\ln(1-\alpha) = \frac{AE}{\beta R}P(u) \tag{4.12}$$

$$g(\alpha) = \frac{1}{2(1-\alpha)} = \frac{AE}{\beta R}P(u) \tag{4.13}$$

Further, the pre-exponential factor is determined by using the average activation energy in Eq. 4.1. The linear fitted curve between $-\ln(1-\alpha)$ and $\frac{E}{\beta R}P(u)$ (Fig. 4.20a) gives the value of the pre-exponential factor for stage I. The pre-exponential factor for stage II is calculated from the slope of the linear fitted curve between $(1/2(1-\alpha)$ and $\frac{E}{\beta R}P(u)$ (Fig. 4.20b). The variation of pre-exponential w.r.t. heating rates along with the standard error is shown in Fig. 4.21. Finally, Table 4.8 represents the calculated kinetic triplets involved during the formation of Cr_2AlC MAX phase.

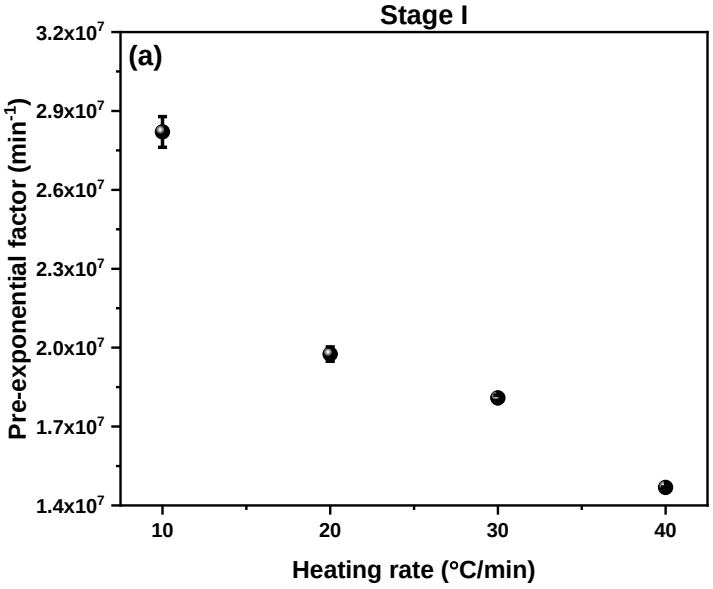

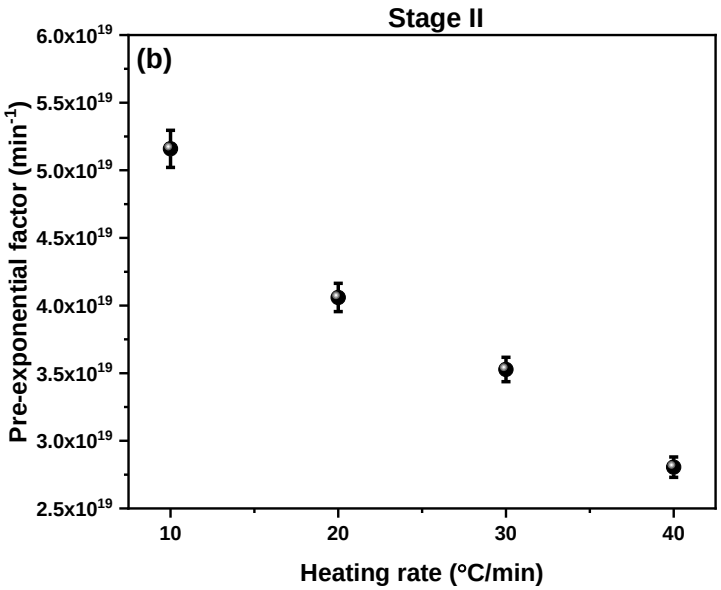

Fig. 4.21 The variation of pre-exponential w.r.t. heating rates along with the standard error for (a) oxidation stage I and (b) oxidation stage II.

Table 4.8 Kinetic triplets involved during oxidation of Cr_2AlC MAX phase.

	Kinetic triplets			
	Average activation energy (kJ/mol)		Average pre-exponential factor (min^{-1})	Reaction mechanism
	KAS	FWO		
Stage I	146.37 ± 0.54	154.62 ± 1.07	$2.02\times10^{7} \pm 2.47\times10^{5}$	F1
Stage II	513.44 ± 5.86	511.80 ± 5.61	$3.89\times10^{19} \pm 1.02\times10^{18}$	F3

References

[1] M.W. Barsoum, The Mn+1AXn phases: a new class of solids: thermodynamically stable nanolaminates, Prog. Solid State Chem. 28 (2000) 201–281. https://doi.org/10.1016/S0079-6786(00)00006-6.

[2] M.W. Barsoum, MAX phases: properties of machinable carbides and nitrides, 2013th ed., Wiley-VCH, Singapore, n.d.

[3] Z.J. Lin, M.S. Li, J.Y. Wang, Y.C. Zhou, High-temperature oxidation and hot corrosion of Cr_2AlC, Acta Mater. 55 (2007) 6182–6191. https://doi.org/10.1016/j.actamat.2007.07.024.

[4] W. Tian, P. Wang, G. Zhang, Y. Kan, Y. Li, D. Yan, Synthesis and thermal and electrical properties of bulk Cr_2AlC, Scr. Mater. 54 (2006) 841–846. https://doi.org/10.1016/j.scriptamat.2005.11.009.

[5] J. Zhu, E. Ha, G. Zhao, Y. Zhou, D. Huang, G. Yue, L. Hu, N. Sun, Y. Wang, L.Y.S. Lee, C. Xu, K.Y. Wong, D. Astruc, P. Zhao, Recent advance in MXenes: A promising 2D material for catalysis, sensor and chemical adsorption, Coord. Chem. Rev. 352 (2017) 306–327. https://doi.org/10.1016/j.ccr.2017.09.012.

[6] C.L. Yeh, Y.G. Shen, Effects of Al content on formation of Ta_2AlC by self-propagating high-temperature synthesis, J. Alloys Compd. 482 (2009) 219–223. https://doi.org/10.1016/j.jallcom.2009.03.184.

[7] R. Yembadi, B.B. Panigrahi, Thermodynamic Assessments and mechanically activated synthesis of ultrafine Cr_2AlC MAX phase powders, Adv. Powder Technol. 28 (2017) 732–739. https://doi.org/10.1016/j.apt.2016.11.020.

[8] M. Imtyazuddin, A.H. Mir, E. Aradi, V. Vishnyakov, Effect of aluminium concentration on phase formation and radiation stability of Cr_2AlC thin film, Nanotechnology. 31 (2020). https://doi.org/10.1088/1361-6528/ab991c.

[9] Z. Su, S. Zeng, J. Zhou, Z. Sun, Synthesis and characterization of Cr_2AlC with nanolaminated particles, Chinese Sci. Bull. 59 (2014) 3266–3270. https://doi.org/10.1007/s11434-014-0315-5.

[10] D. Aksu Demirezen, Y.Ş. Yıldız, D. Demirezen Yılmaz, Amoxicillin degradation using green synthesized iron oxide nanoparticles: Kinetics and mechanism analysis, Environ. Nanotechnology, Monit. Manag. 11 (2019) 100219. https://doi.org/10.1016/j.enmm.2019.100219.

[11] X. jie Wang, Z. Huang, M. yu Wei, T. Lu, D. dan Nong, J. xu Zhao, X. yang Gao, L. jun Teng, Catalytic effect of nanosized ZnO and TiO_2 on thermal degradation of poly(lactic acid) and isoconversional kinetic analysis, Thermochim. Acta. 672 (2019) 14–24. https://doi.org/10.1016/j.tca.2018.12.008.

[12] P. Sharma, P. Uniyal, Investigating thermal and kinetic parameters of lithium titanate formation by solid-state method, J. Therm. Anal. Calorim. 51 (2017) 1081–1094. https://doi.org/10.1007/s10973-016-5977-6.

[13] P. Sharma, P.K. Diwan, O.P. Pandey, Impact of environment on the kinetics involved in the solid-state synthesis of bismuth ferrite, Mater. Chem. Phys. 233 (2019) 171–179. https://doi.org/10.1016/j.matchemphys.2019.05.055.

[14] M. Hu, Z. Chen, S. Wang, D. Guo, C. Ma, Y. Zhou, J. Chen, M. Laghari, S. Fazal, B. Xiao, B. Zhang, S. Ma, Thermogravimetric kinetics of lignocellulosic biomass slow pyrolysis using distributed activation energy model, Fraser-Suzuki deconvolution, and iso-conversional method, Energy Convers. Manag. 118 (2016) 1–11. https://doi.org/10.1016/j.enconman.2016.03.058.

[15] E.N. Lysenko, A.P. Surzhikov, E. V. Nikolaev, V.A. Vlasov, Thermal analysis study of $LiFeO_2$ formation from Li_2CO_3–Fe_2O_3 mechanically activated reagents, J. Therm. Anal. Calorim. 134 (2018) 81–87. https://doi.org/10.1007/s10973-018-7113-2.

[16] E.N. Lysenko, E. V. Nikolaev, A.P. Surzhikov, S.A. Nikolaeva, I. V. Plotnikova, The influence of reagents ball milling on the lithium ferrite formation, J. Therm. Anal. Calorim. 138 (2019) 2005–2013. https://doi.org/10.1007/s10973-019-08334-1.

[17] T. Akahira, T. Sunose, Method of determining activation deterioration constant of electrical insulating materials, Res. Rep. Chiba. Inst. Technol. (Sci Technol). 16 (1971) 22–31.

[18] M.J. Starink, The determination of activation energy from linear heating rate experiments: A comparison of the accuracy of isoconversion methods, Thermochim. Acta. 404 (2003) 163–176. https://doi.org/10.1016/S0040-6031(03)00144-8.

[19] H.L. Friedman, Kinetics of thermal degradation of char-forming plastics from thermogravimetry. Application to a phenolic plastic, J. Polym. Sci. Part C Polym. Symp. 6 (2007) 183–195. https://doi.org/10.1002/polc.5070060121.

[20] J. Chen, Y. Wang, X. Lang, X. Ren, S. Fan, Evaluation of agricultural residues pyrolysis under non-isothermal conditions: Thermal behaviors, kinetics, and thermodynamics, Bioresour. Technol. 241 (2017) 340–348. https://doi.org/10.1016/j.biortech.2017.05.036.

[21] C. Quan, A. Li, N. Gao, Thermogravimetric analysis and kinetic study on large particles of printed circuit board wastes, Waste Manag. 29 (2009) 2353–2360. https://doi.org/10.1016/j.wasman.2009.03.020.

[22] C. Ratcliffe, B. Ratcliffe, Propagation of Uncertainty An Uncertainty Budget Example, 1st ed., Springer International Publishing, Switzerland, 2015. https://doi.org/10.1007/978-3-319-12063-8_5.

[23] I. Dueramae, C. Jubsilp, T. Takeichi, S. Rimdusit, Thermal degradation mechanism of highly filled nano-SiO_2 and polybenzoxazine, J. Therm. Anal. Calorim. 116 (2014) 435–446. https://doi.org/10.1007/s10973-013-3542-0.

[24] F. Zhu, Y. Xu, Q. Feng, Q. Yang, Thermal kinetics study and flammability evaluation of polyimide fiber material, J. Therm. Anal. Calorim. 131 (2018) 2579–2587. https://doi.org/10.1007/s10973-017-6752-z.

[25] S. Wang, H. Lin, P.K. Nayak, S. Chang, J. Huang, Carbothermal reduction process for synthesis of nanosized chromium carbide via metal-organic vapor deposition, Thin Solid Films. 518 (2010) 7360–7365. https://doi.org/10.1016/j.tsf.2010.05.001.

[26] M. Mullet, F. Demoisson, B. Humbert, L.J. Michot, D. Vantelon, Aqueous Cr(VI) reduction by pyrite: Speciation and characterisation of the solid phases by X-ray photoelectron, Raman and X-ray absorption spectroscopies, Geochim. Cosmochim. Acta. 71 (2007) 3257–3271. https://doi.org/10.1016/j.gca.2006.09.008.

[27] E.I. Zamulaeva, E.A. Levashov, E.A. Skryleva, T.A. Sviridova, P. V. Kiryukhantsev-Korneev, Conditions for formation of MAX phase Cr_2AlC in electrospark coatings deposited onto titanium alloy, Surf. Coatings Technol. 298 (2016) 15–23. https://doi.org/10.1016/j.surfcoat.2016.04.058.

[28] A.M. Abdelkader, Molten salts electrochemical synthesis of Cr_2AlC, J. Eur. Ceram. Soc. 36 (2016) 33–42. https://doi.org/10.1016/j.jeurceramsoc.2015.09.003.

[29] Z. Zhang, S. Hon, J. Chai, D. Mei, Y. Lai, A. Kok, H. Cheong, K. Leong, S. Jie, H. Jin, J. Sheng, Surface & Coatings Technology Plasma spray of Ti_2AlC MAX phase powders : Effects of process parameters on coatings ' properties, Surf. Coat. Technol. 325 (2017) 429–436. https://doi.org/10.1016/j.surfcoat.2017.07.006.

[30] O. Berger, R. Boucher, M. Ruhnow, Part I. Mechanism of oxidation of Cr_2AlC films in temperature range 700–1200°C, Surf. Eng. 31 (2015) 373–385. https://doi.org/10.1179/1743294414Y.0000000417.

[31] S. Li, L. Xiao, G. Song, X. Wu, W.G. Sloof, S. Van Der Zwaag, Oxidation and crack healing behavior of a fine-grained Cr2 AlC ceramic, J. Am. Ceram. Soc. 96 (2013) 892–

899. https://doi.org/10.1111/jace.12170.
[32] M. Sundberg, G. Malmqvist, A. Magnusson, T. El-Raghy, Alumina forming high temperature silicides and carbides, Ceram. Int. 30 (2004) 1899–1904. https://doi.org/10.1016/j.ceramint.2003.12.046.
[33] X.H. Wang, Y.C. Zhou, Oxidation behavior of Ti_3AlC_2 at 1000-1400 ??C in air, Corros. Sci. 45 (2003) 891–907. https://doi.org/10.1016/S0010-938X(02)00177-4.
[34] L.F. Hea, Y.C. Zhoua, Y.W. Baoa, J.Y. Wanga, M.S. Li, Synthesis and oxidation of Zr3Al3C5 powders, Int. J. Mater. Res. 98 (2007) 3–9.
[35] P. Sharma, P.K. Jha, P.K. Diwan, O.P. Pandey, Impact of CuS on the crystallization kinetics of Na_2S-P_2S_5 glasses, J. Non. Cryst. Solids. 477 (2017) 31–41. https://doi.org/10.1016/j.jnoncrysol.2017.09.046.
[36] R.A. Mir, P. Sharma, O.P. Pandey, Thermal and structural studies of carbon coated Mo_2C synthesized via in-situ single step reduction-carburization, Sci. Rep. 7 (2017) 3518. https://doi.org/10.1038/s41598-017-03197-8.
[37] A. Perejón, P.E. Sánchez-Jiménez, J.M. Criado, L.A. Pérez-Maqueda, Thermal stability of multiferroic $BiFeO_3$: Kinetic nature of the β-γ transition and peritectic decomposition, J. Phys. Chem. C. 118 (2014) 26387–26395. https://doi.org/10.1021/jp507831j.
[38] A. Perejón, P.E. Sánchez-Jiménez, J.M. Criado, L.A. Pérez-Maqueda, A Promising approach to the kinetics of crystallization processes: The sample controlled thermal analysis, J. Am. Ceram. Soc. 100 (2017) 1125–1133. https://doi.org/10.1111/jace.14604.
[39] M.A. Islam, M. Asif, B.H. Hameed, Pyrolysis kinetics of raw and hydrothermally carbonized Karanj (Pongamia pinnata) fruit hulls via thermogravimetric analysis, Bioresour. Technol. 179 (2015) 227–233. https://doi.org/10.1016/j.biortech.2014.11.115.
[40] P. Sharma, P.K. Diwan, Study of thermal decomposition process and the reaction mechanism of the eucalyptus wood, Wood Sci. Technol. 128 (2017) 875–882. https://doi.org/10.1007/s00226-017-0924-7.
[41] S. Vyazovkin, A.K. Burnham, J.M. Criado, L.A. Pérez-Maqueda, C. Popescu, N. Sbirrazzuoli, ICTAC Kinetics Committee recommendations for performing kinetic computations on thermal analysis data, Thermochim. Acta. 520 (2011) 1–19. https://doi.org/10.1016/j.tca.2011.03.034.
[42] H.L. Friedman, Kinetics of thermal degradation of char-forming plastics from thermogravimetry. Application to a phenolic plastic, J. Polym. Sci. Part C Polym. Symp. 6 (1964) 183–195. https://doi.org/10.1002/polc.5070060121.
[43] T. Ozawa, A New Method of Analyzing Thermogravimetric Data, Bull. Chem. Soc. Jpn. 38 (1965) 1881–1886. https://doi.org/10.1246/bcsj.38.1881.
[44] A.W. Coats, J.P. Redfern, Kinetic Parameters from Thermogravimetric Data, Nature. 201 (1964) 464–466. https://doi.org/10.1038/201464a0.
[45] H.E. Kissinger, Reaction Kinetics in Differential Thermal Analysis, Anal. Chem. 29 (1957) 1702–1706. https://doi.org/10.1021/ac60131a045.
[46] J.H. Flynn, L.A. Wall, A quick, direct method for the determination of activation energy from thermogravimetry data, J. Polym. Sci. Part C Polym. Lett. 4 (1966) 323–328.

CHAPTER 5

SYNTHESIS & OXIDATION KINETICS OF Ti_3AlC_2 MAX PHASE

Overview

Ti_3AlC_2 MAX phase was prepared by using pressureless sintering route. The role of aluminium content during the synthesis of Ti_3AlC_2 was examined. The impact of temperature was also studied to obtain Ti_3AlC_2 MAX phase. A highly pure Ti_3AlC_2 MAX phase was obtained at 1500 ºC when stoichiometric ratio was Ti:TiC:Al = 1:1:1.3. The formation reaction pathway involved during synthesis of Ti_3AlC_2 MAX phase was identified through XRD analysis. The synthesis kinetics was also studied and kinetic parameters were determined. The non-isothermal oxidation stability of Ti_3AlC_2 MAX phase was also examined through TGA/DTA technique. The reaction pathway during oxidation was identified. The oxidation of Ti_3AlC_2 MAX phase occurred in three stages. The kinetic parameters responsible for the oxidation of Ti_3AlC_2 MAX phase were determined.

5.1. Introduction

Ti_3AlC_2 MAX phase emerged as potential candidate for variety of technological applications such as heating element, coating material, pantographs and many more [1,2]. This phase is also used as a precursor for the development of two dimensional Ti_3C_2 MXene [3]. The outstanding merits of Ti_3AlC_2 MAX phase includes high temperature stability, corrosion resistance, oxidation resistance, superior electrical properties, machinability and high damage tolerance [4]. This blend of interesting properties made Ti_3AlC_2 phase suitable for high temperature applications. The isothermal oxidation stability of Ti_3AlC_2 MAX phase is studied extensively [5,6]. In the process of oxidation, a protective layer of oxides (TiO_2 and Al_2O_3) form on the surface of Ti_3AlC_2 phase. This protective layer enhances the oxidation resistance. It is critically important to know the kinetics involved during oxidation. This will help for better material designing for a particular purpose. However, non-isothermal oxidation stability of Ti_3AlC_2 MAX phase is scarce in literature.

In the present work, the formation of Ti_3AlC_2 MAX phase was investigated by changing the aluminium content. The role of sintering temperature was examined. The reaction pathway involved during formation of Ti_3AlC_2 MAX phase was identified. The formation kinetics was also studied. The formation of Ti_3AlC_2 MAX phase was confirmed with the help of XRD, FESEM, TEM and XPS analysis. The main motto of the work was to determine the suitable experimental conditions to obtain Ti_3AlC_2 phase. Moreover, oxidation stability of the Ti_3AlC_2 was examined with the help of the Thermogravimetry Analysis (TGA) and the Differential Thermal Analysis (DTA) techniques. The oxidation reaction pathway and kinetics involved during oxidation of Ti_3AlC_2 phase was studied. The kinetic parameters such as activation energy, pre-exponential factor and reaction mechanism were calculated.

5.2. Synthesis of Ti_3AlC_2 MAX phase

According to the experimental details mentioned in the chapter 3, synthesis parameters to achieve Ti_3AlC_2 MAX phase is studied. Firstly, the synthesis temperature of Ti_3AlC_2 MAX phase was determined. In this process, the TAC 4 sample (Ti:TiC:Al = 1:1:1.4) was sintered at 800, 1000, 1200, 1400 and 1500 ℃ in an argon atmosphere for 1 hr. followed by optimization of Al content. The nomenclature of the samples prepared at different experimental conditions are presented in Table 5.1.

5.2.1. XRD analysis

Fig. 5.1 shows the XRD patterns of 8TAC 4, 10TAC 4, 12 TAC 4, 14 TAC 4 and 15 TAC 4 samples. Firstly, the aluminium melts at ~ 660 ℃ (Eq. 5.1) and reacts with titanium to form Al_3Ti (Eq. 5.2) phase. The peaks corresponding to Al_3Ti are prominent in 8TAC 4 sample

sintered at 800 °C. The volume fraction of different compounds is calculated with the help of XRD patterns observed in Fig. 5.1 and presented in Table 5.1.

$$Al_{(s)} \rightarrow Al_{(l)} \quad (5.1)$$

$$Ti + 3Al \rightarrow Al_3Ti \quad (5.2)$$

Table 5.1 Nomenclature of all the samples prepared at different experimental conditions.

Samples ID	Molar ratio			Sintering temperature (°C) for 1 hr.	Volume Fraction (%)					
	Ti	TiC	Al		Ti	C	TiC	Al_3Ti	TiC_8	Ti_3AlC_2
8TAC 4	1	1	1.4	800	2.92	8.13	69.32	19.63	–	–
10TAC 4	1	1	1.4	1000	4.36	–	82.96	6.32	4.87	1.49
12TAC 4	1	1	1.4	1200	5.29	–	71.04	6.93	12.43	4.31
14TAC 1	1	1	1.1	1400	–	–	8.31	–	–	91.69
14TAC 2	1	1	1.2	1400	–	–	8.13	–	–	91.87
14TAC 3	1	1	1.3	1400	–	–	4.28	–	–	95.72
14TAC 4	1	1	1.4	1400	–	–	2.87	–	6.22	90.91
15TAC 1	1	1	1.1	1500	–	–	4.11	–	–	95.89
15TAC 2	1	1	1.2	1500	–	–	4.03	–	–	95.97
15TAC 3	1	1	1.3	1500	–	–	2.06	–	–	97.94
15TAC 4	1	1	1.4	1500	–	–	3.88	–	–	96.12

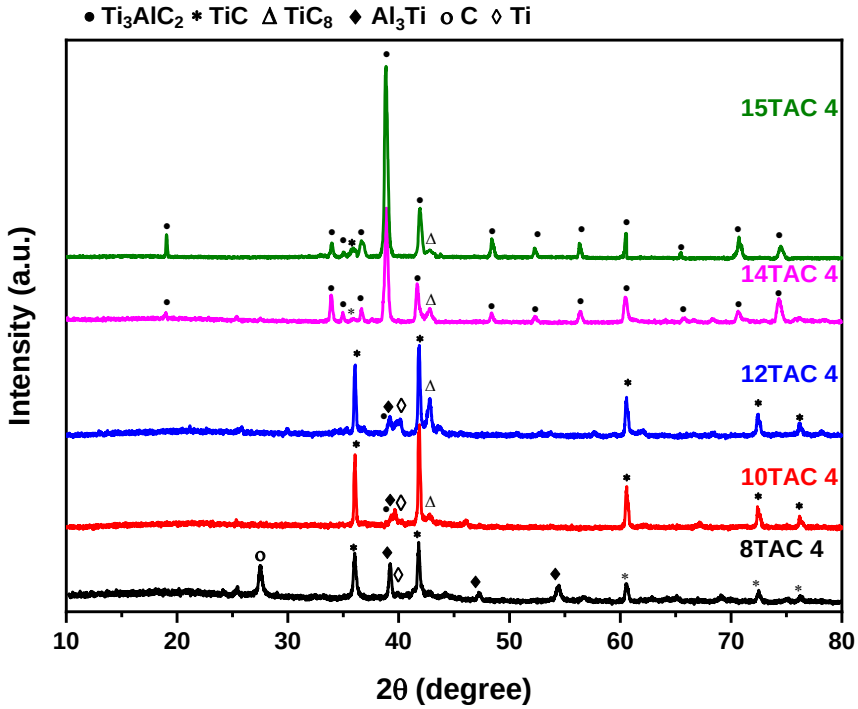

Fig. 5.1 The formation of intermediate phases at different temperatures during the synthesis of Ti_3AlC_2.

The peaks associated with TiC, Ti and C are also observed in 8TAC 4 sample. Hendaoui and co-workers [7] also observed the presence of Al_3Ti during the synthesis of Ti_3AlC_2 by

taking excess Al content. The samples (10 TAC4 and 12 TAC4) sintered at 1000 and 1200 °C demonstrated the peaks associated with TiC, Ti, Al_3Ti and TiC compounds.

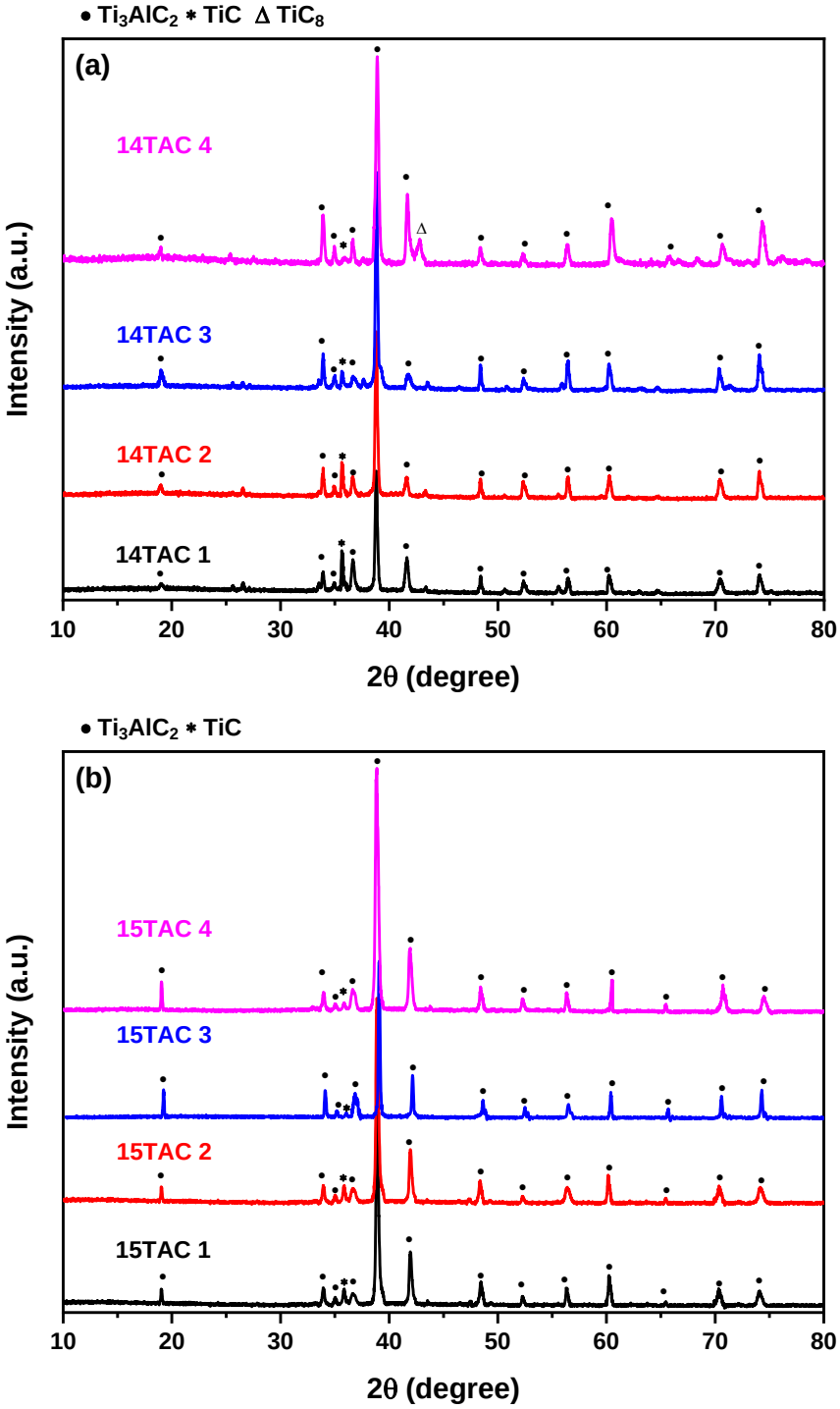

Fig. 5.2 XRD patterns of (a) 14TAC 1 – 14TAC 4 samples and (b) 15TAC 1 – 15TAC 4 samples sintered at 1400 °C and 1500 °C, respectively.

In addition, a peak associated with Ti_3AlC_2 MAX phase is also observed in the samples sintered at 1000 and 1200 °C. Further increase in temperature to 1400 °C resulted in the formation of Ti_3AlC_2 MAX phase with the presence of small amount of TiC and TiC_8

compounds. This indicated that TiC and Al_3Ti reacted to form Ti_3AlC_2 MAX phase by following reaction Eq. 5.3 – 5.4.

$$Al_3Ti + 2TiC \rightarrow Ti_3AlC_2 + 2Al \quad (5.3)$$

$$7Al_3Ti + 58TiC \rightarrow 21Ti_3AlC_2 + 2TiC_8 \quad (5.4)$$

At 1500 °C, the peaks associated Ti_3AlC_2 becomes more pronounced along with minor phases of TiC in 15TAC 4 sample. The results revealed that the formation of Ti_3AlC_2 MAX phase is favorable at 1400 and 1500 °C. Consequently, the role of aluminium content is investigated at 1400 and 1500 °C. The concentration of aluminium is varied from 10 – 40 mol %. In this regard, four samples TAC 1, TAC 2, TAC 3 and TAC 4 are sintered at 1400 and 1500 °C for an hour in argon atmosphere. The labelling samples are presented in Table 5.1. Fig. 5.2a presents the XRD diffractograms of 14TAC 1 – 14TAC 4 samples. The volume fraction of phases present in these samples is given in Table 5.3. The results indicated that the formation of Ti_3AlC_2 depends on the aluminium content. The formation of Ti_3AlC_2 alongwith TiC, Al_3Ti and TiC_8 is observed in samples 14TAC 1, 14TAC 2 and 14TAC 4. However, the peak associated with TiC_8 is not seen in 14TAC 3 sample. This designated the synthesis of Ti_3AlC_2 phase depends on the aluminium content.

Table 5.2 The lattice parameters of Ti_3AlC_2 phase present in prepared samples.

Samples	Lattice Parameters of Ti_3AlC_2				
	a (Å)	**c (Å)**	**χ^2**	**Cell Volume (Å^3)**	**R_{wp}**
14TAC 1	3.071	18.568	1.12	91.03	19.23
14TAC 2	3.075	18.562	1.22	90.45	18.26
14TAC 3	3.073	18.571	1.02	90.82	18.45
14TAC 4	3.072	18.578	1.18	91.01	19.88
15TAC 1	3.075	18.577	1.09	91.24	17.24
15TAC 2	3.077	18.581	1.29	91.36	18.01
15TAC 3	3.074	18.576	1.08	90.98	16.92
15TAC 4	3.076	18.579	1.16	91.23	18.33

Similar results are also reported during the synthesis of other MAX phases by varying the aluminium content [8,9]. However, excessive increase in Al content led to the formation secondary phases as observed in 14TAC 4 sample. The maximum amount of Ti_3AlC_2 is observed in 14TAC 3 sample sintered at 1400 ºC. It might be possible that secondary phases (TiC, Al_3Ti and TiC_8) could react to form Ti_3AlC_2 MAX phase at higher temperature. Hence, TAC 1 – TAC 4 samples are sintered at 1500 ºC.

Fig. 5.2b shows the XRD patterns of 15TAC 1 – 15TAC 4 samples sintered at 1500 ºC. In these samples, the peaks associated with Ti_3AlC_2 alongwith TiC are observed. This indicates that increase in temperature favored the formation of Ti_3AlC_2 MAX phase. In addition, there is no peak related to Al_3Ti phase. It is observed that increase in Al content upto 30 mol% favored the formation of Ti_3AlC_2. While further increase in Al content favored the formation of carbide. The maximum volume fraction of Ti_3AlC_2 MAX phase is obtained in 15TAC 3 sample, as is evident from Fig. 5.2 and Table 5.2. Moreover, Rietveld refinement is performed to calculate the lattice parameters and cell volume (Table 5.3) for Ti_3AlC_2. Fig. 5.3 presents the Rietveld refinement of 15TAC 3 sample.

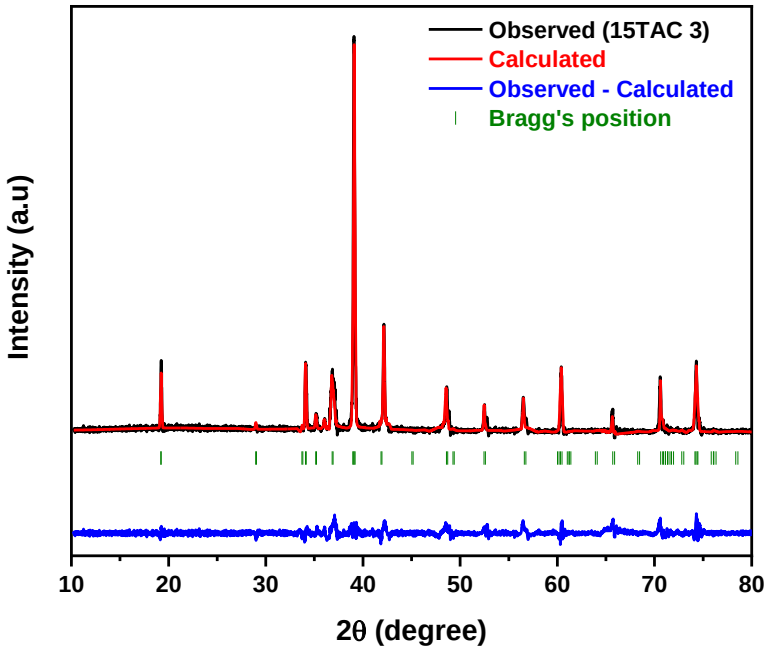

Fig. 5.3 Rietveld refinement plot of 15TAC 3 sample.

5.2.2. Synthesis kinetics of Ti_3AlC_2 MAX phase

To get better knowledge associated with the formation of Ti_3AlC_2 MAX phase, it is crucial to study the synthesis kinetics. Several research groups investigated the synthesis kinetics of variety of materials with thermal analysis techniques (thermogravimetry analysis (TGA), Dilatometry, differential thermal analysis (DTA) and differential scanning calorimetry DSC). In this regard, DTA technique is employed to investigate the synthesis kinetics of Ti_3AlC_2. Accordingly, the milled and pelletized TAC 3 sample is heated from ambient temperature to 1300 °C at various heating rates (5, 10, 15, 20 °C/min) in an argon atmosphere. The heat flow and change in mass w.r.t. temperature and time is recorded. Fig. 5.4 demonstrate the DTA curve of TAC 3 sample. There are two endothermic peaks detected at ~ 665 °C and ~ 965 °C that are observed in DTA curves obtained at heating rate of 10 °C/min (Fig. 5.4a).

The former endothermic peak (Fig. 5.4b) designated to the Al melting. However, the second endothermic peak (Fig. 5.4c) is related to the synthesis of Ti_3AlC_2 MAX phase. These endothermic peaks shifted toward higher temperatures with an increase in heating rates. Similar shifting of peaks is also observed in the case of Cr_2AlC MAX phase (Chapter 4). The initial, maximum, and final endothermic peak temperatures at all heating rates are presented in Table 5.3. Fig. 5.1 and Fig. 5.4 indicated that the second endothermic peak could be associated with the reaction between TiC and Al_3Ti to form Ti_3AlC_2 MAX phase.

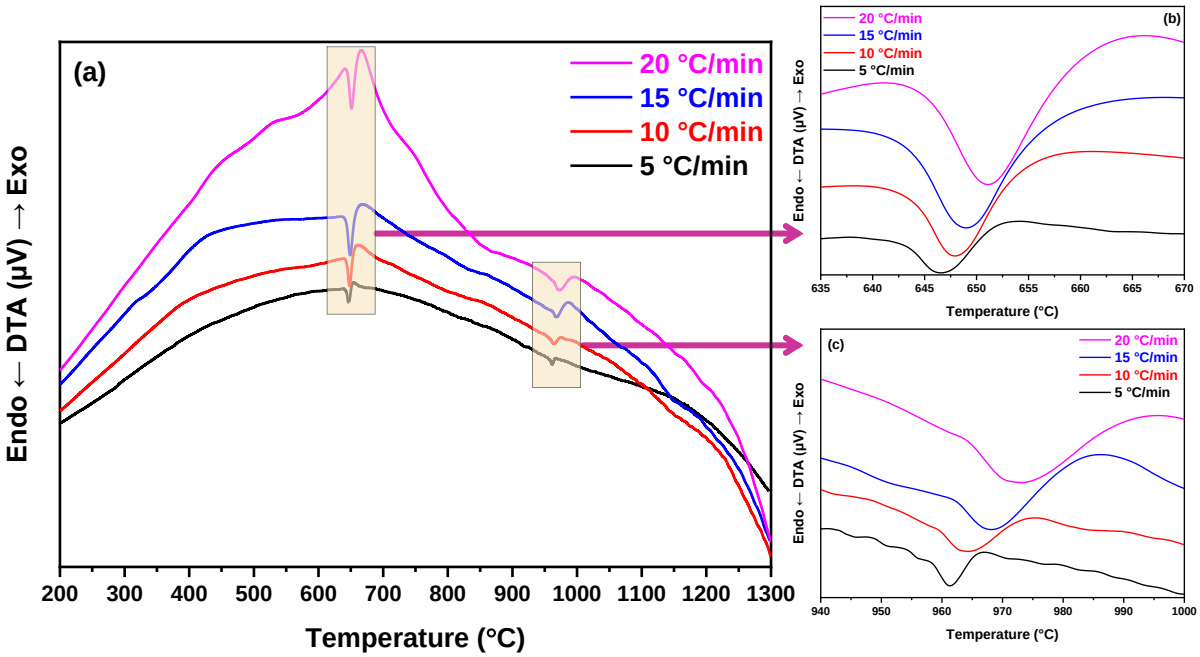

Fig. 5.4 (a) DTA curves of the milled pelletized TAC 3 sample. (b) First endothermic peak, and (c) Second endothermic peak at multiple heating rates (5, 10, 15, 20 °C/min) in an argon atmosphere.

Table 5.3 The initial, maximum, and final temperatures of both endothermic peaks at all heating rates.

Heating Rates	**Peak I**			**Peak II**		
(K/min)	**T_i (°C)**	**T_p (°C)**	**T_f (°C)**	**T_i (°C)**	**T_p (°C)**	**T_f (°C)**
5	657.47	666.31	671.46	1040	1051.76	1058.99
10	657.92	667.25	674.37	1040	1051.84	1063.58
15	658.12	667.37	674.65	1040	1053.22	1066.32
20	659.98	667.39	676.22	1040	1054.38	1070.49

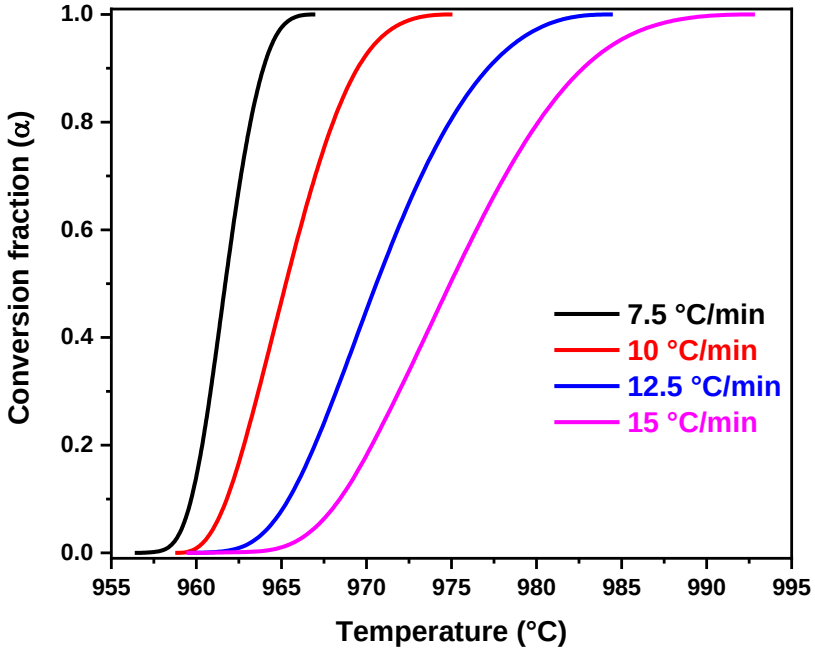

Fig. 5.5 (a) The variation of the conversion value (α) and (b) derivative of conversion value (dα/dt) with temperature.

Fig. 5.5 shows the change in conversion fraction (α) with temperature for second endothermic peak. The kinetic parameters responsible for second endothermic peak are calculated according to the methodology presented in Chapter 3. Fig. 5.6 presents the linear fitted curves obtained from KAS (Fig. 5.6a) and FWO (Fig. 5.6b) methods for TAC 3 sample. The activation energy calculated for each conversion fraction along with standard error is tabulated in Table 5.4. The average activation energy calculated from KAS (632.39 kJ/mol) is higher than the FWO (630.09 kJ/mol).

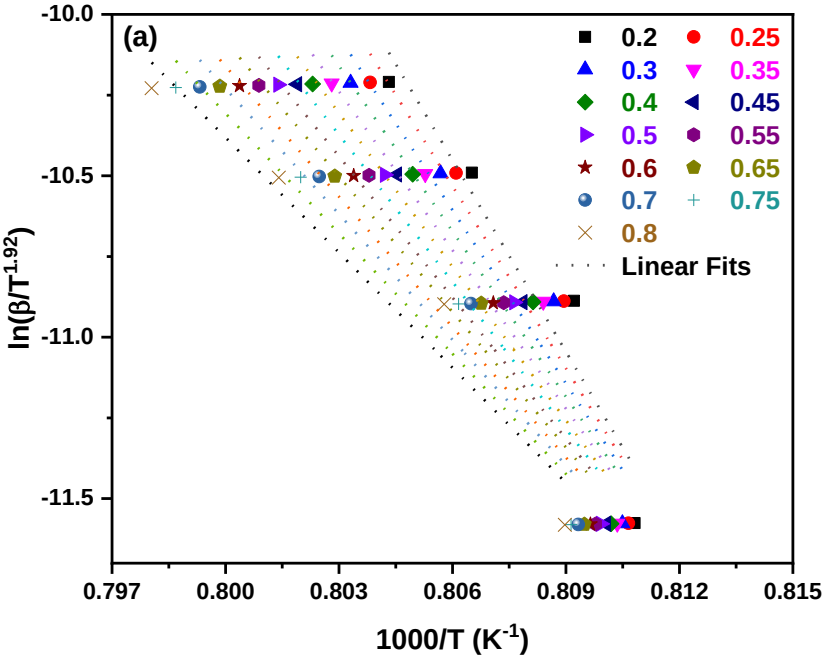

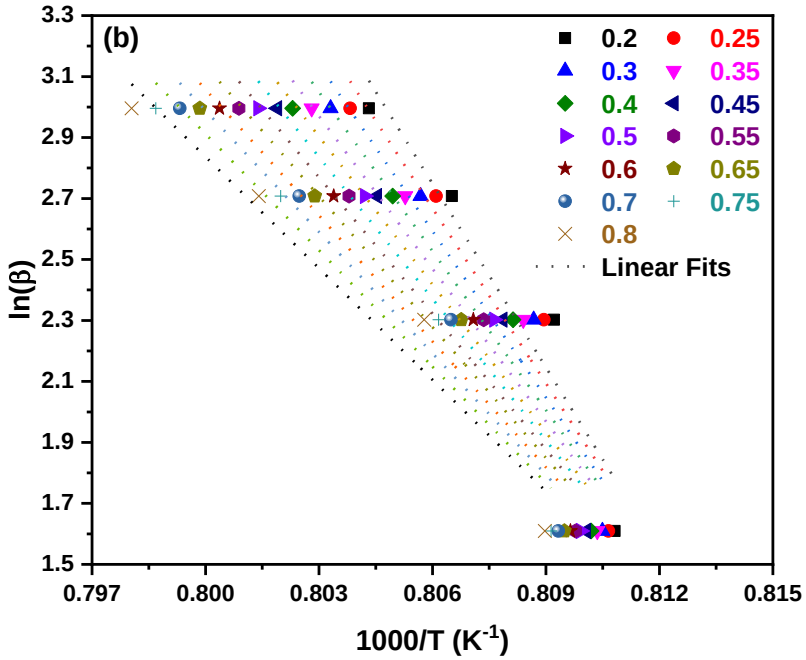

Fig. 5.6 The linear fitted curves obtained from (a) KAS and (b) FWO methods for TAC 3 sample.

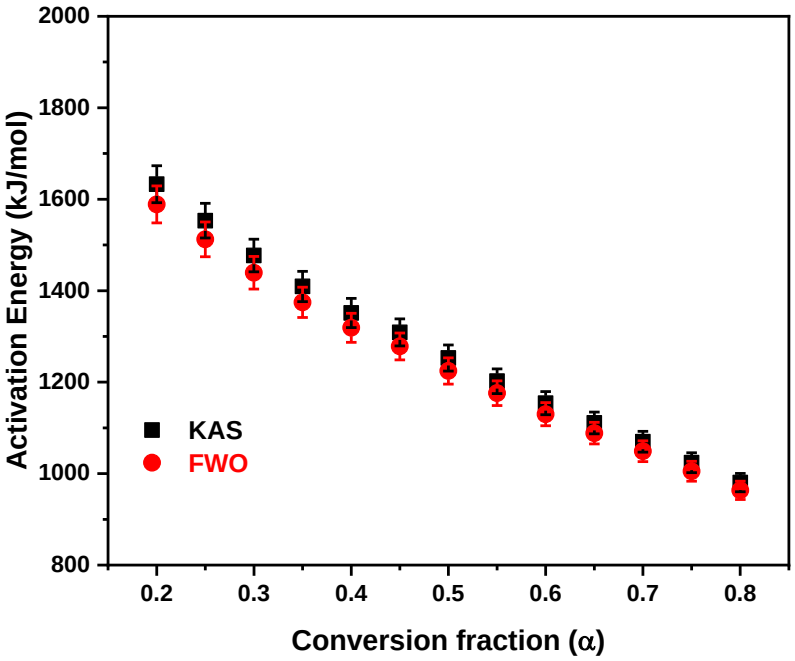

Fig. 5.7 Trend of activation energy calculated from KAS and FWO kinetic methods.

The difference in the average activation energy value is due to different mathematical approximations used in kinetic methods (KAS and FWO). However, the trend of activation energy (Table 5.4 and Fig. 5.7) remains the same, as calculated from both kinetic methods. Furthermore, the reaction mechanism responsible for the formation of Ti_3AlC_2 is recognized by using master integral plot method. According to this method, the theoretical values corresponding to various reaction models are compared with the experimental results. The

detailed description related to the integral master plot method is presented in the Chapter 3. The comparison of theoretical and experimental curves is presented in Fig. 5.8. The results revealed that A4 (nucleation growth model) mechanism is responsible for the formation of Ti_3AlC_2 MAX phase. This suggested that the growth of Ti_3AlC_2 initiated at ~ 960 ºC and later the increase in temperature resulted into complete growth of Ti_3AlC_2 phase.

Table 5.4 The variation of activation energy w.r.t. conversion value (α), as calculated from KAS and FWO methods.

Conversion Value	KAS method			FWO method		
	E_a (kJ/mol)	Error	R^2	E_a (kJ/mol)	Error	R^2
0.2	1632.81	40.48	0.884	1588.62	40.55	0.887
0.25	1553.10	37.95	0.887	1512.25	38.08	0.891
0.3	1476.89	35.61	0.890	1439.24	35.78	0.893
0.35	1409.25	33.10	0.895	1374.43	33.19	0.899
0.4	1351.23	31.81	0.895	1318.85	31.91	0.898
0.45	1308.76	29.45	0.903	1278.16	29.53	0.907
0.5	1252.68	28.60	0.901	1224.43	28.64	0.904
0.55	1202.00	26.90	0.904	1175.88	27.01	0.908
0.6	1154.07	25.43	0.907	1129.96	25.55	0.911
0.65	1110.79	23.63	0.913	1088.50	23.72	0.917
0.7	1069.59	22.72	0.913	1049.03	22.93	0.917
0.75	1023.86	21.65	0.914	1005.22	21.78	0.918
0.8	980.26	19.97	0.920	963.45	20.12	0.924

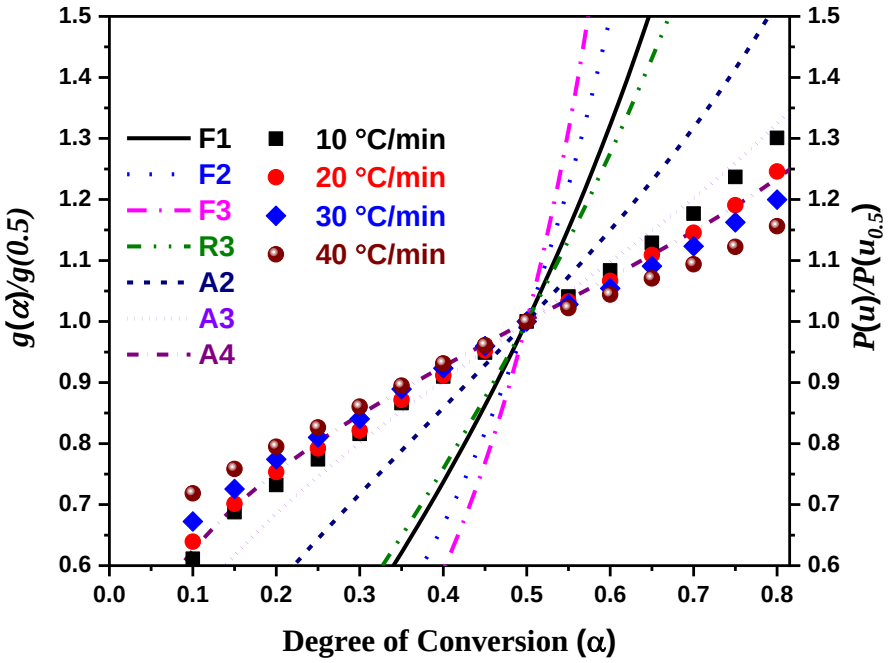

Fig. 5.8 A comparison of the experimental and theoretical master curves.

In general, there are two types of restrictions that hinders the growth of nuclei, i.e., Ingestion and Coalescence [10]. The former restriction occurred due to the growth of an existing nucleation site that eliminate the potential new nucleation site. The later restriction is related to the loss of interface between reactants and products when distinct nuclei merge.

Furthermore, the third kinetic parameter (pre-exponential factor) is calculated by substituting average activation energy and $g(\alpha)$ corresponding to A4 mechanism, i.e., $\left(g(\alpha) = [-\ln(1-\alpha)]^{1/4}\right)$. Hence, eq. (3.8) can be rewritten as:

$$g(\alpha) = [-\ln(1-\alpha)]^{1/4} = \frac{AE}{\beta R} P(u) \tag{5.5}$$

The value of pre-exponential factor is determined from the slope of the linear fitted curve between $[-\ln(1-\alpha)]^{1/4}$ and $\frac{E}{\beta R}P(u)$ (Fig. 5.9a). The variation of pre-exponential w.r.t. heating rates along with the standard error is shown in Fig. 5.9b. Finally, Table 5.5 represents the calculated kinetic triplets involved during the formation of Ti_3AlC_2 MAX phase.

Table 5.5 Kinetic triplets involved during formation of Ti_3AlC_2 MAX phase.

Kinetic triplets			
Average activation energy		Average pre-exponential factor	Reaction mechanism
KAS	FWO		
1271.18 ± 29.02	1242.16 ± 29.13	$3.69 \times 10^{26} \pm 1.23 \times 10^{25}$	A4

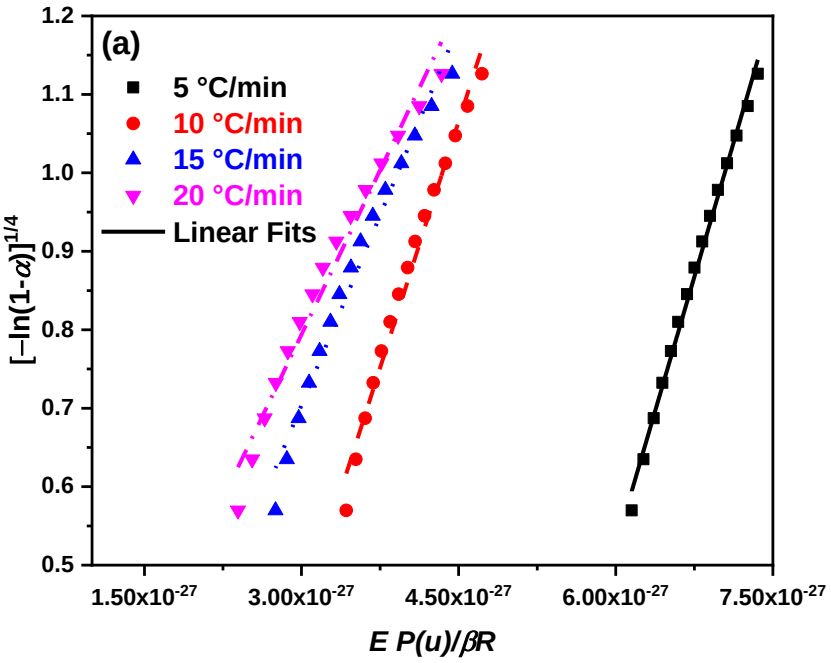

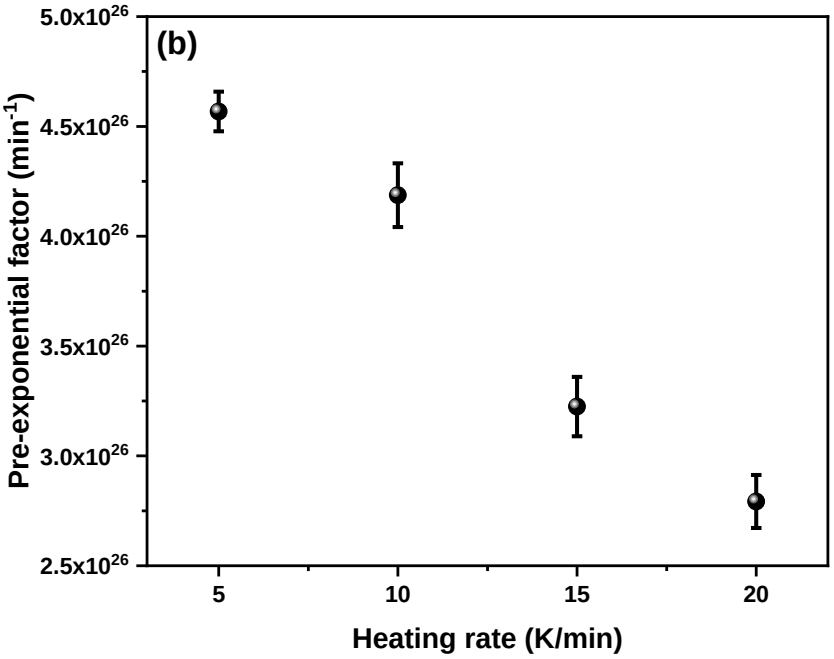

Fig. 5.9 (a) The linear fitted curve between $(1/1-\alpha)$ and $\frac{E}{\beta R}P(u)$. (b) The variation of pre-exponential w.r.t. heating rates along with the standard error.

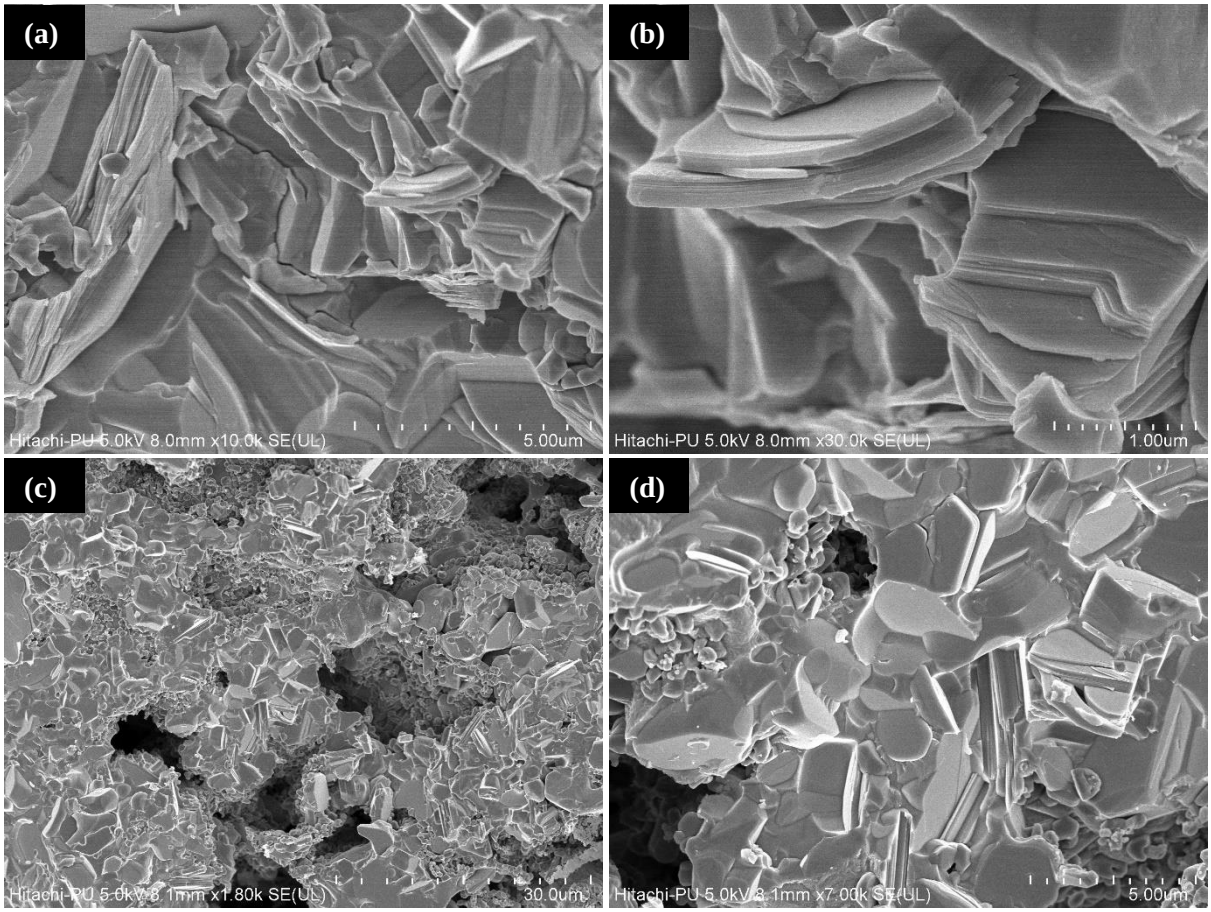

Fig. 5.10 The FE-SEM micrographs of fractured (a-b) 14TAC 3 and (c-d) 15TAC 3 samples.

5.2.3. Microstructure Analysis

The fractured surface morphology of 14TAC 3 and 15TAC 3 samples with higher volume fraction of Ti_3AlC_2 is presented in Fig. 5.10. These micrographs show a typical nanolaminated structure of the MAX phases. Fig. 5.10a-b presents the growth of layered structure, where the layers of Ti_3AlC_2 are bound in 14TAC 3 sample. Delamination in the layered structure is also observed. The stacking of layers became more prominent in 15TAC 3 samples (Fig. 5.10c-d). This might be associated with less carbide content in 15TAC 3 sample. It is also visible that the thickness of the layers is non-uniform (Fig. 5.10c-d). HR-TEM (High-Resolution Transmission Electron Microscopy) and SAED (Selected Area Electron Diffraction) micrographs of a 15TAC 3 sample is shown in Fig. 5.11. These micrographs demonstrated specific traits of the MAX phases. The value of d-spacing (2.63 nm) calculated from lattice fringes of 15TAC 3 sample corresponds to (101) plane of Ti_3AlC_2, as is evident from Fig. 5.11a. The formation of Ti_3AlC_2 MAX phase is also confirmed with the SAED pattern (Fig. 5.11b). The results of microstructure analysis are analogous with the XRD pattern. Further, the distribution of titanium (Ti), aluminium (Al), and carbon (C) in a 15TAC 3 sample (sintered at 1500 ºC) are identified through the EDS mapping (Fig. 5.12). It is observed that all the elements are homogeneously distributed in a 15TAC 3 sample.

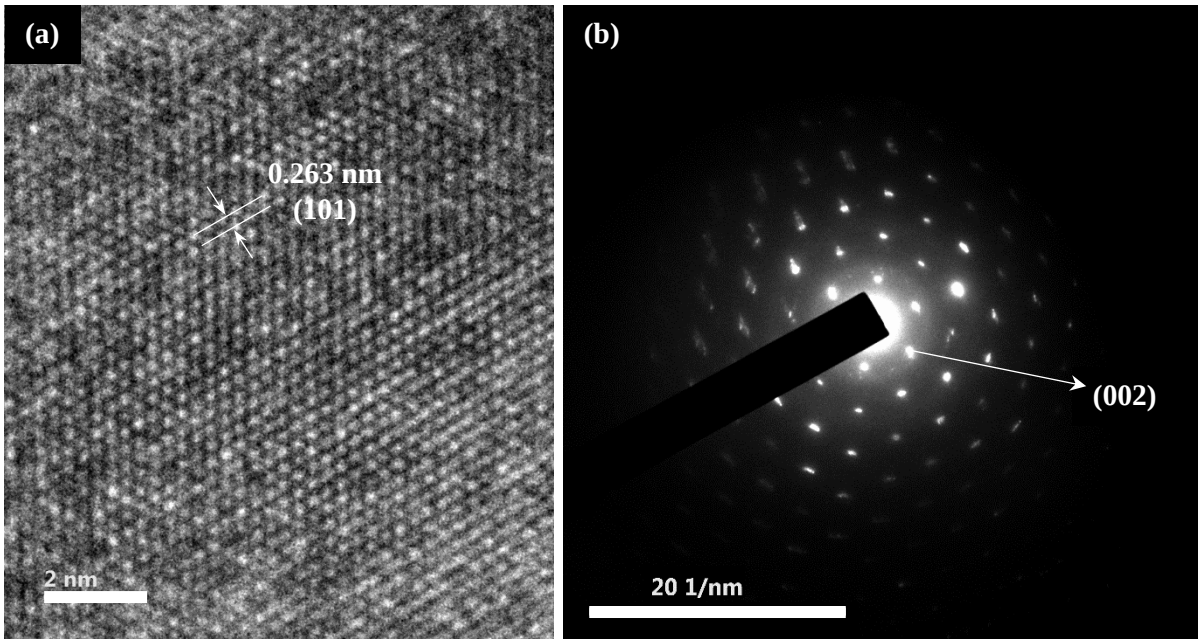

Fig. 5.11 (a) The HRTEM and (b) SAED image of 15TAC 3 sample.

5.2.4. X-ray photoelectron spectroscopy (XPS) analysis

A high resolution XPS spectra of Ti2p, C1s, Al2p and O1s of 15TAC 3 sample is shown in Fig. 5.13. The solid spheres correspond to the experimentally determined data points and

lines are associated with fitting curves through Shirley procedure. In the Ti2p spectra (Fig. 5.13a), six peaks are observed at 453.88, 455.18, 458.04, 459.92, 462.75 and 464.10 eV, as is evident from Fig. 5.13a.

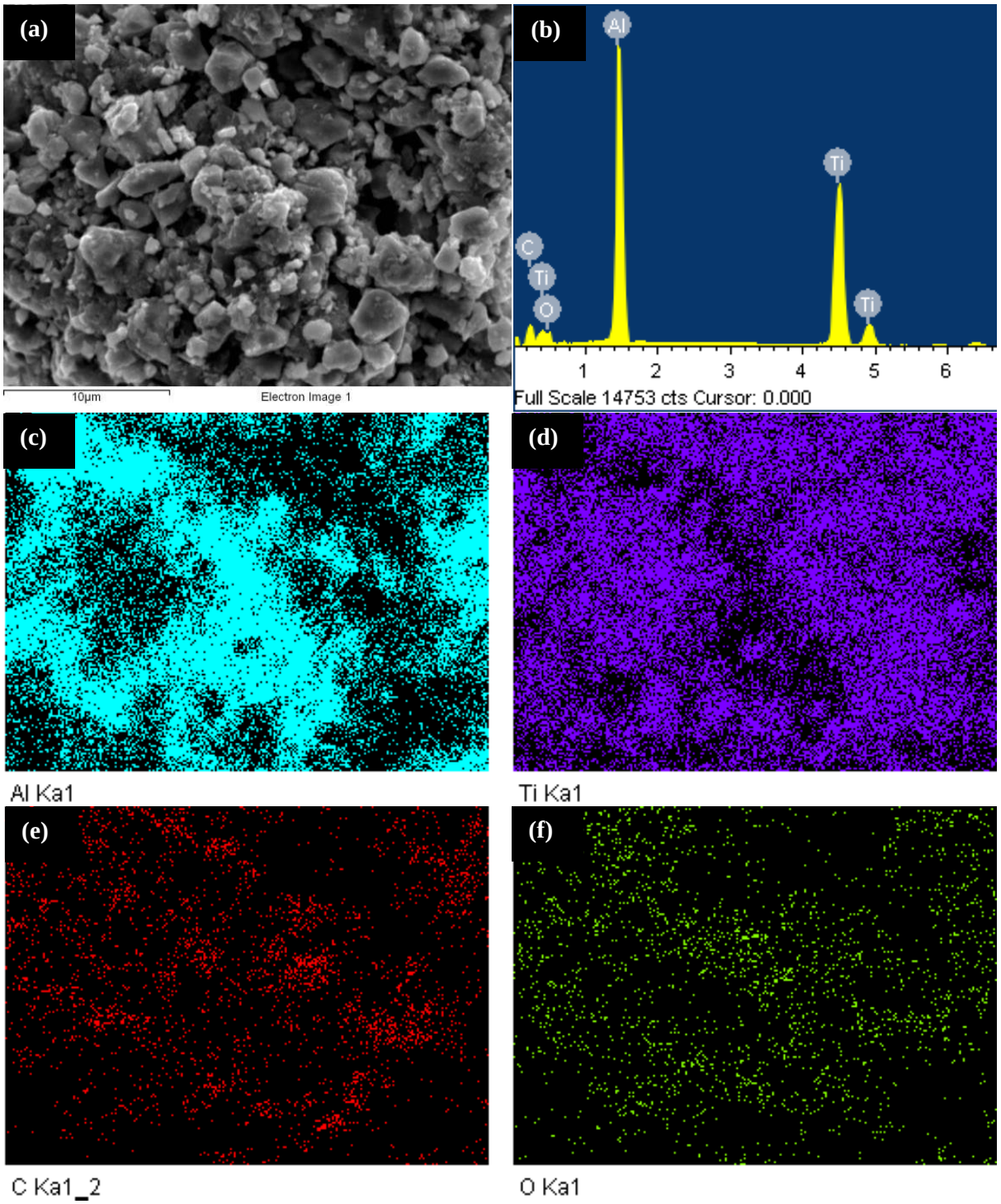

Fig. 5.12 (a) SEM image and (b) elemental composition 15TAC 3 sample. The distribution of (c) Al, (d) Ti, (e) C and (f) O in 15TAC 3 sample.

The peaks at 453.88 and 459.92 correspond to the Ti-C bond [11]. The remaining four peaks are assigned to TiO_2 (458.04 and 464.10 eV) and TiO (455.13 and 462.75 eV) [12–14].

The C1s spectra (Fig. 5.13b) observed for 15TAC 3 sample demonstrated four peaks at 280.98, 284.46, 285.30 and 287.17 eV. The former peak (280.98 eV) is assigned to Ti-C, while peak at 284.46 eV corresponds to the residual adsorbed carbon C-C [11,15–17]. The latter two peaks at 285.30 and 287.17 eV are assigned to C-O [18]. Further, three peaks are observed in Al2p spectra of 15TAC 3 sample. The peak at 71.84, 73.67 and 74.60 eV originated due to Ti-Al, Al-C and Al-O bond, respectively [19,20]. The O_{1s} spectra of 15TAC 3 sample demonstrated two peaks at E_b ~ 530.33 and 531.87 eV. The former peak is assigned to O-Ti_3AlC_2/Ti_2AlC/TiC while the latter peak ascribed to O=C [21]. The XPS results also confirmed the formation of Ti_3AlC_2 MAX phase.

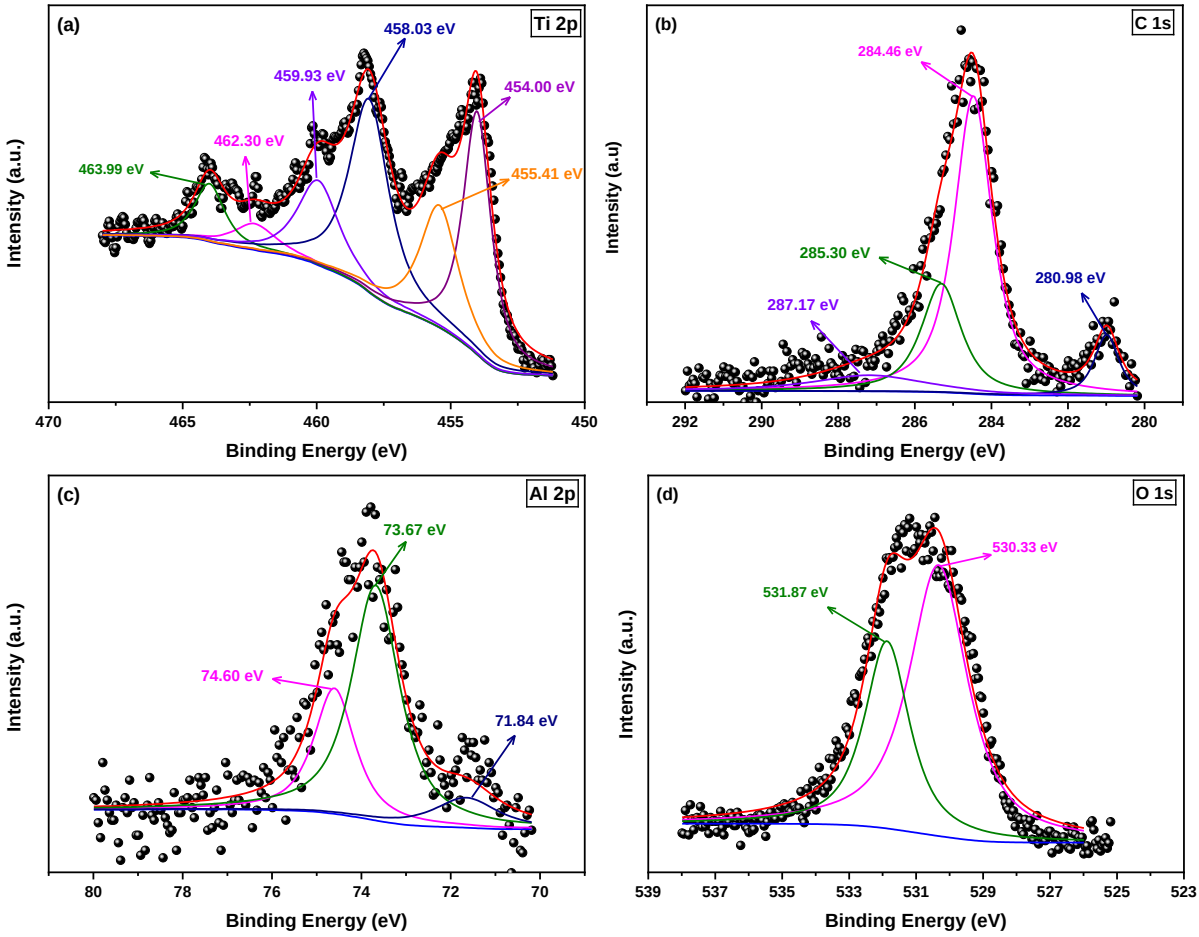

Fig. 5.13 The typical (a) Ti_{2p}, (b) C_{1s}, (c) Al_{2p} and (d) O_{1s} XPS spectra of 15TAC 3 sample.

5.2.5. Oxidation kinetics of Ti_3AlC_2 MAX phase

Ti_3AlC_2 MAX phase offers good oxidation resistance [22]. To design a material with good oxidation resistance, it is important to gain information related to oxidation kinetic under isothermal and non-isothermal conditions. The oxidation kinetic is commonly studied with the help of thermal analysis techniques [23,24]. An exhaustive work has been done to investigate the oxidation kinetics of Ti_3AlC_2 MAX phase under isothermal conditions [25]. However,

studies related to non-isothermal oxidation behavior of Ti_3AlC_2 are scarce in literature. Therefore, non-isothermal oxidation kinetic is performed through TGA/DTA technique.

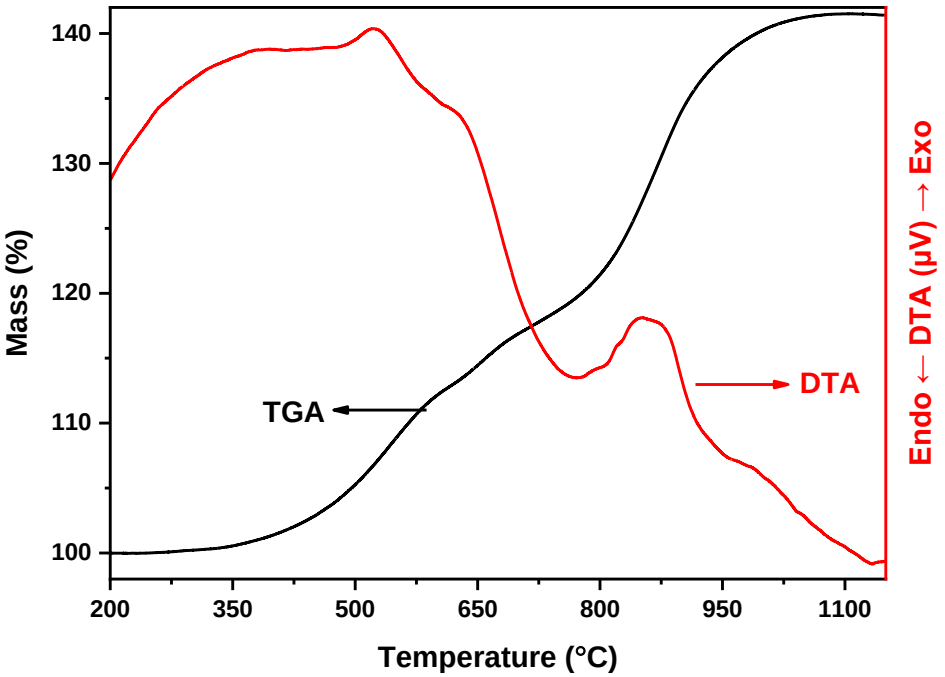

Fig. 5.14 TGA/DTA curves of 15TAC 3 sample in air environment at 10 ºC/min.

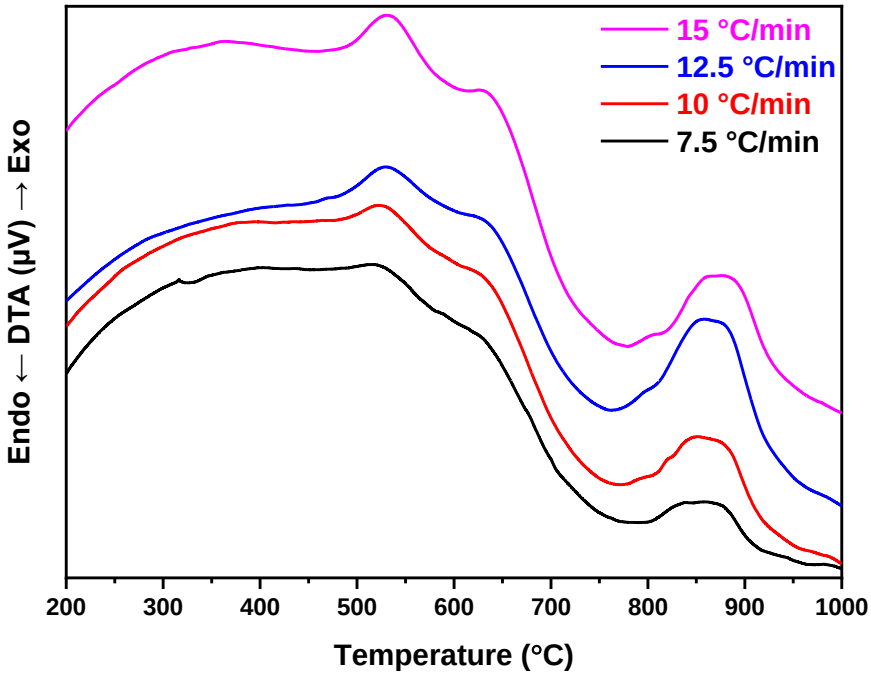

Fig. 5.15 DTA curves of 15TAC 3 sample in air environment at 7.5, 10, 12.5 and 15 ºC/min.

Fig. 5.14 presents TGA/DTA curves of Ti_3AlC_2 MAX phase at heating rate of 10 ºC/min. These curves demonstrated that the mass remained constant upto 350 ºC and then the mass gain occurred due to the oxidation. The oxidation reaction completed at ~ 1100 ºC, as is evident from the stability in mass. There are three exothermic peaks (~ 522, 628 and 860 ºC)

that are observed in the DTA curve (Fig. 5.14). Wang and Zhou [26] also reported similar exothermic peaks in DSC curve of Ti_3AlC_2. The former two peaks correspond to the oxidation of TiC impurity present and formation of Al_2O_3 on the surface of the MAX phase. It is reported that the formation of Al_2O_3 layer occurred underneath the TiO_2 layer [26] . Both these layers protect the Ti_3AlC_2 MAX phase and improve it's oxidation resistance. The total mass gain (~ 40 %) as observed in Ti_3AlC_2 is comparable with the literature. To gain more information related to the oxidation, DTA experiments are performed at various heating rates (7.5, 10, 12.5, 15 ºC/min). Fig. 5.15 demonstrate three oxidation peaks of Ti_3AlC_2 MAX phase. A shifting is observed in all the peaks with increase in heating rate. Similar, shifting is also observed during oxidation of Cr_2AlC MAX phase (Chapter 4). The probable reaction involved during oxidation of Ti_3AlC_2 is given below:

$$4Ti_3AlC_2 + 23O_2 \rightarrow 12TiO_2 + 2Al_2O_3 + 8CO_2 \qquad (5.6)$$

Moreover, conversion fraction for each peak is evaluated to perform kinetic analysis. The detailed procedure opted for kinetic analysis is presented in Chapter 3. Fig. 5.16 presents the calculated value of conversion fraction for all peaks.

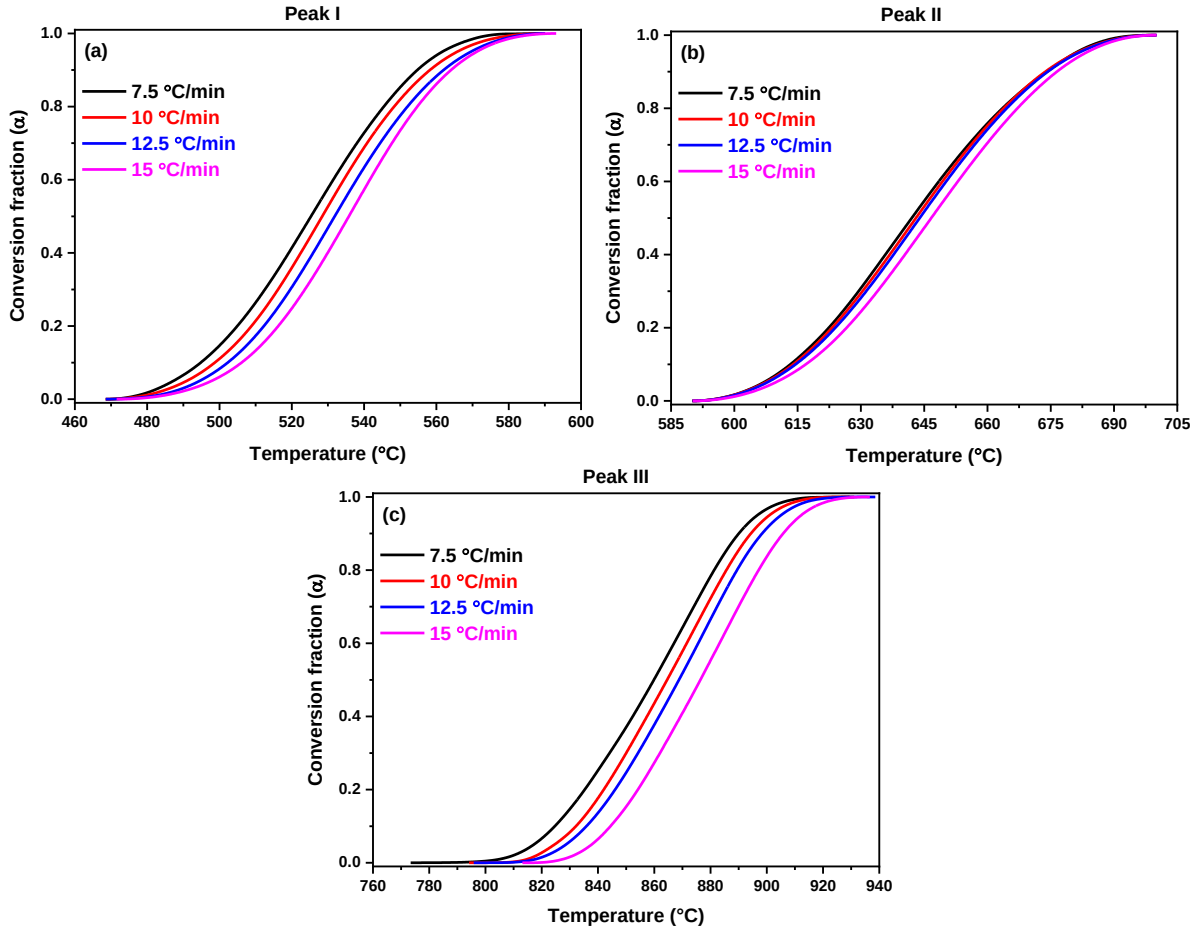

Fig. 5.16 The variation of conversion values with temperature for (a) peak I, (b) peak II and (c) peak III.

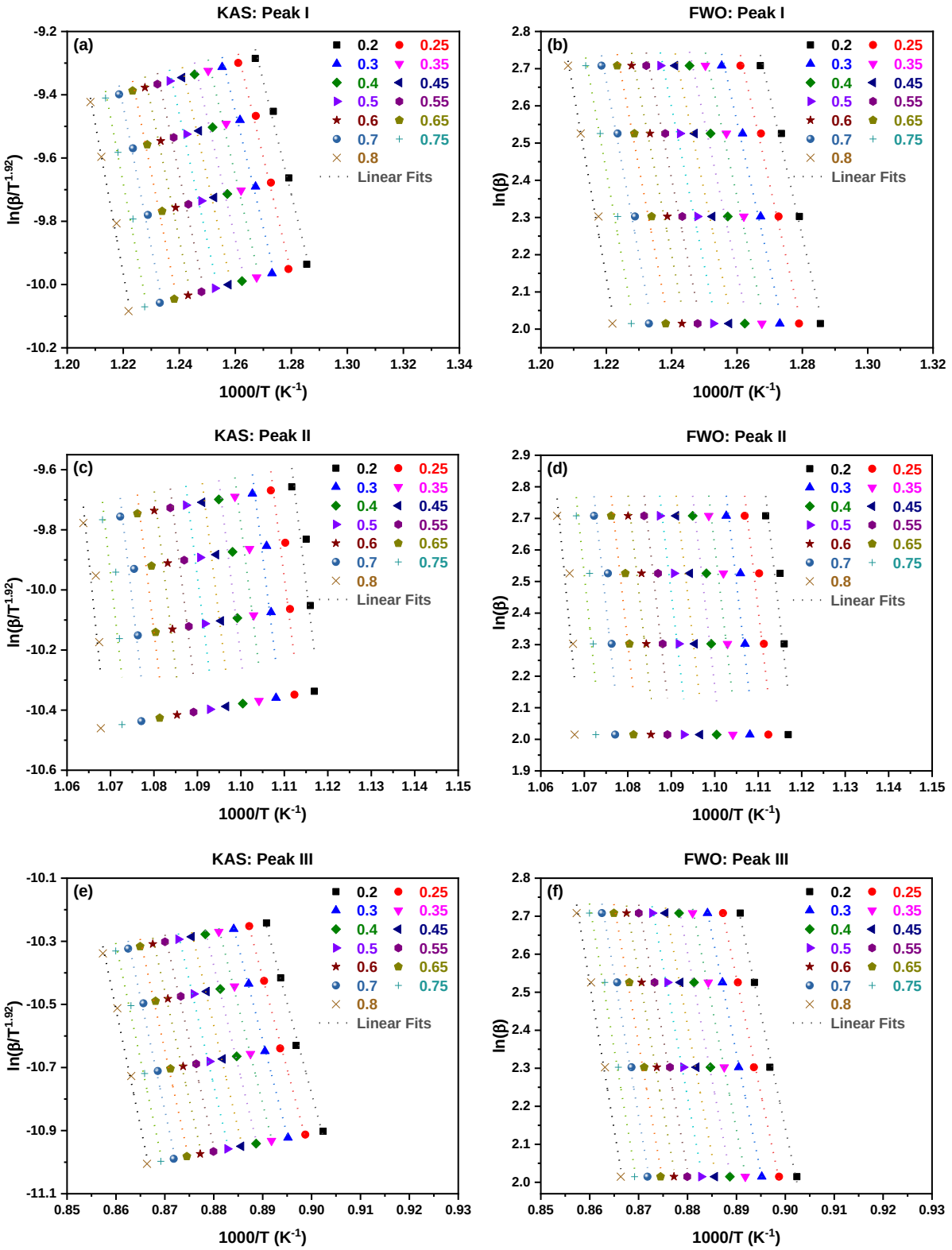

Fig 5.17 Linear fitted plots obtained from KAS and FWO iso-conversional kinetic methods for (a, c, e) oxidation peak I and (b, d, f) oxidation peak II.

Table 5.6 The value of activation energy (E_a) evaluated for each degree of conversion through KAS and FWO methods for oxidation peak I.

Conversion Value	Oxidation Peak I					
	KAS method			FWO method		
	E_a (kJ/mol)	Error	R^2	E_a (kJ/mol)	Error	R^2
0.2	294.15	2.82	0.98	300.10	2.99	0.98
0.25	301.76	2.88	0.98	307.42	2.93	0.98
0.3	302.68	3.38	0.97	308.34	3.46	0.98
0.35	311.60	3.92	0.97	316.94	4.03	0.97
0.4	317.03	4.37	0.96	322.17	4.44	0.97
0.45	324.02	4.03	0.97	328.90	4.18	0.97
0.5	330.73	4.54	0.96	335.36	4.62	0.97
0.55	340.47	4.68	0.96	344.73	4.73	0.97
0.6	346.75	4.90	0.96	350.78	5.02	0.96
0.65	359.28	4.76	0.96	362.82	4.83	0.97
0.7	366.42	4.62	0.97	369.70	4.71	0.97
0.75	381.16	4.37	0.97	383.87	4.45	0.98
0.8	390.43	3.86	0.98	392.79	3.99	0.98

Table 5.7 The value of activation energy (E_a) evaluated for each degree of conversion through KAS and FWO methods for oxidation peak II.

Conversion Value	Oxidation Peak II					
	KAS method			FWO method		
	E_a (kJ/mol)	Error	R^2	E_a (kJ/mol)	Error	R^2
0.2	971.84	39.41	0.73	950.76	39.49	0.74
0.25	943.24	35.19	0.76	923.40	35.26	0.77
0.3	954.75	34.17	0.78	934.48	34.22	0.79
0.35	938.03	34.03	0.77	918.50	34.15	0.78
0.4	959.26	31.17	0.81	938.88	31.24	0.82
0.45	951.30	31.87	0.80	931.29	31.43	0.81
0.5	943.09	32.84	0.79	923.46	32.93	0.80
0.55	969.96	34.60	0.78	949.25	34.88	0.79
0.6	990.04	34.71	0.79	968.52	34.82	0.79
0.65	985.38	39.03	0.74	964.11	39.56	0.75
0.7	1019.74	43.21	0.71	997.08	43.42	0.71
0.75	1071.22	49.13	0.67	1046.45	49.38	0.68
0.8	1157.01	58.07	0.62	1128.70	58.56	0.63

Table 5.8 The value of activation energy (E_a) evaluated for each degree of conversion through KAS and FWO methods for oxidation peak II.

Conversion Value	Oxidation Peak III					
	KAS method			FWO method		
	E_a (kJ/mol)	Error	R^2	E_a (kJ/mol)	Error	R^2
0.2	473.12	2.94	0.99	475.74	2.98	0.99
0.25	478.98	1.66	1.00	481.42	1.73	1.00
0.3	494.72	0.98	1.00	496.55	1.03	1.00
0.35	511.14	1.70	1.00	512.34	1.79	1.00
0.4	527.93	2.07	1.00	528.48	2.13	1.00
0.45	541.37	2.60	1.00	541.41	2.65	1.00
0.5	547.50	3.33	0.99	547.34	3.42	0.99
0.55	554.44	4.08	0.99	554.04	4.69	0.99
0.6	566.53	3.70	0.99	565.66	3.83	0.99
0.65	576.60	4.55	0.99	575.37	4.58	0.99
0.7	591.09	4.86	0.99	589.29	4.92	0.99
0.75	600.13	4.84	0.99	598.00	4.89	0.99
0.8	611.32	4.47	0.99	608.78	4.53	0.99

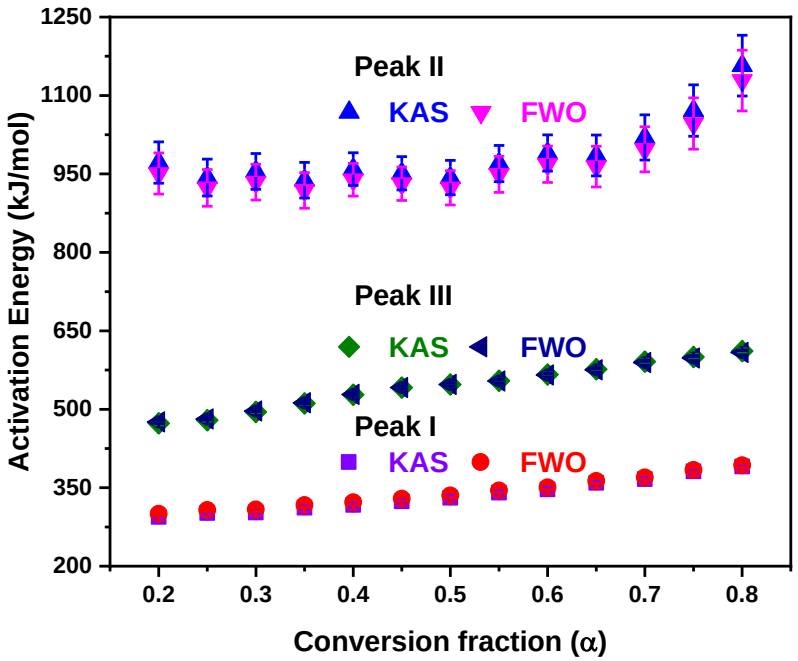

Fig. 5.18 The variation in activation energy at each conversion value calculated for oxidation peak I, peak II and peak III.

The kinetic parameters (activation energy, pre-exponential factor and reaction mechanism) are determined by following the procedure mentioned in Chapter 3. To determine the activation energy, the linear fitted plots obtained from KAS and FWO kinetic methods for

all peaks are presented in Fig. 5.17. The activation energy calculated from these linear fitted curves is tabulated in Table 5.6 – 5.8. The average value of activation energy calculated for KAS method for peak I, peak II and peak III is 335.88, 988.83 and 544.22 kJ/mol, respectively. There is a slight difference in the magnitude of activation energy calculated from FWO method for peak I (340.30 kJ/mol), peak II (967.30 kJ/mol) and peak III (544.19 kJ/mol). This variation in the magnitude arises due to different temperature integral approximations used in KAS and FWO kinetic methods.

Furthermore, the variation of activation energy with change in conversion fraction remains identical as calculated from KAS and FWO iso-conversional kinetic methods. Fig. 5.18 shows the variation in activation energy for peak I, peak II and peak III. The figures indicate that the trend of activation energy remains identical as calculated from the KAS and FWO methods for all peaks. The higher activation energy for peak II might be associated with the formation of protective layers of Al_2O_3 and TiO_2. The reaction mechanism responsible for the oxidation corresponding to peak I, peak II and peak III is recognized by using integral master method. The exact reaction mechanism is determined by comparing the experimental and theoretical curves for peak I (Fig. 5.19), peak II (Fig. 5.20) and peak III (Fig. 5.21).

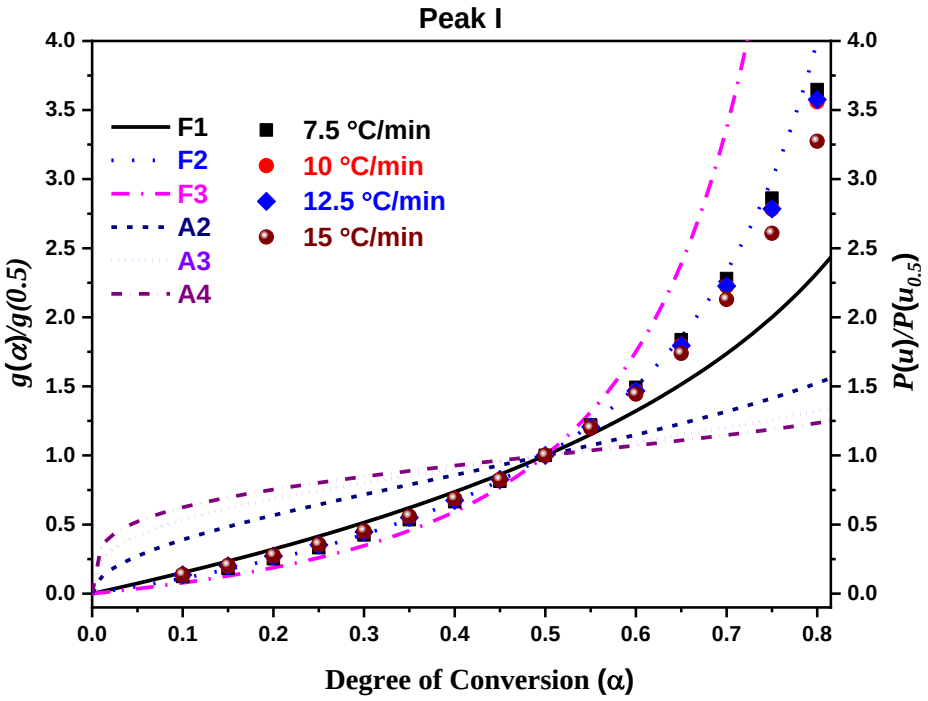

Fig. 5.19 The comparison of the theoretical master curves and the experimental curves for the oxidation peak I 15TAC 3 sample.

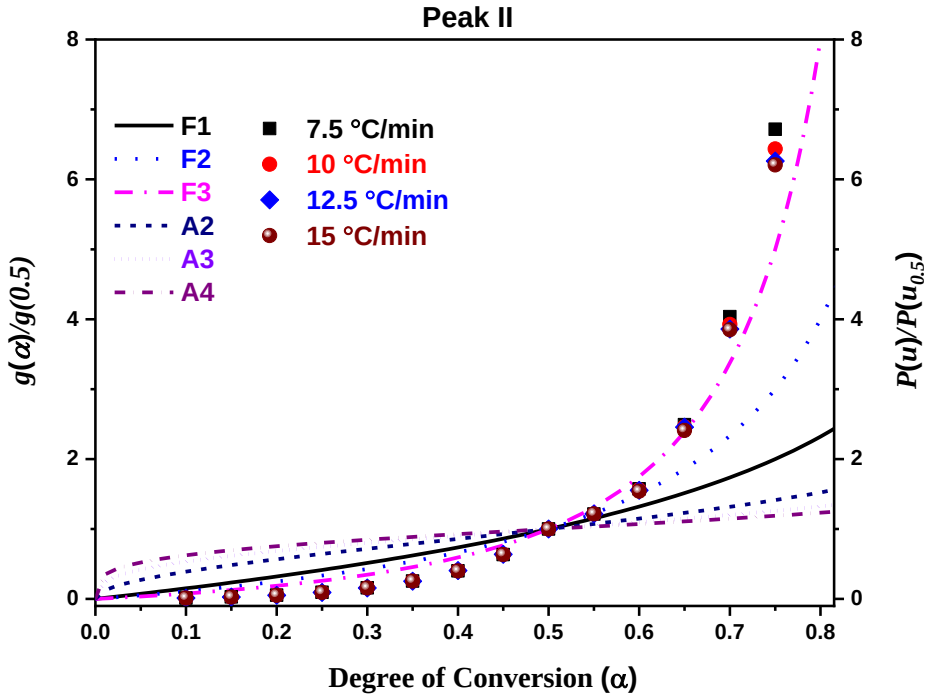

Fig. 5.20 The comparison of the theoretical master curves and the experimental curves for the oxidation peak II 15TAC 3 sample.

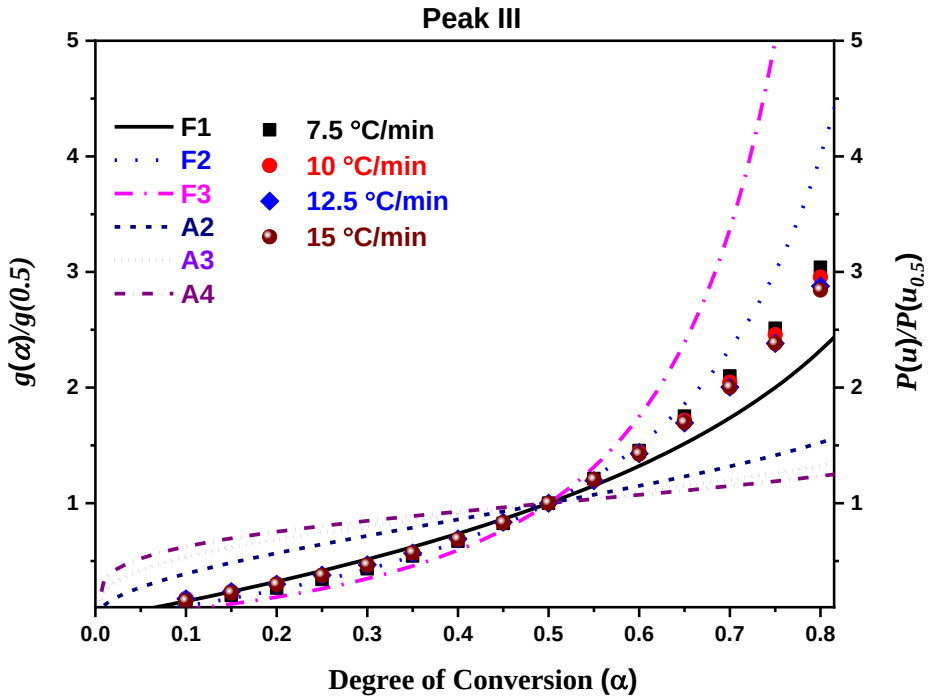

Fig. 5.21 The comparison of the theoretical master curves and the experimental curves for the oxidation peak III 15TAC 3 sample.

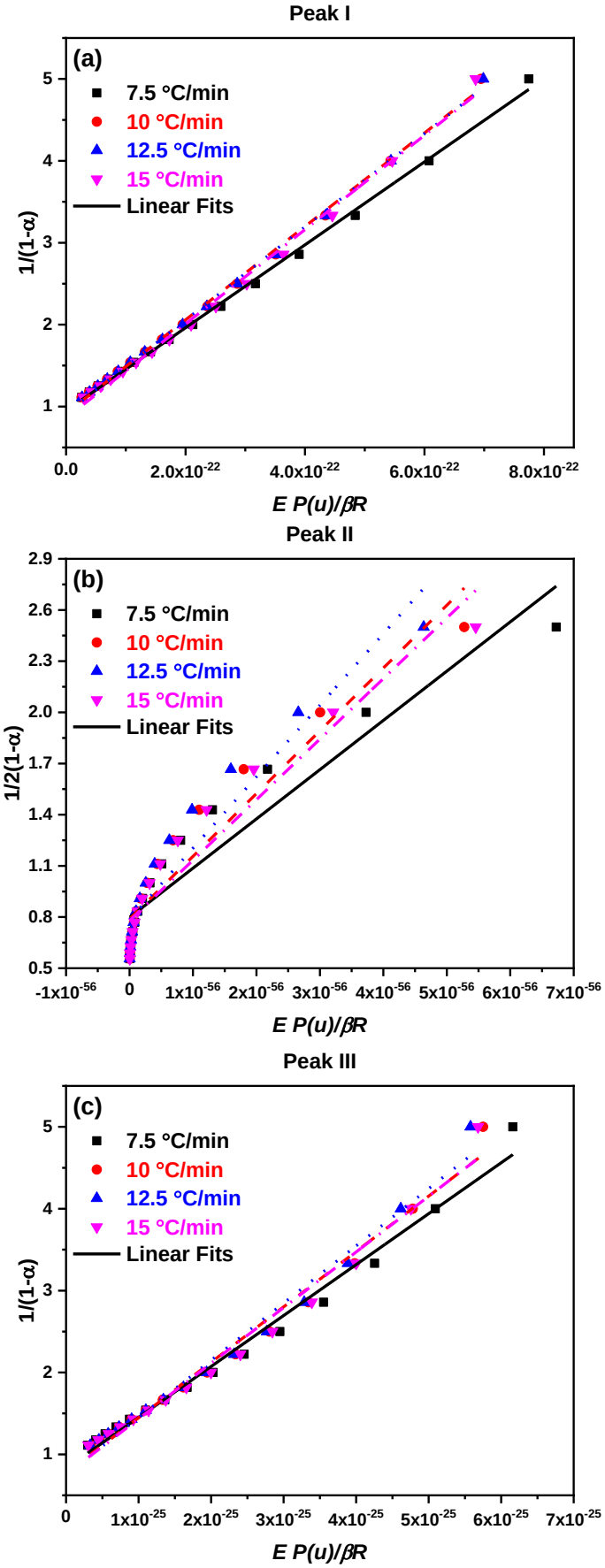

Fig. 5.22 The linear fitted curves to determine pre-exponential factor for (a) peak I, (b) peak II and (c) peak III.

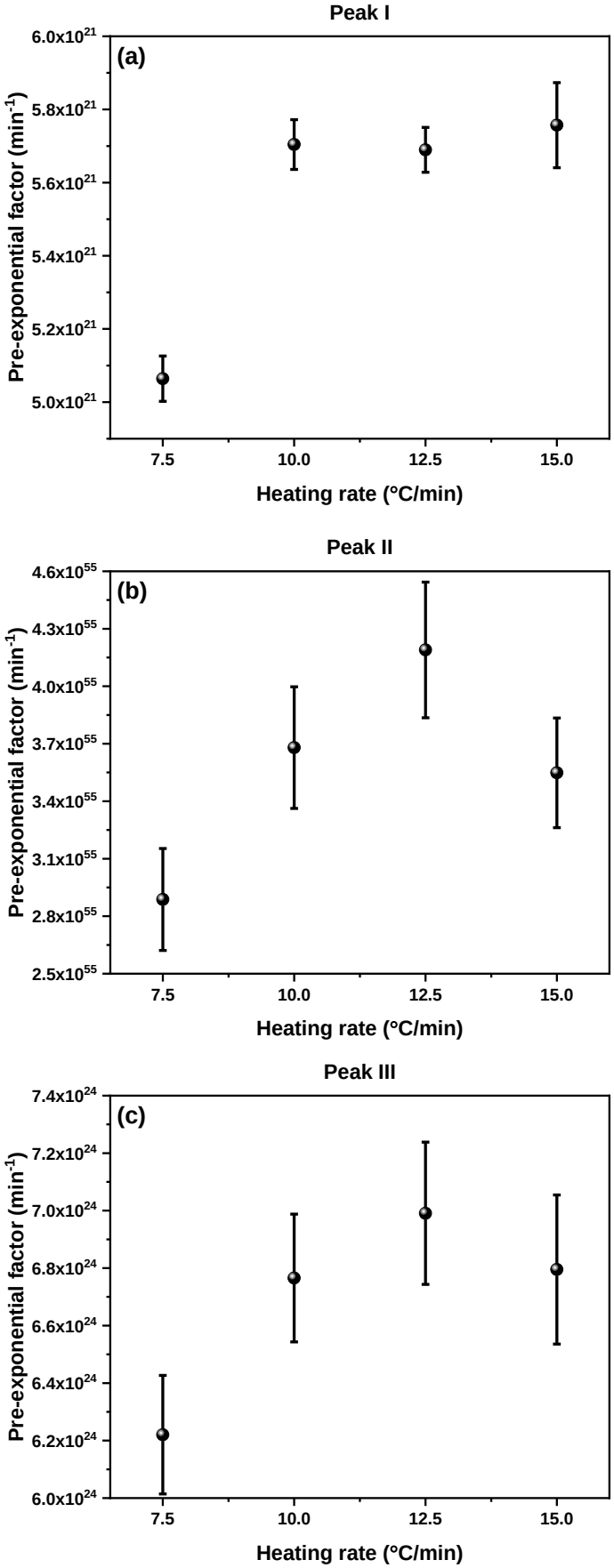

Fig. 5.23 The variation of pre-exponential w.r.t. heating rates along with the standard error for oxidation (a) peak I, (b) peak II and (c) peak III.

The comparison reveals that F2 reaction mechanism dominates the oxidation peak I and peak III. However, F3 reaction mechanism is found to be responsible for oxidation peak II. The change in the mechanism is associated with the formation of protective oxidation layer of Al_2O_3 and TiO_2. Furthermore, the third kinetic parameter, i.e., pre-exponential factor is determined by substituting the value of reaction mechanism in Eq. 3.8. Accordingly, Eq. 3.8 can be rewritten for peak I (Eq. 5.7), peak II (Eq. 5.8) and peak III (Eq. 5.7):

$$g(\alpha) = \frac{1}{(1-\alpha)} = \frac{AE}{\beta R} P(u) \tag{5.7}$$

$$g(\alpha) = \frac{1}{2(1-\alpha)} = \frac{AE}{\beta R} P(u) \tag{5.8}$$

To calculate the pre-exponential factor the average value of activation energy as calculated from KAS method for peak I, peak II and peak III is employed. Fig. 5.22 demonstrates the linear fitted curves to determine the pre-exponential factor for peak I, peak II and peak III. The trend of pre-exponential factor with change in heating rate is presented in Fig. 5.23. Finally, the kinetic triplets responsible for the oxidation of Ti_3AlC_2 in peak I, peak II and peak III are tabulated in Table 5.9.

Table 5.9 Kinetic triplets involved during oxidation of Ti_3AlC_2 MAX phase.

	Kinetic triplets			
	Average activation energy (kJ/mol)		Average pre-exponential factor (min^{-1})	Reaction mechanism
	KAS	FWO		
Peak I	335.88 ± 4.09	340.30 ± 4.10	$5.55\times10^{22} \pm 7.69\times10^{19}$	F2
Peak II	988.83 ± 38.26	967.30 ± 38.22	$3.58\times10^{55} \pm 3.06\times10^{54}$	F3
Peak III	544.22 ± 3.21	544.19 ± 3.19	$6.69\times10^{24} \pm 2.34\times10^{23}$	F2

References

[1] J.E. von Treifeldt, K.L. Firestein, J.F.S. Fernando, C. Zhang, D.P. Siriwardena, C.E.M. Lewis, D. V. Golberg, The effect of Ti_3AlC_2 MAX phase synthetic history on the structure and electrochemical properties of resultant Ti_3C_2 MXenes, Mater. Des. 199 (2021). https://doi.org/10.1016/j.matdes.2020.109403.

[2] A. Ivasyshyn, O. Ostash, T. Prikhna, V. Podhurska, T. Basyuk, Oxidation Resistance of Materials Based on Ti_3AlC_2 Nanolaminate at 600 °C in Air, Nanoscale Res. Lett. 11 (2016). https://doi.org/10.1186/s11671-016-1571-x.

[3] Z. Xia, Q. Huang, S. Guo, Recent progress on synthesis, structure and electrocatalytic applications of MXenes, FlatChem. 17 (2019). https://doi.org/10.1016/j.flatc.2019.100129.

[4] M.W. Barsoum, MAX phases: properties of machinable carbides and nitrides, 2013th ed., Wiley-VCH, Singapore, n.d.

[5] D.J. Tallman, B. Anasori, M.W. Barsoum, A critical review of the oxidation of Ti_2AlC, Ti_3AlC_2 and Cr_2AlC in Air, Mater. Res. Lett. 1 (2013) 115–125. https://doi.org/10.1080/21663831.2013.806364.

[6] X.H. Wang, Y.C. Zhou, Oxidation behavior of Ti_3AlC_2 at 1000-1400 °C in air, Corros. Sci. (2003). https://doi.org/10.1016/S0010-938X(02)00177-4.

[7] A. Hendaoui, D. Vrel, A. Amara, P. Langlois, M. Andasmas, M. Guerioune, Synthesis of high-purity polycrystalline MAX phases in Ti-Al-C system through Mechanically Activated Self-propagating High-temperature Synthesis, J. Eur. Ceram. Soc. 30 (2010) 1049–1057. https://doi.org/10.1016/j.jeurceramsoc.2009.10.001.

[8] C.L. Yeh, Y.G. Shen, Effects of Al content on formation of Ta_2AlC by self-propagating high-temperature synthesis, J. Alloys Compd. 482 (2009) 219–223. https://doi.org/10.1016/j.jallcom.2009.03.184.

[9] R. Yembadi, B.B. Panigrahi, Thermodynamic Assessments and mechanically activated synthesis of ultrafine Cr_2AlC MAX phase powders, Adv. Powder Technol. 28 (2017) 732–739. https://doi.org/10.1016/j.apt.2016.11.020.

[10] A. Khawam, D.R. Flanagan, Solid-state kinetic models: Basics and mathematical fundamentals, J. Phys. Chem. B. 110 (2006) 17315–17328. https://doi.org/10.1021/jp062746a.

[11] M. Tahir, Enhanced photocatalytic CO_2 reduction to fuels through bireforming of methane over structured 3D MAX Ti3AlC2/TiO2 heterojunction in a monolith photoreactor, J. CO2 Util. 38 (2020) 99–112. https://doi.org/10.1016/j.jcou.2020.01.009.

[12] H. Zhao, Y. Feng, Z. Zhou, G. Qian, J. Zhang, X. Zhang, High-voltage arc erosion behavior and mechanism of Ti_3AlC_2 under different ambient atmospheres, J. Eur. Ceram. Soc. (2020). https://doi.org/10.1016/j.jeurceramsoc.2020.11.041.

[13] S. Myhra, J.A.A. Crossley, M.W. Barsoum, Crystal-chemistry of the Ti_3AlC_2 and Ti_4AlN_3 layered carbide/nitride phases - characterization by XPS, J. Phys. Chem. Solids. 62 (2001) 811–817. https://doi.org/10.1016/S0022-3697(00)00268-7.

[14] M. Harju, S. Areva, J.B. Rosenholm, T. Mäntylä, Characterization of water exposed plasma sprayed oxide coating materials using XPS, Appl. Surf. Sci. 254 (2008) 5981–5989. https://doi.org/10.1016/j.apsusc.2008.03.168.

[15] J. Low, L. Zhang, T. Tong, B. Shen, J. Yu, TiO_2/MXene Ti_3C_2 composite with excellent photocatalytic CO_2 reduction activity, J. Catal. 361 (2018) 255–266. https://doi.org/10.1016/j.jcat.2018.03.009.

[16] L. Pan, J. Zhang, X. Jia, Y.H. Ma, X. Zhang, L. Wang, J.J. Zou, Highly efficient Z-scheme WO_{3-x} quantum dots/TiO_2 for photocatalytic hydrogen generation, Cuihua Xuebao/Chinese J. Catal. 38 (2017) 253–259. https://doi.org/10.1016/S1872-

2067(16)62576-7.

[17] E.I. Zamulaeva, E.A. Levashov, E.A. Skryleva, T.A. Sviridova, P. V. Kiryukhantsev-Korneev, Conditions for formation of MAX phase Cr_2AlC in electrospark coatings deposited onto titanium alloy, Surf. Coatings Technol. 298 (2016) 15–23. https://doi.org/10.1016/j.surfcoat.2016.04.058.

[18] A. Pazniak, P. Bazhin, N. Shplis, E. Kolesnikov, I. Shchetinin, A. Komissarov, J. Polcak, A. Stolin, D. Kuznetsov, $Ti_3C_2T_x$ MXene characterization produced from SHS-ground Ti_3AlC_2, Mater. Des. 183 (2019). https://doi.org/10.1016/j.matdes.2019.108143.

[19] Z. Mahmoudi, S.H. Tabaian, H.R. Rezaie, F. Mahboubi, M.J. Ghazali, Synthesis of Ti_2AlC & Ti_3AlC_2 MAX phases by Arc-PVD using Ti–Al target in C_2H_2/Ar gas mixture and subsequent annealing, Ceram. Int. 46 (2020) 4968–4975. https://doi.org/10.1016/j.ceramint.2019.10.235.

[20] R. Hauert, J. Patscheider, M. Tobler, R. Zehringer, XPS investigation of the a-C : H/Al interface, Surf. Sci. 292 (1993) 121–129. https://doi.org/10.1016/0039-6028(93)90395-Z.

[21] Z. Zhang, S. Hon, J. Chai, D. Mei, Y. Lai, A. Kok, H. Cheong, K. Leong, S. Jie, H. Jin, J. Sheng, Surface & Coatings Technology Plasma spray of Ti_2AlC MAX phase powders : Effects of process parameters on coatings ' properties, Surf. Coat. Technol. 325 (2017) 429–436. https://doi.org/10.1016/j.surfcoat.2017.07.006.

[22] M. Sokol, V. Natu, S. Kota, M.W. Barsoum, On the Chemical Diversity of the MAX Phases, Trends Chem. 1 (2019) 210–223. https://doi.org/10.1016/j.trechm.2019.02.016.

[23] P. Sharma, T. Kaur, O.P. Pandey, In-situ single step reduction and silicidation of the MoO_3 to form the $MoSi_2$, J. Am. Ceram. Soc. 102 (2019) 1522–1534. https://doi.org/10.1111/jace.15994.

[24] W.M. Guo, H.N. Xiao, G.J. Zhang, Kinetics and mechanisms of non-isothermal oxidation of graphite in air, Corros. Sci. 50 (2008) 2007–2011. https://doi.org/10.1016/j.corsci.2008.04.017.

[25] X.H. Wang, Y.C. Zhou, Oxidation behavior of Ti_3AlC_2 at 1000-1400 °C in air, Corros. Sci. 45 (2003) 891–907. https://doi.org/10.1016/S0010-938X(02)00177-4.

[26] X.H. Wang, Y.C. Zhou, Layered Machinable and Electrically Conductive Ti_2AlC and Ti_3AlC_2 Ceramics: a Review, J. Mater. Sci. Technol. 26 (2010) 385–416. https://doi.org/10.1016/S1005-0302(10)60064-3.

CHAPTER 6

SYNTHESIS & OXIDATION KINETICS OF V_2AlC MAX PHASE

Overview

Nanolaminated V_2AlC MAX phase has been synthesized through pressureless sintering. The effect of change in aluminium content (10 – 40 mol%) is investigated. The optimum sintering temperature is also identified by varying sintering temperature from 800 – 1500 ºC. It is observed that V_2AlC MAX phase is obtained at 1500 ºC, when V:Al:C = 2:1.3:1. The formation reaction pathway of V_2AlC is studied through XRD analysis. The oxidation stability of the V_2AlC is studied under non-isothermal conditions through a TGA/DTA technique at multiple heating rates in the air atmosphere. It is observed that the oxidation of V_2AlC occurred in two different stages. Thermodynamic calculations are also performed to predict the oxidation reaction pathway of V_2AlC MAX phase. The kinetic triplets (activation energy, pre-exponential factor and reaction mechanism) involved during oxidation of V_2AlC are determined for both stages of oxidation.

6.1. Introduction

V_2AlC is a ternary nano-laminated hexagonal compound that belongs to the family of MAX phases. The general formula of the family is $M_{n+1}AX_n$, where M refers to the transition metal, A is metal and X is carbon or nitrogen [1]. The MAX phases emerge as a promising candidate for a plethora of applications such as protective coatings, sensors, low friction surfaces, electrical contacts, cladding material, heat exchangers, concentrated solar power and higher temperature applications [2]. The MAX phases are also used to synthesize their 2D derivatives, i.e., MXenes [3]. The MXenes have shown tremendous potential for a wide range of applications especially in energy conversion and storage [4]. The discovery of MXenes has further boosted the interest of the scientific community in MAX phases.

MAX phases offer high resistance to oxidation that makes them suitable for many industrial applications. The oxidation behavior of Ti_2AlC, Ti_3AlC_2, Cr_2AlC and Ti_3SiC_2 MAX phases have been extensively studied [5–8]. In the MAX phase, oxygen diffuses inward but M and X elements diffuse outward. This results in the formation of a protective oxide layer that improves the oxidation behaviour of MAX phases. The aluminium-based MAX phases are proven to exhibit higher oxidation resistance due to the formation of a stable Al_2O_3 layer. In addition, self-crack healing behaviour is also observed in MAX phases [9–11]. The weakly bonded oxides formed during the oxidation reaction fills the crack. The self-crack healing behaviour is mainly associated with the near value of the thermal expansion coefficient of oxides and MAX phases. In addition, stiffness of the oxide filler with that of MAX phase helps to regain the strength of the filled crack [12].

In the present study, the effect of Al content on the synthesis of V_2AlC is investigated. The non-isothermal oxidation behaviour of the V_2AlC MAX phase is studied through Thermogravimetry Analysis (TGA) and the Differential Thermal Analysis (DTA) techniques. The thermal kinetics analysis is also performed during the oxidation of V_2AlC. The kinetic triplets such as activation energy, reaction mechanism and pre-exponential factors are determined. Moreover, thermodynamic calculations are performed to identify the reaction pathway involved during oxidation of the V_2AlC MAX phase.

6.2. Synthesis of V_2AlC MAX phase

The details related to the experiments performed are presented in the previous chapter 3. Initially, the synthesis temperature of V_2AlC MAX phase was determined. In this process, the VAC 4 sample (V:Al:C = 2:1.4:1) was sintered at 800, 1000, 1100, 1200, 1300, 1400 and 1500 °C in an argon atmosphere for 1 hour. Accordingly, the nomenclature and experimental conditions of all the prepared samples are tabulated Table 6.1.

Table 6.1 Nomenclature of all the samples prepared at different experimental conditions.

Samples ID	Molar ratio			Sintering temperature (ºC) for 1 hr	Volume Fraction (%)					
	V	C	Al		V	C	Al_3V	V_3Al_2	V_8C_7	V_2AlC
8VAC 4	2	1	1.4	800	16.04	11.23	72.73	–	–	–
10VAC 4	2	1	1.4	1000	2.32	10.32	78.25	9.11	–	–
12VAC 4	2	1	1.4	1200	–	4.22	74.53	21.25	–	–
13VAC 4	2	1	1.4	1300	–	–	–	61.62	8.23	15.24
14VAC 1	2	1	1.1	1400	–	–	–	5.23	12.34	82.43
14VAC 2	2	1	1.2	1400	–	–	–	4.96	8.04	86.98
14VAC 3	2	1	1.3	1400	–	–	–	0.83	7.85	91.32
14VAC 4	2	1	1.4	1400	–	–	–	6.93	9.31	83.77
15VAC 1	2	1	1.1	1500	–	–	–	–	6.18	93.82
15VAC 2	2	1	1.2	1500	–	–	–	–	5.45	94.55
15VAC 3	2	1	1.3	1500	–	–	–	–	4.02	95.98
15VAC 4	2	1	1.4	1500	–	–	–	–	7.64	92.36

6.2.1. XRD analysis

Fig. 6.1 presents the diffraction pattern of 8VAC 4, 10VAC 4, 12 VAC 4, 13VAC 4, 14 VAC 4 and 15 VAC 4 samples. In this case, Al metal melts and reacts with vanadium to form Al_3V compound. At 800 ºC, the peaks corresponding to Al_3V, V and C are observed.

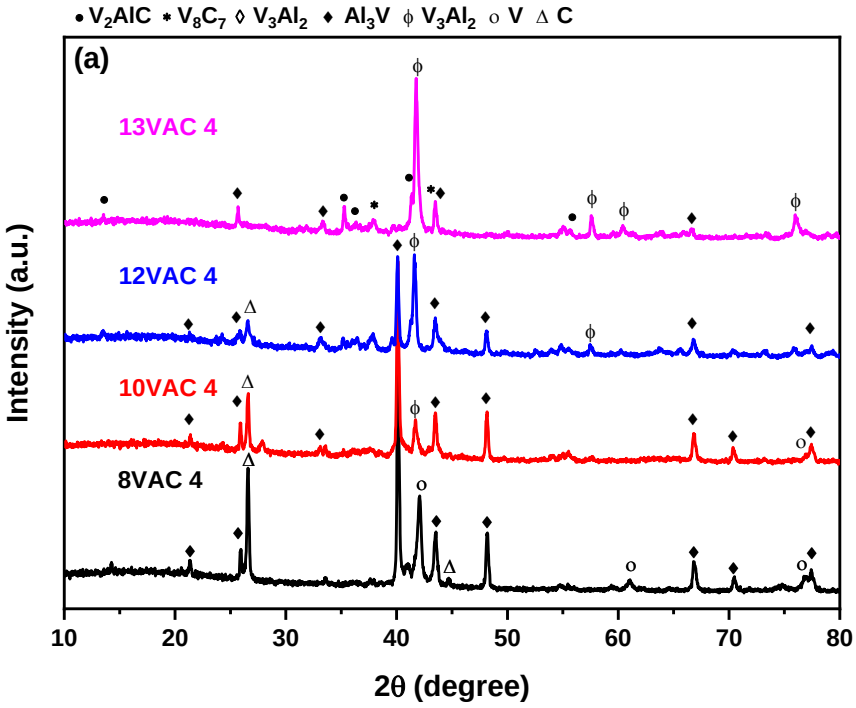

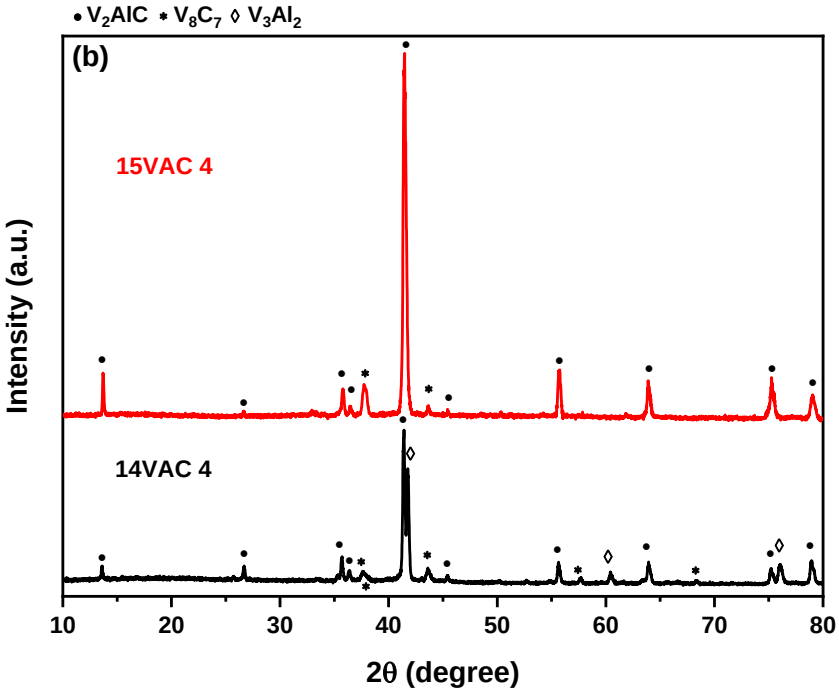

Fig. 6.1 The formation of intermediate phases at different temperatures during the synthesis of V_2AlC MAX phase.

This indicated that the formation of V_2AlC phase require higher temperature due to the presence of unreacted C and V, as observed in XRD patterns. In 10VAC 4 samples, the formation of V_3Al_2 compound is observed. Afterwards, the peaks associated with V_3Al_2 became more prominent in 12VAC 4 and 13VAC 4. A few peaks related to V_8C_7 and V_2AlC compounds are also observed. To investigate the formation of V_2AlC MAX phase temperature is further increased to 1400 ºC and 1500 ºC.

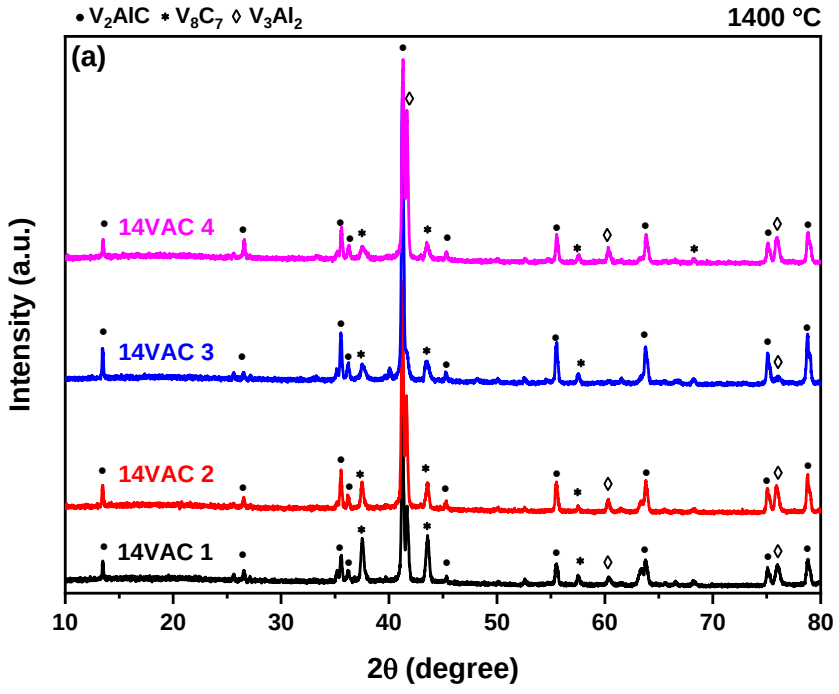

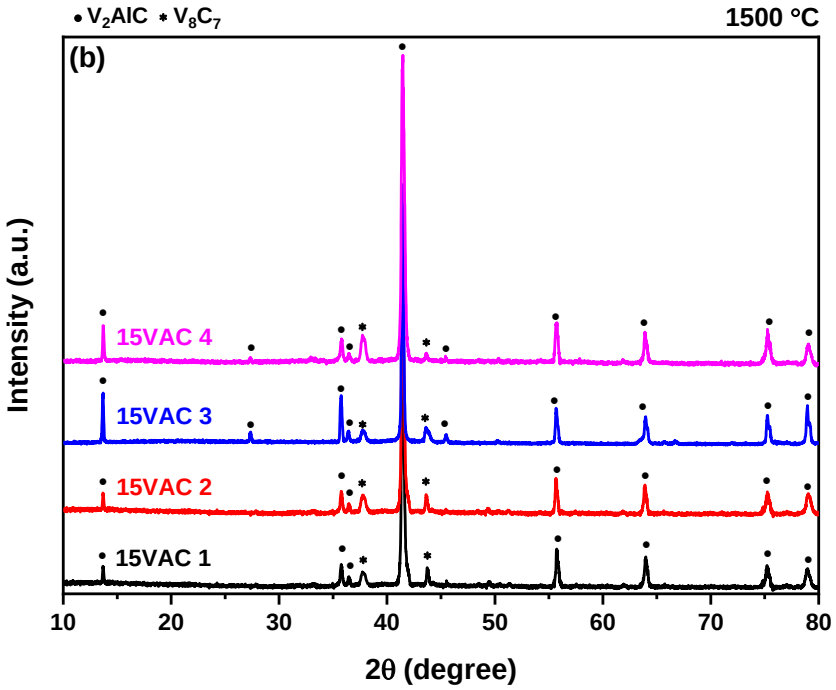

Fig. 6.2 XRD patterns of (a) 14VAC 1 – 14VAC 4 samples and (b) 15VAC 1 – 15VAC 4 samples sintered at 1400 °C and 1500 °C, respectively

At 1400 ºC, the peaks associated with V_2AlC MAX phase became more prominent. In addition, some peaks of V_8C_7 and V_3Al_2 are also observed. Further increase in temperature to 1500 ºC resulted into formation of V_2AlC phase alongwith V_8C_7 phase. The results revealed that 1400 and 1500 ºC are the suitable temperatures to obtain V_2AlC MAX phase. Therefore, effect of Al composition on the synthesis of V_2AlC at 1400 and 1500 ºC is studied. The X-ray diffractograms of samples (14VAC 1 – 14VAC 4) sintered at 1400 ºC are presented in Fig. 6.2a. The volume fraction of different phases observed is tabulated in Table 6.1. There are four phases (V_2AlC, V_8C_7, V_4Al_{23} and V_3Al_2) observed in all the samples sintered at 1400 °C. The peaks associated with V_2AlC becomes more pronounced with the increase in Al content upto 30% in 14VAC 3 sample. However, a further increase in Al content to 40% in 14 VAC 4 resulted in a decrease in the intensity of peaks associated with MAX phases. Similar results are also reported during the synthesis of other MAX phases by varying the Al content [8,13,14]. The increment in the Al content favours the formation of V_2AlC MAX phase upto some extent. However, after a certain limit excessive amount of Al content favours the formation of V-Al based alloys. This results in more residual carbon in the system that reacts to form V_8C_7 carbide. In this way, variation in Al content significantly affects the formation of MAX phase. The volume fraction of V_2AlC MAX phase is found to be maximum in 14VAC 3 sample sintered at 1400 ºC. The intermediate phases observed at 1400 ºC (Fig. 6.2a) indicated that the reaction temperature for the formation of the V_2AlC MAX phase is not sufficient. The possibilities of

reaction between intermediate phases (V_8C_7, V_4Al_{23} and V_3Al_2) could increase at a higher temperature to form the V_2AlC MAX phase. Therefore, the samples are sintered at a higher temperature (1500 °C).

Table 6.2 The lattice parameters of V_2AlC MAX phase present in prepared samples.

Temperature (°C)	Samples	Lattice Parameters of V_2AlC				R_{wp}
		a (Å)	c (Å)	χ^2	Cell Volume (Å^3)	
1400 °C	14VAC 1	2.911	12.155	1.16	97.86	17.23
	14VAC 2	2.912	13.156	1.19	97.23	18.37
	14VAC 3	2.918	13.149	1.24	97.09	19.22
	14VAC 4	2.915	13.158	1.29	96.99	17.56
1500 °C	15VAC 1	2.919	12.155	1.30	97.33	19.44
	15VAC 2	2.915	13.153	1.12	97.38	19.02
	15VAC 3	2.916	13.163	1.08	97.44	17.05
	15VAC 4	2.916	13.169	1.15	97.08	18.88

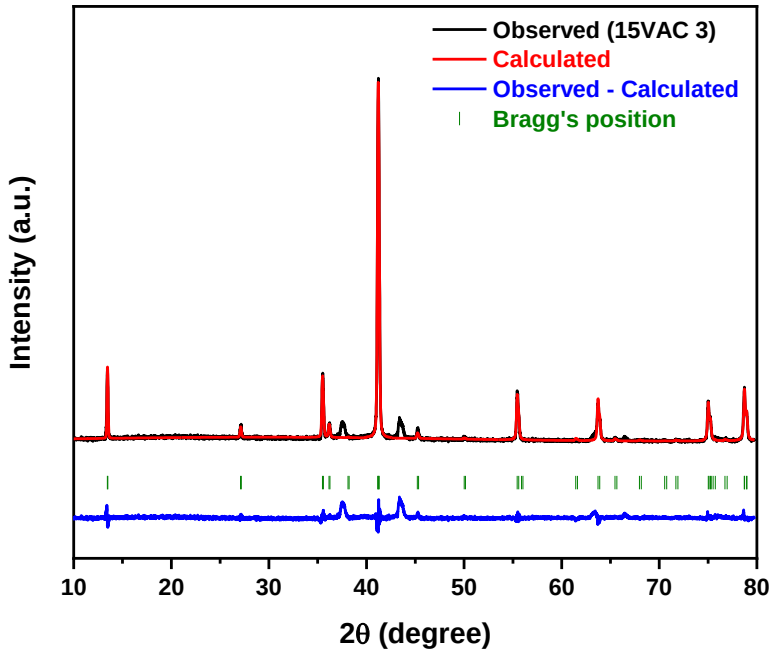

Fig. 6.3 Rietveld refinement plot of 15VAC 3 sample.

Fig. 6.2b shows the diffractograms of samples (15VAC 1 – 15VAC 4) sintered at 1500 °C. There are two phases (V_2AlC and V_8C_7) observed in all the samples. Most of the prominent peaks observed in XRD (Fig. 6.2b) are associated with the V_2AlC MAX phase in all the samples. The formation of V_2AlC is favoured with increase in the temperature. In addition, no peak(s) related to V-Al based alloys are observed in these samples. This could be ascribed to the reaction of intermediate phases to form the V_2AlC MAX phase at higher temperatures. When the Al content is 30 % in 15VAC 3, then the amount of V_2AlC phase is maximum. However, a further increase in Al content to 40 % (15VAC 4) enhanced the intensity of the

secondary phase (V_8C_7). It is observed from Table 6.1 that the 15VAC 3 samples demonstrated a maximum (94.6 %) volume fraction of V_2AlC MAX phase among all the prepared samples. Furthermore, the lattice parameters and cell volume for V_2AlC phase are also calculated through Rietveld refinements and presented in Table 6.2. Fig. 6.3 shows the Rietveld refinement of 15VAC 3 sample.

6.2.2. Synthesis kinetics of V_2AlC MAX phase

To investigate the synthesis kinetic of V_2AlC MAX phase, DTA technique is employed. VAC 3 sample is heated at multiple heating rates (5, 10, 15, 20 ºC/min) in an argon atmosphere from room temperature to 1300 ºC. Fig. 6.4 shows the DTA curve of VAC 3 sample.

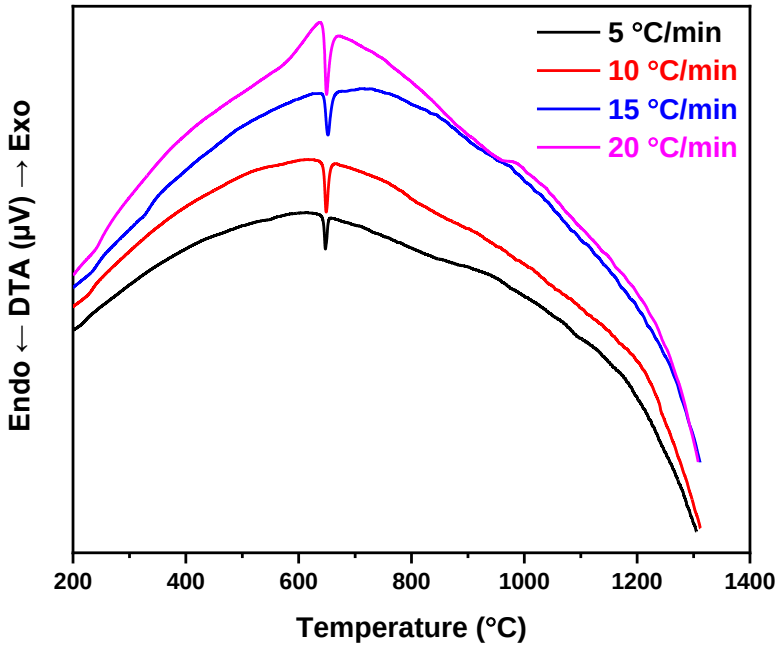

Fig. 6.4 DTA of VAC 3 sample at 5, 10, 15 and 20 ºC/min.

It is observed from the Fig. 6.4 that the formation of V_2AlC MAX phase did not show any endo or exothermic peak. There is only one endothermic peak assigned to melting of Al is observed. In comparison to Cr_2AlC and Ti_2AlC MAX phases, the synthesis kinetic analysis of V_2AlC MAX phase is not feasible. However, on the basis of XRD results the reaction pathway involved during formation of V_2AlC MAX phase is proposed. When the mixture of V, Al and C are subjected to heat treatment then Al melts (Eq. 6.1) first at around ~ 660 ºC. Afterwards, Al reacts with V (Eq. 6.2 – 6.4) to form V-Al based alloys and V_8C_7 carbide. Finally, V-Al based alloys reacts with carbon or V_8C_7 (Eq. 6.5 – 6.6) to form V_2AlC MAX phase. The reaction responsible for the formation of the product phase(s) are as follows:

$$Al_{(s)} \rightarrow Al_{(l)} \quad (6.1)$$

$$V + 3Al \rightarrow Al_3V \quad (6.2)$$

$$3V + 2Al \rightarrow V_3Al_2 \quad (6.3)$$

$$8V + 7C \rightarrow V_8C_7 \quad (6.4)$$

$$9Al_3V + 7V_8C_7 + 11V_3Al_2 \rightarrow 49V_2AlC \quad (6.5)$$

$$8V_3Al_2 + V_8C_7 + 9C \rightarrow 16V_2AlC \quad (6.6)$$

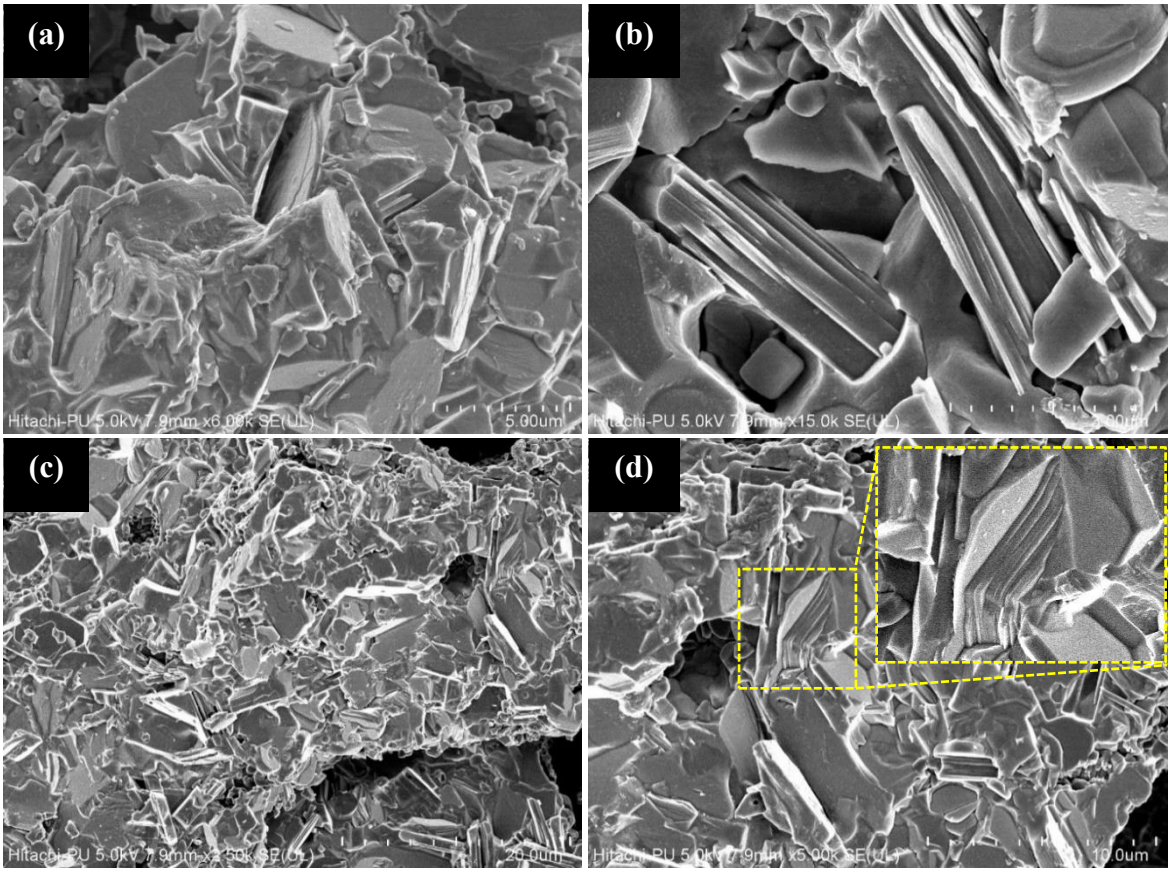

Fig. 6.5 The FE-SEM micrographs of fractured (a-b) 14VAC 3 and (c-d) 15VAC 3 samples.

6.2.3. Microstructure Analysis

The morphology of the fractured 15VAC 2 and 15VAC 3 samples sintered at 1500 ºC are presented in Fig. 6.5. These FE-SEM images demonstrated the typical layered structure of the MAX phases in both the samples. Fig. 6.5a-b presents the formation of a nanolaminated structure, where the layers of V_2AlC are bound in 15VAC 2 sample. The nanolaminated layers are found to be delaminated and formation kink bands are also observed. Moreover, the thickness of these nanolaminated layers is non-uniform as observed from Fig. 6.5b. The stacking of V_2AlC MAX phase layers (Fig. 6.5c-d) is more pronounced when the Al content is 30 % in 15VAC 3 sample. The reason behind improved stacking (inset of Fig. 6.3d) is ascribed to the lower content of the secondary phase in 15VAC 3 sample.

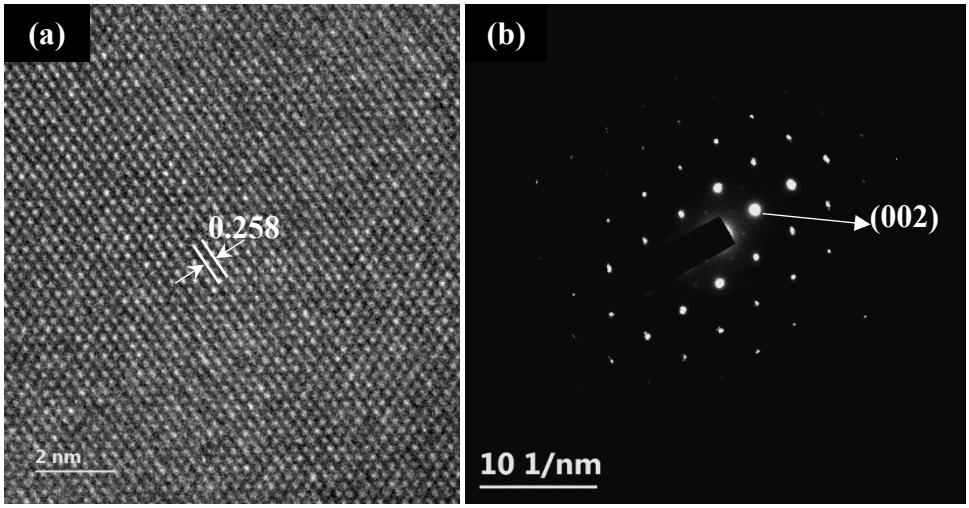

Fig. 6.6 The HRTEM (a) and SAED (b) image of 15VAC 3 sample.

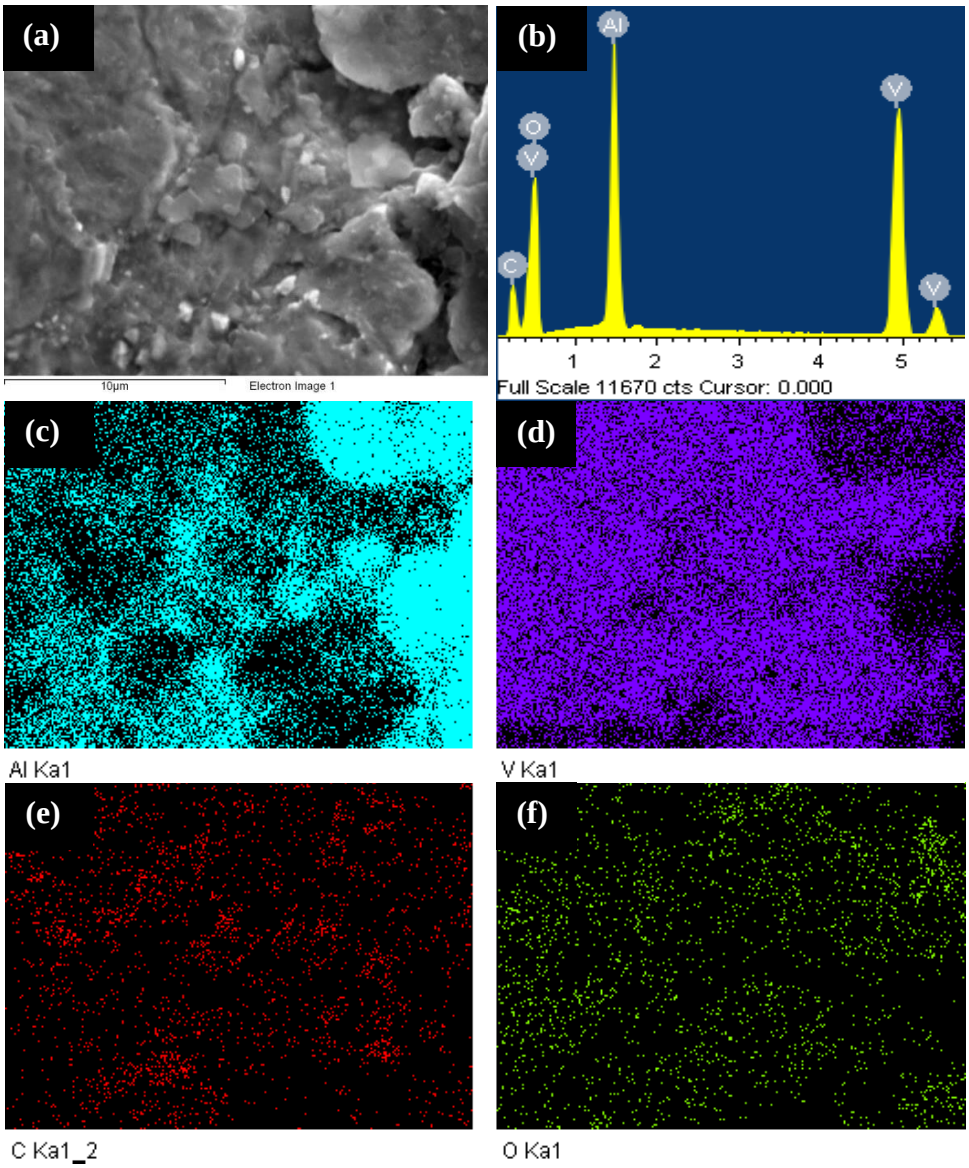

Fig. 6.7 (a) SEM image and (b) elemental composition 15VAC 3 sample. The distribution of (c) Al, (d) V, (e) C and (f) O in 15VAC 3 sample.

HR-TEM (High-Resolution Transmission Electron Microscopy) and SAED (Selected Area Electron Diffraction) image of a 15VAC 3 sample is presented in Fig. 6.6. The figure demonstrated characteristic features of MAX phase. The lattice fringes corresponding to the (100) plane is observed in Fig. 6.6a. The SAED pattern (Fig. 6.6b) also confirmed the formation of the hexagonal V_2AlC MAX phase. Further, the distribution of vanadium (V), aluminum (Al), and carbon (C) in a 15VAC 3 sample (sintered at 1500 ºC) are identified through the EDS mapping (Fig. 6.7). It is observed that all the elements are homogeneously distributed in a 15VAC 3 sample.

6.2.4. X-ray photoelectron spectroscopy (XPS) analysis

Fig. 6.8 presents high-resolution XPS spectra of V2p, C1s, Al2p and O1s of 15VAC 3 sample. The solid circles represent original measured data and solid lines correspond to the fitted curves using the Shirley deconvolution method. There are three peaks observed in V2p XPS spectra (Fig. 6.8a) that corresponds to 2p3/2 and 2p1/2 spin orbitals. These peaks are further deconvoluted into four peaks, i.e., 524.79, 523.21, 517.08 and 513.46 eV.

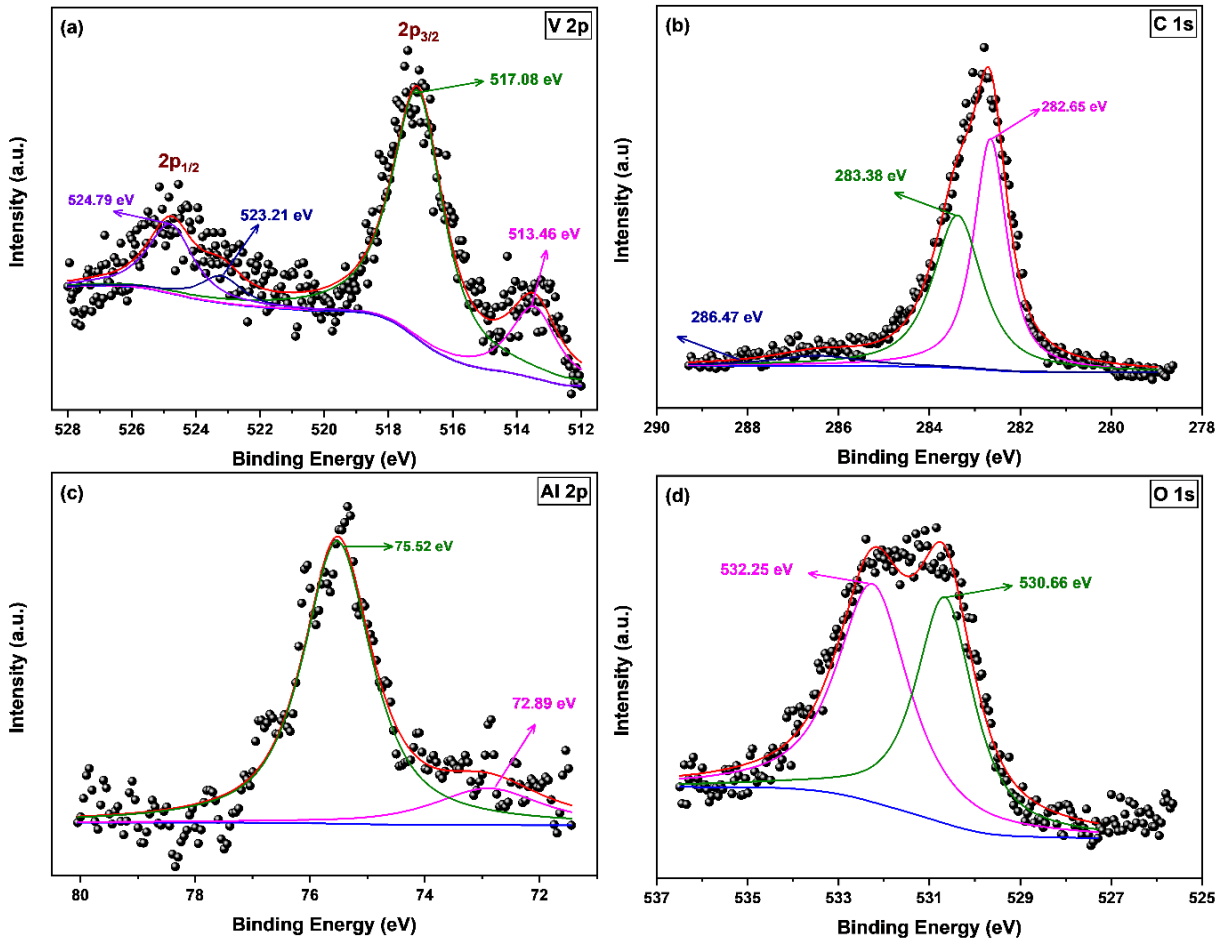

Fig. 6.8 The typical (a) V2p, (b) C1s, (c) Al2p and (d) O1s XPS spectra of 15VAC 3 sample.

The peaks at 532.21 and 513.46 eV are associated with the V-C bond with oxidation state V^{2+}. Whereas, the peaks at 527.79 and 517.08 eV correspond to V-O bond with V^{4+} oxidation state [15]. Fig. 6.8b shows three peaks (286.47, 283.38 and 282.65 eV) in C1s XPS spectra of 15VAC 3 sample. The first peak is related to the C-O bonds, while the other two are associated with the C-C (283.38 eV) and C-V (282.65 eV) bonds [16,17]. Basically, the peak at 283.38 eV arises due to the free carbon adsorbed on the surface of the MAX phase. In the XPS spectra of Al2p, two peaks (75.52 and 72.89 eV) are related to Al-O and Al-C/Al-Al bonds, respectively [15]. In addition, O1s spectra also demonstrated two peaks at 532.25 and 530.66 eV in 15VAC 3 samples. The former peak is ascribed to Al-O bonding. The later peak is associated with V-O bonding [18]. The XPS results revealed the formation of the V_2AlC MAX phase.

6.2.5. Oxidation kinetics of V_2AlC

MAX phases are promising industrial material due to their high oxidation resistance. In comparison to other MAX phases, few studies are conducted to investigate the oxidation behaviour of V_2AlC MAX phase. Kulkarni and co-workers [19] studied the thermal stability of V_2AlC in an inert atmosphere. They confirmed that V_2AlC MAX phase remains stable in an inert atmosphere upto 950 °C. Baben et al. [20] studied the oxidation of V_2AlC thin film and reported that the oxygen replaces carbon in V_2AlC that resulted in the formation of oxides. The oxidation behaviour of bulk V_2AlC was also investigated by Gupta and Barsoum [21] through isothermal TGA (Thermogravimetry Analysis) experiments. In 2017, Wang et al. [22] studied the non-isothermal oxidation behaviour of V_2AlC prepared through the molten salt method. However, thermal kinetics involved during non-isothermal oxidation behaviour of bulk V_2AlC MAX phase is scarce in the literature. To gain more insight, it is critically important to conduct comprehensive non-isothermal oxidation studies on the bulk V_2AlC MAX phase.

The TGA/DTA curves of 15VAC 3 sample in the temperature range from 300 °C to 800 °C at heating rate7.5 °C/min are presented in Fig. 6.9. It is observed that mass (%) remains nearly constant till 450 °C. Afterward, a mass gain of ~ 60 % is observed in two stages. Similar mass gain is also observed by Wang and co-workers [22] during oxidation of V_2AlC MAX phase. In addition, two sharp exothermic peaks in the DTA curve (Fig 6.9) are also observed at ~ 629 °C and ~ 666 °C. These exothermic peaks are associated with the oxidation of V_2AlC MAX phase. Gupta and Barsoum [21] proposed that the isothermal oxidation of the V_2AlC MAX phase occurred by the following reaction:

$$2V_2AlC + (4.25 - 1.25x - 0.75y + 0.5z)O_2$$
$$\rightarrow 0.5(1 - x + y)V_2O_5 + (1 - y)VAlO_4 + V_xAl_yO_z + CO_2 \quad (6.7)$$

Later, Wang and co-workers [22] did non-isothermal oxidation of V_2AlC and confirmed the formation of V_2O_5. According to them, the oxidation of V_2AlC might have occurred leading to formation of V_2O_5 with the help of the following reaction:

$$2V_2AlC + 8.5O_2 \rightarrow 2V_2O_5 + 1Al_2O_3 + 2CO_2 \quad (6.8)$$

The results of the above studies are contradictory. Hence, thermodynamic calculations and oxidation kinetic analysis are performed to identify the exact oxidation pathway.

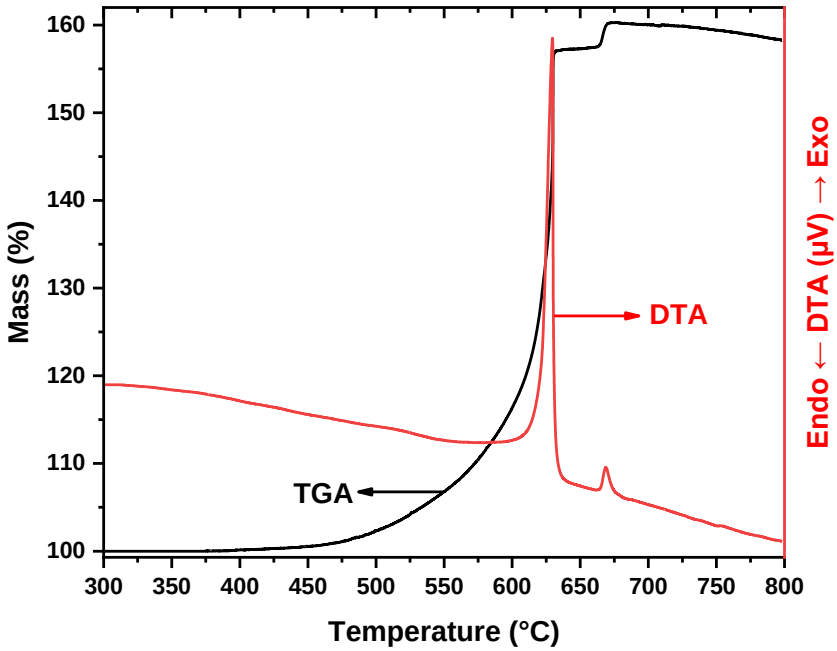

Fig. 6.9 TGA/DTA of 15VAC 3 sample at 7.5 °C/min.

Fig. 6.10 shows the XRD patterns to confirm the formation of phases at 500 °C, 650 °C and 800 °C. The peaks related of V_2AlC MAX phase dominated the XRD pattern of 15VAC 3 sample heated at 500 °C. An increase in temperature to 650 °C, resulted in the oxidation of V_2AlC phase. The peaks associated with V_2AlC, V_2O_5, VO_2, Al_2O_3 and V_8C_7 are observed at 650 °C. It is observed that the prominent peaks are related to V_2AlC followed by V_2O_5, Al_2O_3, VO_2 and V_8C_7. The presence of peaks corresponding to V_2AlC phase indicated that complete oxidation is not achieved. At 800 °C, most of the XRD peaks correspond to V_2O_5. The observed mass gain might correspond to the formation of various vanadium-based oxides or carbides and alumina. It might be possible that the formation of carbides occurred first and then oxidized to form different vanadium-based oxides.

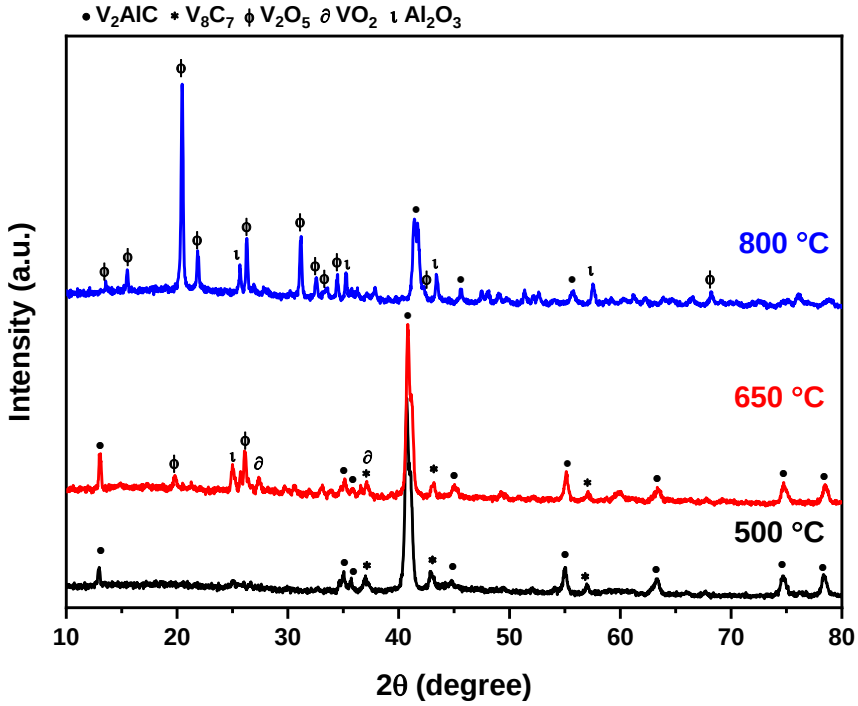

Fig. 6.10 XRD patterns of 15VAC 3 sample oxidized at 500 °C, 650 °C and 800 °C.

The probable reactions involved during oxidation of V_2AlC MAX phase are listed in Table 6.3. The value of Gibb's free energy is calculated and the initial parameters required for calculations are presented in Table 6.4 [23–25]. The reaction with the least value of Gibb's free energy is considered to be favourable. To calculate the Gibb's free energy from given heat capacity (C_p) equation (Table 6.4) following empirical expressions are used:

$$\Delta G = \Delta H - T\Delta S \tag{6.9}$$

$$\Delta H_T = \Delta H_{298} + \int_{298}^{T} C_p^o \, dT \tag{6.10}$$

$$\int_{298}^{T} C_p \, dT = a[T - 298] + b.[0.5.10^{-3}.(T^2 - 298^2)] + c.[10^6(298^{-1} - T^{-1})] + d.\left[\frac{1}{3}.10^{-6}(T^3 - 298^3)\right] \tag{6.11}$$

$$S_T = S_{298} + \int_{298}^{T} C_p \frac{dT}{T} \tag{6.12}$$

$$\int_{298}^{T} C_p \frac{dT}{T} = a.\ln\left(\frac{T}{298}\right) + b.[10^{-3}.(T - 298)] - c.0.5.[10^6(T^{-2} - 298^{-2})] + d.\left[\frac{1}{2}.10^{-6}(T^2 - 298^2)\right] \tag{6.13}$$

Table 6.3 List of possible reactions involved during oxidation of V_2AlC MAX phase.

R1	$4V_2AlC + 11O_2 \rightarrow 8VO + 2Al_2O_3 + 4CO_2$
R2	$4V_2AlC + 15O_2 \rightarrow 8VO_2 + 2Al_2O_3 + 4CO_2$
R3	$4V_2AlC + 13O_2 \rightarrow 4V_2O_3 + 2Al_2O_3 + 4CO_2$
R4	$4V_2AlC + 17O_2 \rightarrow 4V_2O_5 + 2Al_2O_3 + 4CO_2$
R5	$12V_2AlC + 41O_2 \rightarrow 8V_3O_5 + 6Al_2O_3 + 12CO_2$
R6	$2V_2AlC + 7O_2 \rightarrow V_4O_7 + Al_2O_3 + 2CO_2$
R7	$28V_2AlC + 33O_2 \rightarrow 4V_8C_7 + 14Al_2O_3 + 24VO$
R8	$28V_2AlC + 45O_2 \rightarrow 4V_8C_7 + 14Al_2O_3 + 24VO_2$
R9	$28V_2AlC + 39O_2 \rightarrow 4V_8C_7 + 14Al_2O_3 + 12V_2O_3$
R10	$28V_2AlC + 51O_2 \rightarrow 4V_8C_7 + 14Al_2O_3 + 12V_2O_5$
R11	$28V_2AlC + 41O_2 \rightarrow 4V_8C_7 + 14Al_2O_3 + 8V_3O_5$
R12	$14V_2AlC + 21O_2 \rightarrow 2V_8C_7 + 7Al_2O_3 + 3V_4O_7$
R13	$4V_2AlC + 3O_2 \rightarrow 4V_2C + 2Al_2O_3$
R14	$4V_2AlC + 5.68O_2 \rightarrow 4VC_{0.83} + 2Al_2O_3 + 4VO + 0.68CO_2$
R15	$4V_2AlC + 7.68O_2 \rightarrow 4VC_{0.83} + 2Al_2O_3 + 4VO_2 + 0.68CO_2$
R16	$2V_2AlC + 3.34O_2 \rightarrow 2VC_{0.83} + Al_2O_3 + V_2O_3 + 0.34CO_2$
R17	$2V_2AlC + 4.34O_2 \rightarrow 2VC_{0.83} + Al_2O_3 + V_2O_5 + 0.34CO_2$
R18	$12V_2AlC + 21.04O_2 \rightarrow 12VC_{0.83} + 6Al_2O_3 + 4V_3O_5 + 2.04CO_2$
R19	$8V_2AlC + 14.36O_2 \rightarrow 8VC_{0.83} + 4Al_2O_3 + 2V_4O_7 + 1.36CO_2$
R20	$4V_2AlC + 5.68O_2 \rightarrow 4VC_{0.87} + 2Al_2O_3 + 4VO + 0.68CO_2$
R21	$4V_2AlC + 7.68O_2 \rightarrow 4VC_{0.87} + 2Al_2O_3 + 4VO_2 + 0.68CO_2$
R22	$2V_2AlC + 3.34O_2 \rightarrow 2VC_{0.87} + Al_2O_3 + V_2O_3 + 0.34CO_2$
R23	$2V_2AlC + 4.34O_2 \rightarrow 2VC_{0.87} + Al_2O_3 + V_2O_5 + 0.34CO_2$
R24	$12V_2AlC + 21.04O_2 \rightarrow 12VC_{0.87} + 6Al_2O_3 + 4V_3O_5 + 2.04CO_2$
R25	$8V_2AlC + 14.36O_2 \rightarrow 8VC_{0.87} + 4Al_2O_3 + 2V_4O_7 + 1.36CO_2$
R26	$4V_2AlC + 5.68O_2 \rightarrow 4VC_{0.88} + 2Al_2O_3 + 4VO + 0.68CO_2$
R27	$4V_2AlC + 7.68O_2 \rightarrow 4VC_{0.88} + 2Al_2O_3 + 4VO_2 + 0.68CO_2$
R28	$2V_2AlC + 3.34O_2 \rightarrow 2VC_{0.88} + Al_2O_3 + V_2O_3 + 0.34CO_2$
R29	$2V_2AlC + 4.34O_2 \rightarrow 2VC_{0.88} + Al_2O_3 + V_2O_5 + 0.34CO_2$
R30	$12V_2AlC + 21.04O_2 \rightarrow 12VC_{0.88} + 6Al_2O_3 + 4V_3O_5 + 2.04CO_2$
R31	$8V_2AlC + 14.36O_2 \rightarrow 8VC_{0.88} + 4Al_2O_3 + 2V_4O_7 + 1.36CO_2$
R32	$4V_2AlC + 5.68O_2 \rightarrow 4VC_{0.61} + 2Al_2O_3 + 4VO + 0.68CO_2$
R33	$4V_2AlC + 7.68O_2 \rightarrow 4VC_{0.61} + 2Al_2O_3 + 4VO_2 + 0.68CO_2$
R34	$2V_2AlC + 3.34O_2 \rightarrow 2VC_{0.61} + Al_2O_3 + V_2O_3 + 0.34CO_2$
R35	$2V_2AlC + 4.34O_2 \rightarrow 2VC_{0.61} + Al_2O_3 + V_2O_5 + 0.34CO_2$
R36	$12V_2AlC + 21.04O_2 \rightarrow 12VC_{0.61} + 6Al_2O_3 + 4V_3O_5 + 2.04CO_2$
R37	$8V_2AlC + 14.36O_2 \rightarrow 8VC_{0.61} + 4Al_2O_3 + 2V_4O_7 + 1.36CO_2$
R38	$12V_2AlC + 13O_2 \rightarrow 4V_4C_3 + 6Al_2O_3 + 8VO$
R39	$12V_2AlC + 17O_2 \rightarrow 4V_4C_3 + 6Al_2O_3 + 8VO_2$
R40	$12V_2AlC + 15O_2 \rightarrow 4V_4C_3 + 6Al_2O_3 + 4V_2O_3$
R41	$12V_2AlC + 19O_2 \rightarrow 4V_4C_3 + 6Al_2O_3 + 4V_2O_5$
R42	$36V_2AlC + 47O_2 \rightarrow 12V_4C_3 + 18Al_2O_3 + 8V_3O_5$
R43	$6V_2AlC + 8O_2 \rightarrow 2V_4C_3 + 3Al_2O_3 + V_4O_7$
R44	$V_8C_7 + 11O_2 \rightarrow 8VO + 7CO_2$
R45	$V_8C_7 + 15O_2 \rightarrow 8VO_2 + 7CO_2$
R46	$V_8C_7 + 13O_2 \rightarrow 4V_2O_3 + 7CO_2$
R47	$V_8C_7 + 17O_2 \rightarrow 4V_2O_5 + 7CO_2$
R48	$3V_8C_7 + 41O_2 \rightarrow 8V_3O_5 + 21CO_2$
R49	$V_8C_7 + 14O_2 \rightarrow 2V_4O_7 + 7CO_2$
R50	$V_2C + 2O_2 \rightarrow 2VO + CO_2$
R51	$V_2C + 3O_2 \rightarrow 2VO_2 + CO_2$
R52	$2V_2C + 5O_2 \rightarrow 2V_2O_3 + 2CO_2$
R53	$2V_2C + 7O_2 \rightarrow 2V_2O_5 + 2CO_2$
R54	$3V_2C + 8O_2 \rightarrow 2V_3O_5 + 3CO_2$
R55	$4V_2C + 11O_2 \rightarrow 2V_4O_7 + 4CO_2$
R56	$2VO + O_2 \rightarrow 2VO_2$
R57	$4VO + O_2 \rightarrow 2V_2O_3$
R58	$4VO + O_2 \rightarrow 2V_2O_5$
R59	$3VO + O_2 \rightarrow V_3O_5$
R60	$8VO + 3O_2 \rightarrow 2V_4O_7$
R61	$4VO_2 + O_2 \rightarrow 2V_2O_5$
R62	$2V_2O_3 + O_2 \rightarrow 4VO_2$
R63	$V_2O_3 + O_2 \rightarrow 2V_2O_5$
R64	$6V_2O_3 + O_2 \rightarrow 4V_3O_5$
R65	$4V_2O_3 + O_2 \rightarrow 2V_4O_7$
R66	$2V_3O_5 + O_2 \rightarrow 6VO_2$
R67	$4V_3O_5 + 5O_2 \rightarrow 6V_2O_5$
R68	$8V_3O_5 + O_2 \rightarrow 6V_4O_7$
R69	$2V_4O_7 + O_2 \rightarrow 8VO_2$
R70	$2V_4O_7 + 3O_2 \rightarrow 4V_2O_5$

Table 6.4 Initial parameters required to calculate the Gibb's free energy.

Phases	ΔG (kJ/mol)	$\Delta G = f_o + f_1 T + f_2 T^2 + f_4 T ln(T)$ (kJ/mol)					$C_p = a + b10^{-3}T + c10^{6}T^{-2} + d10^{-6}T^{2}$ (J/mol K)			ΔH_{298} (kJ/mol)	ΔS_{298} (J/mol)	Temperature Range (K)	References
		f_o	$f_1.10^3$	$f_2.10^6$	f_3	$f_4.10^3$	a	b	c				
V_2AlC	$-192500 + 28.4.T$	–	–	–	–	–	–	–	–	–	–	298 – 1400	[28]
V_4C_3	$-271005 + 20.5.T$	–	–	–	–	–	–	–	–	–	–	300 – 1400	[28]
$VC_{0.61}$	$-80502 + 0.04.T$	–	–	–	–	–	–	–	–	–	–	300 – 1400	[28]
$VC_{0.88}$	$-101830 + 5.6.T$	–	–	–	–	–	–	–	–	–	–	298 – 1400	[28]
V_2C	–	-180.96	513.67	-1.70	1290	-83.12	–	–	–	–	–	298 – 1600	[29]
$VC_{0.83}$	–	-437.49	-86.23	11.75	932	18.29	–	–	–	–	–	298 – 2000	[29]
$VC_{0.87}$	–	211.36	267.21	0	0	-42.27	–	–	–	–	–	298 – 2000	[29]
V_8C_7	–	-123.89	274.13	-1.56	608	-43.46	–	–	–	–	–	298 – 1400	[29]
VO	–	–	–	–	–	–	50.21	11.84	-1.35	-431.8	39	298 – 1973	[30]
$VO_2(\alpha)$	–	–	–	–	–	–	73.01	2.43	-1.5	-713.8	47.1	298 – 341	[30]
$VO_2(\beta)$	–	–	–	–	–	–	74.68	7.11	-1.65	-707	67.5	341 – 1818	[30]
V_2O_3	–	–	–	–	–	–	112.97	19.29	-1.5	-1218.8	98.1	298 – 2000	[30]
V_2O_5	–	–	–	–	–	–	141	42.86	-2.34	-1550.2	130.5	298 – 952	[30]
V_3O_5	–	–	–	–	–	–	176.46	34.78	-2.46	-1933	163	298 – 1000	[30]
V_4O_7	–	–	–	–	–	–	239.95	50.27	-3.42	-2640	218	298 – 1000	[30]
Al_2O_3	–	–	–	–	–	–	117.49	10.38	-3.71	-1675.7	51	298 – 2000	[30]
CO_2	–	–	–	–	–	–	51.13	4.37	-1.47	-393.5	213.8	298 – 3000	[30]

Here, ΔG, ΔH and ΔS are the Gibb's free energy, change in enthalpy and change in entropy, respectively. ΔH_{298} and S_{298} are enthalpy and entropy at 298 K. C_p, ΔH_T and S_T are the specific heat, change in enthalpy and change in entropy at absolute temperature T (K). a, b, c and d are the thermodynamic parameters.

In the scheme II, V_2AlC could react with oxygen to form vanadium carbides (V_2C, V_8C_7, V_4C_3, $VC_{0.61}$, $VC_{0.83}$, $VC_{0.87}$, $VC_{0.88}$), different vanadium oxides (VO, VO_2, V_2O_3, V_2O_5, V_3O_5 and V_4O_7) and alumina (Al_2O_3). Accordingly, there are 37 probable reactions (R7 – R43) as listed in Table 6.3.

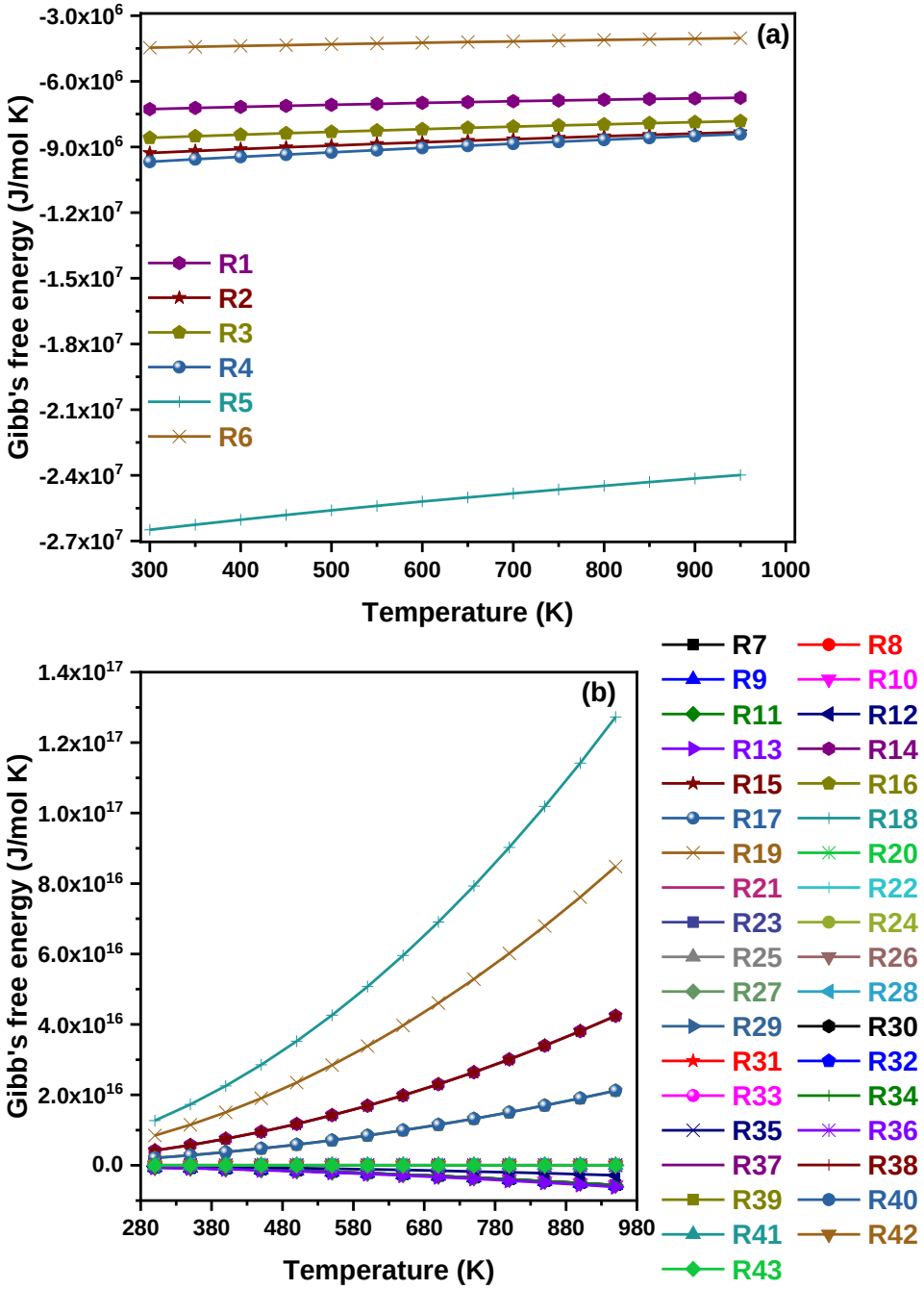

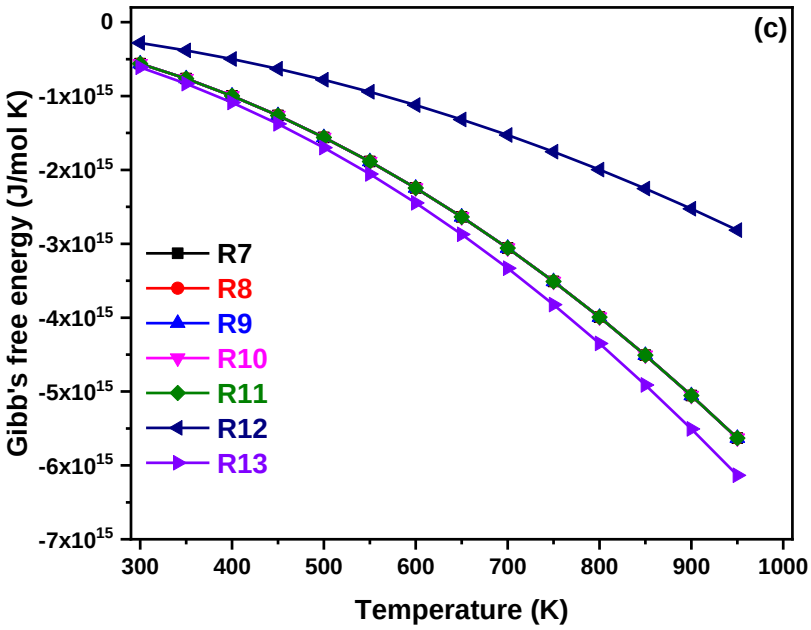

Fig. 6.11 The variation of the Gibb's free energy w.r.t. temperature for reactions (a) R1 – R6, (b) R7 – R43 and (c) R7 – R13.

The variation of the Gibb's free energy for all probable reactions are shown in Fig. 6.11b. The suitable reactions among R7 – R43 are presented in Fig. 6.11c. The figure clearly indicated that the R13 reaction is most favorable among all the reactions. In addition, R7 – R11 reactions are second most favorable reactions. The results indicated that V_2AlC MAX phase could oxidize to form different vanadium-based oxides and alumina alongwith V_2C or V_8C_7.

Furthermore, V_2C or V_8C_7 phases could oxidize to from various vanadium oxides and carbon dioxide by following reactions R44 – R55. Fig. 6.12a shows the variation of Gibb's free energy for the reactions that might be responsible for the oxidation of V_2C or V_8C_7. It is observed that reactions related to the formation of VO, VO_2, V_2O_3, V_2O_5 and V_4O_7 are more favorable during oxidation of V_8C_7. However, the formation of VO and VO_2 is found to be favorable during oxidation of V_2C. Among these vanadium-based oxides, V_2O_5 is the most stable. There are 15 probable reactions (R56 – R70) that could be responsible for the formation of V_2O_5 from other vanadium oxides (VO, VO_2, V_2O_3, and V_4O_7). Fig. 6.12b shows the variation of Gibb's free energy for reactions R56 – R70. It is observed from the figure that vanadium-based oxides such as VO, VO_2, V_2O_3 and V_3O_5 could react with oxygen to form V_4O_7. Later, V_4O_7 converts to more stable vanadium oxide, i.e., V_2O_5. Accordingly, the oxidation reaction pathway of V_2AlC MAX phase is predicted via thermodynamic calculations and presented in Fig. 6.13.

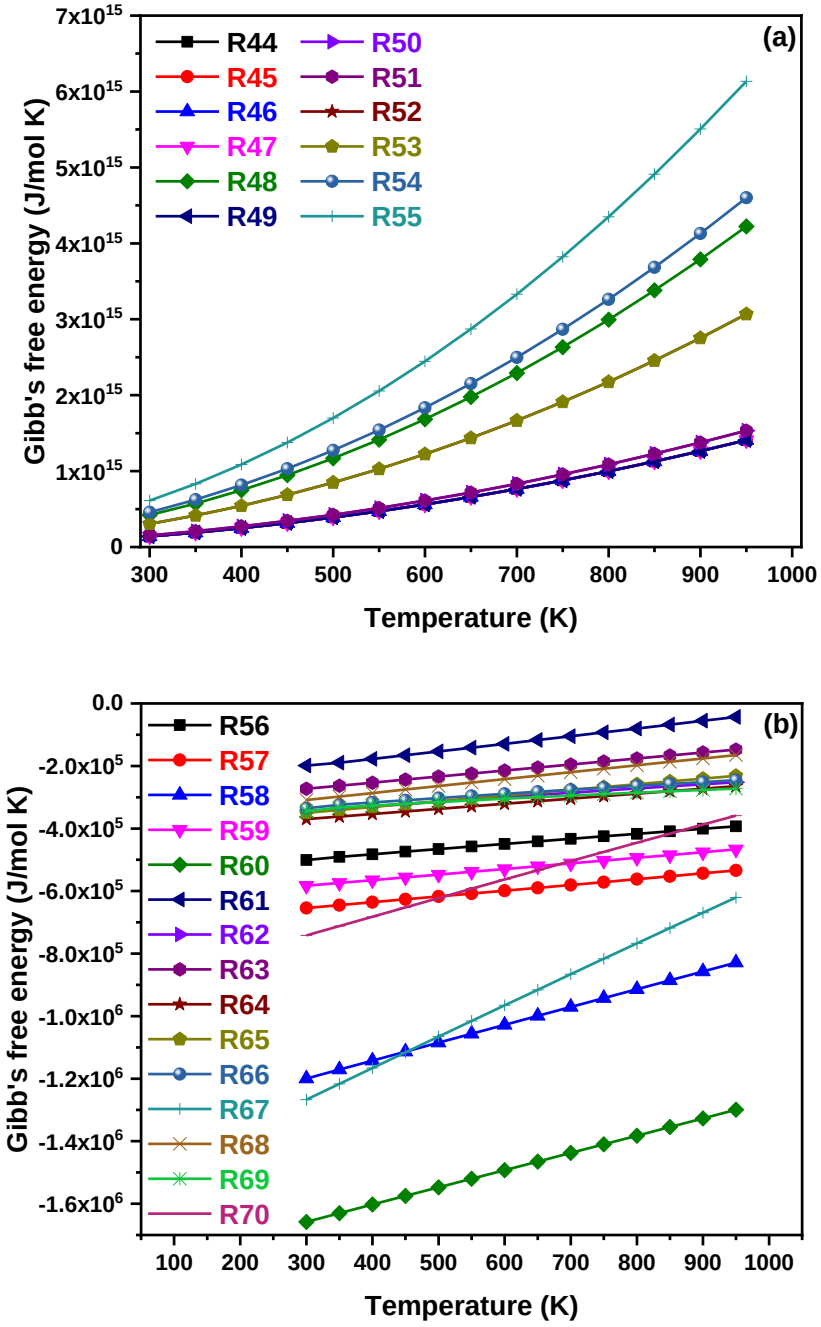

Fig. 6.12 The variation of the Gibb's free energy w.r.t. temperature for reactions (a) R44 – R55 and (b) R56 – R70.

To gain further knowledge about the oxidation behavior of V_2AlC MAX phase, multi-stage kinetic analysis is done upto 800 °C. The multi-stage kinetic analysis enables to evaluate kinetic parameters (activation energy, pre-exponential factor, and reaction mechanism) responsible for oxidation of V_2AlC MAX phase. The background of the kinetic analysis is published elsewhere [26–28]. To perform kinetic analysis effectively, DTA curves (Fig. 6.14a) are obtained at various heating rates (7.5, 10, 12.5 and 15 °C/min).

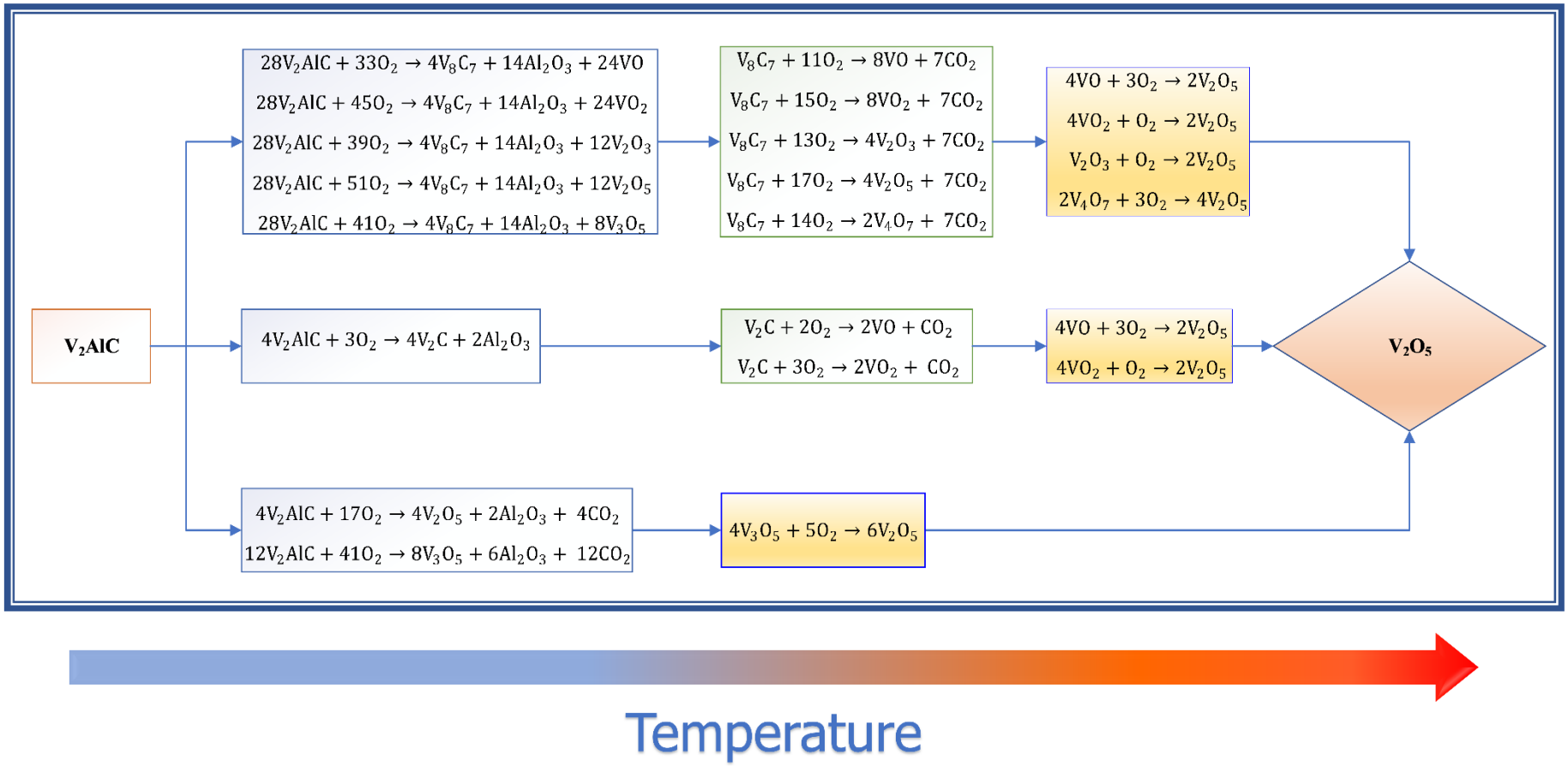

Fig. 6.13 The oxidation reaction pathway of V_2AlC MAX phase predicted via thermodynamic calculations.

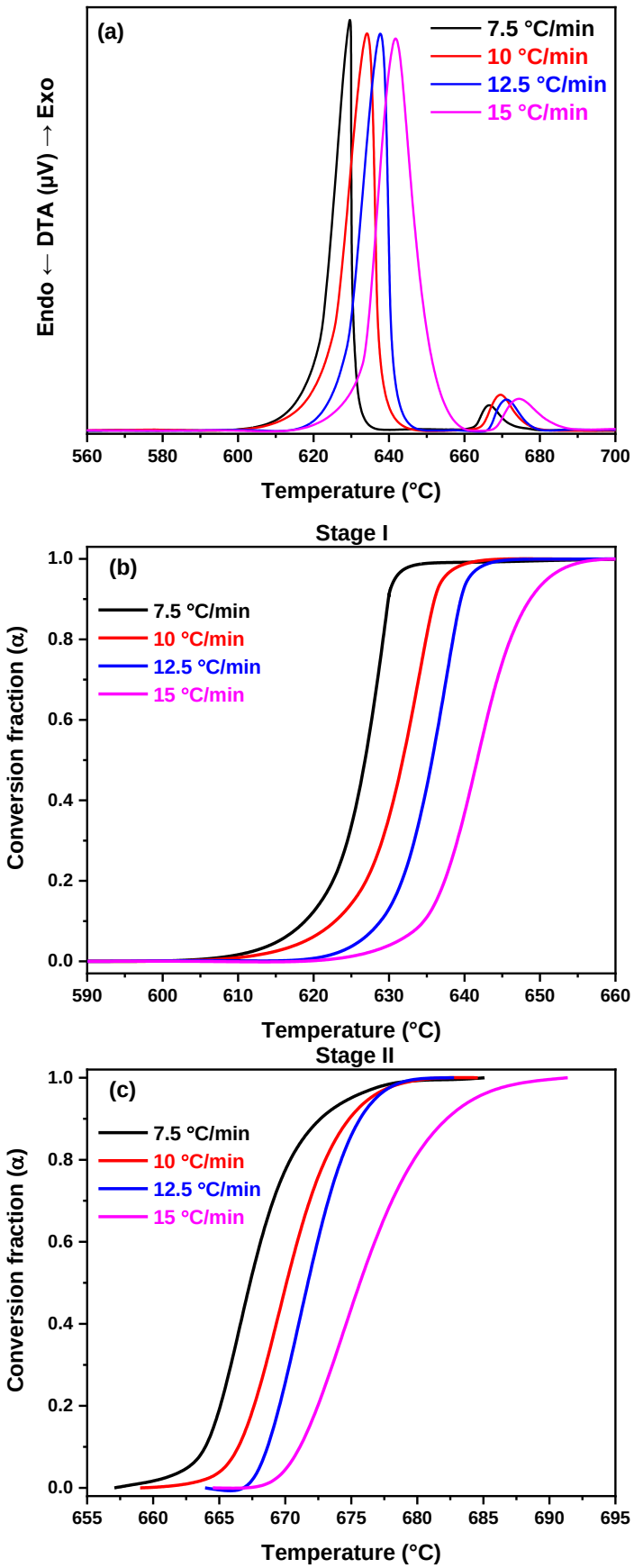

Fig. 6.14 (a) DTA of 15VAC 3 sample at 7.5, 10, 12.5 and 15 K/min. The variation of conversion fraction (α) w.r.t. temperature for (b) stage I and (c) stage II.

The exothermic peaks observed at all heating rates shifted towards higher temperatures with increased heating rate. The variation in conversion fraction w.r.t. temperature for both stages of oxidation is presented in Fig. 6.14 (b-c). The activation energy is calculated for both stages of oxidation by using model-free kinetic methods such as Kissinger-Akahira-Sunose (KAS) [29] and Flynn-Wall-Ozawa (FWO) [30]. These methods are helpful to calculate the activation energy at each conversion value without assuming any reaction model. Several kinetic methods by using different temperature approximations have been proposed [31]. Among all kinetics methods, KAS and FWO kinetic methods are considered suitable methods for the calculation of activation energy. The activation energy is determined through linear fitted curves obtained from KAS $\left(ln\left(\frac{\beta}{T^{1.92}}\right) \text{vs.} \frac{1}{T}\right)$ and FWO $\left(ln(\beta) \text{ vs.} \frac{1}{T}\right)$ kinetic methods at each conversion fraction. Fig. 6.15 shows the linear fitted curves obtained from KAS and FWO kinetic methods for both oxidation stages.

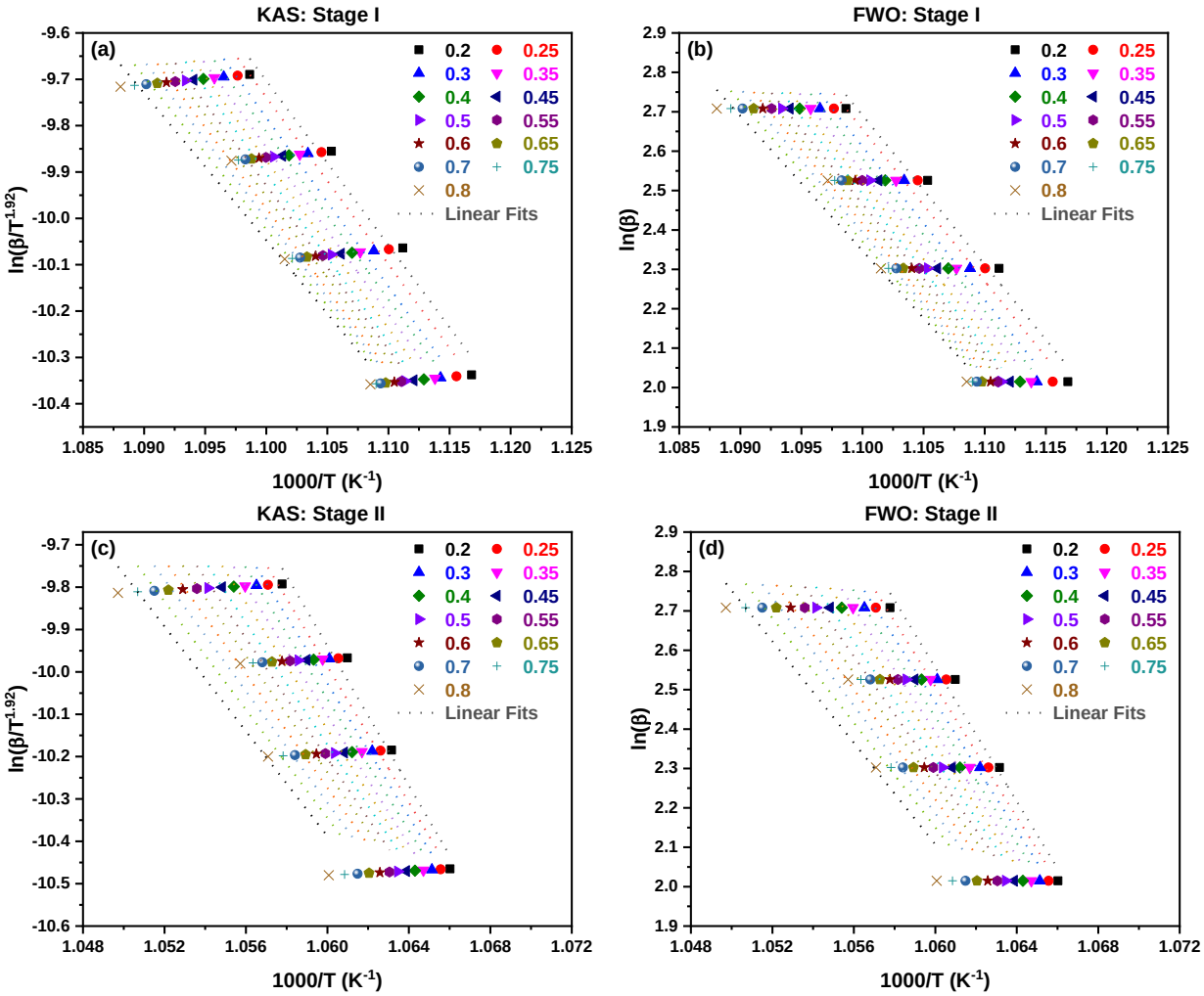

Fig. 6.15 Linear fitted plots obtained from KAS and FWO iso-conversional kinetic methods for (a-b) oxidation stage I and (c-d) oxidation stage II.

The variation in activation energy w.r.t. conversion fraction (Fig. 6.16) calculated from KAS and FWO methods is found to be identical for oxidation stage I (Fig. 6.16a) and stage II (Fig. 6.16b). However, the activation energy value calculated from FWO method is slightly higher than the KAS method. Furthermore, the average value of activation energy calculated from KAS and FWO methods for oxidation stage I is 290.02 kJ/mol and 313.05 kJ/mol, respectively. However, activation energy is higher for stage II as compared to stage I. The average activation energy for stage II is 596.55 kJ/mol and 622.54 kJ/mol as calculated from KAS and FWO methods, respectively.

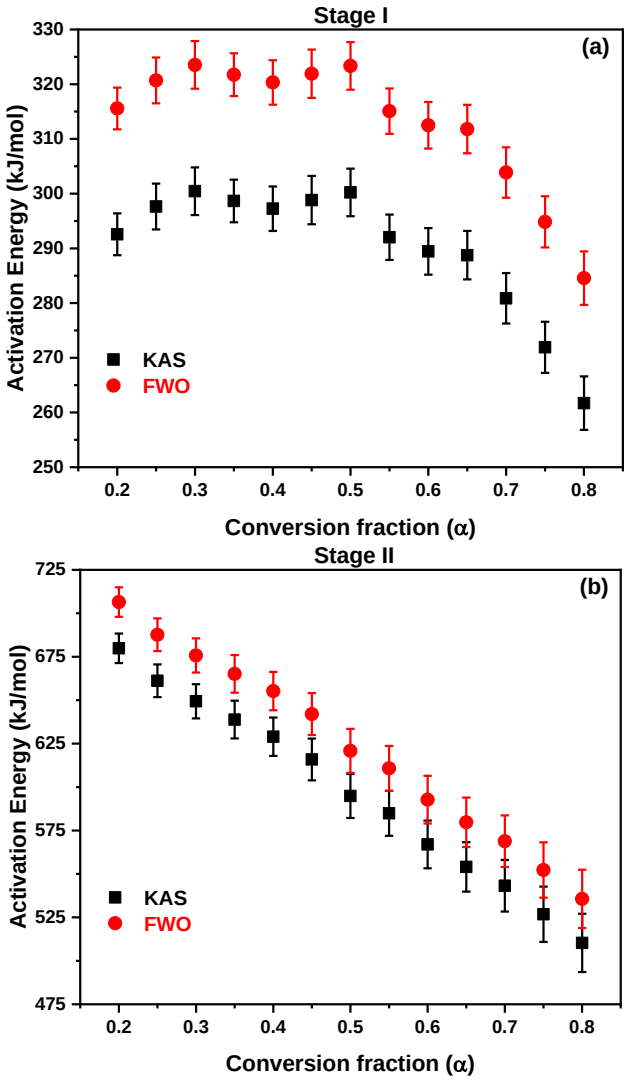

Fig. 6.16 The variation of activation energy w.r.t. temperature for (a) oxidation stage I and (b) oxidation stage II of the 15VAC 3 sample.

The integral master plots method is used to estimate the reaction mechanism involved during oxidation of V_2AlC MAX [32,33]. The detailed description related to the integral master plots method is published elsewhere [34,35]. In this method, the experimental curves are compared with theoretical curves corresponding to various kinetic mechanisms (Table 3.1).

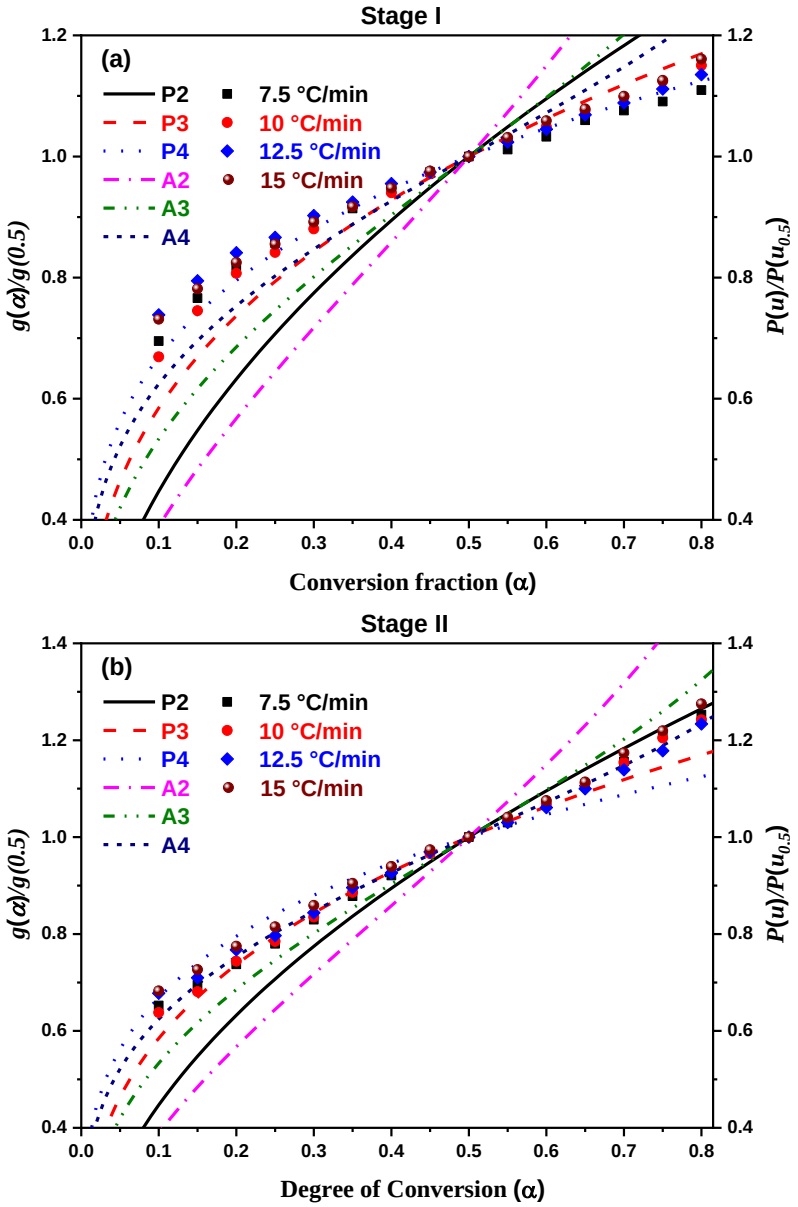

Fig. 6.17 The comparison of the theoretical master curves and the experimental curves for the oxidation stage II of the 15VAC 3 sample.

The theoretical curves are calculated from $g(\alpha)/g(0.5)$ based on different kinetic mechanisms (Table 3.1). The experimental curves are calculated from $P(u)/P(0.5)$ by using the average activation energy calculated from KAS method. Fig. 6.17 demonstrated the comparison of the theoretical and experimental curves for both the oxidation stages. It is observed that P4 and A4 nucleation reaction mechanisms dominated the oxidation of V_2AlC in stage I (Fig. 6.17a) and stage II (Fig. 6.17b), respectively. The value of pre-exponential factor is calculated by substituting the predetermined value of activation energy and reaction mechanism in a relation below:

$$g(\alpha) = \frac{AE}{\beta R} P(u) \tag{12}$$

The linear fitted curves (Fig. 6.18a-b) between $g(\alpha)$ and $\frac{E}{\beta R} P(u)$ gives the value of pre-exponential factor for both stages of oxidation. The value of pre-exponential factor calculated at all heating rates for both stages of oxidation is presented in Fig. 6.18c-d. Finally, Table 6.5 shows the value of kinetic triplets calculated for both oxidation stages of V_2AlC MAX phase.

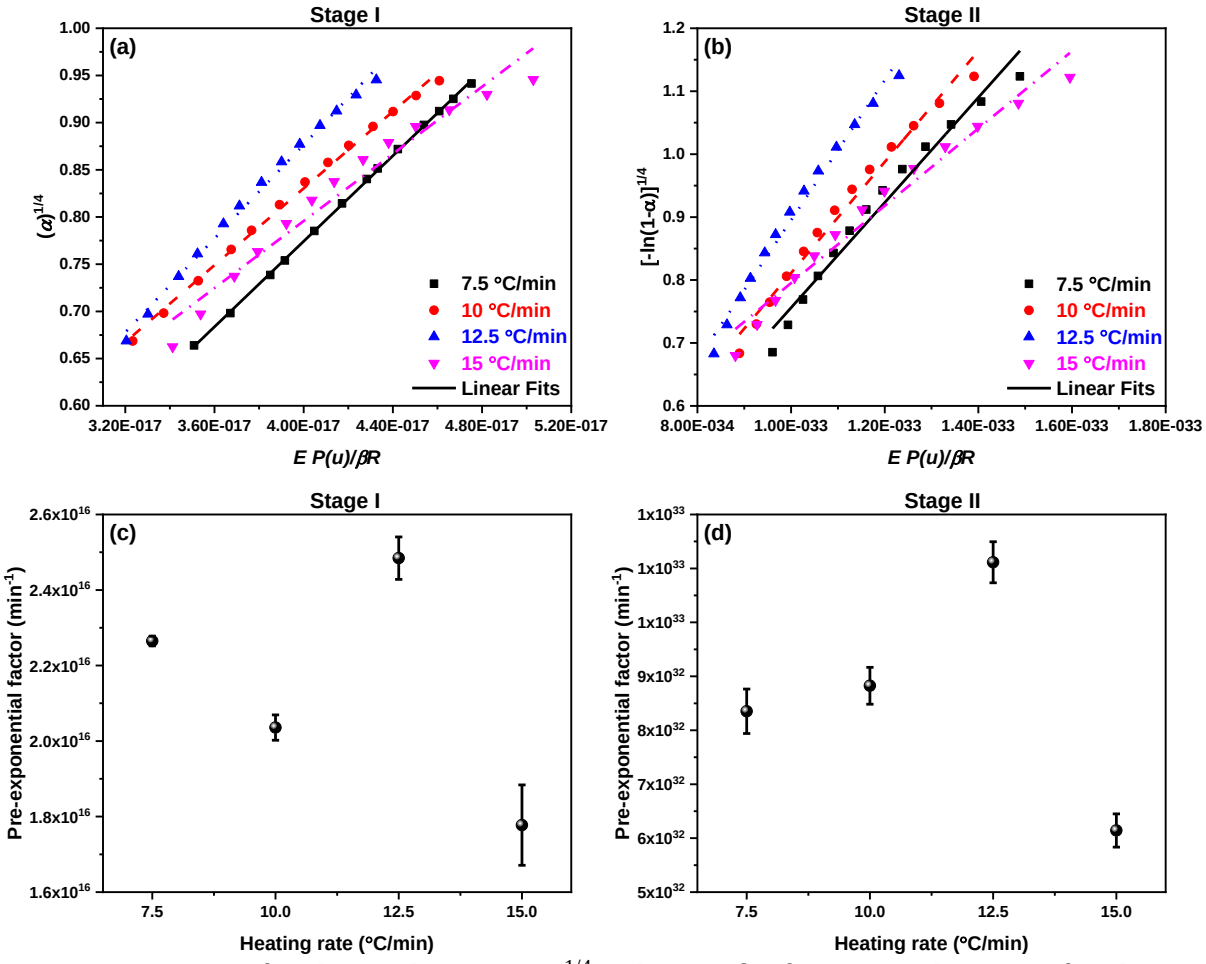

Fig. 6.18 (a) Linear fitted curve between $(\alpha)^{1/4}$ and EP(u)/βR for stage I. (b) Linear fitted curve between $[-\ln(1-\alpha)]^{1/4}$ and EP(u)/βR for stage II. Variation of pre-exponential w.r.t. heating rates along with the standard error for (c) stage I and (d) stage II.

Table 6.5 Kinetic triplets involved during oxidation of V_2AlC MAX phase.

	Kinetic triplets			
	Average activation energy (kJ/mol)		**Average pre-exponential factor (min^{-1})**	**Reaction mechanism**
	KAS	**FWO**		
Stage I	290.02 ± 4.32	313.05 ± 4.31	$2.14 \times 10^{16} \pm 0.052 \times 10^{16}$	P4
Stage II	596.55 ± 12.52	622.54 ± 12.51	$8.61 \times 10^{32} \pm 0.36 \times 10^{32}$	A4

References

[1] W. Hu, Z. Huang, Y. Wang, X. Li, H. Zhai, Y. Zhou, L. Chen, Layered ternary MAX phases and their MX particulate derivative reinforced metal matrix composite:A review, J. Alloys Compd. (2020). https://doi.org/10.1016/j.jallcom.2020.157313.

[2] J. Gonzalez-Julian, Processing of MAX phases: From synthesis to applications, J. Am. Ceram. Soc. (2020). https://doi.org/10.1111/jace.17544.

[3] Y. Zhong, X.H. Xia, F. Shi, J.Y. Zhan, J.P. Tu, H.J. Fan, Transition metal carbides and nitrides in energy storage and conversion, Adv. Sci. 3 (2015) 1–28. https://doi.org/10.1002/advs.201500286.

[4] M. Sokol, V. Natu, S. Kota, M.W. Barsoum, On the Chemical Diversity of the MAX Phases, Trends Chem. 1 (2019) 210–223. https://doi.org/10.1016/j.trechm.2019.02.016.

[5] D.J. Tallman, B. Anasori, M.W. Barsoum, A critical review of the oxidation of Ti_2AlC, Ti_3AlC_2 and Cr_2AlC in Air, Mater. Res. Lett. 1 (2013) 115–125. https://doi.org/10.1080/21663831.2013.806364.

[6] I.M. Low, An overview of parameters controlling the decomposition and degradation of Ti-based $M_{n+1}AX_n$ phases, Materials (Basel). 12 (2019) 473. https://doi.org/10.3390/ma12030473.

[7] J. Frodelius, J. Lu, J. Jensen, D. Paul, L. Hultman, P. Eklund, Phase stability and initial low-temperature oxidation mechanism of Ti_2AlC thin films, J. Eur. Ceram. Soc. 33 (2013) 375–382. https://doi.org/10.1016/j.jeurceramsoc.2012.09.003.

[8] P. Sharma, O.P. Pandey, Non-isothermal oxidation kinetics of nano-laminated Cr_2AlC MAX phase, J. Alloys Compd. 773 (2019) 872–882. https://doi.org/10.1016/j.jallcom.2018.09.326.

[9] R. Pei, S.A. McDonald, L. Shen, S. van der Zwaag, W.G. Sloof, P.J. Withers, P.M. Mummery, Crack healing behaviour of Cr_2AlC MAX phase studied by X-ray tomography, J. Eur. Ceram. Soc. 37 (2017) 441–450. https://doi.org/10.1016/j.jeurceramsoc.2016.07.018.

[10] Z. Wang, J. Sun, B. Xu, Y. Liu, P. Ke, A. Wang, Reducing the self-healing temperature of Ti_2AlC MAX phase coating by substituting Al with Sn, J. Eur. Ceram. Soc. 40 (2020) 197–201. https://doi.org/10.1016/j.jeurceramsoc.2019.09.009.

[11] G.M. Song, Y.T. Pei, W.G. Sloof, S.B. Li, J.T.M. De Hosson, S. van der Zwaag, Oxidation-induced crack healing in Ti_3AlC_2 ceramics, Scr. Mater. 58 (2008) 13–16. https://doi.org/10.1016/j.scriptamat.2007.09.006.

[12] W.G. Sloof, R. Pei, S.A. McDonald, J.L. Fife, L. Shen, L. Boatemaa, A.S. Farle, K. Yan, X. Zhang, S. Van Der Zwaag, P.D. Lee, P.J. Withers, Repeated crack healing in MAX-phase ceramics revealed by 4D in situ synchrotron X-ray tomographic microscopy, Sci. Rep. 6 (2016). https://doi.org/10.1038/srep23040.

[13] Z. Su, S. Zeng, J. Zhou, Z. Sun, Synthesis and characterization of Cr_2AlC with nanolaminated particles, Chinese Sci. Bull. 59 (2014) 3266–3270. https://doi.org/10.1007/s11434-014-0315-5.

[14] M.T. Agne, M. Radovic, G.W. Bentzel, M.W. Barsoum, Stability of V_2AlC with Al in 800-1000 °C temperature range and in situ synthesis of V_2AlC/Al composites, J. Alloys Compd. 666 (2016) 279–286. https://doi.org/10.1016/j.jallcom.2016.01.050.

[15] G. Greczynski, D. Primetzhofer, L. Hultman, Reference binding energies of transition metal carbides by core-level x-ray photoelectron spectroscopy free from Ar + etching artefacts, Appl. Surf. Sci. 436 (2018) 102–110. https://doi.org/10.1016/j.apsusc.2017.11.264.

[16] G. Greczynski, S. Mráz, L. Hultman, J.M. Schneider, Venting temperature determines surface chemistry of magnetron sputtered TiN films, Appl. Phys. Lett. 108 (2016). https://doi.org/10.1063/1.4940974.

[17] C. Azina, S. Mráz, G. Greczynski, M. Hans, D. Primetzhofer, J.M. Schneider, P. Eklund, Oxidation behaviour of V_2AlC MAX phase coatings, J. Eur. Ceram. Soc. 40 (2020) 4436–4444. https://doi.org/10.1016/j.jeurceramsoc.2020.05.080.

[18] J. Halim, K.M. Cook, M. Naguib, P. Eklund, Y. Gogotsi, J. Rosen, M.W. Barsoum, X-ray photoelectron spectroscopy of select multi-layered transition metal carbides (MXenes), Appl. Surf. Sci. 362 (2016) 406–417. https://doi.org/10.1016/j.apsusc.2015.11.089.

[19] S.R. Kulkarni, M. Merlini, N. Phatak, S.K. Saxena, G. Artioli, S. Gupta, M.W. Barsoum, High-temperature thermal expansion and stability of V_2AlC Up to 950°C, J. Am. Ceram. Soc. 90 (2007) 3013–3016. https://doi.org/10.1111/j.1551-2916.2007.01847.x.

[20] M. Baben, L. Shang, J. Emmerlich, J.M. Schneider, Oxygen incorporation in M_2AlC (M = Ti, V, Cr), Acta Mater. 60 (2012) 4810–4818. https://doi.org/10.1016/j.actamat.2012.05.011.

[21] S. Gupta, M.W. Barsoum, Synthesis and Oxidation of V_2AlC and $(Ti_{0.5},V_{0.5})_2AlC$ in Air, J. Electrochem. Soc. 151 (2004) D24. https://doi.org/10.1149/1.1639160.

[22] B. Wang, A. Zhou, Q. Hu, L. Wang, Synthesis and oxidation resistance of V_2AlC powders by molten salt method, Int. J. Appl. Ceram. Technol. 14 (2017) 873–879. https://doi.org/10.1111/ijac.12723.

[23] M.T. Agne, M.W. Barsoum, Enthalpy of formation and thermodynamic parameters of the MAX phase V_2AlC, J. Alloys Compd. 665 (2016) 218–224. https://doi.org/10.1016/j.jallcom.2015.12.204.

[24] V.N. Lipatnikov, A.I. Gusev, P. Ettmeier, W. Lengauer, Order-disorder phase transformations and specific heat of nonstoichiometric vanadium carbide, Phys. Solid State. 41 (1999) 474–480. https://doi.org/10.1134/1.1130806.

[25] M. Binnewies, E. Milke, Thermochemical Data of Elements and Compounds: Second, Revised and Extended Edition, 2008. https://doi.org/10.1002/9783527618347.

[26] P. Sharma, P.K. Diwan, O.P. Pandey, Impact of environment on the kinetics involved in the solid-state synthesis of bismuth ferrite, Mater. Chem. Phys. 233 (2019) 171–179. https://doi.org/10.1016/j.matchemphys.2019.05.055.

[27] P. Sharma, P.K. Diwan, Study of thermal decomposition process and the reaction mechanism of the eucalyptus wood, Wood Sci. Technol. 128 (2017) 875–882. https://doi.org/10.1007/s00226-017-0924-7.

[28] G. Kaur, P. Sharma, R. Priya, O.P. Pandey, Thermal dehydration kinetics involved during the conversion of gadolinium hydroxide to gadolinium oxide, J. Alloys Compd. 822 (2020). https://doi.org/10.1016/j.jallcom.2019.153450.

[29] T. Akahira, T. Sunose, Method of determining activation deterioration constant of electrical insulating materials, Res. Rep. Chiba. Inst. Technol. (Sci Technol). 16 (1971) 22–31.

[30] J.H. Flynn, L.A. Wall, A quick, direct method for the determination of activation energy from thermogravimetry data, J. Polym. Sci. Part C Polym. Lett. 4 (1966) 323–328.

[31] S. Vyazovkin, A.K. Burnham, J.M. Criado, L.A. Pérez-Maqueda, C. Popescu, N. Sbirrazzuoli, ICTAC Kinetics Committee recommendations for performing kinetic computations on thermal analysis data, Thermochim. Acta. 520 (2011) 1–19. https://doi.org/10.1016/j.tca.2011.03.034.

[32] S. Vyazovkin, A.K. Burnham, J.M. Criado, L.A. Pérez-Maqueda, C. Popescu, N. Sbirrazzuoli, ICTAC Kinetics Committee recommendations for performing kinetic computations on thermal analysis data, Thermochim. Acta. 520 (2011) 1–19. https://doi.org/10.1016/j.tca.2011.03.034.

[33] J. Chen, Y. Wang, X. Lang, X. Ren, S. Fan, Evaluation of agricultural residues pyrolysis under non-isothermal conditions: Thermal behaviors, kinetics, and thermodynamics,

Bioresour. Technol. 241 (2017) 340–348. https://doi.org/10.1016/j.biortech.2017.05.036.

[34] P. Sharma, O.P. Pandey, P.K. Diwan, Non-isothermal kinetics of pseudo-components of waste biomass, Fuel. 253 (2019) 1149–1161. https://doi.org/10.1016/j.fuel.2019.05.093.

[35] P. Sharma, O.P. Pandey, Thermal kinetics involved during the solid-state synthesis of Cr_2AlC MAX phase, J. Therm. Anal. Calorim. (2020). https://doi.org/10.1007/s10973-020-09390-8.

CHAPTER 7

CONCLUSIONS & FUTURE SCOPE

Overview

This chapter outlines the complete work done on the synthesis of Cr_2AlC, Ti_3AlC_2 and V_2AlC MAX phases. The optimization of synthesis parameters such as composition and temperature are discussed. The reaction pathway involved during formation of these MAX phases on the basis of experimental results is proposed. The non-isothermal oxidation performance of the MAX phases is compiled. The course of oxidation in the MAX phases is summarized. The outcomes of oxidation kinetics analysis of Cr_2AlC, Ti_3AlC_2 and V_2AlC MAX phases are summed up. The kinetic triplets (activation energy, pre-exponential factor and reaction mechanism) responsible for the oxidation in the MAX phases are concluded. The future scope on the behalf of current research outcome is presented at the end of this chapter.

7.1. Conclusions

MAX phases are the layered ternary carbides or nitrides that own rare combination of metal and ceramic properties. These remarkable properties of MAX phases made them suitable candidate for a wide range of industrial applications. The efficacy of a MAX phase substantially depends on its purity. The methodology and experimental condition play an indispensable role during the synthesis of high purity MAX phases. The MAX phases are also proven to be good oxidation resistant even at elevated temperature. On the basis of research work conducted in the present thesis, the conclusions drawn are presented below:

- The impact of the aluminum (Al) content on the formation of the Cr_2AlC MAX phase is systematically studied. A highly pure Cr_2AlC MAX phase is obtained, when a CAC-4 sample is sintered at 1300 ºC. The formation of Cr_2AlC was confirmed through X-ray diffraction (XRD) analysis. The kinetic involved in the formation of Cr_2AlC MAX phase has been studied by using differential thermal analysis (DTA) at multiple heating rates. The kinetic triples (activation energy, pre-exponential factor and reaction mechanism) responsible for the formation of Cr_2AlC MAX phase are determined. Furthermore, a typical signature of the MAX phase is identified in the micrographs. The results of the FE-SEM and TEM analysis are analogous to the XRD results. The X-ray photoelectron spectroscopy (XPS) of Cr2p, C1s, Al2p, and O1s also confirms the formation of the Cr_2AlC MAX phase. The non-isothermal oxidation kinetics of the Cr_2AlC MAX phase is studied. The TGA/DTA results reveal that the oxidation occurred in two stages. It is observed that the value of the activation energy is considerably greater for the oxidation stage II as compared to the oxidation stage I. The higher activation energy in the oxidation stage II may correspond to the formation of the Al_2O_3 layer over the surface of the Cr_2AlC MAX phase. Finally, the reaction mechanism involved during oxidation of the Cr_2AlC MAX phase is proposed. The first order random nucleation (F1) dominates the oxidation process in stage I, while the third order random nucleation (F3) dominates in the oxidation stage II of the Cr_2AlC MAX phase.
- A ternary nanolaminated Ti_3AlC_2 MAX phase is successfully synthesized through pressureless sintering route. The composition and the sinterring temperature is optimized to obtain highly pure Ti_3AlC_2 MAX phase. The reactions involved during formation of Ti_3AlC_2 are identified and reaction pathway is proposed. The thermal kinetics accountable during synthesis of Ti_3AlC_2 is detemined through DTA technique.

In addition, kinetic triplets are calculated for the endothermic peak assigned to the formation of Ti_3AlC_2. The morphological features of fractured surface of Ti_3AlC_2 phase shared a typical nanolaminated structure of the MAX phases. The stacking of layers became more prominent in highly pure Ti_3AlC_2 due to less carbide content. The thickness of the stacked layers is found to be non-uniform. The HRTEM (High-Resolution Transmission Electron Microscopy) and SAED (Selected area (electron) diffraction) demonstrated planes corresponding to hexagonal Ti_3AlC_2 phase. The synthesis of Ti_3AlC_2 is also verified through XPS spectra of Ti2p, C1s, Al2p, and O1s. Moreover, non-isothermal oxidation behaviour of Ti_3AlC_2 is also examined by using DTA technique. The MAX phase is heated from room temperature to 1300 ℃ in air atmosphere at multiple heating rates. The oxidation reaction route is determined through XRD and DTA techniques. Three exothermic peaks (~ 522, 628 and 860 ºC) are observed during DTA analysis of the Ti_3AlC_2 phase. The former two peaks correspond to the oxidation of TiC impurity present and formation of Al_2O_3 on the surface of the MAX phase. The oxidation kinetics involved in all three exothermic peaks is studied. The value of activation energy and pre-exponential factor are determined. The results of kinetic analysis demonstrated that the oxidation in peak I and peak III occurred due to F2 (second order reaction) reaction mechanism. However, the F3 (third order reaction) reaction mechanism dominated the oxidation in peak II.

- The variation in aluminium content is found to be helpful to obtain nanolaminated V_2AlC MAX phase through pressureless sintering. The V_2AlC MAX phase is successfully synthesized at 1500 ºC when the initial composition is V:Al:C = 2:1.3:1. The reaction pathway involved during formation of V_2AlC is proposed with the help of XRD results. The characteristic morphology of MAX phase is observed in the prepared samples. The formation of V_2AlC MAX phase is confirmed through XPS spectra of V2p, C1s, Al2p, and O1s. The oxidation stability of the V_2AlC is studied under non-isothermal conditions through a DTA technique at multiple heating rates in the air atmosphere. It is observed that the oxidation of V_2AlC occurred in two different stages. Moreover, thermodynamic calculations are presented to predict the oxidation reaction route of V_2AlC MAX phase. The kinetic triplets (activation energy, pre-exponential factor and reaction mechanism) are determined for both stages of oxidation. The results indicated that the nucleation mechanism dominated the oxidation process in the V_2AlC MAX phase. P4 and A4 nucleation reaction mechanisms are found to be responsible during oxidation stage I and stage II, respectively.

7.2. Summary

The outcome of the present work related to the synthesis and oxidation kinetics of Cr_2AlC, Ti_3AlC_2 and V_2AlC MAX phase is presented in Table 7.1 – 7.2. Table 7.1 shows the synthesis parameters and the volume fraction of the MAX phases observed in the work done. Table 7.2 shows the results of oxidation kinetic analysis and kinetic triplets determined for the synthesized MAX phases.

Table 7.1 Experimental conditions and the volume fraction (%) of phases present in the prepared MAX phases

MAX Phases	Molar ratio			Sintering temperature	Volume Fraction (%)					
	Ti/V/Cr	TiC/C	Al		Cr_7C_3	TiC	V_8C_7	Cr_2AlC	Ti_3AlC_2	V_2AlC
Cr_2AlC	Cr = 2	C = 1	1.4	1300 ℃	1.82	–	–	98.17	–	–
Ti_3AlC_2	Ti = 1	TiC = 1	1.3	1500 ℃	–	2.06	–	–	97.94	–
V_2AlC	V = 2	C = 1	1.3	1500 ℃	–	–	4.02	–	–	95.98

Table 7.2 Kinetic triplets involved during oxidation of Cr_2AlC, Ti_3AlC_2 and V_2AlC MAX phases.

MAX Phases		Kinetic triplets			
		Average activation energy (kJ/mol)		Average pre-exponential factor (min^{-1})	Reaction mechanism
		KAS	FWO		
Cr_2AlC	Stage I	146.37 ± 0.54	154.62 ± 1.07	$2.02\times10^{7} \pm 2.47\times10^{5}$	F1
	Stage II	513.44 ± 5.86	511.80 ± 5.61	$3.89\times10^{19} \pm 1.02\times10^{18}$	F3
Ti_3AlC_2	Stage I	335.88 ± 4.09	340.30 ± 4.10	$5.55\times10^{22} \pm 7.69\times10^{19}$	F2
	Stage II	988.83 ± 38.26	967.30 ± 38.22	$3.58\times10^{55} \pm 3.06\times10^{54}$	F3
	Stage III	544.22 ± 3.21	544.19 ± 3.19	$6.69\times10^{24} \pm 2.34\times10^{23}$	F2
V_2AlC	Stage I	290.02 ± 4.32	313.05 ± 4.31	$2.14\times10^{16} \pm 0.052\times10^{16}$	P4
	Stage II	596.55 ± 12.52	622.54 ± 12.51	$8.61\times10^{32} \pm 0.36\times10^{32}$	A4

7.3. Future Prospective

The synthesis protocol suggested in the thesis can be utilized for the synthesis of other MAX phases and MAX phase-based composites. The prepared MAX phases are promising candidates for the development of their two-dimensional derivatives, i.e., MXenes. The MXenes are promising candidates for plethora of technological applications. In addition, the good oxidation resistance of the prepared MAX phases even at elevated temperatures makes them suitable for several applications such as heating elements, coating material, foil bearing and gas nozzle. Further, a systematic isothermal oxidation kinetic analysis must be performed to get more information related to the oxidation of the MAX phases. The doping or substitution of rare earth elements or other transition metals need to be investigated to improve the oxidation performance of the prepared MAX phases. This will bring new opportunities and expansion in the MAX phase family.